

Inverse and optimization problems in piezoelectric materials using Extended Finite Element Method and Level sets

**Inverse und Optimierungsprobleme für piezoelektrische
Materialen mit der *Extended* Finite Elemente Methode und *Level
sets***

CUMULATIVE DISSERTATION

Zur Erlangung des akademischen Grades eines

Doktor-Ingenieur

an der Fakultät Bauingenieurwesen

der Bauhaus-Universität Weimar

vorgelegt von

SRIVILLIPUTTUR SUBBIAH NANTHAKUMAR

(interner Doktorand)

aus

Indien

Mentor: Prof. Dr.-Ing. Timon Rabczuk

Weimar, 30. Juni 2015

Acknowledgements

I feel very happy to write this acknowledgement. My heartfelt thanks to Prof. Timon Rabczuk. I feel lucky to have got an opportunity to work under Prof. Rabczuk. I learnt many attributes from Prof. Rabczuk. I specially thank Professor for the freedom I got so that I was able to work without much effort. The encouraging words and support from Professor helped to easily overcome the few tough times during the research.

My heartfelt thanks to Prof. Tom Lahmer, for i learnt all the basics about inverse problems and piezoelectricity from Professor. I thank Professor for the interest he showed and the readiness with which he came forward to support whenever I asked for one. I thank Professor for making me appear in symposiums to exhibit my work and for the time and effort Professor spent in correcting my manuscripts and in discussion.

I thank Prof. Harold S Park. I thank Professor for the time and effort spent in improving the quality of writing in the manuscripts. I thank Professor for introducing me to new field of nano material modelling.

I thank Navid for the time he spent in discussion regarding nano elasticity and help in deriving the shape derivative for optimization of nano elastic structures. I thank Luu Mai, for the support and help during my stay in Weimar. I thank Vu Bac Nam, for supporting and encouraging me throughout my PhD. I thank Mohammed Altay for helping me without hesitation in many circumstances inspite of his works. I thank Hamdia, Pattabhi Budarapu, Chao Zhang and other ISM friends.

I thank Frau. Marlies Terber for readily helping me whenever needed. I thank Rosemarie for supporting me in several circumstances.

I thank my friends Dixon Arulraj, Shanmugam, Naren Prabakaran for considering me as their brother and offering me food and shelter (!), supporting me morally all these three years. I thank my master students Satheesha Reddy and Jhansi for their patience and for the discussions during which I

understood certain aspects of my work better.

Finally, I thank my amma and naina, for giving me freedom to change my career from company to research. I thank them for bearing with the difficulties I gave them during my research. I dedicate all my effort in this research work to my parents. I thank my sister Nandhini for her constant moral support in making my dream to do research possible.

I thank my wife, Iniya Nanthakumar for her extreme strength and ability to encourage and support me inspite of her work.

I thank creation for giving me a happy life.

Weimar, 30. Juni 2014

Srivilliputtur Subbiah Nanthakumar

Abstract

Piezoelectric materials are used in several applications as sensors and actuators where they experience high stress and electric field concentrations as a result of which they may fail due to fracture. Though there are many analytical and experimental works on piezoelectric fracture mechanics. There are very few studies about damage detection, which is an interesting way to prevent the failure of these ceramics.

An iterative method to treat the inverse problem of detecting cracks and voids in piezoelectric structures is proposed. Extended finite element method (XFEM) is employed for solving the inverse problem as it allows the use of a single regular mesh for large number of iterations with different flaw geometries.

Firstly, minimization of cost function is performed by Multilevel Coordinate Search (MCS) method. The XFEM-MCS methodology is applied to two dimensional electromechanical problems where flaws considered are straight cracks and elliptical voids. Then a numerical method based on combination of classical shape derivative and level set method for front propagation used in structural optimization is utilized to minimize the cost function. The results obtained show that the XFEM-level set methodology is effectively able to determine the number of voids in a piezoelectric structure and its corresponding locations.

The XFEM-level set methodology is improved to solve the inverse problem of detecting inclusion interfaces in a piezoelectric structure. The material interfaces are implicitly represented by level sets which are identified by applying regularisation using total variation penalty terms. The formulation is presented for three dimensional structures and inclusions made of different materials are detected by using multiple level sets. The results obtained prove that the iterative procedure proposed can determine the location and approximate shape of material subdomains in the presence of higher noise levels.

Piezoelectric nanostructures exhibit size dependent properties because of surface elasticity and surface piezoelectricity. Initially a study to understand the influence of surface elasticity on optimization of nano elastic

beams is performed. The boundary of the nano structure is implicitly represented by a level set function, which is considered as the design variable in the optimization process. Two objective functions, minimizing the total potential energy of a nanostructure subjected to a material volume constraint and minimizing the least square error compared to a target displacement, are chosen for the numerical examples. The numerical examples demonstrate the importance of size and aspect ratio in determining how surface effects impact the optimized topology of nanobeams.

Finally a conventional cantilever energy harvester with a piezoelectric nano layer is analysed. The presence of surface piezoelectricity in nano beams and nano plates leads to increase in electromechanical coupling coefficient. Topology optimization of these piezoelectric structures in an energy harvesting device to further increase energy conversion using appropriately modified XFEM-level set algorithm is performed .

Contents

1	Summary	1
1.1	Piezoelectricity	1
1.1.1	Piezoelectric effect	1
1.1.2	Basic Piezoelectric Relations	3
1.2	Extended Finite Element Method	4
1.2.1	Basic XFEM approximation	5
1.2.2	Level set function	7
1.2.3	Inverse Problem	7
1.3	Optimization problems	11
1.3.1	Mathematical form of a structural optimization problem . . .	13
1.3.2	Solid isotropic material with penalization (SIMP)	14
1.3.3	Level set based optimization	14
1.4	Nanoelasticity	15
1.5	Nanopiezoelectricity	17
1.6	Objectives and outline of the thesis	18
1.6.1	Chapter 2	18
1.6.2	Chapter 3	19
1.6.3	Chapter 4	19
1.6.4	Chapter 5	20
1.6.5	Chapter 6	20
1.7	State of Art	21
1.8	Results and discussion	32
1.8.1	XFEM-MCS methodology for inverse problem of flaw detection	32
1.8.2	XFEM-level set methodology for inverse problem of flaw de- tection	37
1.8.3	XFEM and level sets for the inverse problem of inclusion de- tection	40
1.8.4	XFEM and level sets for optimization of nano beams	44
1.8.5	XFEM and level sets for optimization of nano piezoelectric structures	48

CONTENTS

2	Detection of a single flaw in Piezoelectric Structures using XFEM	52
2.1	Contribution of authors	52
2.2	Introduction	53
2.3	Basic Piezoelectric Relations	54
2.4	Extended Finite Element Formulation	56
2.5	Inverse Problem	58
2.5.1	Multilevel Coordinate Search-MCS	59
2.5.2	Key components of MCS	60
2.6	Numerical Examples	61
2.6.1	Edge Crack	62
2.6.2	Interior Crack	64
2.6.3	Elliptical Void	65
2.6.4	Non-Elliptical void configurations	65
2.6.5	Influence of Noise and inexactness in material parameters	70
2.7	Conclusion	71
3	Detection of multiple flaws in piezoelectric structures using XFEM and level sets	76
3.1	Contribution of authors	76
3.2	Introduction	77
3.3	Shape derivative and level set method	77
3.4	Numerical Examples	80
3.4.1	Single void	81
3.4.2	Multiple voids	81
3.4.3	Cracks	83
3.4.4	Voids and cracks	85
3.5	Conclusion	87
4	Detection of material interfaces using a regularised level set method in piezoelectric structures	90
4.1	Contribution of authors	90
4.2	Introduction	91
4.3	Inverse problem	92
4.3.1	The Level set method	92
4.3.2	Measurement techniques	93
4.3.3	Selection of the regularisation parameter, β	93
4.4	The forward and adjoint problem	94
4.5	Numerical Examples	98
4.5.1	Multiple inclusions	100
4.5.2	Multiple inclusions in a 3D piezoelectric structure	103
4.5.3	Multiple defects	104

CONTENTS

4.5.4	Multiple level sets	109
4.6	Conclusion	111
5	Topology optimization of nano elastic beams	114
5.1	Contribution of authors	114
5.2	Introduction	115
5.3	Continuum model	116
5.4	Level set method	118
5.5	Material derivative approach and sensitivity analysis	121
5.5.1	Material derivative	121
5.5.2	Sensitivity analysis	123
5.6	Extended finite element method	124
5.7	Numerical examples	126
5.7.1	Cantilever beam	128
5.7.2	Fixed beam	136
5.8	Conclusion	140
6	Topology optimization of nano piezoelectric structures	142
6.1	Contribution of authors	142
6.2	Introduction	143
6.3	Governing equations of surface piezoelectricity	144
6.4	XFEM formulation for nano-piezoelectricity	146
6.5	Topology optimization of piezoelectric nano energy harvesters	147
6.5.1	Objective function	147
6.5.2	Level set method and sensitivity analysis	148
6.6	Numerical Examples	150
6.6.1	Piezoelectric nano beam	151
6.6.2	Three-Dimensional Piezoelectric Nanoplate	154
6.6.3	Piezoelectric nano bimorph	155
6.7	Conclusion	159
7	Conclusions	162
7.1	Summary of findings	162
7.2	Scope for future work	164
A		165
A.1	Derivation of shape derivative	165
B		169
B.1	Derivation of adjoint problem	169
B.2	Bulk and Surface Stiffness Matrices	171

CONTENTS

B.3 Finite element modelling of piezoelectric nano energy harvester plate	172
References	175
Curriculum Vitae	186

List of Figures

1.1	The crystal structure of Zinc Oxide and the deformation of the ZnO tetrahedra under compressive and tensile stresses ¹	2
1.2	The orientation of crystal domains (a) Before poling and (b) After poling ²	3
1.3	The nodes that belong to set J and set K in equation 1.10.	5
1.4	Absolute signed distance enrichment function ³	7
1.5	Partitioning of elements cut by void boundary	8
1.6	Levelset functions	8
1.7	(a) Forward problem, (b) Inverse problem.	9
1.8	A standard L-Curve ⁴	12
1.9	Structural optimization - Geometry of domain Ω to be determined such that objective function, J is minimized and the constraints are satisfied	13
1.10	(a) Initialization (b) Optimum topology for a short cantilever beam subjected to a point load at free end by Level set method (c) by SIMP ⁵ .	16
1.11	A typical cantilever energy harvester with piezoelectric layer, substrate and proof mass	17
1.12	Boundary conditions and Loads on the modeled Piezoelectric plate . .	33
1.13	Best crack parameters obtained using XFEM-MCS algorithm for Edge crack estimation	34
1.14	Convergence of XFEM-MCS methodology for two parameter estimation (Edge Crack) showing the variation of residual with number of function calls.	34
1.15	Convergence of XFEM-MCS methodology for 1 st parameter estimation (Edge Crack) - X - coordinate of the interior crack tip.	35
1.16	Convergence of XFEM-MCS methodology for 2 nd parameter estimation (Edge Crack) - Y - coordinate of the interior crack tip.	35
1.17	Best result determined by MCS for an inclined crack	36
1.18	Boundary conditions and loads on the modeled Piezoelectric plate . .	37
1.19	Initialization	38
1.20	Void configuration after 40 and the final void configuration	39
1.21	The variation of residual norm with increase in percentage of noise . .	40

LIST OF FIGURES

1.22	Piezoelectric domain with defects	41
1.23	Top row : Initial assumption and interface after 50 iterations, second row : Interface after 100 and 300 iterations, bottom row : Inclusion locations detected by the proposed algorithm (stiffness and permittivity ratio = 0.1).	42
1.24	Convergence of the objective function with iterations.	43
1.25	The smallest inclusion detected with a mesh of 50X50 and with 50 pseudo sensors. The radius of the actual void = 0.25 units	44
1.26	Optimal topology for objective function J_1 for a 80×10 nm simply supported nanobeam (a) with and (b) without surface effects.	46
1.27	Optimal topology for objective function J_2 for a simply supported (a) 80×10 , (b) 160×20 , (c) 320×40 , and (d) 480×60 nanobeam.	47
1.28	A piezoelectric nano cantilever plate subjected to point load, F at free end.	48
1.29	(a) Optimized topology (top view) of a $600 \times 300 \times 10$ nm cantilever piezoelectric nano bimorph plate subjected to point load at free end including surface effects; (b) Optimized topology (top view) of a $600 \times 300 \times 10$ nm cantilever piezoelectric nano bimorph plate subjected to point load at free end including surface effects.	50
1.30	Optimized topology (top view) of same geometry but without surface effects.	51
2.1	Piezoelectric domain with a Crack	55
2.2	Levelset Functions	56
2.3	3D Contour plot of the negative of objective function defined in equation 2.18 for a crack identification problem with $N=2$. The optimum is located at point (5.25,5.25)	59
2.4	Boundary conditions and Loads on the modeled Piezoelectric plate . .	62
2.5	Convergence of XFEM-MCS methodology for two parameter estimation (Edge Crack)	63
2.6	Best crack parameters obtained using XFEM-MCS algorithm for edge crack estimation	64
2.7	Convergence of XFEM-MCS methodology for Four parameter estimation (Interior Crack)	66
2.8	Best crack parameters obtained using XFEM-MCS algorithm for interior crack estimation	67
2.9	Convergence of XFEM-MCS methodology for Four parameter estimation (Elliptical Void)	68
2.10	Best Void parameters obtained using XFEM-MCS algorithm for detection of Elliptical Void	69
2.11	Best Void boundary determined by MCS for an inclined elliptical void	71

LIST OF FIGURES

2.12	Best Void boundary determined by MCS for non-elliptical voids . . .	72
2.13	Best result determined by MCS for an inclined crack	73
2.14	Influence of noise on inverse problem solution	74
2.15	Influence of inexactness in material properties on inverse problem solution	75
3.1	(a) Contour plot of level set function, (b) The corresponding irregular void boundary.	78
3.2	Boundary conditions and loads on the modeled Piezoelectric plate . .	80
3.3	Top row : Initial void configuration, Void configuration after 20 iterations, second row : Void configuration after 40 and 80 iterations, Bottom row : Final void configuration	82
3.4	(a) Convergence of the objective function, J with iteration, (b) Convergence of L^2 norm of error in parameter space with iterations. P , approximated level set value at nodes and P^f , level set values corresponding to true void configuration	83
3.5	Top row : Initial void configuration, Void configuration after 20 iterations, second row : Void configuration after 30 and 50 iterations, Bottom row : Void configuration after 100 and 150 iterations, Final void configuration	84
3.6	(a) Convergence of the objective function, J with iteration, (b) Convergence of L^2 norm of error in parameter space with iterations. P , approximated level set value at nodes and P^f , level set values corresponding to true void configuration	85
3.7	Top row : Initial void configuration, Void configuration after 20 iterations, second row : Void configuration after 50 and 100 iterations, Bottom row : Final void configuration.	86
3.8	(a) Convergence of the objective function, J with iterations, (b) Convergence of L^2 norm of error in parameter space with iterations. P , approximated level set value at nodes and P^f , level set values corresponding to true void configuration	87
3.9	Top row : Initial void configuration, Void configuration after 20 iterations, second row : Void configuration after 50 and 100 iterations, Bottom row : Final void configuration.	88
3.10	(a) Convergence of the objective function, J with iterations, (b) Convergence of L^2 norm of error in parameter space with iterations. P , approximated level set value at nodes and P^f , level set values corresponding to true void configuration	89
3.11	The influence of noise on accuracy of the algorithm	89
3.12	The influence of number of sensors on accuracy of the algorithm . . .	89

LIST OF FIGURES

4.1	Multiple level sets representation : The union of two level set functions, ϕ_1 and ϕ_2 gives the actual domain with inclusions	93
4.2	Boundary conditions and loads on the modelled Piezoelectric cube . .	99
4.3	(a) Multiple inclusions in a piezoelectric specimen, (b) Energy density contour	101
4.4	Level set function, Φ ; Top row : Initial interface configuration, Interface configuration after 50 iterations, Second row : Interface configuration after 75 iterations and final interface configuration determined by the algorithm.	101
4.5	(a) Convergence of the objective function, J with iterations, (b) Convergence of l^2 norm of error in parameter space with iterations. P , approximated level set value at nodes and P^f , level set values corresponding to true interface configuration.	102
4.6	Final reconstruction: (a) with 2% noise, (b) with 5% noise	102
4.7	(a) Variation of l^2 norm of error in parameter space with different levels of noise, (b) Variation of regularisation parameter β with different levels of noise	102
4.8	The smallest inclusion detected with a mesh of 50×50 and with 50 pseudo sensors. The radius of the actual void = 0.25 units	103
4.9	(a) Multiple inclusions in a 3D piezoelectric specimen, (b) Energy density contour across plane A, (c) Energy density contour across plane B	105
4.10	Top row : Initial interface configuration, Interface configuration after 20 iterations, second row : Void configuration after 50 and 100 iterations, Bottom row : Final void configuration and actual void configuration.	106
4.11	(a) Convergence of the objective function, J with iterations, (b) Convergence of l^2 norm of error in parameter space with iterations. P , approximated level set value at nodes and P^f , level set values corresponding to true interface configuration.	107
4.12	Final reconstruction: (a) with 2% noise, (b) with 5% noise	107
4.13	(a) Variation of l^2 norm of error in parameter space with different levels of noise, (b) Variation of regularisation parameter β with different levels of noise	107
4.14	Residual L-curve - Noise level = 5%	108
4.15	The regularised solution for (a) $\beta = 1e-3$, (b) $\beta = 2.5e-3$, (c) $\beta = 1e0$	108
4.16	Piezoelectric domain with defects	109
4.17	Top row : Initial assumption and interface after 50 iterations, second row : Interface after 100 and 300 iterations, bottom row : Inclusion locations detected by the proposed algorithm (stiffness and permittivity ratio = 0.1).	110

LIST OF FIGURES

4.18	(a) Convergence of the objective function, J with iterations, (b) Convergence of l^2 norm of error in parameter space with iterations. P , approximated level set value at nodes and P^f , level set values corresponding to true interface configuration.	111
4.19	Evolution of level set functions, ϕ_1 and ϕ_2 ; Top row : Initial interface configuration, Second row : Interface configuration after 100 iterations, Third row : Interface configuration after 250 iterations, Fourth row : Final configuration of ϕ_1 and ϕ_2 , Bottom row : Union of ϕ_1 and ϕ_2 and true interface configuration.	112
4.20	(a) Convergence of l^2 norm of error in parameter space with iterations. P , approximated level set value at nodes and P^f , level set values corresponding to true level set function ϕ_1 , (b) Convergence of l^2 norm of error in parameter space with iterations. P , approximated level set value at nodes and P^f , level set values corresponding to true level set function ϕ_2	113
5.1	Level set description of a plate with a hole. (<i>left</i>) Design domain (<i>right</i>) level set function.	120
5.2	Flowchart showing steps involved in the process of optimizing nano structures with surface effects	127
5.3	(a) Initialization (b) Optimum topology for a short cantilever beam subjected to a point load at free end by Level set method (c) by SIMP ⁵	129
5.4	Optimal topology for 80×20 nm cantilever nano beam for objective function J_1 (a) with surface effects , (b) without surface effects, i.e. taking \mathbb{C}_s and τ_s to be zero.	131
5.5	Optimal topology for 200×20 nm cantilever nano beam for objective function J_1 (a) with surface effects , (b) without surface effects, i.e. taking \mathbb{C}_s and τ_s to be zero.	132
5.6	The optimal topology obtained for J_2 objective function for 40×10 nm and 320×80 nm cantilever beams without surface effects (a),(c) and with surface effects (b),(d).	133
5.7	Intermediate topologies for optimization of objective function J_2 for 40×10 nm cantilever nanobeam with surface effects at iteration (a)1, (b)15, (c)35, (d)75, (e)200.	134
5.8	Convergence of Volume ratio, for objective function J_2 with iterations	134
5.9	Optimal topology for objective function J_2 for 40×10 nm cantilever nanobeam with surface effects for mesh sizes (a) 120×30 (b) 160×40 and (c) 180×45	135
5.10	Optimal topology for objective function J_1 for 80×10 nm fixed nanobeam (a) with surface effects, (b) without surface effects, i.e. taking \mathbb{C}_s and τ_s to be zero.	137

LIST OF FIGURES

5.11	Optimal topology for objective function J_2 for (a) 80×10 nm and (b) 160×20 nm fixed nanobeam.	138
5.12	Optimal topology for objective function J_2 for (a) 120×10 nm and (b) 240×20 nm fixed nanobeam.	139
5.13	Initialization (a),(c) and their corressponding Optimal topologies (b),(d) for objective function J_2 for 120×10 nm	140
6.1	Variation of nominal energy conversion factor with nanobeam depth, with the beam aspect ratio constant at 20.	151
6.2	Optimal topology for maximizing ECF of a piezoelectric nano cantilever beam, 40×10 nm.	153
6.3	A cantilever energy harvester with piezoelectric nano layer subjected to point load, F at free end.	154
6.4	Optimized topology (top view) of the piezoelectric layer of an EHD subjected to point load at free end. (a) 100 nm thick nanoplate; (b) 10 nm thick nanoplate.	156
6.5	The variation of nominal EMCC with varying thickness of piezo layer in EHD under open and closed circuit conditions.	157
6.6	A piezoelectric nano cantilever plate subjected to point load, F at free end.	157
6.7	Variation of dimensionless maximum deflection with depth of plate.	158
6.8	(a) Optimized topology (top view) of a $600 \times 300 \times 10$ nm cantilever piezoelectric nano bimorph plate subjected to point load at free end including surface effects; (b) Optimized topology (top view) of a $600 \times 300 \times 10$ nm cantilever piezoelectric nano bimorph plate subjected to point load at free end including surface effects.	160
6.9	Optimized topology (top view) of same geometry but without surface effects.	161
B.1	Discretization for electric potential field with top and bottom layers having surface material properties	173

List of Tables

2.1	Properties of Piezoelectric Material, PZT-5H	61
4.1	Properties of Piezoelectric Material, PZT-4	98
5.1	E (bulk Youngs modulus), ν (Poisson ratio) and S_{ijkl} (surface stiffness) for Gold (Au) from atomistic calculations. ⁶	128
6.1	Electromechanical properties of bulk ZnO	150
6.2	Electromechanical properties of surface ZnO	150
6.3	Nominal EMCC of optimized piezoelectric nano beam under open cir- cuit condition	152
6.4	Nominal EMCC of optimized piezoelectric nano beam under closed circuit condition	152

Nomenclature

Symbol	Description
a	Enriched degrees of freedom (Heaviside nodes)
B_u	Strain-displacement matrix)
B_ϕ	Electric field-potential matrix)
C	Elastic stiffness tensor
C^{bulk}	Bulk fourth order elastic stiffness tensor
C^s	Surface fourth order elastic stiffness tensor
C_r	Stiffness ratio
d	Piezoelectric coupling tensor for Strain-Charge form
D	Electric displacement tensor
D_s	Surface electric displacement vector
e	Piezoelectric coupling tensor for Stress-Charge form
e^s	Surface piezoelectric coupling tensor
E	Electric field vector
f	normal level set function
f_u	Mechanical force vector
f_u^α	Mechanical enriched force vector
f_ϕ	Electrical force vector
f_ϕ^α	Electrical enriched force vector
F	Step enrichment function
g	tangential level set function
G	Crack tip enrichment function
H	Heaviside function
I	Second order unit tensor
J	Objective function
K^{UU}	Mechanical stiffness matrix
$K^{U\Phi}$	Electro-mechanical stiffness matrix
$K^{\Phi\Phi}$	Electrical stiffness matrix
L	<i>Lagrangiano f objective functional</i>
M	Mass matrix
n	Outward unit normal vector
P	Tangential projection tensor
S	Elastic compliance tensor
r	Material ratio
u	mechanical displacement vector
V	Velocity of level set function
w	adjoint displacement vector
W	Tranverse displacement vector in plates

z	distance of mid-surface of sublayers from neutral surface
α	Enriched degrees of freedom (Cracktip nodes)
β	Regularisation parameter
γ	Surface energy density
Γ	Boundary of piezoelectric domain
Γ_N	Neumann boundary
Γ_D	Dirichlet boundary
$\boldsymbol{\varepsilon}$	Strain tensor
$\boldsymbol{\varepsilon}_s$	Surface strain tensor
$\boldsymbol{\kappa}$	Permittivity tensor
$\boldsymbol{\kappa}^s$	Surface dielectric permittivity tensor
κ_r	Permittivity ratio
η	Curvature
λ	Lagrange multiplier
Π_{bulk}	Bulk elastic strain energy
Π_s	Surface elastic strain energy
Π_{ext}	Work of external forces
Π_m	Elasto-dielectric energy
Π_e	Elastic energy
Π_d	Dielectric energy
$\boldsymbol{\sigma}$	Mechanical stress tensor
$\boldsymbol{\sigma}_s$	Surface stress tensor
$\boldsymbol{\tau}_s$	Surface residual stress tensor
$\boldsymbol{\phi}$	Electric potential vector
Φ	Level set function
χ^{EXP}	Experimental target response
χ^{NUM}	Numerical response
$\boldsymbol{\psi}$	Adjoint electric potential vector
$\boldsymbol{\omega}_s$	Surface residual electric field vector
Ω	Piezoelectric domain

Chapter 1

Summary

1.1 Piezoelectricity

Piezoelectricity is the generation of electricity or electric polarity in dielectric crystals subjected to mechanical stress, or the generation of stress in such crystals subjected to an applied voltage. The piezoelectric effect was discovered in 1880 by Pierre and Jacques Curie. They found that certain materials had the ability to convert mechanical stress to electrical charge. The converse effect was predicted one year later and subsequently confirmed by the Curie brothers. In 30 years the discovery was put into practice with the development of a piezoelectric based sonar or hydrophone. The cause of this phenomenon was found to lie in the atomic structure.

1.1.1 Piezoelectric effect

The structure of certain crystalline materials have negative and positive polarization that neutralize along polar axis. When an external mechanical stress disturbs this charge balance, electric charge carriers create current in the crystal. This is called the direct effect. On the other hand, a mechanical stress is created when an external charge creates an imbalance in neutral charge state, which is termed as the converse effect. Piezoelectric materials under converse effect can be used as an actuator and under direct effect can be used as a sensor or energy transducer. The crystal structure of Zinc Oxide (ZnO), a common piezoelectric material is shown in figure 1.1. In the figure the all the ZnO tetrahedra has the same orientation with the Zinc having one Oxygen directly above it along the c axis and the three other oxygen neighbours below it. When ZnO is compressed along the c axis, the material deforms by change in angle of O-Zn-O bond. When the tetrahedron deforms, the positive and negative charge of the unit are displaced leading to polarization. On the other hand, if a tensile stress is

1.1 Piezoelectricity

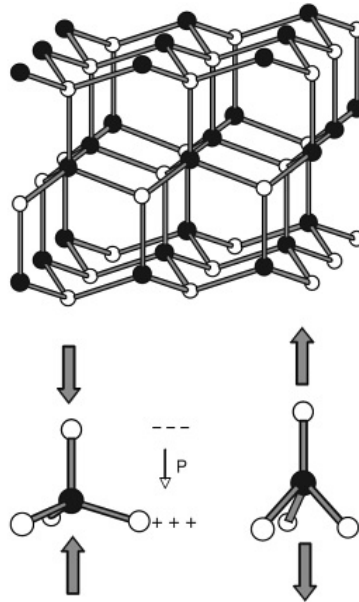


Figure 1.1: The crystal structure of Zinc Oxide and the deformation of the ZnO tetrahedra under compressive and tensile stresses¹.

applied parallel to c axis, the tetrahedra elongates, developing a surface charge of opposite polarity as shown in figure 1.1. In case of mono crystals, the polarization is set by the crystal orientation. In case of poly crystals each domain has its own orientation and so a collective piezoelectric effect is attained by subjecting such polycrystals to a process called poling.

In practice, poling usually involves heating the polycrystal above the Curie point, application of the electric field, cooling below the Curie point, and finally removal of the electric field. Upon heating the material above the Curie point, the crystal structure becomes centrosymmetric, and all electric dipoles vanish. When the material is cooled in the presence of a sufficiently large electric field, the dipoles tend to align with the applied field, all together giving rise to a nonzero net polarisation. After cooling and removal of the electric field, not all dipoles can return to their original direction. The result is a remanent polarisation throughout the ceramic as well as a permanent deformation. The polycrystalline ceramic now does exhibit an artificial anisotropy, enabling piezoelectric behaviour. The piezoelectricity is maintained as long as the material is not depoled, due to for example a temperature above the Curie point, or extreme electric or mechanical conditions. The poling direction in a polycrystal before and after poling is shown in figure 1.2.

The material possessing piezoelectric effect when deformed along the poling direction

1.1 Piezoelectricity

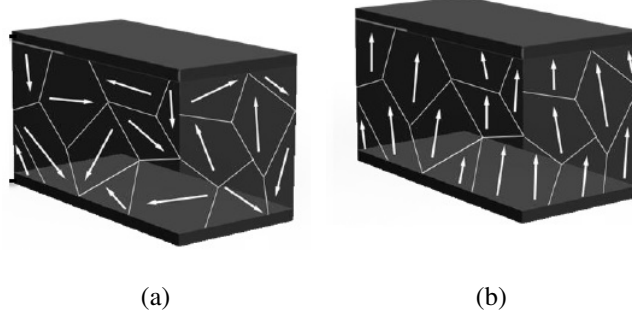


Figure 1.2: The orientation of crystal domains (a) Before poling and (b) After poling².

produces high voltage of same or opposite polarity as that of the poling voltage, depending on load direction. When a voltage difference is applied across the electrodes placed above and below the piezoelectric material, deformation takes place. An input AC signal leads to vibration of the piezomaterial at the same frequency as the AC signal.

1.1.2 Basic Piezoelectric Relations

The electro-elastic response of a piezoelectric body of volume Ω and regular boundary surface S , is governed by the mechanical and electrostatic equilibrium equations,

$$\sigma_{ij,j} + f_i = 0 \text{ in } \Omega \quad (1.1)$$

$$D_{i,i} - q = 0 \text{ in } \Omega \quad (1.2)$$

where f_i , q are mechanical body force components and electric body charge respectively. σ_{ij} and D_i are the symmetric Cauchy stress tensor and electric displacement vector components. They are related to the linear Lagrange symmetric strain tensor, ϵ_{kl} and electric field vector, E_k through the converse and direct linear piezoelectric constitutive equations,

$$\sigma_{ij} = C^E_{ijkl} \epsilon_{kl} - e_{kij} E_k \quad (1.3)$$

$$D_i = e_{ikl} \epsilon_{kl} + \kappa^E_{ik} E_k \quad (1.4)$$

C^E_{ijkl}, e_{kij} and κ^E_{ik} denote elastic stiffness at constant electric field, piezoelectric constant and dielectric permittivity at constant strain respectively. This constitutive equation is in stress-charge form. The strain-charge form of piezoelectric constitutive equation is,

$$\epsilon_{ij} = S^E_{ijkl} \sigma_{kl} - d_{kij} E_k \quad (1.5)$$

$$D_i = d_{ikl} \sigma_{kl} + \kappa^\sigma_{ik} E_k \quad (1.6)$$

1.2 Extended Finite Element Method

These two commonly used forms are related to each other as shown below,

$$C_{ijkl}^E = S_{ijkl}^{E^{-1}} \quad (1.7)$$

$$e_{ikl} = d_{ikl} \cdot S_{ijkl}^{E^{-1}} \quad (1.8)$$

$$\kappa_{ik}^E = \kappa_{ik}^\sigma - d_{ikl} \cdot S_{ijkl}^{E^{-1}} \cdot d_{ikl}^T \quad (1.9)$$

1.2 Extended Finite Element Method

Finite element method (FEM) is the most popular numerical method to determine approximate solution of partial differential equations. FEM is successfully adopted in several areas of engineering sciences to understand, simulate and predict the behavior of structures. The fields in which FEM is applied ranges from aeronautical and aerospace engineering, automobile industry, mechanical engineering, civil engineering, biomechanics, geomechanics, material sciences and many more. Nevertheless in many applications which involves presence of discontinuities in the design domain, FEM involves remeshing to align the element boundaries with the discontinuity. In FEM, mesh refinement is usually necessary near the crack tips in order to represent the asymptotic fields associated with the crack tips. As the crack propagates remeshing is needed which is computationally expensive especially in complex geometries and 3D domains. In some cases when remeshing, results need to be projected from one mesh to the other which further increases the computational cost. In addition to that, modeling holes and inclusions present another form of problems where the usual FEM becomes an expensive choice to get optimal convergence of the solution.

In case of iterative problems in which the geometry of the domain changes in each iteration, FEM requires the domain to be remeshed such that mesh conforms with geometry modelled.

Extended finite element method (XFEM) is a numerical technique which is able to include discontinuities into the finite element shape functions with the help of additional degrees of freedom. The incorporation of any function, typically non-polynomials, is realized through the notion of partition of unity. Any special functions, not just polynomials can be incorporated to approximate any complex local field. Analytical solution of the problem or any available knowledge of the solution from the experimental test results may be used as these special functions. The enriched basis is formed by the combination of the nodal shape functions associated with the mesh and the product of nodal shape functions with discontinuous functions. These enriched basis functions allow modeling of domain shapes that are independent of the mesh. In addition, the enrichment is introduced only locally, while the solution in the rest of the domain has simple finite element approximation. The resulting algebraic system of equations consists of two types of unknowns, i.e classical degrees of freedom and

1.2 Extended Finite Element Method

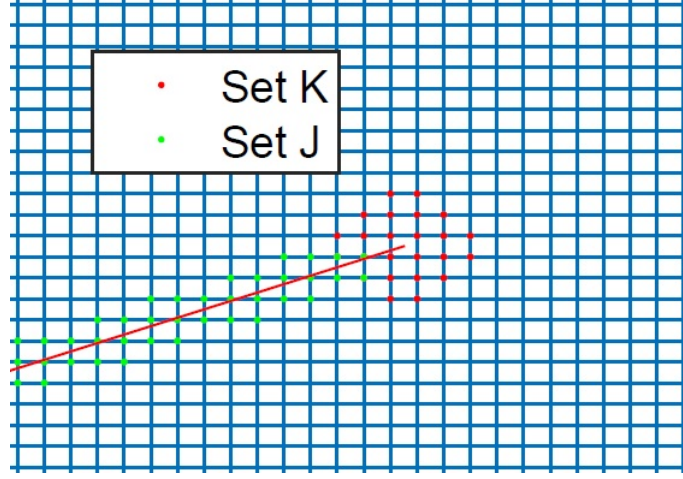


Figure 1.3: The nodes that belong to set J and set K in equation 1.10.

enriched degrees of freedom. The enrichment functions are incorporated using the notion of partition of unity which in turn ensures sparsity is maintained in the algebraic system of equations. These above mentioned features provide the extended finite element method to have significant advantages over standard finite element especially for modeling arbitrary discontinuities.

1.2.1 Basic XFEM approximation

Consider x , a point in a finite element model. In the extended finite element method, the following approximation is utilised to calculate the displacement for the point x located within the domain⁷,

$$u^h(x) = \sum_{i \in I} N_i(X) u_i + \sum_{N=1}^{n_c} \sum_{j \in J} N_j(X) a_j^N F_j^N + \sum_{M=1}^{m_t} \sum_{k \in K} N_k(X) \left(\sum_{i=1}^4 G_i^M(r, \theta) b_k^i \right) \quad (1.10)$$

The modelling of crack using XFEM requires two types of enrichment functions. F corresponds to a step or Heaviside enrichment function. G corresponds to an asymptotic crack tip enrichment function. The set J corresponds to the nodes of the elements that are completely cut by the crack while set K corresponds to nodes in the neighborhood of the crack tip as shown in figure 1.3. The elements that are completely cut by the crack are enriched with the Heaviside/step function. As the element is completely split displacement jump occurs across the crack, the Heaviside/step function gives the desired behavior to approximate the true displacement field. The Heaviside function is

1.2 Extended Finite Element Method

defined as follows,

$$H(x) = \begin{cases} 1 & \text{for } f > 0 \\ -1 & \text{for } f < 0 \end{cases} \quad (1.11)$$

f is the function that defines geometry of the crack, which has a positive value on one side of the crack and a negative value on the other side. The set of nodes J in equation 1.10 corresponds to the nodes of those elements that are cut by the crack. One additional degree of freedom to each of these nodes is required to approximate this strong discontinuity.

The asymptotic crack tip enrichment function is defined as follows,

$$G(r, \theta) = \left\{ \sqrt{r} \sin\left(\frac{\theta}{2}\right), \sqrt{r} \cos\left(\frac{\theta}{2}\right), \sqrt{r} \sin\left(\frac{\theta}{2} \sin\theta\right), \sqrt{r} \cos\left(\frac{\theta}{2} \sin\theta\right) \right\} \quad (1.12)$$

where (r, θ) are the local polar coordinates at the crack tip. The set of nodes K in equation 1.10 corresponds to the nodes of those elements in which the crack tips are present. The set K may also be considered as those nodes which lie in the support or influence domain of the crack tips. The number of additional degrees of freedom in these nodes is four. Based on the exact solution of displacement and stress field around the crack tip, these solutions are found to be contained within the span of these four enrichment functions. The elements that has some of its nodes enriched while the rest unenriched are called as blending elements. Partition of unity is not satisfied in these elements, the unwanted terms in blending elements affect the convergence of XFEM. In order to overcome this disadvantage, shifting of enrichment functions is performed. The shifting removes enrichment from the elements which are not either split elements or crack tip elements. For example, in case of inclusions the absolute signed distance function is used as the enrichment function.

$$F_1 = \left| \sum_{i \in I} N_i \Phi_i \right| \quad (1.13)$$

This enrichment function is shifted as proposed in Moes et al³,

$$F_2 = \sum_{i \in I} N_i |\Phi_i| - \left| \sum_{i \in I} N_i \Phi_i \right| \quad (1.14)$$

The enrichment function, F_2 has zero value on the elements which are not crossed by the interface. Therefore shifting of enrichments can overcome the convergence issues in XFEM due to blending elements.

The usual Gauss quadrature rule may not integrate the field in the elements cut by crack or void boundary correctly. So it is necessary to partition the cut and crack tip elements, in order to integrate the field properly on either sides of the discontinuity. In order to integrate the field properly on both sides of the crack, the elements cut

1.2 Extended Finite Element Method

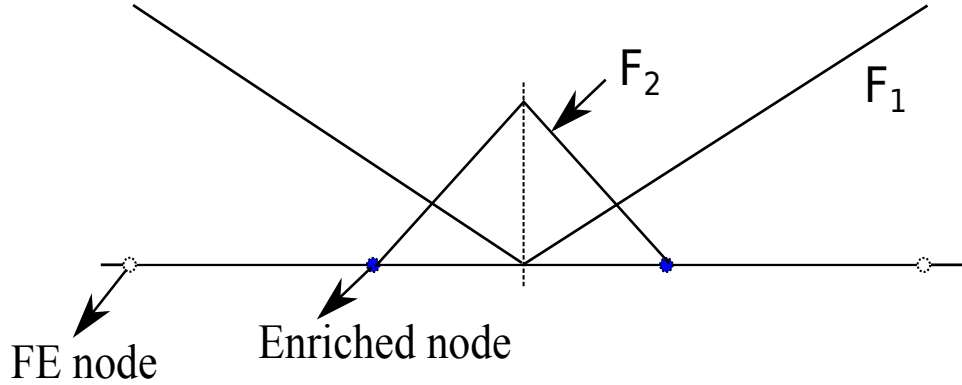


Figure 1.4: Absolute signed distance enrichment function³

by the crack are partitioned into sub triangles where usual Gauss quadrature could be used. The partitioning scheme in XFEM is shown in figure 1.5. Once the element is partitioned, the integration of the weak form for the cut element is performed by replacing the loop over an element by loop over sub polygons/sub-triangles.

1.2.2 Level set function

Level set method offers an interesting way of modeling discontinuities. Level set function coupled with XFEM is applied in modelling crack and void geometries. The main point in modeling a discontinuity using level set function is that the discontinuity i.e. the crack or the void boundary is considered as a zero level set function. For the modeling of voids or inclusions, we define the level set function as a signed distance function. The cracks completely cut certain elements, there are also elements that are partly cut by the crack, these elements comprise the crack tips. So definition of a crack geometry requires not just one but two level set functions, a normal level set function and a tangential level set function. Both these level set functions are defined as signed distance functions. The location of a node with respect to the crack can be determined from the value of these level set functions at the nodal point. As evident from the figure 1.6, the normal level set function, f defines the shape of the crack while the tangential level set function, g defines the span or length of the crack.

1.2.3 Inverse Problem

A direct problem is one in which the input and system parameters are known while output of the model is to be determined. A reconstruction problem is one in which the system parameters and output are known and input that has led to this output is to be determined. In an identification problem, the input and output are known and the

1.2 Extended Finite Element Method

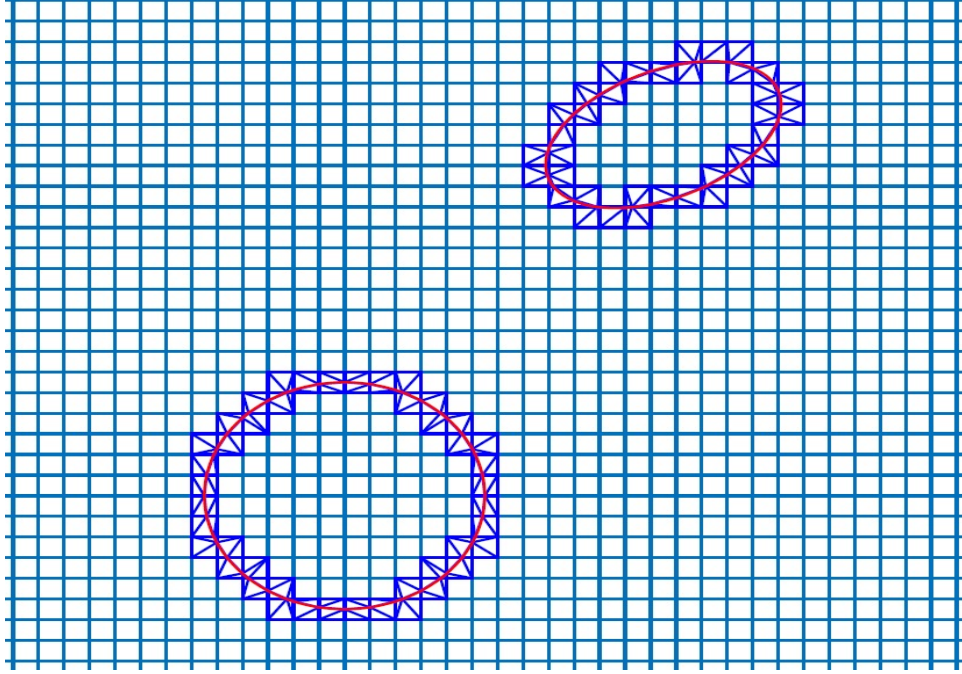


Figure 1.5: Partitioning of elements cut by void boundary

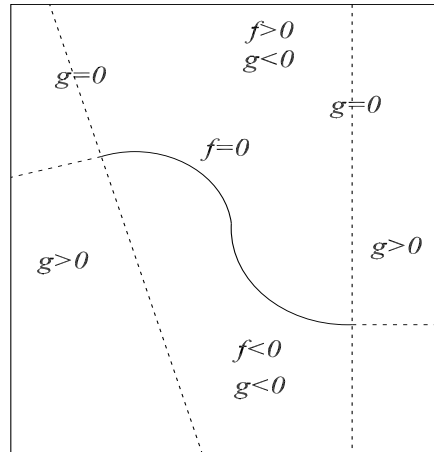


Figure 1.6: Levelset functions

1.2 Extended Finite Element Method

system parameters which are in agreement with the relation between input and output is to be determined. The direct problem is a forward problem, in which the cause is known and effect is determined. The reconstruction and identification problems are called inverse problems because they involve finding out unknown causes of known consequences. The difference between forward and inverse problem in the context of structural mechanics is as shown in figure 1.7. The following list of inverse problems

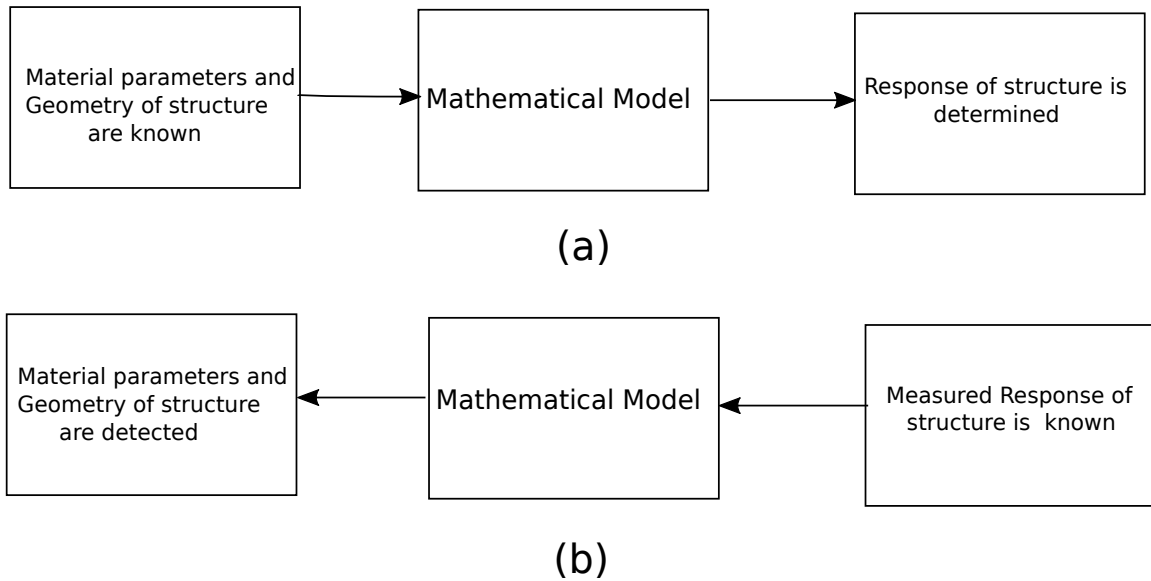


Figure 1.7: (a) Forward problem, (b) Inverse problem.

gives a good impression of the wide variety of applications⁸

- the inverse problem of geomagnetic induction
- X-ray tomography, ultrasound tomography, laser tomography
- acoustic scattering, scattering in quantum mechanics
- radio-astronomical imaging, image analysis
- locating cracks or mines by electrical prospecting
- seismic exploration, seismic tomography
- the use of electrocardiography and magneto-cardiography
- evolution backwards in time, inverse heat conduction

1.2 Extended Finite Element Method

- the inverse problem of potential theory
- can you hear the shape of a drum/manifold?
- deconvolution, reconstruction of truncated signals
- compartmental analysis, parameter identification
- data assimilation
- determining the volatility in models for financial markets
- Discrete tomography, shape from probing

The French mathematician Jacques Hadamard in 1902 introduced the term well-posed for a mathematical problem. A well-posed problem has these features,

- A solution always exists
- The solution is unique
- A small change in the initial conditions leads to a small change in the solution (i.e.) the behavior of solution changes continuously with the initial conditions.

The opposite of a well-posed problem is an ill-posed problem,

- A solution may not exist
- There may be more than one solution
- A small change in the initial conditions leads to a big change in the solution.

Inverse problems are usually ill posed. The inverse problems described and solved in this thesis are to detect following flaws in a piezoelectric domain,

- Detection of an edge or an interior crack
- Detection of an elliptical void
- Detection of an irregular shaped void
- Detection of multiple voids
- Detection of multiple cracks
- Detection of location of both cracks and voids
- Detection of interface of multiple inclusions, all of them made of same material

1.3 Optimization problems

- Detection of interface of three inclusions, two of them made of material A and the rest made of material B.

The ill-posedness of these inverse problems is negotiated by increasing the number of experimental setups from which the measurement or target data is obtained. The measured data may not be exact and may contain noise. The presence of noise in target data leads to poor performance of the detection algorithm. Regularization of inverse problem is performed in order to overcome the influence of noise and obtain a better detection quality. The commonly adopted regularization methods are,

- Tikhonov regularization
- Truncated Singular Value Decomposition (TSVD)
- Total Variation (TV) regularization

Total variation regularization is adopted in this thesis work. The total variation regularization is widely adopted in solving inverse problems using level set based schemes. Total variation is a regularization technique that does takes in to consideration that the data set is discontinuous. Most of the regularization methods assume the data sets to be smooth and continuous, but total variation does not assume the same. The common form of total variation regularization is as shown in the following equation,

$$T = \frac{1}{2} \|Ax - b\| + \beta \int_{\Omega} \sqrt{|\nabla x|^2} d\Omega \quad (1.15)$$

The second term containing the total variation norm of the solution x regularises the inverse problem and improves the quality of the solution. The term, β in the above equation is termed as regularisation parameter. A value of this regularisation parameter beyond a tolerance smoothens the solution while a value lesser than the tolerance leads to lack of regularisation. The most popular method to determine the suitable value of regularisation parameter β is the L-curve method. The L-curve is a log-log plot between the squared norm of the regularized solution and the squared norm of the regularized residual for a range of values of regularization parameter. A standard L curve for determining the regularisation parameter is shown in figure 1.8 obtained from Hansen et al⁴. The regularisation parameter is denoted by λ in the figure.

1.3 Optimization problems

The structural optimization is the subject of making an assemblage of materials sustain loads in the best way. As shown in figure 1.9, the process of determining the shape,

1.3 Optimization problems

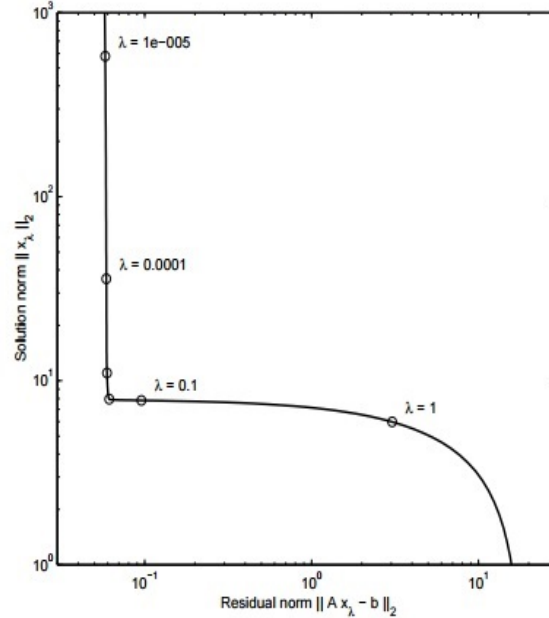


Figure 1.8: A standard L-Curve⁴

size or topology of the domain in question, Ω such that the minimum weight or minimum compliance or any other objective of this sort is achieved and the constraints imposed are satisfied. Based on the geometric feature which is to be optimized, structural optimization problems can be classified as,

- Sizing optimization
- Shape optimization
- Topology optimization

Sizing optimization: Especially in case of trusses, the cross-sectional area of the truss members can be varied so that the intended objective function is minimized.

Shape optimization: In this case, some parts of the boundary of the structural domain is optimized to minimize the objective function. Considering a solid body, the behavior of which is described by a set of partial differential equations, shape optimization consists in choosing the domain for integrating the differential equations in an optimal manner. The important aspect of this type of optimization is that connectivity of the structure is not changed during the optimization process. The shape of the boundary is modified but new surfaces cannot be formed in this optimization.

Topology optimization: The most general form of structural optimization is topology

1.3 Optimization problems

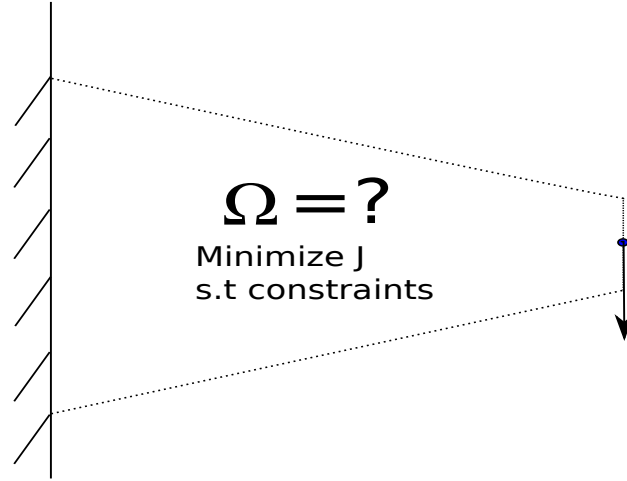


Figure 1.9: Structural optimization - Geometry of domain Ω to be determined such that objective function, J is minimized and the constraints are satisfied

optimization. For example, in case of a truss, when the cross-sectional areas of truss members is considered as the design variable, a bar is removed from the truss when the value of the design variable corresponding to this truss member is set as zero. During the optimization process, the connectivity of nodes is varied such that the topology of the truss gets modified. On the other hand if a discrete structure like truss is replaced by a continuum structure like a beam or plate, then topology changes can be achieved by letting the density of material to zero in certain subdomains of the structure. The number of subdomains in which density can be reduced to zero is restricted by a volume or a weight constraint. Ideally, shape optimization is a subclass of topology optimization, but practical implementations are based on very different techniques, so the two types are usually treated separately. When the state problem is a differential equation, we can say that shape optimization concerns control of domain of the equation, while sizing and topology optimization concern control of its parameters.

1.3.1 Mathematical form of a structural optimization problem

The function and variables that are basic components of a structural optimization problem are,

- Objective function (J): The function which is to be minimized. In most of the optimization problems the objective function remains as the measure of quality or efficiency of the design. Generally J is such that a small value is better than a large one (i.e.) a minimization problem. In literature and in practical applications

1.3 Optimization problems

the most commonly used objective functions are minimum weight, minimum compliance or minimum least square error compared to a target value.

- Design variable (Ω): The objective function varies in each iteration with change in the value of design variable. In the optimization problems solved in this thesis, the geometry of the domain, Ω is taken as the design variable. The geometry of the domain has to be defined in terms of parameters. Parametrization may be either explicit or implicit. Explicit parametrization corresponds to parametrizing the geometry of the design domain in terms of polynomials or splines. Implicit parametrization corresponds to level set representation of the geometry.
- State variable (U): The vector U corresponds to the response of the structure which are required to determine the value of objective function in each iteration. For an electro-mechanical structure, response means mechanical displacement, stress, strain, electric displacement, field or potential.

1.3.2 Solid isotropic material with penalization (SIMP)

The principle idea is an ersatz material approach where the pseudo density parameter is applied to each cell of the finite element mesh. By varying the parameters arbitrary structures can be modeled on a fixed finite element discretization. The SIMP method is very efficient in solving the resulting optimization problems which typically comprise several design variables. In solid isotropic material with penalization (SIMP) the intermediate designs are penalized by using the following constitutive matrix in Hookes law,

$$D = \frac{\rho^p E}{1 - \nu^2} \begin{pmatrix} 1 & \nu & 0 \\ \nu & 1 & 0 \\ 0 & 0 & \frac{1-\nu}{2} \end{pmatrix} \quad (1.16)$$

SIMP provides large regions with $\rho=0$ or $\rho=1$. When the value of ρ is zero, there is no material in the subdomain while when $\rho=1$, then effective Young's modulus is E .

1.3.3 Level set based optimization

Level set methods first devised by Osher and Sethian⁹ have become popular recently for tracking, modeling and simulating the motion of dynamic interfaces (moving free boundaries). The interface is closed, nonintersecting and Lipschitz-continuous and represented implicitly through a Lipschitz-continuous level set function $\Phi(x)$, and the interface itself is the zero isosurface or zero level set $\{x \in R^d | \Phi(x) = 0\}$ ($d = 2$

1.4 Nanoelasticity

or 3). The level set function may be utilised to define different regions in a domain as,

$$\begin{aligned} \text{Solid} : \quad & \Phi(\mathbf{x}) < 0 \quad \forall \mathbf{x} \in \Omega \setminus \partial\Omega \\ \text{Boundary} : \quad & \Phi(\mathbf{x}) = 0 \quad \forall \mathbf{x} \in \partial\Omega \cap \mathbf{D} \\ \text{Void} : \quad & \Phi(\mathbf{x}) > 0 \quad \forall \mathbf{x} \in \mathbf{D} \setminus \Omega \end{aligned} \tag{1.17}$$

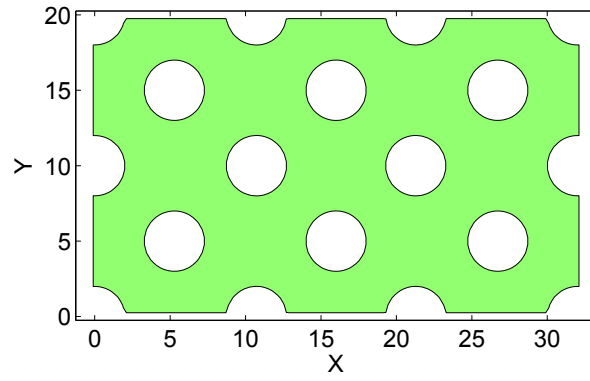
In the conventional level set methods, the Hamilton-Jacobi PDE is solved to evolve the interface using an Eulerian approach. The solving procedure requires appropriate choice of the upwind schemes, reinitialization algorithms and extension velocity methods. The figure 1.10 shows the optimal topology obtained for minimum compliance problem for a short cantilever beam of size 32×20 units, subjected to point load at the bottom of the free end, obtained both using SIMP and level set based optimization.

1.4 Nanoelasticity

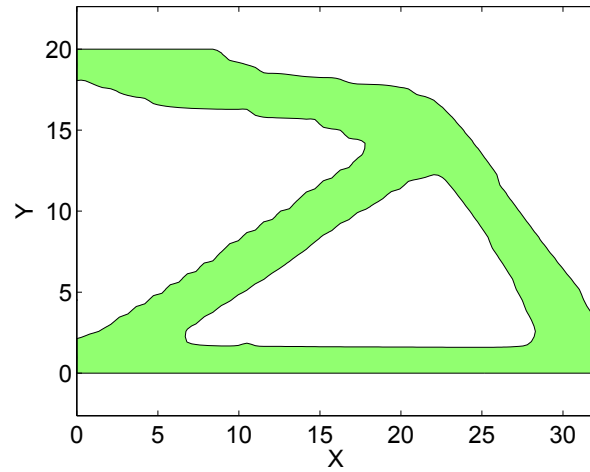
The commonly synthesized structures in the order of a nanometer are nanotubes, oxide nanobelts and semiconductor nanowires. Though these materials have technological potential in applications such as nanoelectronic and photonic circuits, nano-sensors and electromechanical nanodevices, these applications require knowledge about the mechanical behavior of the nano materials. For example, application of piezoelectric nano wire in a nano generator requires understanding about their elastic, electric and coupling piezoelectric behaviour. As a first step as the energy conversion of a nano wire depends on its mechanical strain, the study of the elastic properties of nanostructures is essential. The study of behaviour of nano elastic structures is challenging both from an experimental and theoretical point of view. In the experimental side, the difficulties include the lack of reliable methods to quantitatively measure the elasticity and sometimes the friction at the nanoscale. The problems are related to spatial and force resolution, instrument calibration as well as not well defined surface shape and chemistry because at this scale each atom makes a difference. From the theoretical side, developing a theory of elasticity at the nanoscale is an intriguing theoretical challenge, which lies at the cross-over between the atomic level and the continuum.

The physical origin of the surface effects is that atoms at the surfaces of a material have fewer bonding neighbors than atoms that lie within the material bulk¹⁰. This so-called undercoordination of the surface atoms causes them to exhibit different elastic properties than atoms in the bulk, which can lead to either stiffening or softening of the nanostructure. These unique mechanical properties have motivated researchers to develop computational approaches that capture these surface effects based on either linear or nonlinear continuum theories. It is critical to consider surface effects when discussing the mechanical behavior and properties of nanomaterials, particularly when

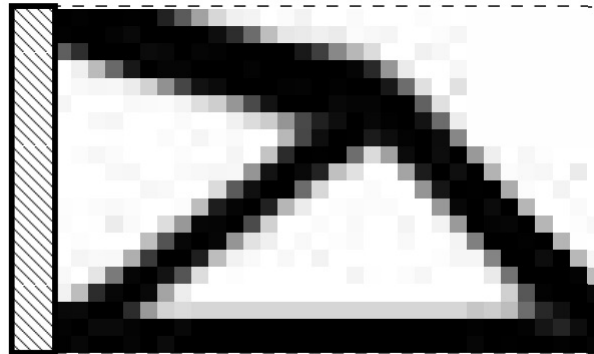
1.4 Nanoelasticity



(a)



(b)



(c)

Figure 1.10: (a) Initialization (b) Optimum topology for a short cantilever beam subjected to a point load at free end by Level set method (c) by SIMP⁵.

1.5 Nanopiezoelectricity

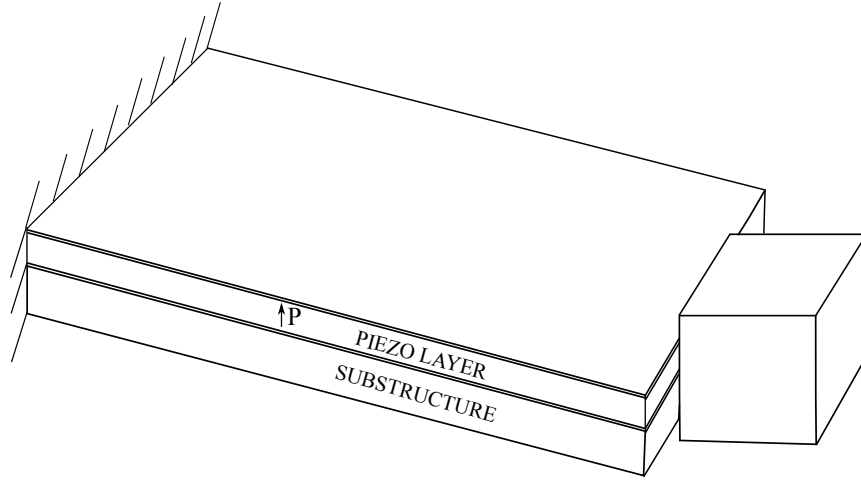


Figure 1.11: A typical cantilever energy harvester with piezoelectric layer, substrate and proof mass

any characteristic dimension of the nanostructure is smaller than about 100 nm¹¹. The computational approaches are based on the well-known Gurtin-Murdoch linear surface elasticity theory¹², which considers the surface to be an entity of zero thickness that has its own elastic properties that are distinct from the bulk. Other approaches have considered a bulk plus surface ansatz of various forms incorporating finite deformation kinematics.

1.5 Nanopiezoelectricity

Energy harvesting which means capturing minute amounts of energy from one or more of the surrounding energy sources where a remote application is deployed, and where such energy source is inexhaustible, is an increasingly attractive alternative to conventional batteries. The recent advances in micro-electromechanical systems has led to considerable increase in portable electronics and wireless sensors. Powering such devices with batteries of finite life span is a problematic task. If the ambient energy can be captured as useful energy then ideally the device can be powered for infinite span. Several energy harvesting approaches are proposed using solar, electromagnetic, thermoelectric and piezoelectric materials at micro and nano scales. Marin et al¹³ concluded that the output power of piezoelectric mechanism is proportional to $v^{9/4}$ at mm^3 dimensions, where v is effective volume ratio. The main advantages of piezoelectric materials in energy harvesting compared to other transduction mechanisms are their large power densities and ease of application. Ambient vibrations provide energy to

1.6 Objectives and outline of the thesis

the system through base excitation. This excitation is converted to cyclic oscillation, which is then converted to cyclic electrical energy through piezoelectric effect. Electromechanical coupling coefficient, k defines the efficiency of energy conversion. A proof mass is attached at the free end of cantilever to modify the resonant frequency to match with ambient frequency as shown in figure 1.11. In d_{31} operating mode stress along direction 1 leads to an induced electric field in direction 3, that is the poling and mechanical load direction are perpendicular to each other. In d_{33} mode, the stress and electric field are in the same direction, while d_{15} mode indicates shear stress harvesters. Commonly adopted resonance based piezoelectric generators are of d_{31} mode. The d_{33} mode based vibration generators are less effective than d_{31} mode because of the percentage of piezoelectric material that does not contribute to energy conversion².

However, most piezoelectric energy harvesters have been used in bulk material systems. The exciting possibility of using nanoscale piezoelectric energy harvesters emerged in 2006 with the discovery of piezoelectricity from ZnO nanowires by Wang et al¹⁴. Many researchers have since extended the original seminal work, including the development of self-powered nano generators that can provide gate voltage to effectively control charge transport¹⁴, lateral and vertical integration of ZnO nanowires into arrays that are capable of producing sufficient power to operate real devices as presented in Xu et al¹⁵. In this thesis work the energy conversion ability of nano piezoelectric beams and plates is studied. Possibility of performing topology optimization of such nano structures to further increase their energy conversion is explored.

1.6 Objectives and outline of the thesis

1.6.1 Chapter 2

The piezoelectric materials that are used in several applications as sensors and actuators experience high stress and electric field concentrations as a result of which they may fail due to fracture. Besides these materials are inhomogeneous, inherently brittle and have low fracture toughness. So assessment of defects like cracks and voids is needed to ensure the reliability of piezoelectric components. Though there are many analytical and experimental works on piezoelectric fracture mechanics. There are very few studies about damage detection, which is an interesting way to prevent the failure of these ceramics. In literature inverse problem of flaw detection in piezoelectric structures is modified into an iterative optimization problem and solved using probabilistic methods like genetic algorithm¹⁶. Besides in these works geometry of defect is explicitly parametrized which restricts the number of flaws that can be detected. In such algorithms finite element method (FEM) is adopted for analysis of the structures. Finite element requires remeshing the domain in each iteration as the crack or void configuration varies with iterations. In order to overcome these disadvantages a new

1.6 Objectives and outline of the thesis

methodology is proposed and tested in chapter 2.

Chapter 2 presents a coupled XFEM-MCS methodology to detect flaws in piezoelectric structures. The extended finite element method (XFEM) offers the advantage of maintaining a fixed background mesh irrespective of the flaw configuration. The multilevel coordinate search (MCS) is a deterministic method unlike genetic algorithm. The number of function evaluation is comparatively much lesser in case of MCS. In this chapter the XFEM-MCS methodology is introduced and several numerical examples are solved. The method is able to detect the location of an edge crack, an interior crack, an elliptical void and an equivalent ellipse representing an irregular void in a piezoelectric structure.

1.6.2 Chapter 3

Though the XFEM-MCS methodology is capable of detecting cracks and voids in a domain, this method requires information about the number of flaws in the domain. Apriori information also about the nature of flaws in the domain is required. The algorithm relies on explicit parametrization of the defects. So there is a need for a method that can detect the location of voids even without knowing before hand, the number of voids in the domain. The method should be capable of determining the number, location and approximate shape of the voids.

Chapter 3 presents a coupled XFEM-level set methodology. Level set method (LSM) commonly used for shape and topology optimization is adopted to solve the inverse problem of flaw detection. An algorithm coupling XFEM and level sets is presented in this chapter. The efficiency of the method is tested in the numerical examples. It is shown in this chapter, that this method works inspite of lack of information about the number of voids in the piezoelectric domain

1.6.3 Chapter 4

The XFEM-LSM algorithm proposed in the previous chapter is capable of detecting the location of voids in the piezoelectric domain. If there are inclusions located in the domain, the method has to be appropriately modified. The methodology is tested for two dimensional structures and there is a need to test whether the method can work also in three dimensions. If there are inclusions made of different materials, the previously proposed algorithm has to be improved to handle detection of multiple material subdomains.

Chapter 4 presents an improved XFEM-LSM methodology to detect the location of inclusions in both two and three dimensional structures. The method is regularized in order to improve the quality of detection in case of higher level of noise in target data. The problem of multiple material subdomains is solved by introducing multiple level

1.6 Objectives and outline of the thesis

sets. Numerical examples shown in this chapter prove that this method can detect the interface of inclusions made of two different materials.

1.6.4 Chapter 5

The elastic behaviour of beams is size dependent. The thickness of beams that approach the nano scale show increased stiffness when compared to macro beams. The optimization of elastic structures can be performed using XFEM-LSM algorithm. The optimization of nano elastic structures is an open problem.

Chapter 5 presents improvements in XFEM-LSM algorithm to deal with optimization of nano elastic structures. The main issue is to determine whether the surface elasticity in nano beams will have any influence on the optimized topology for a structural optimization problem. Several objective functions are checked to know which one of them influences the optimal topology. The numerical examples show the optimal topology obtained for two different objective functions with and without including surface effects under different boundary conditions.

1.6.5 Chapter 6

The main reason for studying the optimization of nano elastic structures in the previous chapter, is with an intention to extend them to understand the behaviour of nano piezoelectricity. The piezoelectric materials are utilised in energy harvesting. The dimension of these energy harvesting devices is approaching nano scale. Nano piezoelectric wires are adopted as components in nano electromechanical systems (NEMS). Chapter 6 presents improvements in XFEM-LSM algorithm to optimize the topology of nano piezoelectric structures, so that their energy conversion is maximized. Though nano wires are studied as components in NEMS, in this chapter we propose a modification in a conventional cantilever energy harvester with the piezoelectric layer approaching nano scale. The numerical examples show the topology optimization of these piezoelectric layers performed to increase their nominal electromechanical coupling coefficient.

1.7 State of Art

In this section, the various research works that are related to this thesis are presented. These works have offered motivation and information to perform the research works detailed in this thesis.

- *Optimal measurement setup for damage detection in piezoelectric plate*¹⁶ (2008), G. Rus, R. Palma and J.L. Prez-Aparicio

In this work, a numerical method to determine the location and extent of defects in piezoelectric plates is developed. The method involves combining genetic algorithms and gradient-based methods to minimize a cost functional, and using an optimized finite element code and meshing algorithm. It is concluded that the presented technique would allow to successfully and accurately locate and size a defect from measurements with realistic levels of noise (more than 1%). Two search procedures are compared, based on genetic algorithms and the Broyden-Fletcher-Goldfarb-Shanno (BFGS) algorithm. The first one showed a more robust convergence as long as its higher computational cost is affordable, whereas the second may provide more precise results for moderate noise levels in measurements.

- *XFEM-based crack detection scheme using a genetic algorithm*¹⁷ (2007), D. Rabinovich, D. Givoli and S. Vigdergauz

The inverse problem of crack detection is solved using a genetic algorithm. The GA optimization process requires the solution of a very large amount of forward problems. The latter are solved via the extended finite element method. This enables one to employ the same regular mesh for all the forward problems. A single straight crack is detected. By applying restrictions on the GA population generation routine the search space is constrained such that all candidate cracks were globally straight. This is the first work in which XFEM is adopted for solving the inverse problem of flaw detection.

- *Detection and quantification of flaws in structures by the extended finite element method and genetic algorithms*¹⁸ (2010), H. Waisman, E. Chatzi and A. W. Smyth

In this paper the XFEM-GA detection algorithm proposed by Rabinovich et al¹⁷, is employed on elastostatic problems with different types of flaws. XFEM-GA methodology is applied to elastostatic domains where flaws are considered as straight cracks, circular holes and non-regular-shaped holes. Measurements are obtained from strain sensors that are attached to the surface of the structure at specific locations and provide the target solution to the GA. In the case of holes with non-regular shapes, the algorithm converges to the best circular hole that minimizes the error of the actual hole.

1.7 State of Art

- *Experimental application and enhancement of the XFEM-GA algorithm for the detection of flaws in structures*¹⁹ (2011), E. N. Chatzi, B. Hiriur , H. Waisman and A. W. Smyth

In this study several advances to the XFEM-GA algorithm such as (i) a novel genetic algorithm that accelerates the convergence of the scheme and alleviates entrapment in local optima, (ii) a generic XFEM formulation of an elliptical hole which is utilized to detect any type of flaw (cracks or holes) of any shape, and (iii) experimental verification of the approach for an arbitrary crack in a 2D plate, are included. The Weighted Average Mutation GA (WAM-GA) is implemented herein which makes use of a weighted average approach for the mutation of the design parameters towards areas of increased fitness.

- *A finite element method for crack growth without remeshing*²⁰ (1999), N. Möes, J. Dolbow and T. Belytschko

This is the paper in which extended finite element method is introduced. A standard displacement based approximation is enriched near a crack by incorporating both discontinuous fields and the near tip asymptotic fields through a partition of unity method. A methodology that constructs the enriched approximation from the interaction of the crack geometry with the mesh is developed. The stress intensity factors are determined using a coarse mesh by using asymptotic enrichment functions. The method treats the crack as a completely separate geometric entity and the only interaction with the mesh occurs in the selection of the enriched nodes and the quadrature of the weak form. The quadrature schemes that use a subdivision of the elements cut by the crack is adopted. The only requirement is that the quadrature scheme integrate on both sides of the discontinuity for the nodes enriched. The drawback of the present method is the need for a variable number of degrees of freedom per node. The partition of unity also has the desirable feature that the FEM equations retain the sparsity properties of the original mesh.

- *Modeling holes and inclusions by level Sets in the extended finite element method*²¹ (2000), N. Sukumar, D. L. Chopp, N. Moës and T. Belytschko

In the XFEM, the finite element approximation is enriched by additional functions through the notion of partition of unity. In this work the level set method is used for representing the location of holes and material interfaces, and in addition, the level set function is used to develop the local enrichment for material interfaces. Numerical examples in 2-dimensional linear elastostatics were presented to test the accuracy of the new technique. For the plate with a hole problem, a convergence study was performed for two different radii of the hole. Optimal rate of convergence in energy norm is obtained using the new technique. The modeling of voids in the XFEM is carried out using an enrichment function

1.7 State of Art

$V(x)$ for nodes that intersect the boundary of the void. If the node lies outside the void $V(x) = 1$ and $V(x) = 0$, if the node is in the interior of the void. In case of inclusions the absolute value of level set function (signed distance function) is adopted as the enrichment to those nodes whose support are intersected by the inclusion boundary.

- *Study of some optimal XFEM type methods*²² (2007), E. Chahine, P. Laborde, J. Pommier, Y. Renard and M. Salaiin

An improvement to extended finite element method presented in this work is using an enlarged fixed enrichment subdomain around the crack tip and a bonding condition for the corresponding degrees of freedom. An efficient numerical integration rule is introduced for the nonsmooth enrichment functions. A new XFEM type method is proposed where the crack tip enrichment functions are localized by using a smooth cut-off function. A mathematical result of optimal error estimate is stated and confirmed by numerical tests for linear finite elements. A piecewise linear cut-off function is considered for the singular enrichment. The method introduces some bonding condition between the enrichment degrees of freedom in XFEM with a fixed enrichment area. The numerical rate of convergence is improved for high order finite elements (of degree two or three) with respect to the classical XFEM. However, optimality is not achieved because of the lack of accuracy coming from the elements in the transition layer (the finite elements between the enrichment area and the rest of the body). An efficient numerical integration rule for the nonsmooth enrichment functions is presented.

- *Application of the X-FEM to the fracture of piezoelectric materials*²³ (2009), E. Bechet, M. Scherzer and M. Kuna

In this paper an application of the extended finite element method to the analysis of fracture in piezoelectric materials is presented. This paper focuses at first on the definition of new enrichment functions suitable for cracks in piezoelectric structures. The generalized domain integrals are used for the determination of crack tip parameters. However, a comparison made with the classical four-fold enrichment used for isotropic elasticity shows that, with an accuracy higher than usually expected for engineering problems, the four-fold enrichment is almost as efficient, concerning accuracy both in energy and in the SIFs. The advantage is that it is simpler to implement and involves less computational overhead, because it adds only four degrees of freedom (dofs) per regular dof, instead of six. It is concluded in the paper that for piezoelectric problems, it is advisable to use the regular enrichment functions stemming from the isotropic elasticity.

- *Extended finite element method for dynamic fracture of piezo-electric materials*²⁴ (2011), H. Nguyen-Vinh, I. Bakar, M.A. Msekh, J. -H. Song, J. Muthu, G.

1.7 State of Art

Zi, P. Le, S. Bordas, R. Simpson, S. Natararajan, T. Lahmer, T. Rabczuk

An extended finite element formulation for dynamic fracture of piezo-electric materials is presented. The method is developed in the context of linear elastic fracture mechanics. It is applied to mode I and mixed mode-fracture for quasi-steady cracks. An implicit time integration scheme is exploited. The method is applied to two examples with mechanical and electrical boundary conditions, that concern with quasi-steady cracks. Since no analytical results are available for dynamic fracture problems of piezoelectric materials, the XFEM results were compared to results obtained by the boundary element method, BEM and they show excellent agreement.

- *Global optimization by multilevel coordinate search*²⁵ (1999), *W. Huyer, A. Neumaier*

Based on the method, DIRECT by Jones et al., a global optimization algorithm based on multilevel coordinate search is presented. It is guaranteed to converge if the function is continuous in the neighborhood of a global minimizer. By starting a local search from certain good points, an improved convergence is obtained. The algorithm presented in this paper has significant theoretical convergence properties if the function is continuous in the neighborhood of a global minimizer. In the current implementation, the test results show that MCS is strongly competitive with existing algorithms in the case of problems with reasonable finite bound constraints. The global minimizer is found in these cases, the number of function evaluations is usually much smaller than for competing algorithms.

- *Structural optimization using sensitivity analysis and a level-set method*²⁶ (2003), *G. Allaire, F. Jouve and A. M. Toader*

In this work a method for shape and topology optimization in two and three dimensions is presented. The numerical method based on a combination of the classical shape derivative and of the level set method for front propagation. Several objective functions with weight and perimeter constraints are considered. The shape derivative is computed by an adjoint method. The method proposed allows for drastic topology changes during the optimization process. The cost is moderate in terms of CPU time since this is an Eulerian shape capturing method. The method can handle very general objective functions and mechanical models, including nonlinear elasticity and design-dependent loads. If a suitable initialization is provided this method is as efficient as the homogenization method. In two dimensions the method does not create new holes since there is no nucleation mechanism in this algorithm. Therefore, care should be taken in the choice of the initialization that should contain a large number of holes if one seeks a non-trivial topology.

1.7 State of Art

- *Fronts propagating with curvature dependent speed: Algorithms based on Hamilton-Jacobi formulations*⁹ (1988), S. Osher and J. A. Sethian

In this work, new numerical algorithms for following fronts propagating with curvature-dependent speed are proposed. The speed may be an arbitrary function of curvature, and the front can also be passively advected by an underlying flow. These algorithms approximate the equations of motion, which resemble Hamilton-Jacobi equations. The algorithms handle topological merging and breaking naturally, work in any number of space dimensions, and do not require that the moving surface be written as a function. The efficiency of the algorithms proposed is tested by adopting in several surface motion problems.

- *XFEM schemes for level set based structural optimization*²⁷ (2012), L. Li, P. Wei and M.Y. Wang

In this work, the extended finite element method is combined with the level set method to solve structural shape and topology optimization problems. Numerical comparisons with the conventional finite element method in a fixed grid show that the XFEM leads to more accurate results without increasing the mesh density and the degrees of freedom. As the mesh in XFEM is independent of the physical boundary of the design, there is no need for remeshing during the optimization process. Numerical experiments illustrate that the higher order XFEM elements with coarse finite element mesh have a very similar accuracy compared to the corresponding lower order XFEM element using high-density mesh, but the computational cost is reduced by more than 20%. The numerical examples of mean compliance minimization are studied to validate the proposed XFEM schemes. The results of two and three dimensional numerical examples illustrate that the proposed XFEM schemes are effective tools for structural optimization using the level set method.

- *Electrical impedance tomography using level set representation and total variational regularization*²⁸ (2005), E. T. Chung, T. F. Chan and X. C. Tai

In this paper, a numerical scheme for the identification of piecewise constant conductivity coefficient for a problem arising from electrical impedance tomography is proposed. The key feature of the scheme is the use of level set method for the representation of interface between domains with different values of coefficients. Reconstruction of regular and irregular shapes is performed. Regularization using total variation norm is included in order to overcome the influence of noise in the target data. Sensitivity of noise level and regularisation parameter on the interface detection is studied.

- *A binary level set model for elliptic inverse problems with discontinuous coefficients*²⁹ (2007), L. K. Nielsen, X. C. Tai, S. I. Aanonsen and M. Espedal

A binary level set approach for solving elliptic inverse problems is presented in

1.7 State of Art

this paper. The multi-level set representation is regularised by a total variational norm. Detection of interface of more than two material subdomains each made of different material is presented. The interfaces are not moved during the iterative process, but the level set functions are changed to -1 or 1 at every grid point. This gives some advantages when matching special geometries, sharp corners can be recovered very accurately. The reinitialisation of the level set functions used in the continuous formulation is not needed for the binary level set method. The numerical results show that rather complicated geometries can be recovered under moderate amount of noise.

- *Are surfaces elastically softer or stiffer?*³⁰ (2004), L. G. Zhou and H. Huanga
A combination of molecular statics and ab initio calculations is performed to conclude that a surface of a nano plate may be softer or stiffer than the corresponding bulk. The overall softening or stiffening depends on the competition between electron redistribution and the lower coordination on surfaces. Both the softening and stiffening effects can have major impacts on the mechanics of nanoplates. Taking Cu as an example, we demonstrate that the Young's modulus along $\langle 110 \rangle$ direction on $\{100\}$ surface is larger than its bulk counterpart; meanwhile, it is smaller along $\langle 100 \rangle$ direction on $\{100\}$ surface.
- *Mechanics of crystalline nanowires*¹¹ (2009), H. S. Park, W. Cai, H. D. Espinosa and H. Huang
In this work, the unique mechanical properties of nanowires, which emerge from surface atoms having different electron densities and fewer bonding neighbors than atoms lying within the nanowire bulk are studied. In this respect, atomistic simulations are done to reveal novel surface-driven mechanical behavior and properties, including both increases and decreases in elastic stiffness, phase transformations, shape memory and pseudoelastic effects. The properties of Silver, Gold and ZnO nano wires are studied in detail.
- *Atomistic calculations of interface elastic properties in noncoherent metallic bilayers*⁶ (2008), C. Mi, S. Jun, D. A. Kouris and S. Y. Kim
The magnitudes of surface and interface elastic constants depend on crystalline orientations. These material constants are generally smaller in close packed surfaces and interfaces, i.e., bcc (110) and fcc (111), than those in less closepacked systems, e.g., (001). Surface energy, surface stress and surface modulus of the free surface calculated for fcc and bcc metals using Johnson embedded atom method potential. Similarly interface energy, interface stress, and interface modulus calculated for parallel-oriented fcc-fcc bicrystals using the Johnson EAM potential.

1.7 State of Art

- *An XFEM/level set approach to modelling surface/interface effects and to computing the size-dependent effective properties of nanocomposites*³¹ (2008), J. Yvonnet, H. L. Quang and Q. C. He

The present work aims to elaborate an efficient numerical approach to dealing with the interface effects described by the coherent interface model and to determining the size-dependent effective elastic moduli of nanocomposites. To achieve this two fold objective, a computational technique combining the level set method and the extended finite element method is developed and implemented. The numerical results obtained by the developed computational technique in the two-dimensional context are compared and discussed with respect to the relevant exact analytical solutions used as benchmarks. The code is validated by comparing the analytical solution for cylindrical inclusion under plane strain and with the coherent interface model. Size dependent properties of a structure with nano voids, a spherical nano inclusion and a random nanostructure are also studied in this work.

- *An extended finite element/level set method to study surface effects on the mechanical behavior and properties of nanomaterials*³² (2010), M. Farsad, F. J. Vernerey and H. S. Park

The coupled XFEM-level set approach is adopted to solve nanomechanical boundary value problems in which discontinuities in both strain and displacement due to surfaces and interfaces can be easily handled, while simultaneously accounting for critical nanoscale surface effects, including surface energy, stress, elasticity and interface decohesion. The proposed approach is validated by studying the surface-stress driven relaxation of homogeneous and bi-layer nanoplates as well as the contribution from the surface elasticity to the effective stiffness of nanobeams. The numerical results are compared with new analytical solutions that are derived for these simple problems and also for the problem involving the surface-stress-driven relaxation of a homogeneous nanoplate. The results are also validated by comparing with those obtained from both fully atomistic simulations and previous multiscale calculations based upon the surface Cauchy-Born model.

- *An electromechanical finite element model for piezoelectric energy harvester plates*³³ (2009), C. D. Marqui Junior, A. Erturk, D. J. Inman

In this paper, an electromechanical FE plate model is derived for piezoelectric energy harvesting from base excitations. The mechanics of the plate is based on the classical (Kirchhoff) plate theory, which is appropriate for modeling of typical piezoelectric energy harvesters since they are usually designed and manufactured as thin plates. Presence of conductive electrodes is taken into account in the FE model. The predictions of the FE model are verified against the ana-

1.7 State of Art

lytical solution for a unimorph cantilever and then against the experimental and analytical results of a bimorph cantilever with a tip mass reported in the literature.

- *Topology optimization of energy harvesting devices using piezoelectric materials*³⁴ (2009), B. Zheng, C. J. Chang and H. C. Gea

In this work, SIMP based topology optimization is extended to piezoelectric materials. The optimised topology of piezoelectric plates subjected to static point load or axial load at the free end and pressure load over the plate is determined. Topology optimization has been applied to the design of piezoelectric transducers, the locations of piezoelectric materials are predefined and only the optimal layout of elastic materials is considered. In this paper, both elastic materials as well as piezoelectric materials are considered for the design of energy harvesting devices under the topology optimization formulation. The objective function for this study is to maximize the energy conversion factor. The sensitivities of both stored strain energy and electrical energy are derived by the adjoint method.

- *A level set approach for optimal design of smart energy harvesters*³⁵ (2010), S. Chen, S. Gonella, W. Chen and W. K. Liu

A level set based topology optimization scheme to maximize energy conversion in piezoelectric energy harvesters is proposed. A cantilever under 31 mode is optimized and the optimized topology is compared with the minimum compliance optimal topology of a cantilever beam of ratio 2:1. The material is concentrated close to the clamped end as against an elastic beam in which material is concentrated far from the neutral axis. A cylindrical energy harvester is optimized initially with a single material and then with multiple materials. The shape gradient of the energy conversion efficiency is analytically derived using the material time derivative approach and the adjoint variable method. A design velocity field is then constructed using the steepest descent method, which is further integrated into level set methods. The reconciled level set (RLS) method is employed to solve multi-material shape and topology optimization problems, using the Merriman-Bence-Osher (MBO) operator.

- *Topology optimization of piezoelectric energy harvesting devices considering static and harmonic dynamic loads*³⁶ (2012), J. Y. Noh and G. H. Yoon

The design optimal layouts for piezoelectric energy harvesting devices (EHDs) by considering the effect of static and harmonic dynamic mechanical loads is determined. The optimal material distributions of a piezoelectric material considering the harmonic dynamic coupling effects between the electric energy and a structure for efficient EHDs, harmonic dynamic responses and the complex sensitivity analyses for various objectives related to the energy efficiency are calculated and derived. For the relaxation method of the density design variable

1.7 State of Art

for TO, material properties such as the anisotropic linear elasticity coefficients, piezoelectric coefficients, and permittivity coefficients are independently interpolated through the solid isotropic material with penalization (SIMP) approach with three penalization values. It is concluded in this work that for dynamic load whose excitation frequency is below the first peak of the objective function such as power, electric energy, and conversion factor, it is likely that static results can be used. But for dynamic loads with higher excitation frequencies, the present approach should be considered.

- *First-principles based multiscale model of piezoelectric nanowires with surface effects*³⁷ (2012), M. T. Hoang, J. Yvonnet, A. Mitrushchenkov and G. Chambaud
A methodology for computation of the surface piezoelectric coefficients e_{33} , e_{31} and e_{15} for $(10\bar{1}0)$ surfaces for wurtzite AlN, GaN and ZnO nanowires by first-principles calculations through the Berry phase theory is proposed. The coefficients can be used within a continuum piezoelectric model extended with a surface energy. We have solved the equations of the continuum model with a finite element technique and compared the results with full first-principles calculations of nanowires with diameters ranging from 0.6 nm to 3.9 nm. A good agreement is found between the continuum and first-principles results for the effective piezoelectric coefficient along the axial direction of the nanowire. It is concluded that for all materials, an increase of the effective piezoelectric coefficients is found when the diameter of the nanowire decreases.
- *Piezoelectric nanogenerators based on zinc oxide nanowire arrays*³⁸ (2006), Z. L. Wang and J. Song
This is the first paper to propose the energy conversion ability of Zinc Oxide piezoelectric nano wires. Nano wire (NW) array is constructed to convert nanoscale mechanical energy to electrical energy. The nano wires are made of piezoelectric Zinc Oxide. The aligned nano wires are deflected by a conductive atomic force microscope tip in contact mode. The bending of the nanowire creates a strain field and charge separation in the nanowire. The rectifying characteristic of the Schottky barrier formed between the metal tip and the NW leads to electrical current generation. The efficiency of the NW-based piezoelectric power generator is estimated to be 17 to 30%.
- *Surface piezoelectricity: Size effects in nanostructures and the emergence of piezoelectricity in non-piezoelectric materials*³⁹ (2011), S. Dai, M. Gharbi, P. Sharma and H. S. Park
A combination of a theoretical framework and atomistic calculations, the concept of surface piezoelectricity is highlighted, which can be used to interpret the piezoelectricity of nanostructures. Three specific material systems (ZnO,

1.7 State of Art

$SrTiO_3$, and $BaTiO_3$) are considered and the renormalization of apparent piezoelectric behavior at small scales is discussed. The interesting finding of this paper is that interplay of symmetry and surface effect lead nanostructures of certain non-piezoelectric materials to exhibit piezoelectric behavior.

- *Surface effects on the piezoelectricity of ZnO nanowires*⁴⁰ (2013), S. Dai and H. S. Park

The results in this paper show that the [2110] oriented nanowires have a larger effective piezoelectric constant than the [0110] oriented nanowires. If proper treatment of the polar surfaces is performed, the effective piezoelectric constants for all nanowires are found to decrease with decreasing size, with all values smaller than the respective bulk ones. It is demonstrated that the underlying atomistic mechanism is responsible for the reduction in piezoelectric constants. Regardless of whether the surface is expanded or contracted in response to surface stresses, the bond length of the ZnO dimer closest to the surface was found to decrease, thus causing a decrease in polarization at the nanowire surface and thereby reduction in effective piezoelectric constant. It is concluded that due to the observed decrease in piezoelectric constant for all three nanowire orientations with decreasing size, larger diameter square or nearly square cross-section nanowires may be utilized in practical applications if maximum energy generation or harvesting using ZnO nanowires is desired.

- *Surface effects on the electromechanical coupling and bending behaviours of piezoelectric nanowires*⁴¹ (2011), Z. Yan and L. Jiang

In this paper surface effects, including surface elasticity, residual surface stress and surface piezoelectricity, are considered to study the electromechanical coupling behaviour of piezoelectric nanowires with the Euler-Bernoulli beam theory. The surface-layer-based model is used to derive an explicit formula for electromechanical coupling coefficient. The influence of surface effects upon the beam stiffness is found to be more prominent for slender beams. The significant enhancement of electromechanical coupling coefficient due to surface effects is also observed with the decrease in nanobeam thickness, which implies that surface effects can be employed for performance improvement of nanostructured piezoelectric materials in potential applications as nanogenerators.

- *Surface effects on the electroelastic responses of a thin piezoelectric plate with nanoscale thickness*⁴² (2012), Z. Yan and L. Jiang

The electroelastic responses of a thin piezoelectric plate under mechanical and electrical loads with the consideration of surface effects is studied. Surface effects, including surface elasticity, residual surface stress and surface piezoelectricity, are incorporated into the conventional Kirchhoff plate theory for a piezoelectric plate via the surface piezoelectricity model and the generalized Young-

1.7 State of Art

Laplace equations. The proposed model predicts size-dependent behaviours of the piezoelectric thin plate with nanoscale thickness. It is found that surface effects have significant influence on the electroelastic responses of the piezoelectric nanoplate. But with the increase of the plate thickness from nanometer scale, such influence on the electroelastic responses of the plate diminishes and the predicted electromechanical behaviour of the piezoelectric nanoplate approaches that of the conventional piezoelectric plate as expected.

1.8 Results and discussion

1.8.1 XFEM-MCS methodology for inverse problem of flaw detection

An iterative method to treat the Inverse Problem of detecting cracks and voids in two-dimensional piezoelectric structures is proposed. The method involves solving the forward problem for various flaw configurations and at each iteration the response of piezoelectric material is minimized at known specific points along the boundary to match measured data. Extended finite element method (XFEM) is employed for solving the forward problem as it allows the use of a single regular mesh for a large number of iterations with different flaw geometries. Minimization of cost function is performed by Multilevel Coordinate Search (MCS) method. The algorithm is an intermediate between purely heuristic methods and methods that allow an assessment of the quality of the minimum obtained and is in spirit similar to the direct method for global optimization. In this work the XFEM-MCS methodology is applied to 2D electromechanical problems where flaws considered are straight cracks and elliptical voids. The results show that this methodology can be effectively employed for damage detection in piezoelectric materials. The number of flaws in the domain is assumed to be one.

Because no experimental measurements are available in this study, they are simulated by XFEM. In order to avoid inverse-crimes, we used two different mesh sizes for creating the data and for solving the inverse problem, that is, to generate the target data, a mesh finer to the one used for solving the inverse problem is employed. The experimental set up to determine the target data is as shown in the figure 1.12. The XFEM-MCS methodology is adopted to detect following defects,

- Edge crack
- Interior crack
- Elliptical Void
- Irregular void

In this section, the results obtained for edge crack example is shown. More details on this example and the remaining numerical examples can be found in Chapter 2.

The piezoelectric plate containing the edge crack is assumed to be made of PZT-4. The size of the plate is 10×10 units. The The edge crack to be determined can be defined by two independent parameters. The x-coordinate and y-coordinate of the tip inside the piezoelectric domain. The coordinates of the tip along the edge is assumed to know apriori. The coordinate of the tip inside the domain in this example is considered as (2.5,5.75). The mesh size used for the inverse problem is such that $h = \frac{1}{50}$.

1.8 Results and discussion

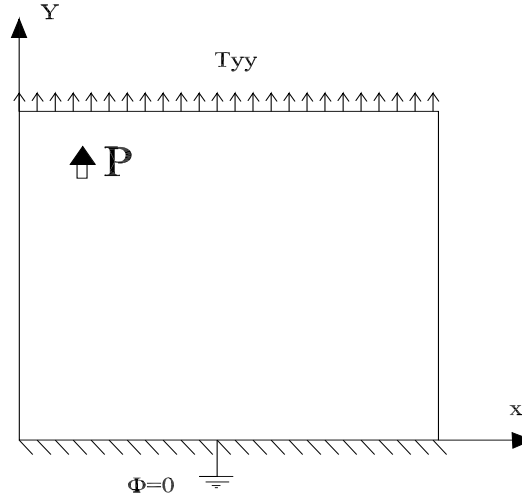


Figure 1.12: Boundary conditions and Loads on the modeled Piezoelectric plate

The plate is assumed to be subjected to a line load along the top end of the plate as shown in figure 1.12. The magnitude of the load is 1 MPa acting vertically upwards. The bottom end of the plate is clamped and the electric potential is set to zero. The measurements are made along the right edge 4 of the plate. The number of discrete points in which the measurements are made is 25. These may be considered as the location of pseudo sensors. The crack pattern detected with varying iterations is shown in figure 1.13. The convergence of the algorithm with the number of function calls is shown in figure 1.14. The method determine the minima in few initial iterations. The algorithm then performs global search to ensure that the minima determined is not local. This global search leads to higher values of objective function as evident from the spikes in the figure 1.14. The convergence of the parameters to be determined, the x and y coordinate of the crack tip, is shown in the figure 1.15 and 1.16. The convergence pattern for the parameters look almost similar. The global search by the algorithm leads to deviations, in these figures, from the actual solution in parameter space inspite of determining the actual parameters within few initial iterations. The optimal parameters are obtained at 194th iteration.

The examples in chapter 2, prove that the algorithm can detect a single straight crack and elliptical void in piezoelectric materials. However one does not know before hand whether flaw present in the specimen is a crack or void. The performance of the algorithm in detecting a crack using parameters defining elliptical void is shown in Figure 1.17. The result obtained is a flat elliptical void like the one shown in figure 1.17.

1.8 Results and discussion

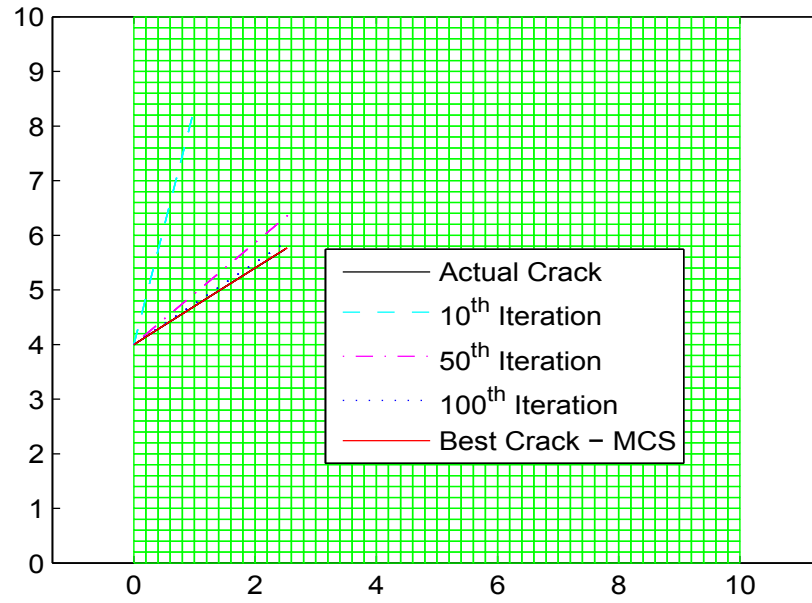


Figure 1.13: Best crack parameters obtained using XFEM-MCS algorithm for Edge crack estimation

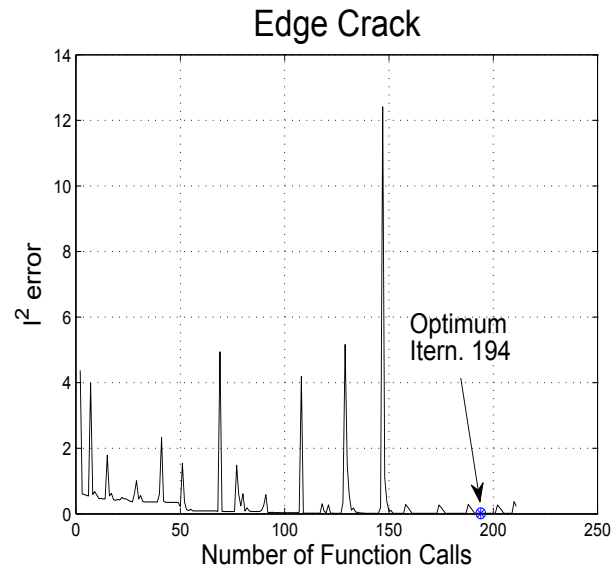


Figure 1.14: Convergence of XFEM-MCS methodology for two parameter estimation (Edge Crack) showing the variation of residual with number of function calls.

1.8 Results and discussion

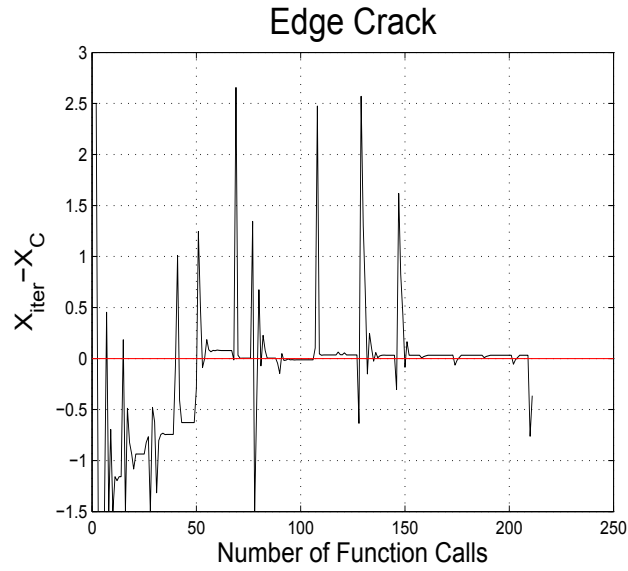


Figure 1.15: Convergence of XFEM-MCS methodology for 1st parameter estimation (Edge Crack) - X - coordinate of the interior crack tip.

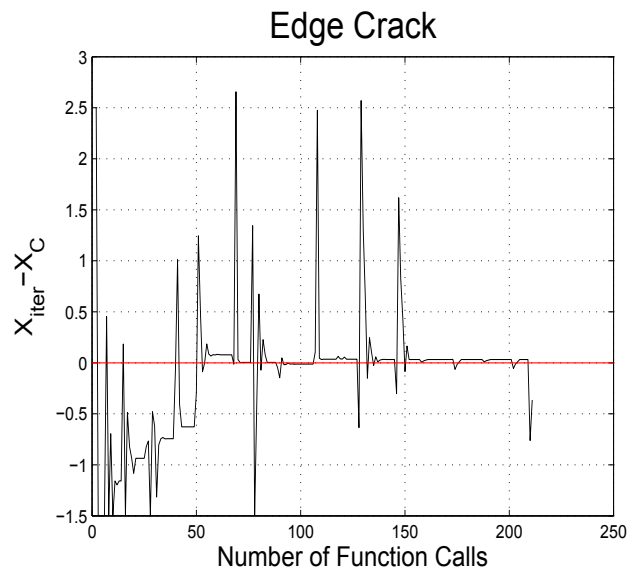


Figure 1.16: Convergence of XFEM-MCS methodology for 2nd parameter estimation (Edge Crack) - Y - coordinate of the interior crack tip.

1.8 Results and discussion

It is possible to know from the outcome that a defect is present in the domain and it could be a crack. So it is recommended that irrespective of problem in hand the elliptical void defined by five parameters can be used to detect defect.

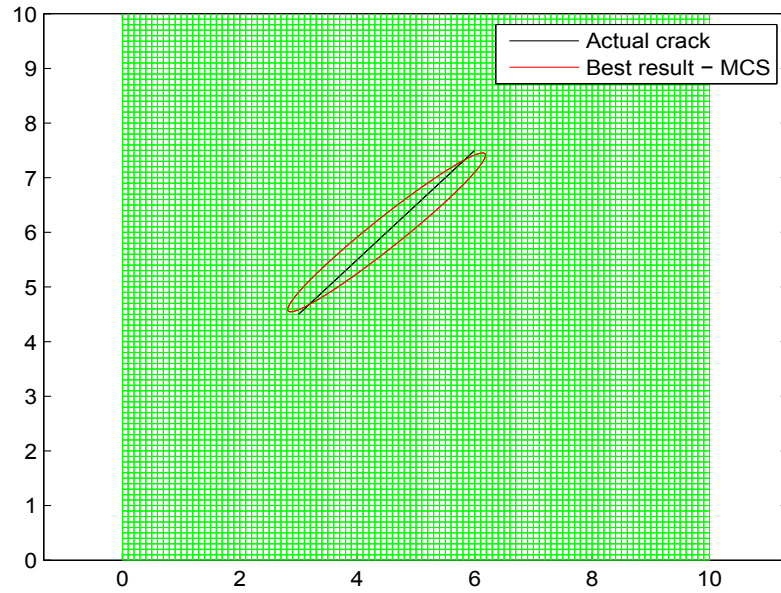


Figure 1.17: Best result determined by MCS for an inclined crack

1.8 Results and discussion

1.8.2 XFEM-level set methodology for inverse problem of flaw detection

An iterative procedure to solve the inverse problem of detecting multiple voids in piezoelectric structure is proposed. In each iteration the forward problem is solved for various void configurations, and at each iteration, the mechanical and electrical responses of a piezoelectric structure is minimized at known specific points along the boundary to match measured data. The numerical method based on combination of classical shape derivative and of the level set method for front propagation used in structural optimization is utilized to minimize the cost function. The results obtained show that this method is effectively able to determine the number of voids in a piezoelectric structure and its corresponding locations.

In this work, the number of flaws to be determined in the piezoelectric domain need not be known apriori. The piezoelectric domain is initialized with uniformly distributed voids all over the domain, in order to enable the algorithm to determine the global minima. The experimental setup is such that the piezoelectric plate is clamped at the bottom end while a line load is applied along the top end of the plate. Several experimental setups are required in order to ensure uniqueness of the solution. Also when there are voids located one above the other, measurement along only one edge may not be sufficient to determine the actual void. The experimental setup is shown in figure 1.18. Four types of measurement data are obtained. The edge 1 is clamped, load

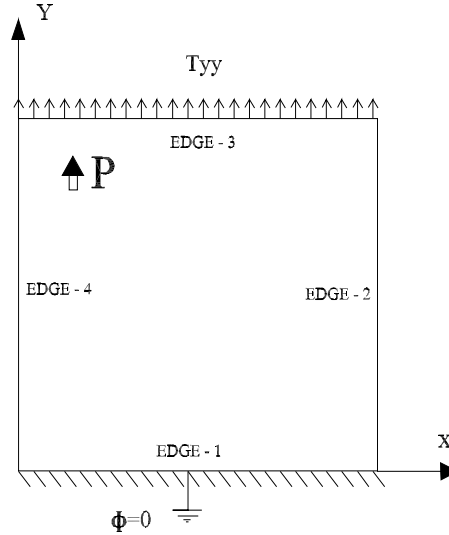


Figure 1.18: Boundary conditions and loads on the modeled Piezoelectric plate

is applied along the edge 3, displacement and electric potential values are determined

1.8 Results and discussion

along the edge 2 at 25 discrete points. Then the edge 2 is clamped, load is applied along the edge 4, measurements are made along the edge 3. Similarly 2 more experiment data are generated. The XFEM-Levelset coupled methodology is adopted to detect following defects,

- Single square void
- Multiple voids
- Multiple cracks
- Multiple voids and cracks

In this section, the detection of single square void is performed. The remaining examples and more details about this example can be found in Chapter 3. The voids closer to the actual one merge together and take the shape of the actual void while the ones far from the actual void reduce in size and vanish finally. The void configurations are modified in each iteration by updating the level set function. The level set function is changed by solving Hamilton-Jacobi equation in each iteration. The level set function is regularized at various intervals so as to smooth the void shapes. The level set values are changed to signed distance function when regularised. The evolution of void configurations is shown in figure 1.20. The noise present in the measurement is $\pm 1\%$.

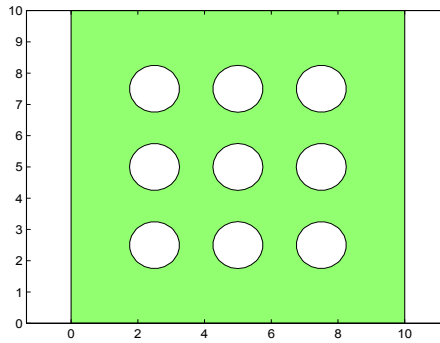


Figure 1.19: Initialization

The variation of detection with increased percentage of noise is shown in figure 1.21. The residual norm increases rapidly with increase in the noise level.

1.8 Results and discussion

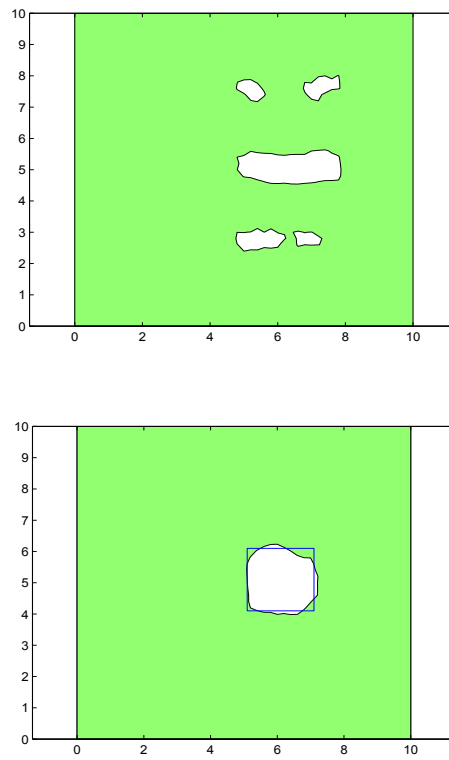


Figure 1.20: Void configuration after 40 and the final void configuration

1.8 Results and discussion

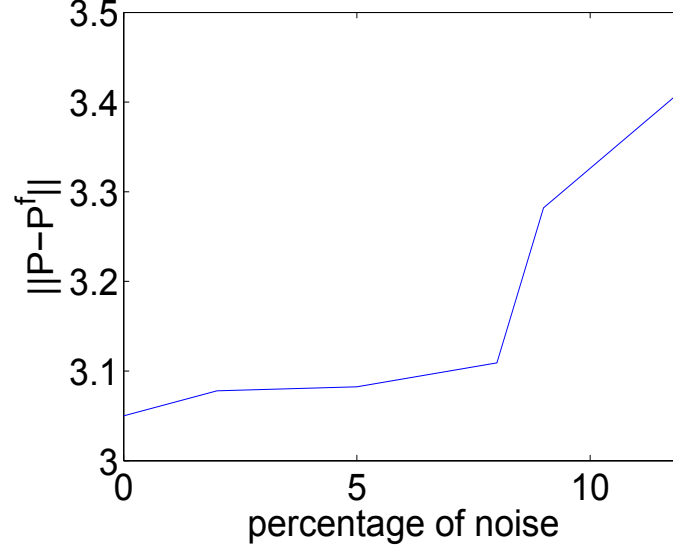


Figure 1.21: The variation of residual norm with increase in percentage of noise

1.8.3 XFEM and level sets for the inverse problem of inclusion detection

An algorithm to solve the inverse problem of detecting inclusion interfaces in a piezoelectric structure is proposed. The material interfaces are implicitly represented by level sets which are identified by applying regularization using total variation penalty terms. The inverse problem is solved iteratively and the extended finite element method is used for the analysis of the structure in each iteration. The formulation is presented for three-dimensional structures and inclusions made of different materials are detected by using multiple level sets. The results obtained prove that the iterative procedure proposed can determine the location and approximate shape of material sub-domains in the presence of higher noise levels.

In this work the number, location and approximate shape of inclusions in a piezoelectric domain is determined. The interface of inclusions is implicitly represented by level sets. The level set has a negative value inside the inclusions and a positive outside the inclusions. The piezoelectric domain is initialized by uniformly distributed circular inclusions all over the domain. The velocity function which depends on the response of the piezoelectric structure is determined, by performing analysis using XFEM. The level set functions are updated by solving Hamilton-Jacobi equation. The material parameters of the inclusion is assumed to be known apriori. The numerical examples solved in this section are,

1.8 Results and discussion

- Detection of multiple inclusions in a piezoelectric plate
- Detection of multiple inclusions in a piezoelectric cube
- Detection of multiple defects in a piezoelectric plate
- Detection of inclusions made of different materials using multiple level sets

The example of determining multiple defects (i.e.) cracks, inclusions and voids in a piezoelectric plate is presented in this section. More details about this example and the other examples can be found in Chapter 4. The XFEM- level set algorithm proposed is employed in determining the number, approximate location and shape of defects in a damaged piezoelectric domain. The defect may be an air void, a crack or inclusion with lower stiffness or permittivity. The piezoelectric domain has two inclusions, one air void and a straight line crack as shown in figure 1.22. Among the two inclusions,

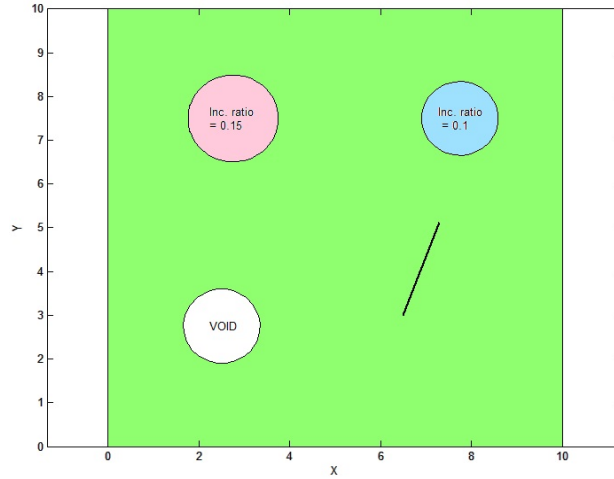


Figure 1.22: Piezoelectric domain with defects

one of them has stiffness ratio $C_r = 0.1$ and permittivity ratio $\kappa_r = 0.1$, while the other inclusion has stiffness ratio $C_r = 0.15$ and permittivity ratio $\kappa_r = 0.15$, with respect to the background material. The initial assumption is such that circular inclusions with stiffness ratio $C_r = 0.1$ and permittivity ratio $\kappa_r = 0.1$, are distributed throughout the domain. The initial interface configuration changes with each iteration so that the objective function decreases. As shown in figure 1.23, the interfaces far from the defects disappear and the ones nearer gradually take the shape of the defects. It is interesting to note that at the crack location a flat elliptical inclusion is formed. Though the algorithm cannot determine the crack profile it can at least detect approximate location of crack like defects. As the inclusion material properties assumed is different from the

1.8 Results and discussion

properties of true defects in the domain, the algorithm over estimates or underestimates the size of the inclusions. The size of voids is over estimated and the size of inclusions with higher stiffness and permittivity ratios than the one assumed are underestimated. This example proves that the algorithm can determine the number of defects present in the piezoelectric structure and their corresponding approximate locations.

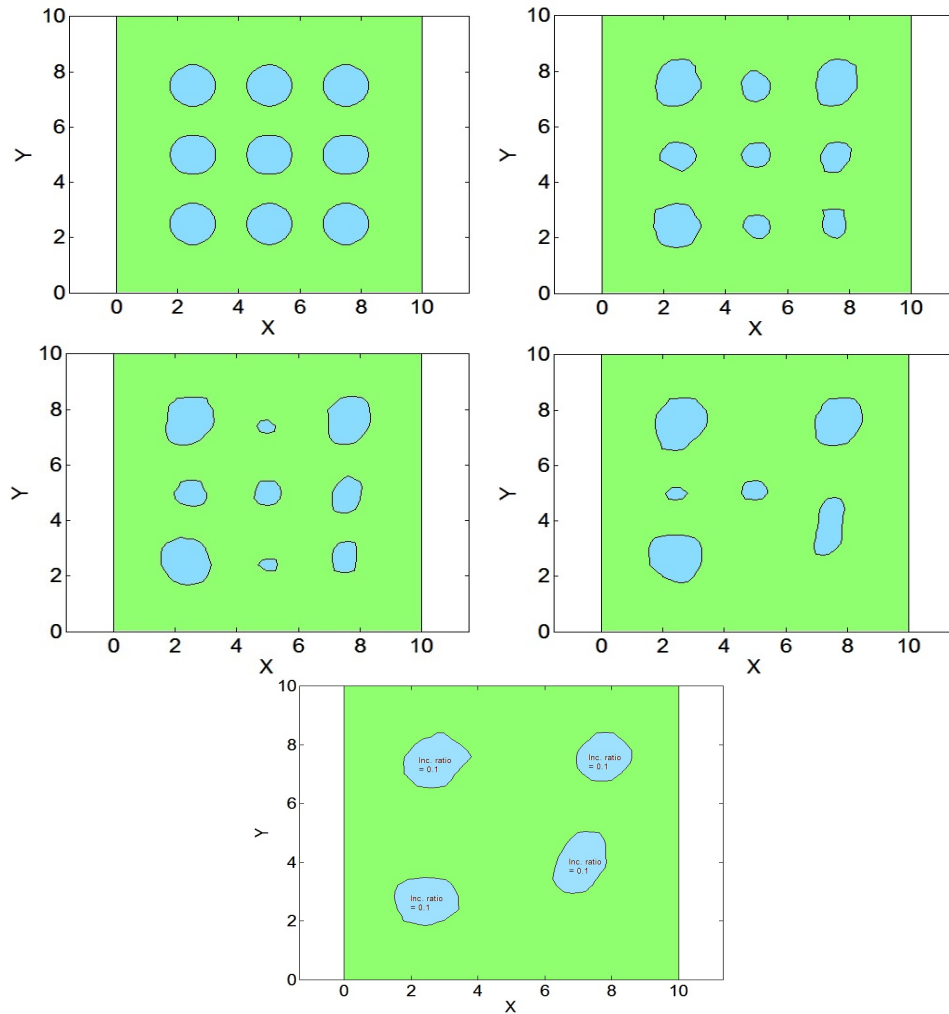


Figure 1.23: Top row : Initial assumption and interface after 50 iterations, second row : Interface after 100 and 300 iterations, bottom row : Inclusion locations detected by the proposed algorithm (stiffness and permittivity ratio = 0.1).

The convergence of the objective function with iterations is shown in figure 1.24. The resolution to which a void/inclusion can be determined depends on two factors,

1.8 Results and discussion

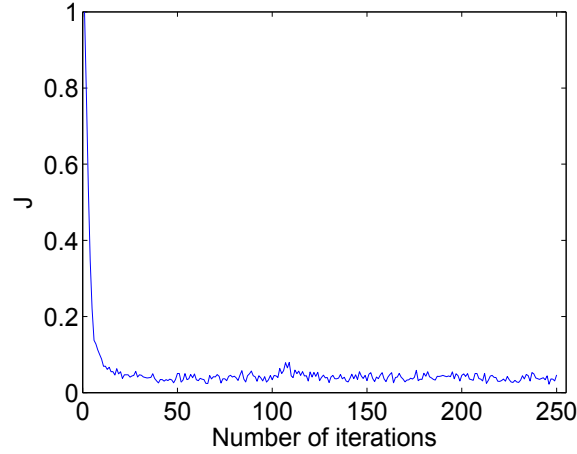


Figure 1.24: Convergence of the objective function with iterations.

the mesh size and spacing of sensors. For example, in a 50×50 mesh, the radius of the smallest circular inclusion that could be detected is almost equal to the width/height of a finite element. Figure 4.8 shows the detected inclusion and the actual interface, the radius of the inclusion is 0.25 units. 50 uniformly spaced pseudo sensors are assumed to be present at the measurement edges. Though a 50×50 mesh is employed in solving the inverse problem in iteration, if the pseudo sensors are restricted to 25, then this inclusion cannot be detected. This is because the inclusion might lie between two sensors and so the response measurements obtained may not be sensitive to the inclusion. The spatial resolution thereby depends on spacing between sensors and the mesh size used in each iteration of the inverse analysis.

1.8 Results and discussion

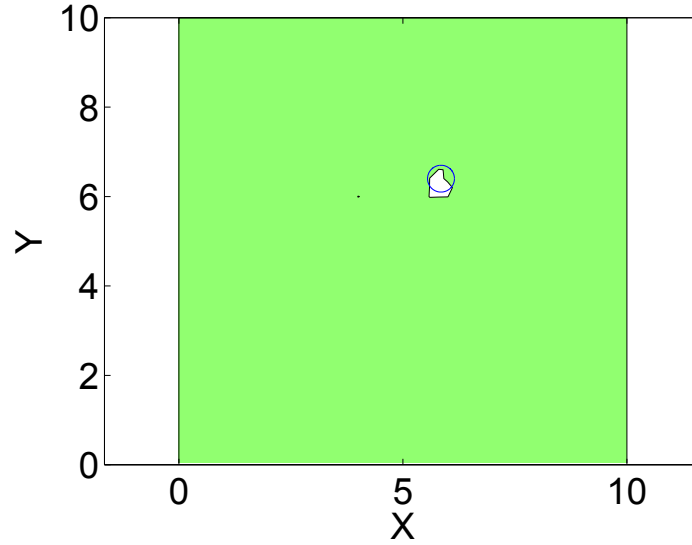


Figure 1.25: The smallest inclusion detected with a mesh of 50X50 and with 50 pseudo sensors. The radius of the actual void = 0.25 units

1.8.4 XFEM and level sets for optimization of nano beams

A computational method for the optimization of nanostructures, where our specific interest is in capturing and elucidating surface stress and surface elastic effects on the optimal nanodesign is presented. XFEM is used to solve the nanomechanical boundary value problem, which involves a discontinuity in the strain field and the presence of surface effects along the interface. The boundary of the nano-structure is implicitly represented by a level set function, which is considered as the design variable in the optimization process. Two objective functions, minimizing the total potential energy of a nanostructure subjected to a material volume constraint and minimizing the least square error compared to a target displacement, are chosen for the numerical examples. The results show optimal topologies of a nanobeam subject to cantilever and fixed boundary conditions. The numerical examples demonstrate the importance of size and aspect ratio in determining how surface effects impact the optimized topology of nanobeams.

Nano beams of thickness lesser than 100 nm exhibit increased stiffness when compared to macro beams of the same aspect ratio. This increased stiffness is attributed the presence of surface elasticity in nano beams. The optimization of such nano beams using XFEM and level sets is performed in chapter 5. Three different nano beams are optimized,

- Cantilever beam

1.8 Results and discussion

- Fixed beam
- simply supported beam

The simply supported nano beam optimization is presented in this section while the remaining examples are shown in chapter 5. Two different objective function are tested, to find which one among them influences the optimal topology,

- J_1 - Minimum compliance
- J_2 - Minimum least square error compared to a target displacement

1.8.4.1 Objective function J_1

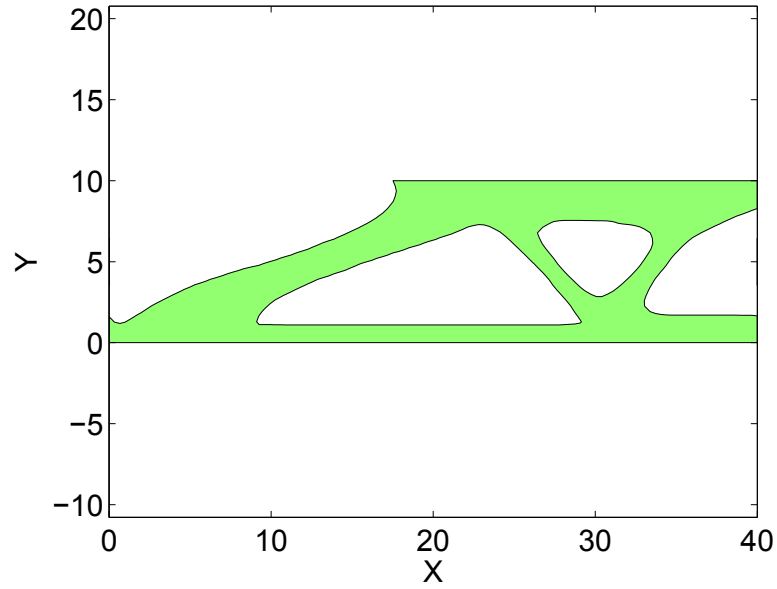
This numerical example concerns the optimization of simply supported nanobeams. For the J_1 objective function, we consider a simply supported beam of aspect ratio 8 of dimension 80×10 nm that is optimized for minimum compliance. A point load of 3.6 nN is applied at the mid span and the volume ratio is constrained to 40%. Taking advantage of the symmetry boundary conditions, half the beam is modeled for computational efficiency. The optimum topology obtained is shown in Figure 1.26(a). The optimization process is repeated by neglecting surface effects, with the result shown in Figure 1.26(b). It is evident from Figures 1.26(a) and 1.26(b) that surface effects do not have influence on the optimum topologies obtained for the minimum total potential energy objective function.

1.8.4.2 Objective function J_2

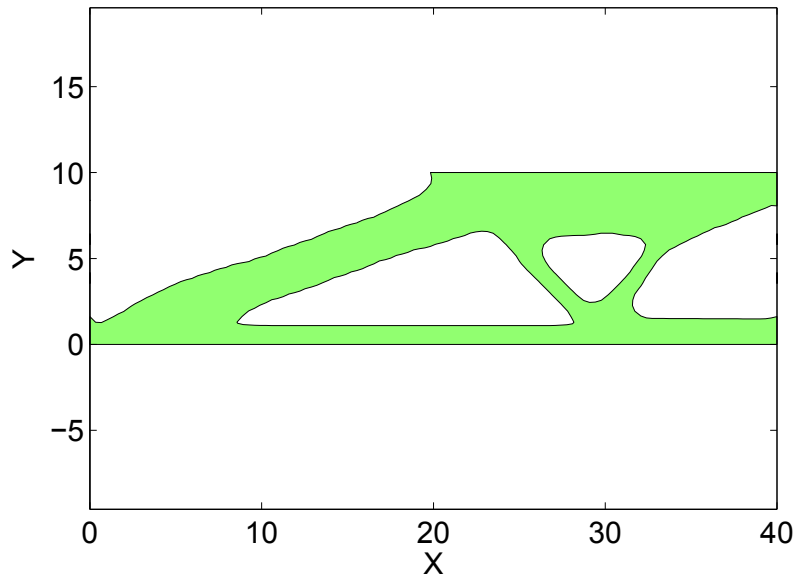
Finally, we consider the optimization of a simply supported beam subject to objective function J_2 . Geometries of 80×10 , 160×20 , 320×40 and 480×60 nm were considered. All beams were subjected to a point load of 3.6 nN at the mid span, while the target displacement at the load location was fixed as 9.3 nm. The stiffness ratios obtained were 11.44%, 6.19%, 3.27%, and 2.5%, respectively, while the volume ratios were 0.57, 0.63, 0.66 and 0.67, respectively.

The optimal topologies are shown in Figure 1.27. As can be seen, the optimal topology changes with dimension, even though the aspect ratio remains constant, and in particular changes dramatically once the nanobeam thickness decreases to 20 nm. For these simply supported nanobeams loaded at the mid span, a stiffness ratio of around 6.2% appears to lead to significant differences in topology.

1.8 Results and discussion



(a)



(b)

Figure 1.26: Optimal topology for objective function J_1 for a 80×10 nm simply supported nanobeam (a) with and (b) without surface effects.

1.8 Results and discussion

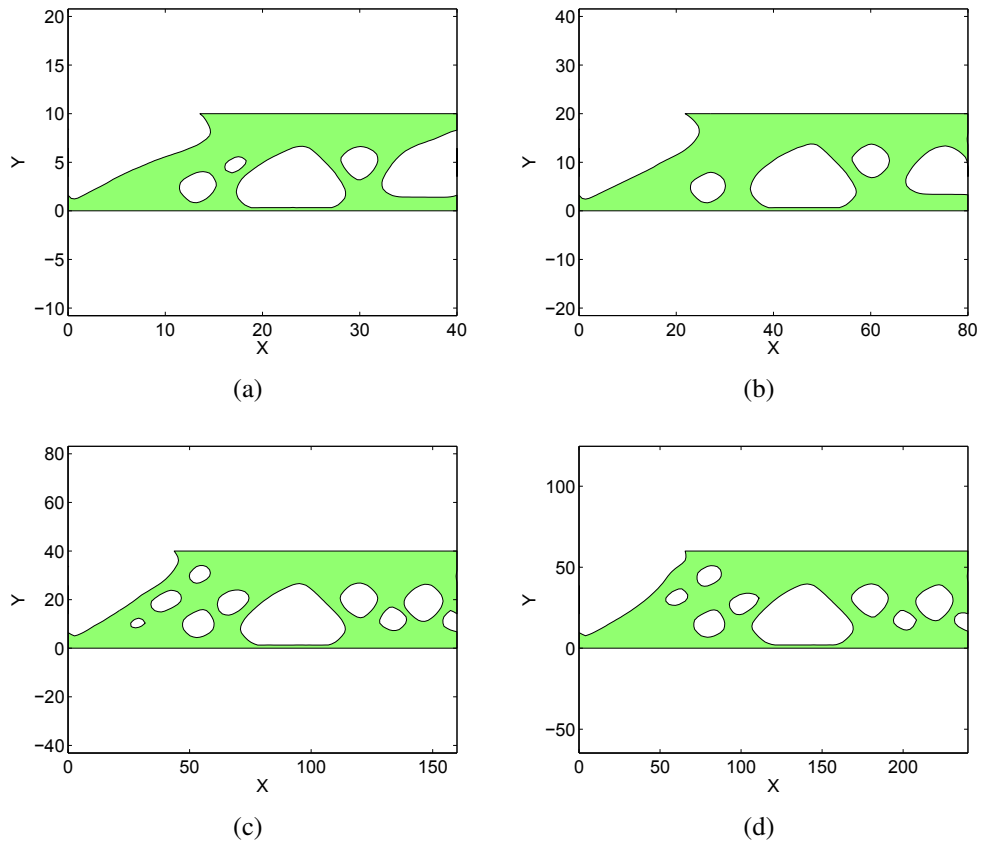


Figure 1.27: Optimal topology for objective function J_2 for a simply supported (a) 80×10 , (b) 160×20 , (c) 320×40 , and (d) 480×60 nanobeam.

1.8 Results and discussion

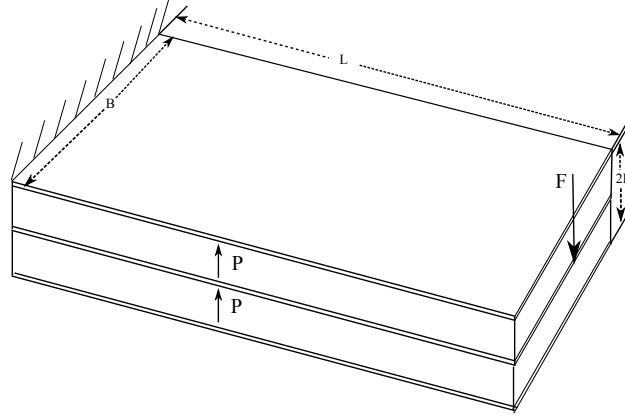


Figure 1.28: A piezoelectric nano cantilever plate subjected to point load, F at free end.

1.8.5 XFEM and level sets for optimization of nano piezoelectric structures

Piezoelectric nanostructures exhibit size dependent properties because of surface elasticity and surface piezoelectricity. In this work, a conventional cantilever energy harvester with piezoelectric nano layers is analysed. An extended finite element formulation is presented for the analysis of piezoelectric nano beams and nano plates. The finite element model for plates is derived based on Kirchhoff plate assumptions and linear through-the-thickness electric potential distribution is assumed. Topology optimization of piezoelectric structures and also piezoelectric layers in an energy harvesting device is performed in order to maximize energy conversion. The influence of surface effects and optimization to maximize energy conversion of nano piezoelectric structures is studied.

Our final example considers a nanoscale bimorph, which as shown in figure 1.28 is comprised of two cantilever piezoelectric nanoplates each of dimension $600 \times 300 \times 10$ nm placed one over another subjected to point load at the free end. Surface elasticity and surface piezoelectricity are accounted for at the top and bottom surfaces of the bimorph, while interface effects between the two nanoplates are neglected. Three electrodes in total, which are placed at the top, middle and bottom of the bimorph, are present. Under open circuit conditions, the electrode at the middle of the bimorph is grounded, while under closed circuit conditions, all the electrodes are grounded.

The approximation of the electric potential field is made by discretizing the plate into several sublayers with linear variation of electric potential within each sublayer⁴³. The number of sublayers for electric potential discretization is taken to be 10.

1.8 Results and discussion

Before performing topology optimization, it was determined that the nominal EMCC of the piezoelectric bimorph, where each plate had dimension $600 \times 300 \times 10$ nm, is 1.25 and 1.07 under closed and open circuit conditions respectively.

We then perform topology optimization of the piezoelectric bimorph to maximize energy conversion. Level set optimization method is adopted and the velocity of level sets is determined by solving an adjoint problem. The volume fraction of the optimized topology is 0.69. The optimized topology of the cantilever piezoelectric nano bimorph is shown in figure 6.8. The optimized topology has more material concentrated close to the fixed end because of higher strain in this region. The ratio of EMCC of the optimized nano cantilever plate with surface effects to a solid nano bimorph plate without surface effects is 1.6 and 1.32 under closed and open circuit conditions respectively.

Maintaining the ratio between dimensions, the depth of each bimorph plate is increased to 20 nm. The ratio of EMCC of the optimized nano cantilever bimorph to a solid nano bimorph without surface effects is 1.45 and 1.27 under closed and open circuit conditions respectively. The optimized topology of the cantilever piezoelectric nano bimorph is shown in figure 1.29. It is clear from the results that as we approach nano scale the inclusion of surface effects leads to increase in efficiency of a nano plate.

The optimized topology without including surface effects for a bimorph made of plates of size $600 \times 300 \times 10$ nm is shown in figure 6.9. When the ratio between the dimensions of the plate is maintained, the optimal topology remains unchanged provided the surface effects are not included.

The inclusion of surface effects has led to removal of more material close to the fixed end. In figure 1.29(a), material is removed upto 150 nm from the clamped end. In figure 1.29(b), material is removed upto around $(2 \times) 225$ nm from the clamped end, while for a cantilever plate without including surface effects material is removed only upto 250 nm from the clamped end as shown in figure 1.30. In figure 1.30, it can be seen that more material is removed far from the clamped end. When the surface piezoelectric effects are included increase in energy conversion occurs inspite of more material removal compared to a nano piezoelectric plate without surface effects.

1.8 Results and discussion

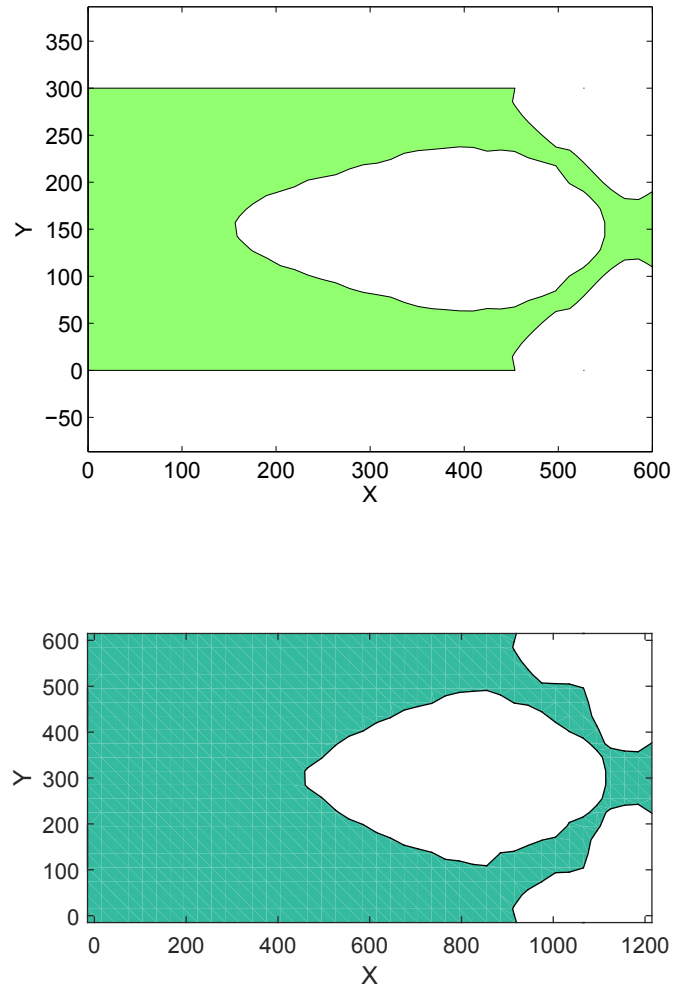


Figure 1.29: (a) Optimized topology (top view) of a $600 \times 300 \times 10$ nm cantilever piezoelectric nano bimorph plate subjected to point load at free end including surface effects; (b) Optimized topology (top view) of a $600 \times 300 \times 10$ nm cantilever piezoelectric nano bimorph plate subjected to point load at free end including surface effects.

1.8 Results and discussion

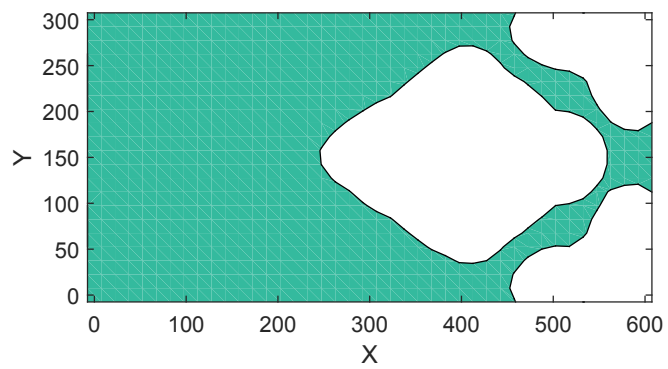


Figure 1.30: Optimized topology (top view) of same geometry but without surface effects.

Chapter 2

Detection of a single flaw in Piezoelectric Structures using XFEM

2.1 Contribution of authors

The work presented in this chapter is published as, S.S.Nanthakumar, T. Lahmer, T. Rabczuk, Detection of flaws in piezoelectric structures using extended FEM, International Journal for Numerical Methods in Engineering 96 (2013) 373389. The final publication is available in <http://onlinelibrary.wiley.com/doi/10.1002/nme.4565/abstract>. The original text from this publication is used in this chapter.

- S.S.Nanthakumar
 - Literature review about various possible methods to be coupled with XFEM
 - Coding of the XFEM-MCS algorithm
 - Solving of numerical examples included
 - Preparing the manuscript
- Prof. Tom Lahmer
 - Assistance in choosing the optimization scheme
 - Discussions to better understand inverse problems
 - Reviewing the manuscript before submission
- Prof. Timon Rabczuk
 - Discussions to better understand XFEM
 - Reviewing the manuscript before submission

2.2 Introduction

The intrinsic electromechanical coupling behavior of piezoelectric materials has found its application in sensors (e.g., sonars), actuators (e.g., ultrasonic cleaners, ultra-precision positioners, ink jetprint heads), signal transmitters (e.g., cellular phone, remote car opener), and surface acoustic wave devices to mention a few. Recently, piezoelectric materials are used in several applications in aircraft industry, for example, shaping the wing of aircraft to improve aerodynamic performance⁴⁴. In diesel engines, solenoid injectors are replaced by piezo actuated injectors⁴⁵. In such applications, piezoelectric materials may experience high stress and electric field concentrations as a result of which they may fail due to fracture or dielectric breakdown. Besides these materials are inhomogeneous, inherently brittle and have low fracture toughness. So assessment of defects like cracks and voids is needed to ensure the reliability of piezoelectric components. Numerical simulation of fracture in piezoelectric ceramics is primarily based on a linear elastic fracture mechanics model⁴⁶. The fundamentals of piezoelectric fracture mechanics can be found in⁴⁷. The analytical work to study the fracture mechanics of piezoelectric ceramics are based on Stroh and Lekhnitskii Formalism. Suo et al.⁴⁸ extended the Stroh formalism to piezoelectric problems, considering a semi infinite piezoelectric ceramic with a crack inside. Sosa⁴⁹ considered an elliptic hole with major axis perpendicular to the polarization direction inside piezoelectric ceramic, and obtained the field variables around the cavity. Xu and Rajapakse⁵⁰ extended this work considering an arbitrarily oriented elliptic hole and concluding that the highest concentrations occur when the elliptical hole is 33° with respect to the polarization direction. A short overview and a critical discussion about the present state in the field of piezoelectric fracture mechanics is given by⁵¹. FEM analysis of cracks in piezoelectric structures under dynamic electro-mechanical loading considering the influence of dielectric medium inside the crack is presented in^{52,53}. A survey on numerical algorithms for crack analyses in piezoelectric structures to be used along with FEM for determining fracture parameters is presented in⁵⁴.

FEM can become cumbersome while modeling crack growth because of the need for remeshing. Mesh free methods offer the advantage of circumventing remeshing in modeling crack growth^{55,56,57} and in FSI problems⁵⁸. One of the mesh free methods, element free Galerkin method^{59,60,61,62} is coupled with optimisation techniques and adopted in NDE applications⁶³ to iteratively solve inverse problems. XFEM algorithm²⁰ also enables crack growth modeling without remeshing. In XFEM a standard displacement-based approximation is enriched near a crack by incorporating both discontinuous fields and the near tip asymptotic fields through a partition of unity method. XFEM exploits the partition of unity property of finite elements identified by Melenk and Babuska⁶⁴, which allows local enrichment functions to be easily incorporated into a finite element approximation. In XFEM, level sets are commonly used to model location of cracks⁶⁵, holes and material interfaces (inclusions)²¹. Several features are

2.3 Basic Piezoelectric Relations

proposed to improve the performance of XFEM^{22,66}. Bechet et al.²³ presented an application of XFEM to the analysis of fracture in piezoelectric materials. His paper focuses on definition of new crack tip enrichment functions suitable for cracks in piezoelectric structures. An extension of XFEM for dynamic fracture in piezoelectric materials is presented in²⁴

Waisman et al¹⁸ investigates an XFEM-GA detection algorithm initially proposed by Rabinovich et al¹⁷ on elastostatic problems with different types of flaws. Rus et al¹⁶ presented a series of studies on damage detection in piezoelectric materials in which the forward problem is solved iteratively using FEM and BEM, the cost functional is minimized by using Genetic Algorithm. An inverse problem to determine the material tensor entries of a piezoelectric transducer by using the measured impedance values for different frequency points as input is solved in Lahmer et al⁶⁷.

The aim of this work is to develop a strategy to uniquely identify straight cracks and elliptical voids in piezoelectric structures. The inverse problem is solved iteratively and XFEM is used in each iteration to solve the forward problem for various trial flaw configurations. For defect identification ill-posedness and missing convexity of the inverse problem has to be considered. Therefore, we need to look for a global optimization method to determine the minimum cost functional. In this work we have employed MCS²⁵, a generalization of the DIRECT algorithm⁶⁸, which can be seen as an intermediate algorithm between methods like implicit filtering, Nelder-Meads, Hooke-Jeeves and the nondeterministic methods like genetic algorithm, simulated annealing or the particle swarm algorithm on the pure heuristical side.

2.3 Basic Piezoelectric Relations

The electro-elastic response of a piezoelectric body of volume Ω and regular boundary surface S , is governed by the mechanical and electrostatic equilibrium equations,

$$\sigma_{ij,j} + f_i = 0 \text{ in } \Omega \quad (2.1)$$

$$D_{i,i} - q = 0 \text{ in } \Omega \quad (2.2)$$

where f_i , q are mechanical body force components and electric body charge respectively. σ_{ij} and D_i are the symmetric Cauchy stress tensor and electric displacement vector components. They are related to the linear Lagrange symmetric strain tensor, ϵ_{kl} and electric field vector, E_k through the converse and direct linear piezoelectric constitutive equations,

$$\sigma_{ij} = C^E_{ijkl} \epsilon_{kl} - e_{kij} E_k \quad (2.3)$$

$$D_i = e_{ikl} \epsilon_{kl} + \kappa^E_{ik} E_k \quad (2.4)$$

2.3 Basic Piezoelectric Relations

$\mathcal{C}_{ijkl}^E, \mathbf{e}_{kij}$ and κ_{ik}^E denote fourth-order elastic stiffness tensor at constant electric field, piezoelectric coupling tensor and dielectric permittivity tensor at constant strain respectively. The strain tensor and electric field vector components are linked to mechanical displacement components u_i and electric field potential ϕ , respectively, by the following relations,

$$\varepsilon_{ij} = \frac{1}{2} ((u_{i,j}) + (u_{j,i})) \quad (2.5)$$

$$E_i = -\phi_{,i} \quad (2.6)$$

The piezoelectric body Ω , could be subjected to the following essential and natural boundary conditions:

Essential boundary conditions

$$u = \bar{u} \text{ (or) } \phi = \bar{\phi} \text{ on } \Gamma_e \quad (2.7)$$

Natural boundary conditions

$$\sigma_{ij}n_j = F_i \text{ (or) } D_i n_i = -Q \text{ on } \Gamma_n \quad (2.8)$$

where $\bar{u}, \bar{\phi}$, F_i , Q and n_i are mechanical displacement, electric potential, surface force components, surface charge and outward unit normal vector components respectively. The crack faces C^+ and C^- are assumed to be both traction-free and electrically impermeable.

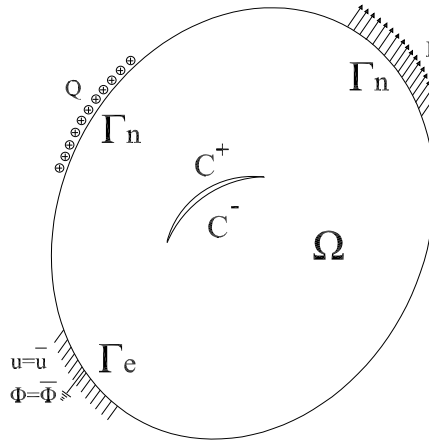


Figure 2.1: Piezoelectric domain with a Crack

2.4 Extended Finite Element Formulation

In XFEM the cracks and void boundaries are implicitly modeled by level set functions^{65,21}. The position of any point of interest with respect to the discontinuity can be uniquely identified using the normal level set function, f and the tangential level set function, g as shown in Figure 2.2. The crack surface is defined as the subset of the zero level set of f , where g is negative. The crack front is defined as the intersection of the two zero level sets.

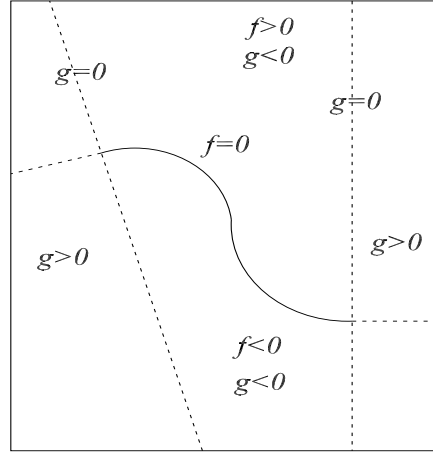


Figure 2.2: Levelset Functions

In XFEM, the approximation of displacement and electric potential field in a piezo-electric material are given by,

$$u^h(x) = \sum_{i \in I} N_i(X) \mathbf{u}_i + \sum_{N=1}^{n_c} \sum_{j \in J} N_j(X) \mathbf{a}_j^{(N)} F_l^{(N)} + \sum_{M=1}^{m_t} \sum_{k \in K} N_k(X) \left(\sum_{i=1}^4 G_i^{(M)}(r, \theta) \mathbf{b}_k^i \right) \quad (2.9)$$

$$\phi^h(x) = \sum_{i \in I} N_i(X) \phi_i + \sum_{N=1}^{n_c} \sum_{j \in J} N_j(X) \boldsymbol{\alpha}_j^{(N)} F_l^{(N)} + \sum_{M=1}^{m_t} \sum_{k \in K} N_k(X) \left(\sum_{i=1}^4 G_i^{(M)}(r, \theta) \boldsymbol{\beta}_k^i \right), \quad (2.10)$$

where J is the set of all nodes whose support is cut by the strong discontinuity or void boundary. The set K contains all the nodes that lies within a fixed region around the crack tip⁶⁹, n_c denotes the number of cracks/voids, m_t is the number of crack tips and l is the number of additional degrees of freedom of crack tip enriched nodes. $\mathbf{a}_j, \mathbf{b}_k, \boldsymbol{\alpha}_j$

2.4 Extended Finite Element Formulation

and β_k are the additional degrees of freedom to be found. For cracks, we choose step function as enrichment in J that ensures jump in displacement and electric potential field,

$$F_I^{(N)} = \text{sign} \left[f^{(N)}(X) \right] - \text{sign} \left[f^{(N)}(X_I) \right] \quad (2.11)$$

$$f^{(N)}(X) = \text{sign} \left[n \cdot (X - X^{(N)}) \right] \min(X - X^{(N)}); X^{(N)} \in \Gamma^{(N)}, \quad (2.12)$$

where n is the outward unit normal of the crack face.

As the approximation does not have Kronecker-delta property, shifting of enrichment functions is performed in order to recover this property.

For voids, $F_I^{(N)} = 0$ and 1, for nodes that lie inside and outside the voids respectively. The nodes that lie exactly over the void boundary are not enriched²¹. The last term in Equation (2.9) and (2.10) will vanish for voids. Bechet et al²³ concluded that comparing results obtained using a specifically designed six-fold enrichment for electromechanical problems with the standard four-fold enrichment of the isotropic elasticity in similar settings shows almost no difference. Also the forward problem has to be solved in each iteration and it is advantageous to have lesser additional degrees of freedom. So in this work the standard four-fold enrichment functions are used for both displacement and electric potential field. Numerical integration of stiffness matrix of the elements containing the crack tip is performed using polar integration approach presented in Chahine et al²². Substituting the displacement field from equation (2.9) and electric potential field from equation (2.10) into the weak form illustrated in Piefort et al⁷⁰, the standard discrete system of equations is obtained,

$$\begin{pmatrix} K_{ij}^{uu} & K_{ij}^{ua} & K_{ij}^{ub} \\ K_{ij}^{au} & K_{ij}^{aa} & K_{ij}^{ab} \\ K_{ij}^{bu} & K_{ij}^{ba} & K_{ij}^{bb} \end{pmatrix} \begin{Bmatrix} u \\ a \\ b \end{Bmatrix} + \begin{pmatrix} K_{ij}^{u\phi} & K_{ij}^{u\alpha} & K_{ij}^{u\beta} \\ K_{ij}^{a\phi} & K_{ij}^{a\alpha} & K_{ij}^{a\beta} \\ K_{ij}^{b\phi} & K_{ij}^{b\alpha} & K_{ij}^{b\beta} \end{pmatrix} \begin{Bmatrix} \phi \\ \alpha \\ \beta \end{Bmatrix} = \begin{Bmatrix} f \\ f^a \\ f^b \end{Bmatrix} \quad (2.13)$$

$$\begin{pmatrix} K_{ij}^{\phi u} & K_{ij}^{\phi a} & K_{ij}^{\phi b} \\ K_{ij}^{\alpha u} & K_{ij}^{\alpha a} & K_{ij}^{\alpha b} \\ K_{ij}^{\beta u} & K_{ij}^{\beta a} & K_{ij}^{\beta b} \end{pmatrix} \begin{Bmatrix} u \\ a \\ b \end{Bmatrix} - \begin{pmatrix} K_{ij}^{\phi\phi} & K_{ij}^{\phi\alpha} & K_{ij}^{\phi\beta} \\ K_{ij}^{\alpha\phi} & K_{ij}^{\alpha\alpha} & K_{ij}^{\alpha\beta} \\ K_{ij}^{\beta\phi} & K_{ij}^{\beta\alpha} & K_{ij}^{\beta\beta} \end{pmatrix} \begin{Bmatrix} \phi \\ \alpha \\ \beta \end{Bmatrix} = \begin{Bmatrix} g \\ g^\alpha \\ g^\beta \end{Bmatrix} \quad (2.14)$$

$$\begin{aligned} K_{ij}^{uu} &= \int_{\Omega} B_{ui}^T C B_{uj} d\Omega; K_{ij}^{ua} = \int_{\Omega} B_{ui}^T C B_{uj} F_j^{(N)} d\Omega = (K_{ji}^{au})^T; \\ K_{ij}^{ub} &= \int_{\Omega} B_{ui}^T C B_{uj} G_j^{(N)} d\Omega = (K_{ji}^{bu})^T; K_{ij}^{aa} = \int_{\Omega} F_i^{(N)} B_{ui}^T C B_{uj} F_j^{(N)} d\Omega; \\ K_{ij}^{ab} &= \int_{\Omega} F_i^{(N)} B_{ui}^T C B_{uj} G_j^{(N)} d\Omega = (K_{ji}^{ba})^T; K_{ij}^{bb} = \int_{\Omega} G_i^{(N)} B_{ui}^T C B_{uj} G_j^{(N)} d\Omega; \\ K_{ij}^{u\phi} &= \int_{\Omega} B_{ui}^T e B_{\phi j} d\Omega = (K_{ji}^{\phi u})^T; K_{ij}^{u\alpha} = \int_{\Omega} B_{ui}^T e B_{\phi j} F_j^{(N)} d\Omega = (K_{ji}^{\alpha u})^T; \end{aligned}$$

2.5 Inverse Problem

$$\begin{aligned}
K_{ij}^{u\beta} &= \int_{\Omega} B_{ui}^T e B_{\phi j} G_j^{(N)} d\Omega = (K_{ji}^{\beta u})^T; K_{ij}^{a\phi} = \int_{\Omega} F_i^{(N)} B_{ui}^T e B_{\phi j} d\Omega = (K_{ji}^{\phi a})^T; \\
K_{ij}^{a\alpha} &= \int_{\Omega} G_i^{(N)} B_{ui}^T e B_{\phi j} F_j^{(N)} d\Omega = (K_{ji}^{\alpha a})^T; K_{ij}^{a\beta} = \int_{\Omega} F_i^{(N)} B_{ui}^T e B_{\phi j} G_j^{(N)} d\Omega = (K_{ji}^{\beta a})^T; \\
K_{ij}^{b\phi} &= \int_{\Omega} G_i^{(N)} B_{ui}^T e B_{\phi j} d\Omega = (K_{ji}^{\phi b})^T; K_{ij}^{b\alpha} = \int_{\Omega} G_i^{(N)} B_{ui}^T e B_{\phi j} F_j^{(N)} d\Omega = (K_{ji}^{b\alpha})^T; \\
K_{ij}^{b\beta} &= \int_{\Omega} G_i^{(N)} B_{ui}^T e B_{\phi j} G_j^{(N)} d\Omega = (K_{ji}^{b\beta})^T; \\
K_{ij}^{\phi\phi} &= \int_{\Omega} B_{\phi i}^T \kappa B_{\phi j} d\Omega; K_{ij}^{\phi\alpha} = \int_{\Omega} B_{\phi i}^T \kappa B_{\phi j} F_j^{(N)} d\Omega = (K_{ji}^{\alpha\phi})^T; \\
K_{ij}^{\phi\beta} &= \int_{\Omega} B_{\phi i}^T \kappa B_{\phi j} G_j^{(N)} d\Omega = (K_{ji}^{\beta\phi})^T; K_{ij}^{\alpha\alpha} = \int_{\Omega} F_i^{(N)} B_{\phi i}^T \kappa B_{\phi j} F_j^{(N)} d\Omega; \\
K_{ij}^{\alpha\beta} &= \int_{\Omega} F_i^{(N)} B_{\phi i}^T \kappa B_{\phi j} G_j^{(N)} d\Omega = (K_{ji}^{\beta\alpha})^T; K_{ij}^{\beta\beta} = \int_{\Omega} G_i^{(N)} B_{\phi i}^T \kappa B_{\phi j} G_j^{(N)} d\Omega;
\end{aligned}$$

2.5 Inverse Problem

The task now is to identify the size and location of straight cracks and elliptical voids, i.e. the determination of N parameters defining the flaw geometries, p_N by measurements on boundary of the piezoelectric structure which is assumed to be stressed by moderate loads that do not cause the crack to grow further. The measurements on the boundary include both the mechanical displacements and the electric potential. The piezoelectric structure is subjected to mechanical loads. We define the following forward operator which maps the parameters defining the flaw to measurements on the boundary of the structure,

$$F : X \rightarrow Y \quad (2.15)$$

$$p_N \mapsto (u, v, \phi)|_{\Gamma} \quad (2.16)$$

In (2.15) X denotes the parameter space, i.e. the space of all possible crack forms and Y , the space of measurements (here displacements and electric potential). Assuming that χ^{EXP} contains measured data with noise, the inverse problem corresponds to solving for p_N in

$$F(p_N) = \chi^{EXP} \quad (2.17)$$

which can be approximated by minimizing the least-squares cost functional,

$$J = \left(\sum_{i=1}^{N_{meas}} |\chi_i^{EXP} - \chi_i^{XFEM}|^2 \right)^{\frac{1}{2}}. \quad (2.18)$$

The forward operator or parameter-to-solution map F is assumed to be continuous in the neighbourhood of the minimum. As mentioned earlier the inverse problem of damage detection is solved iteratively. Iterative methods are computationally more expensive as they need to solve a direct problem at each step. XFEM proves advantageous in

2.5 Inverse Problem

this regard as the background mesh remains the same for all iterations while the flaw configuration alone varies in each iteration. This means that the set of enriched nodes and the stiffness matrices of the associated elements alone vary with each iteration, while the FEM portion of global stiffness matrix, which comprises almost 90% of the elements in the matrix, remains unchanged throughout. The time consuming process of meshing, developing nodal connectivity and assembling the entire stiffness matrix are all circumvented by employing XFEM to solve the forward problem in each iteration. The minimum size of flaw that can be determined depends on the size of background mesh adopted in solving the forward problem, provided boundary measurements are sensitive to such flaws.

2.5.1 Multilevel Coordinate Search-MCS

The inverse problem of flaw detection is generally ill-posed as uniqueness and stable dependency of the solution cannot be guaranteed beforehand. Seeking however, a finite number of parameters defining flaw geometry renders the inverse problem to a finite dimensional nonlinear optimization problem. In order to solve the non-convex inverse

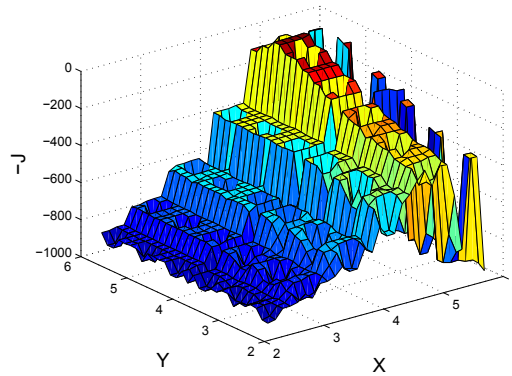


Figure 2.3: 3D Contour plot of the negative of objective function defined in equation 2.18 for a crack identification problem with $N=2$. The optimum is located at point (5.25,5.25)

problem, for example, determining the minimum of the objective function like the one shown in figure 2.3, an optimization technique needs to be applied which,

- starts with global searches, as initial guess cannot be given in high quality.
- allows bound constraints. This is because the trial parameters should be such that crack shall not leave the electromechanical domain.

2.5 Inverse Problem

- performs local search in surroundings of the minima. Smoothness of the cost function closer to the global minimum can be exploited in local searches, which can significantly improve convergence and make the approach more efficient.
- provides a reliable convergence analysis. At the end, we want to present results which stem from an optimization theory that guarantees convergence as opposed to many heuristic global search strategies which only after computing a large number of samples guarantee convergence to a high probability.

Looking at literature, the method of choice is the Multilevel Coordinate Search (MCS) algorithm proposed in Huyer et al²⁵, which has its base on ideas of the DIRECT method⁶⁸. Kelley introduces the DIRECT⁷¹ as “worth considering as an intermediate algorithmic level between methods like implicit filtering, Nelder-Mead or Hooke-Jeeves on the conservative side and nondeterministic methods like simulated annealing or genetic algorithms on the radical side”. The MCS is as stated by the proposers, as an intermediate between purely heuristic methods and methods that allow an assessment of the quality of the minimum obtained. It is in its nature similar to the DIRECT search algorithm (which is a modification of the standard Lipschitzian approach however without the need to specify a Lipschitz constant), however the MCS is additionally guaranteed to converge if the objective function is continuous in the neighbourhood of a global minimizer. The algorithm provides techniques of local search that lead to fast convergence as soon as the global part of the algorithm has indicated regions worth of local search.

2.5.2 Key components of MCS

In this subsection, we briefly summarize the concepts implemented in the MCS. For details we refer however to the main article²⁵. As in DIRECT, the minimizer is tried to be found by successively dividing the search domain into smaller boxes which contain distinguishable points, so-called base points. The algorithm has features of both global and local search where the balance is found by applying multilevel approaches. In this strategy, every box is assigned a value s depending on how often it has already been processed. Boxes with level values exceeding a certain threshold are assumed to be too small for further subdivision. Other boxes have a label zero, indicating that they have already been subdivided and can be ignored at this sweep. Whenever a box is split, the subboxes obtain level number $s + 1$ or $\min(s + 2, s_{max})$. The algorithm proceeds with sweeps over all boxes at low level (large boxes) which comprises the global search and compares the function values. Now the algorithm proceeds to higher levels (generally boxes that have been split more often) and compare on every level the cost function values, then leading to local search. Details about initialization, sweeps, splitting of boxes, the local search based on a local quadratic model by triple searches can be retrieved from Huyer et al²⁵. Additionally in Huyer et al²⁵ a promising convergence

2.6 Numerical Examples

theorem is stated, under the assumption that there is an $\epsilon > 0$ such that $f(y) > f(x)$ for any nonglobal local minimizer y and for any $y \in [u, v]$ with sufficiently large norm, the MCS algorithm with local search finds a global minimizer after at most S sweeps for any large enough s_{max} .

2.6 Numerical Examples

The performance of the algorithm that has been proposed for identifying flaws in piezoelectric structures is demonstrated by applying them to certain flaw detection problems in this section. In all the following examples a piezoelectric plate (10×10 units) made of PZT-5H with material properties shown in Table 2.1 is considered. We have used plane strain assumption in which all field variables depend on (x, y) , where y is the polarization direction.

The material properties correspond to poling in y direction. The fact that the elastic

Table 2.1: Properties of Piezoelectric Material, PZT-5H		
Elastic Constants	Piezoelectric constants	Dielectric constants
$C_{11}=126 \text{ GPa}$	$e_{21}=-6.5 \text{ C/m}^2$	$\kappa_{11}=15.04 \text{ C/(GVm)}$
$C_{12}=84.1 \text{ GPa}$	$e_{22}=23.3 \text{ C/m}^2$	$\kappa_{22}=13 \text{ C/(GVm)}$
$C_{22}=117 \text{ GPa}$	$e_{16}=17 \text{ C/m}^2$	
$C_{66}=23 \text{ GPa}$		

constants, the dielectric permittivity constants and the piezoelectric constants have different orders will make the stiffness matrix ill-conditioned and leads to unstable results. Dimension changing method adopted in⁷² is done to overcome the matrix illness. As shown in figure 2.4, the piezoelectric plate is subjected to mechanical line load (T_{yy}) at top edge, the bottom edge is fixed and electric potential is set to zero. Horizontal displacement, u , vertical displacement, v and electric potential, ϕ are measured along the right edge of the plate at 25 sensor locations. A similar setup is employed in Rus et al for detection of voids in a piezoelectric plate. It is shown in Rus et al.¹⁶ that, excitation of the specimen by a mechanical traction transverse to the polarization direction provides better identifiability than applying an electrical load. Besides, as the measurements are made at boundary of specimen, far away from crack tips in most cases and as the permittivity of air is 10^{-3} orders of magnitude less than that of the piezoelectric material, the impermeable crack assumption holds without much loss of accuracy in most cases.

Measurements

Since no experimental measurements are available in this study, they are simulated by

2.6 Numerical Examples

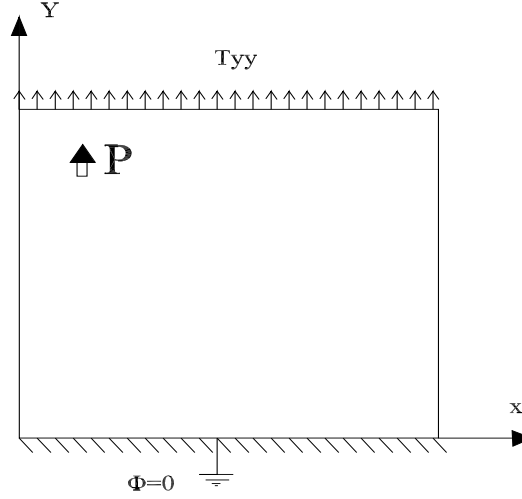


Figure 2.4: Boundary conditions and Loads on the modeled Piezoelectric plate

XFEM. In order to avoid inverse-crimes we used two different mesh sizes for creating the data and for solving forward problem. To generate the target data, a mesh finer to the one used for solving the inverse problem is employed. In addition, the generated synthetic data, are perturbed by a $\pm 1\%$ of random noise : $\chi^{EXP} = \chi^{XFEM}(1 + 0.01B)$, where B is a random number between -1 and +1.

2.6.1 Edge Crack

In case of an edge crack, one end of the crack is visible and the location of interior crack tip is the one to be determined. So the number of parameters to be determined is two, $p_N = (X_c, Y_c)$. The convergence plot indicates that the MCS predicts the global minima well before the total number of iterations. The search algorithm then deviates from the parameter corresponding to global minima and searches the parameter space for better function values. After reaching maximum number of iterations, which depends on the total number of parameters to be determined, the algorithm gives the best parameter value corresponding to the global minima. In this example, the coordinate of crack tip to be determined is (2.5, 5.75). The mesh size used for solving the forward problem is $h = 1/50$. The plate is subjected to $T_{yy} = 1 \text{ GPa}$ at the top edge of the plate. The search space for parameters is set to be $[0.25, 9.75]$. Figure 2.5 shows the convergence of the algorithm for this two parameter identification problem. The algorithm is usually stopped based on two criteria, (1) maximum number of function evaluations (2) number of sweeps to be performed when there is no further improve-

2.6 Numerical Examples

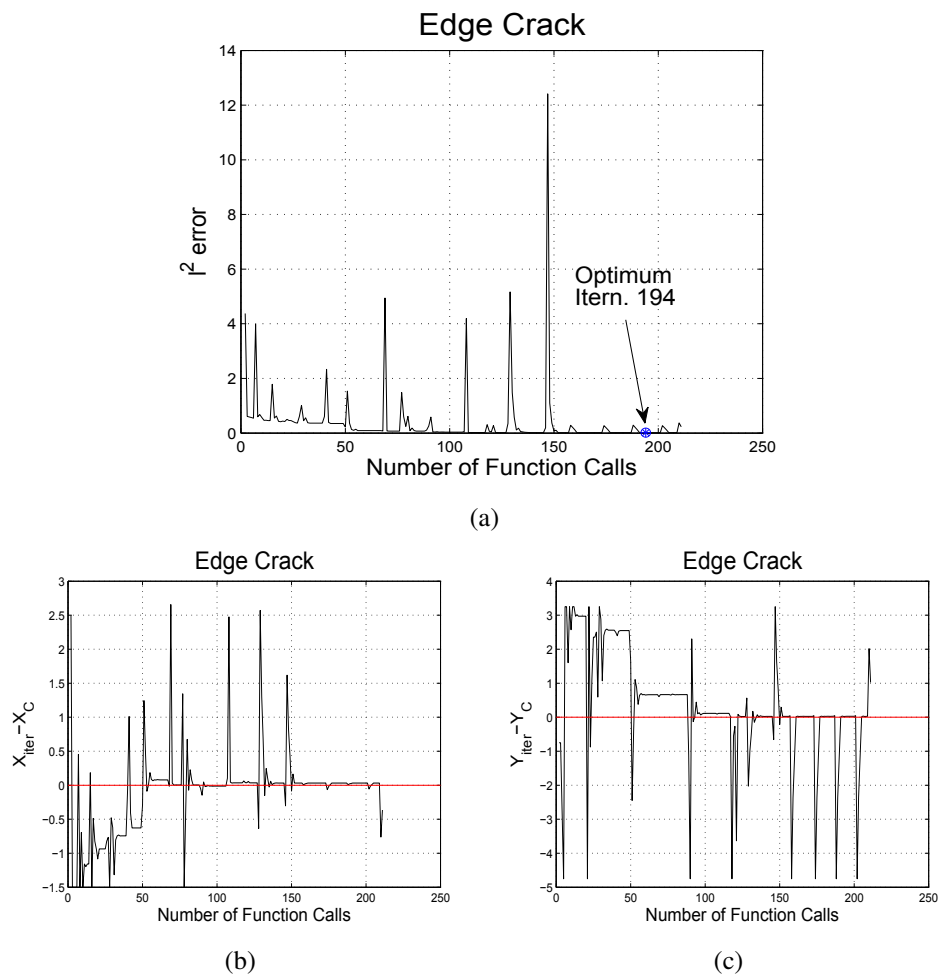


Figure 2.5: Convergence of XFEM-MCS methodology for two parameter estimation (Edge Crack)

2.6 Numerical Examples

ment in solution. The maximum number of function evaluations suggested in Huyer et al.²⁵ is $50 * n^2 + 10$, where n is the number of parameters to be determined. In this work for several test problems solved, the stopping criteria is set as maximum number of function evaluations. The algorithm converges comfortably before reaching the stopping criteria with sufficient accuracy. There is no considerable improvement in solution beyond the maximum number of function evaluations. In this example the optimal parameters are obtained at 194th iteration. The value of s_{max} , which restricts the number of splits performed in each box, is set as $5 * n + 10$ where n is the number of parameters to be determined. This is the default value specified in Huyer et al.²⁵ and changing this value affects the relative number of global and local searches performed. Higher s_{max} values like the one assigned leads to increased global searches which is favourable for the damage detection inverse problem solved in these examples.

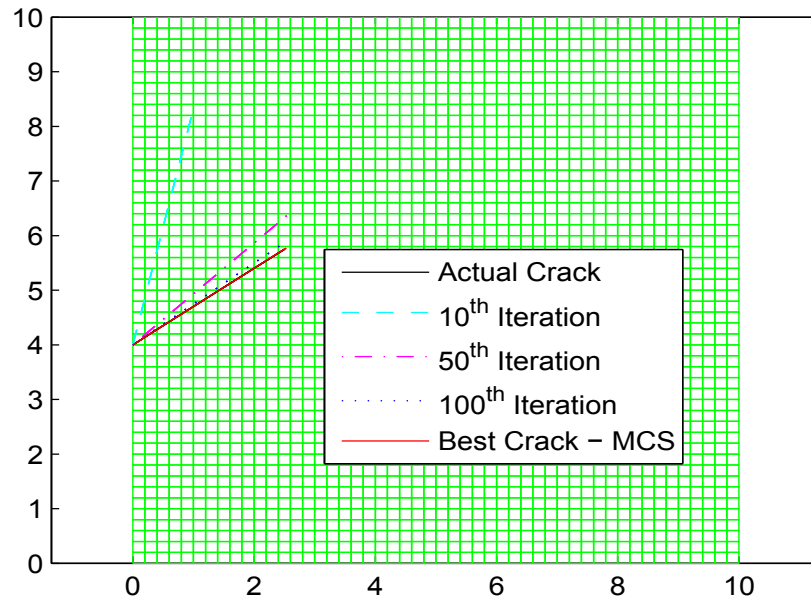


Figure 2.6: Best crack parameters obtained using XFEM-MCS algorithm for edge crack estimation

2.6.2 Interior Crack

In this case the parameters to be identified are the coordinates of the two crack tips that lie in the interior of the piezoelectric plate, $p_N = (x_{1C}, y_{1C}, x_{2C}, y_{2C})$. As the parameter to be identified is four, the maximum number of evaluations increases correspondingly.

2.6 Numerical Examples

In this example the numerical value of crack tip coordinates to be determined are : $(2.0, 5.0), (7.0, 6.5)$. The mesh size used for solving the forward problem is $h = 1/50$. The plate is subjected to $T_{yy}=1 \text{ GPa}$ at the top edge of the plate. The search space for parameters is set to be $[0.25, 9.75]$. Besides this bound the trial parameters that lead to crack whose length is so shorter such that it does not traverse through atleast 3 elements are assigned a higher function value, so that they get neglected during the global search. Figure 2.7 shows the convergence of the algorithm for this four parameter identification problem. Figure 2.8 shows the crack configurations generated by the optimization algorithm at various iterations and the best crack configuration (i.e.) the crack corresponding to least L^2 error of cost functional. It is evident from the plots that the optimisation algorithm converges to the minima but still deviates from it and keeps searching globally for better optima. After specified number of iterations it returns the best parameters which corresponds to least objective function value. In this example the optimal parameters are obtained at 731st iteration.

2.6.3 Elliptical Void

In case of an elliptical void, the parameters to be predicted are length of major axis, length of minor axis and coordinates of center of the ellipse. So the total number of parameters to be determined is again four, $p_N=(a, b, x_C, y_C)$. The elliptical void detected in this test problem is defined by following parameters: center of void $(X_c, Y_c) = (7.0, 6.5)$, length of first axis, $a = 0.5$, length of second axis, $b = 0.75$. The bounds for the coordinates of center of void is $[0.5, 9.5]$. The lengths of the two axis are restricted to one-fourth of the horizontal dimension of the specimen. Besides these bounds the trial parameters which lead to voids whose boundary intersect with the plate boundary are assigned a higher function value, so that they get neglected during the global search. The mesh size used for solving the forward problem is $h= 1/75$. The plate is subjected to $T_{yy}=1 \text{ GPa}$ at the top edge of the plate. Figures 2.9 and 2.10 show convergence of the algorithm to actual parameters and the final void boundary detected. In this example the optimal parameters are obtained at 666th iteration.

2.6.4 Non-Elliptical void configurations

As shown in previous section, the XFEM-MCS algorithm can detect elliptical voids. It is shown in this section that the algorithm can also identify irregular void shapes and determine the equivalent elliptical form of the boundary of such voids. In order to enhance the detection of non elliptical void shapes, the number of parameters to be determined is increased to five. Besides the parameters described in previous section, angle made by one axis of the ellipse with horizontal, is also considered as an additional parameter. The bound for angle is $[0, \pi/2]$.

The algorithm is tested for an inclined elliptical void, angle made by first axis with

2.6 Numerical Examples

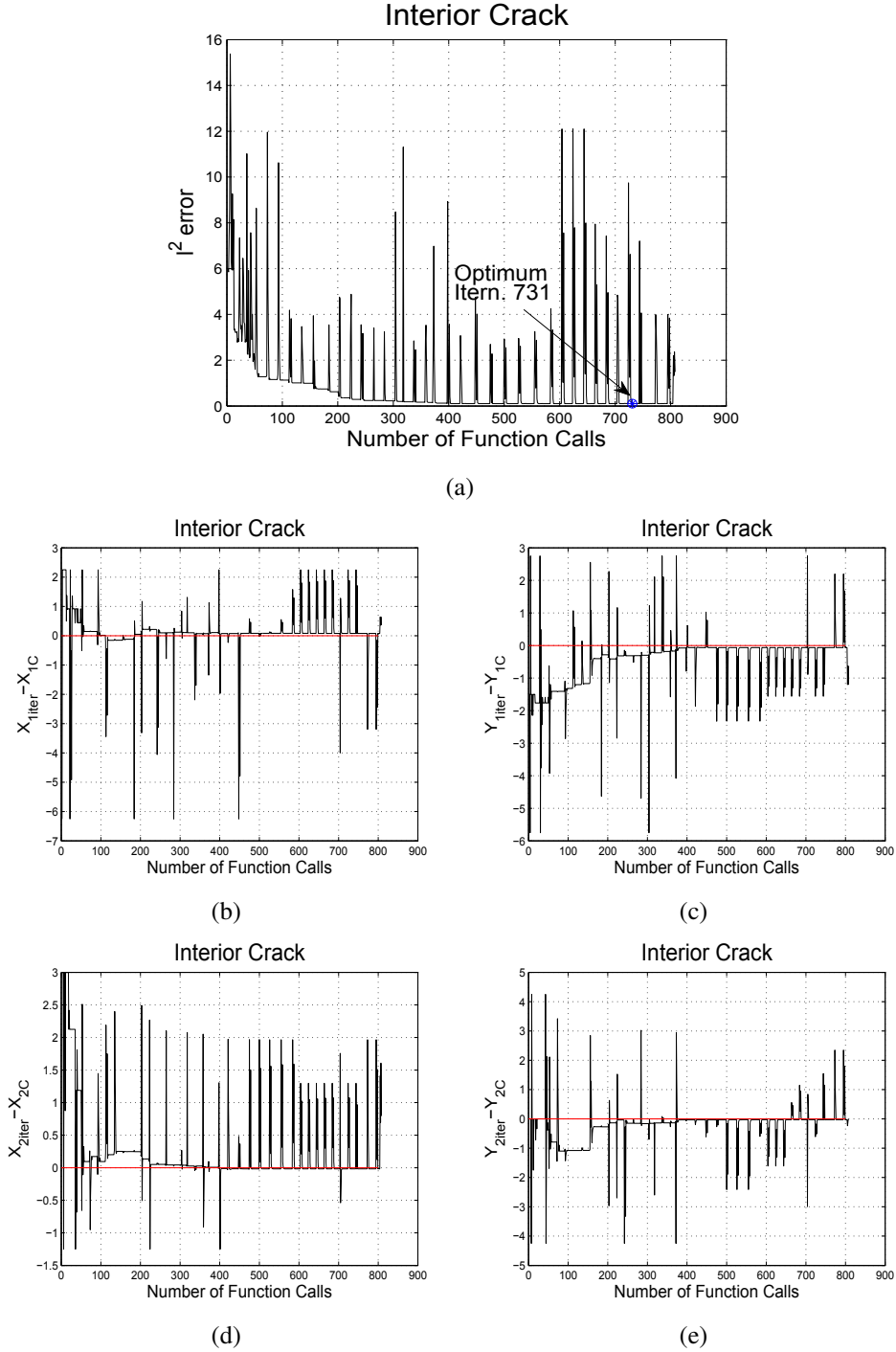


Figure 2.7: Convergence of XFEM-MCS methodology for Four parameter estimation (Interior Crack)

2.6 Numerical Examples

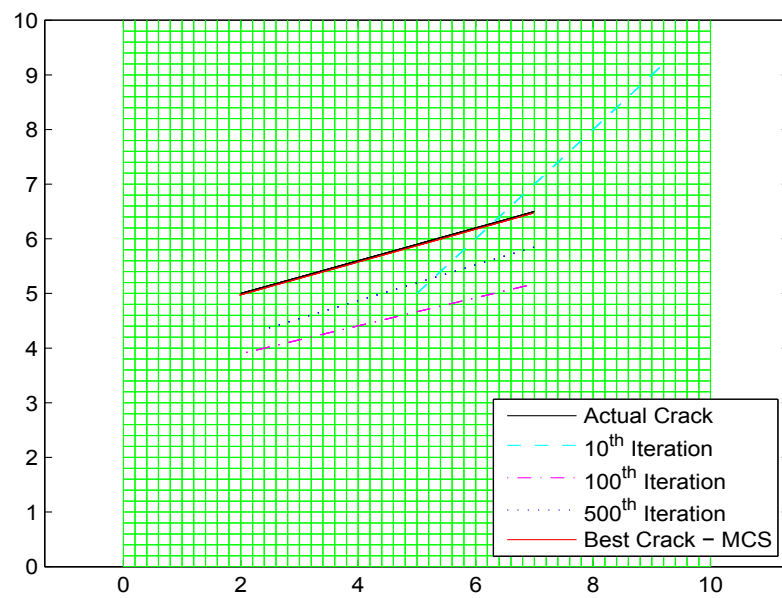


Figure 2.8: Best crack parameters obtained using XFEM-MCS algorithm for interior crack estimation

2.6 Numerical Examples

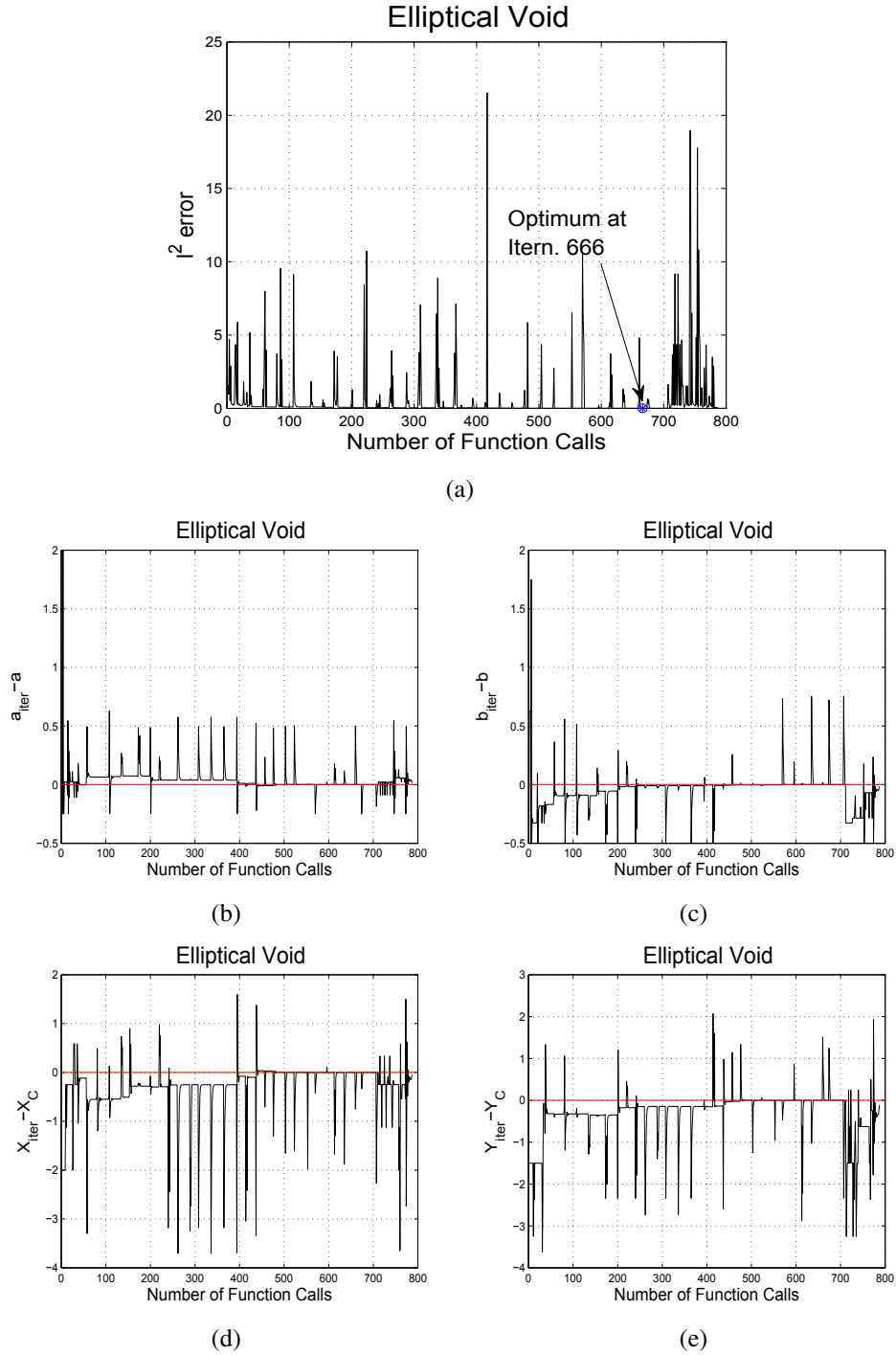


Figure 2.9: Convergence of XFEM-MCS methodology for Four parameter estimation (Elliptical Void)

2.6 Numerical Examples

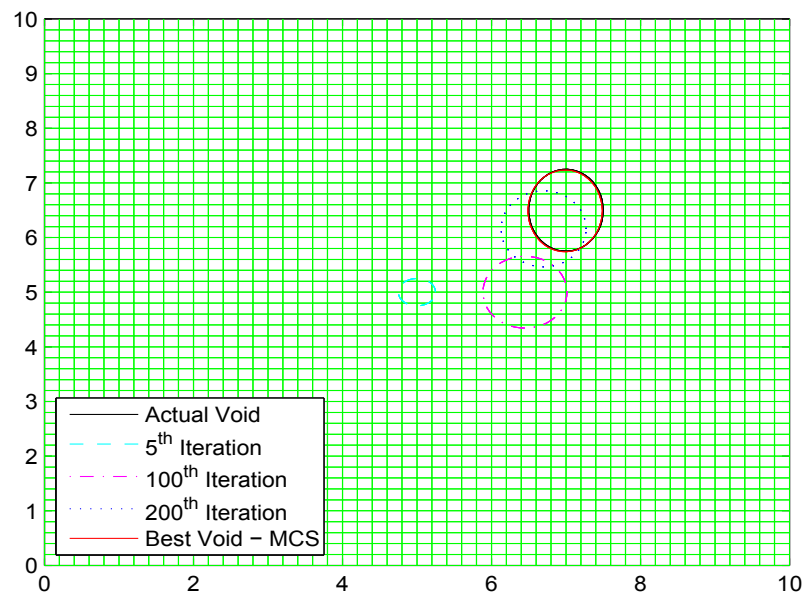


Figure 2.10: Best Void parameters obtained using XFEM-MCS algorithm for detection of Elliptical Void

2.6 Numerical Examples

horizontal = $\pi/4$ (anticlockwise). Besides this bound the trial parameters which lead to voids whose boundary intersect with the plate boundary are assigned a higher function value, so that they get neglected during the global search. Figure 2.11 shows the final void boundary detected. The performance of the algorithm in predicting irregular void boundary is tested by applying them to several non elliptical shapes, two of which are shown in figure 2.12. It is evident from the results that the XFEM-MCS algorithm proves to be handy in identifying irregular voids as well. These examples prove that the algorithm can detect a straight crack and elliptical void in piezoelectric materials. However one does not know before hand whether flaw present in the specimen is a crack or void. The performance of the algorithm in detecting a crack using parameters defining elliptical void is shown in figure 2.13. The result is encouraging, because when a narrow void like the one shown in figure 2.13 is obtained as solution, an engineering mind can judge the nature of flaw in specimen. So it is recommended that irrespective of problem in hand the elliptical void defined by five parameters can be used to detect defect.

2.6.5 Influence of Noise and inexactness in material parameters

It is well known that a small perturbation in measurement data may highly influence the solution of the inverse problem. It is impossible to get noise free data and quality of crack detection falls rapidly with the increase in noise component in the target data. Figure 2.14 shows the rate of divergence of objective function with increase in noise. In the figure, 2-parameter estimation corresponds to edge crack problem solved in section 2.6.1 and 4-parameter estimation corresponds to interior crack problem solved in section 2.6.2. In figure 2.14, systematic noise means a constant value of noise in all sensor locations while random noise means a varying value of noise in each sensor location. For example, 1% of random noise means a varying noise value not exceeding 1% in each sensor location while 1% of systematic noise means a constant 1% of noise value in the sensor locations. It is evident from figure 2.14 that rate of divergence of objective function with increase in noise has an almost linear behavior. The inference is that by discretizing the sought for flaws defined by finite parameters (here ≤ 5) the inverse problem is sufficiently well regularized.

Piezoelectric material constants are estimated by measurements proposed by the IEEE Standard from well-defined test samples or model based identifications⁷³. Also explicit formulas are developed for parameter extraction from resonance characteristics and other measureable quantities. However, these results always provide information on the material coefficients with remaining uncertainty. The influence of inexactness in material constants on the solution of inverse problem is shown in figure 2.15. The results shown in the figure are obtained by solving elliptical void example shown in section 2.6.3 with varying material constant values compared to the one that corresponds to target measurement values. It is evident from the figure that the variation in

2.7 Conclusion

piezoelectric coupling coefficients have more influence on the solution when compared to variation in elastic and permittivity constants.

2.7 Conclusion

In this paper an algorithm to detect and quantify defects in piezoelectric plates is developed. The inverse problem is solved iteratively, XFEM is used for solving the forward problem in each iteration. XFEM offers the advantage of maintaining a fixed background mesh irrespective of the trial flaw configurations. This alleviates the need for remeshing the domain in each forward iteration and therefore is computationally efficient. The cost functional is minimised by using a global search algorithm, Multi-level Coordinate Search (MCS). This optimization method strikes a balance between optimization methods which are fast but converge to local optima and the heuristic optimization methods which are computationally expensive. It is evident from the test problems shown, that the XFEM-MCS algorithm proves to be robust in identifying defects in piezoelectric structures.

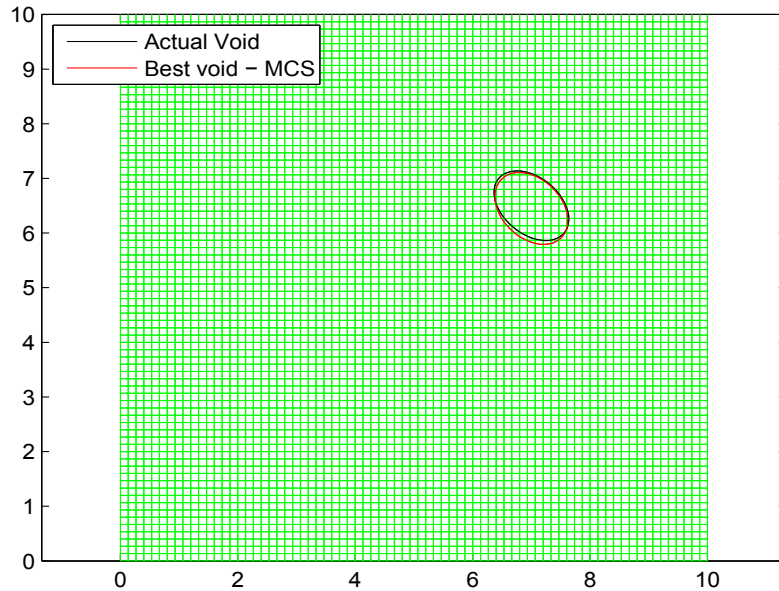
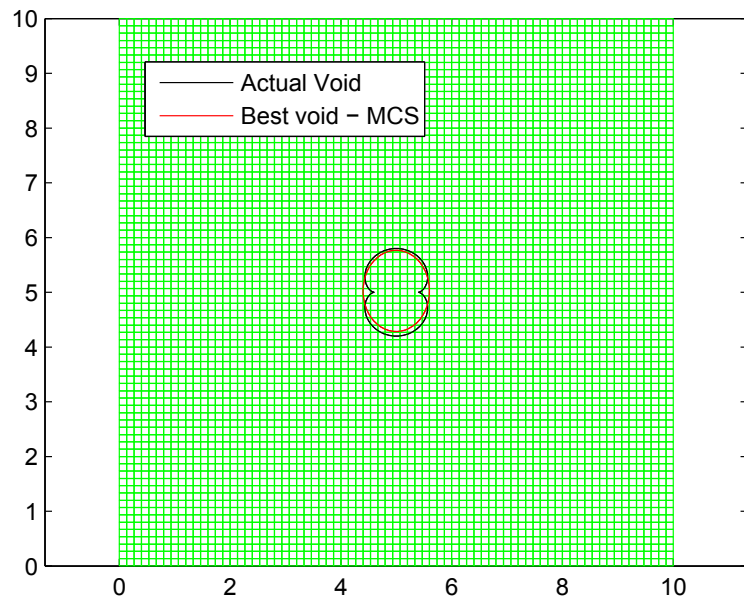
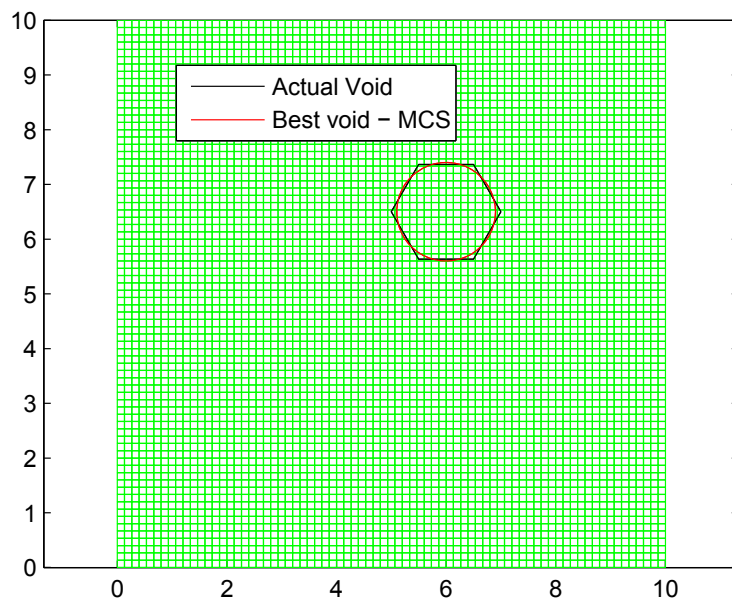


Figure 2.11: Best Void boundary determined by MCS for an inclined elliptical void

2.7 Conclusion



(a)



(b)

Figure 2.12: Best Void boundary determined by MCS for non-elliptical voids

2.7 Conclusion

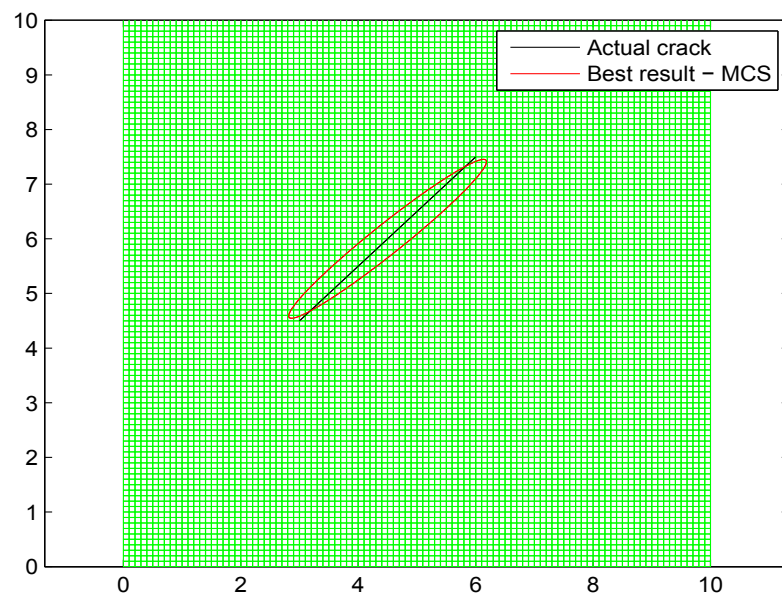


Figure 2.13: Best result determined by MCS for an inclined crack

2.7 Conclusion

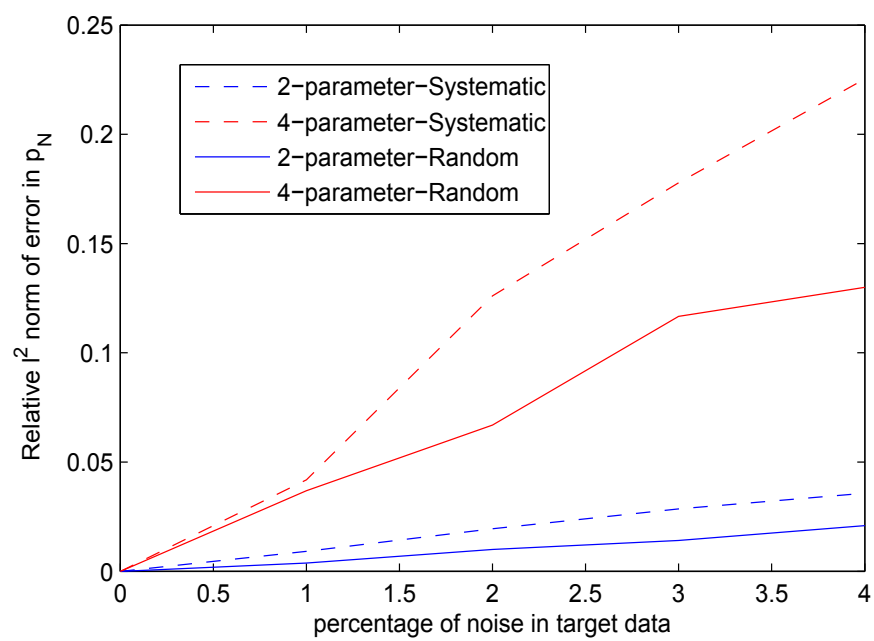


Figure 2.14: Influence of noise on inverse problem solution

2.7 Conclusion

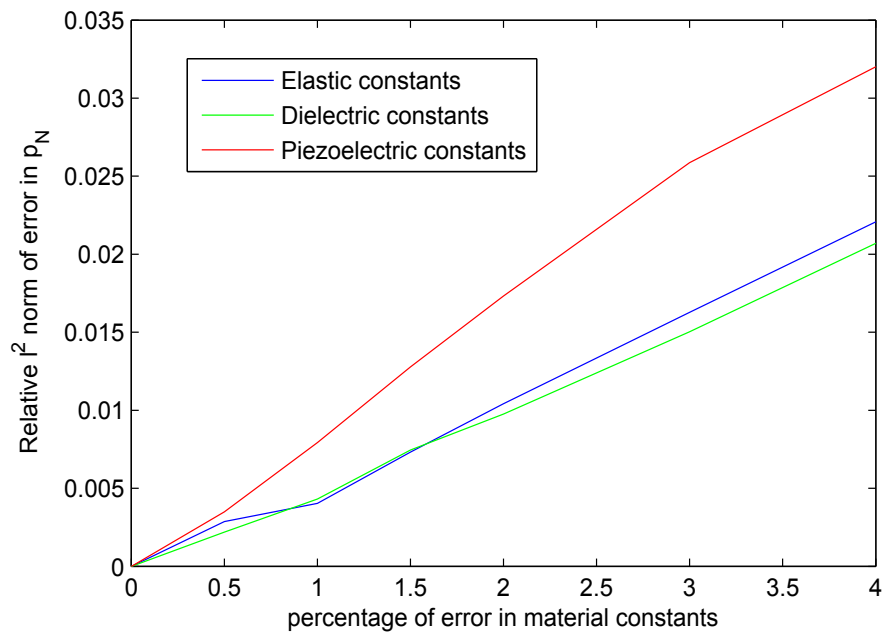


Figure 2.15: Influence of inexactness in material properties on inverse problem solution

Chapter 3

Detection of multiple flaws in piezoelectric structures using XFEM and level sets

3.1 Contribution of authors

The work presented in this chapter is published as, S.S.Nanthakumar, T. Lahmer, T. Rabczuk, Detection of multiple flaws in piezoelectric structures using XFEM and level sets, Computer Methods in Applied Mechanics and Engineering 275 (2014) 98112. The final publication is available in <http://www.sciencedirect.com/science/article/pii/S0045782514000796>.

The original text from this publication is used in this chapter.

- S.S.Nanthakumar
 - Literature review about level set based optimization method
 - Coding of the XFEM-level set algorithm
 - Solving of numerical examples included
 - Preparing the manuscript
- Prof. Tom Lahmer
 - Discussions in various stages of preparing the manuscript and concepts related to inverse problems.
 - Reviewing the manuscript before submission
- Prof. Timon Rabczuk

3.2 Introduction

- Discussions to improve the numerical examples
- Reviewing the manuscript before submission

3.2 Introduction

The optimization schemes utilized commonly in solving the inverse problem of damage detection are genetic algorithm¹⁸ and global search methods like the one shown in Chapter 2. The number of iterations in these methods increase in proportion to the number of parameters used to define the flaws. Because of this limitation, most previous studies were restricted to detecting only one single void or crack of simple geometry. For example, in Chapter 2, the void is explicitly defined by five parameters. The parameters are obtained by minimizing the objective function using Multilevel Coordinate Search algorithm (MCS)²⁵. The method proposed can detect the location and equivalent elliptical shape of only one single void in a piezoelectric structure.

A new numerical method based on the combination of the classical shape derivative and of the level-set method for front propagation in the context of structural optimization is proposed in Allaire et al²⁶. XFEM based level set schemes for structural optimization is presented in Peng et al⁷⁴. The level set function is updated in each iteration by solving transport Hamilton-Jacobi equation explicitly with variable time step^{9,75}.

The aim of this work is to propose a strategy to detect multiple voids in 2D piezoelectric structures by combining shape derivative and level sets as employed in structural optimization problems. XFEM utilizes implicit level set functions for defining flaws which in turn leads to independence of background mesh to flaw configuration, . Thereby it becomes a natural choice for solving the forward problem in each iteration for different flaw configurations.

The outline of this chapter is as follows. Section 3.3 comprises details on combining shape derivative and level set method to minimize the objective function and thereby detecting the location of voids. Section 3.4 shows numerical examples to prove the ability of this method in solving the intended inverse problem iteratively.

3.3 Shape derivative and level set method

The shape, size and location of voids can be implicitly represented using level sets as shown in Figure 3.1. In the process, the location of voids will be identified by change in level set function values, with respect to fictitious time, t . The evolution of void shapes, which corresponds to the change in these implicit function, $\Phi(x(t)) = 0$ with

3.3 Shape derivative and level set method

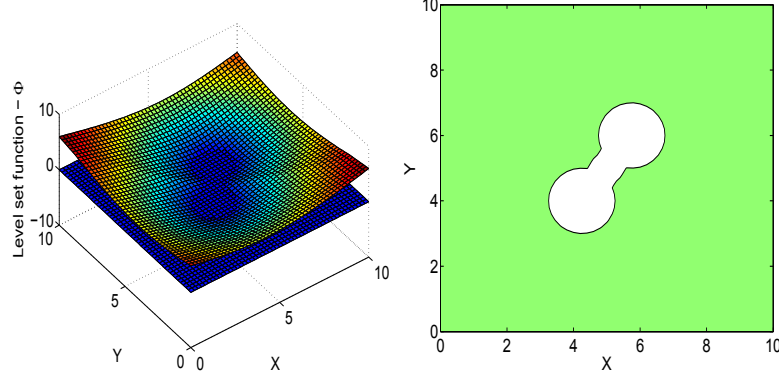


Figure 3.1: (a) Contour plot of level set function, (b) The corresponding irregular void boundary.

respect to time, is governed by the Hamilton-Jacobi equation⁹,

$$\frac{\partial \Phi(x)}{\partial t} + V_n |\nabla \Phi| = 0 \quad (3.1)$$

Moving the level-set isolines along the descent gradient direction is equivalent to transporting Φ by solving the Hamilton-Jacobi equation. This Hamilton-Jacobi equation is posed not only on the void boundaries but on the entire domain, as the velocity V_n is known everywhere. The velocity, V_n is related to the sensitivity of the objective function to variation in level set function values. The change in the objective function due to perturbation of flaw boundaries is given by the shape derivative. The shape derivative is obtained by solving an adjoint problem. In the adjoint case the governing PDEs (2.3) and (2.4) are solved with Neumann boundary condition as,

$$\sigma_{ij} n_j = u - u^{meas} \text{ (and) } D_i n_i = \phi - \phi^{meas} \text{ on } \Gamma_n \quad (3.2)$$

and Dirichlet boundary conditions as shown in equation 2.7. The velocity at iteration n in location of node i , V_i^n is given by the shape derivative as shown below,

$$-V_i^n = \text{grad}_{\Phi} J_n = \sigma^p_{ij} \epsilon^u_{ij} - D^p_i E^u_i \quad (3.3)$$

The subscripts u and p corresponds to actual and adjoint state respectively. The Hamilton-Jacobi equation is posed not only on the void boundary but in the entire domain, as the velocity V_n can be computed everywhere. Hamilton-Jacobi equations do not usually admit smooth solutions. Existence and uniqueness are obtained in the framework of viscosity solutions which help in convenient definition of generalized shape motion. The discrete solution of HJ equation is obtained by an explicit first order upwind

3.3 Shape derivative and level set method

scheme²⁶.

$$\frac{\Phi^{n+1} - \Phi^n}{\Delta t} + \min(V_i^n, 0) g^-(D_x^+ \Phi_i^n, D_x^- \Phi_i^n) + \max(V_i^n, 0) g^+(D_x^+ \Phi_i^n, D_x^- \Phi_i^n) = 0 \quad (3.4)$$

in which,

$$D_x^+ \Phi_i^n = \frac{\Phi_{i+1}^n - \Phi_i^n}{\Delta x}, D_x^- \Phi_i^n = \frac{\Phi_i^n - \Phi_{i-1}^n}{\Delta x}$$

$$g^+(d^+, d^-) = \sqrt{\min(d^+, 0)^2 + \max(d^-, 0)^2},$$

$$g^-(d^+, d^-) = \sqrt{\max(d^+, 0)^2 + \min(d^-, 0)^2}.$$

The level set function is periodically regularized by solving,

$$\frac{\partial \Phi}{\partial t} + \text{sign}(\Phi_0) (|\nabla \Phi| - 1) = 0. \quad (3.5)$$

The solution to this equation is a signed distance function to initial isoline, Φ_0 . Extended finite element analysis performed in each iteration requires signed distance value from crack or inclusion boundary in order to determine enrichment function values and so the regularization step is performed in each iteration.

The steps involved in this void detection algorithm are as follows,

- Initialization of level set function Φ_0 is done. In order to avoid local optima the voids are uniformly distributed all over the domain.
- Computation of actual state u_k and adjoint state p_k is performed. These are determined by solving equations (2.3) and (2.4) posed in domain Ω_k with essential boundary condition shown in equation (2.7) and two different natural boundary conditions shown in equations (2.8) and (3.2) for actual and adjoint states respectively. Using equation (3.3), the velocity to move the void boundary (i.e.) the shape derivative is determined.
- The new void configuration is given by the level-set function Φ_{k+1} by solving the transport Hamilton-Jacobi equation (3.1) after a fictitious time step Δt_k starting from the initial shape Φ_k with velocity V_k computed in terms of u_k and p_k .
- The level set values are regularized by solving equation (3.5) as Φ_{k+1} is no more a signed distance function.
- The algorithm is stopped when the velocity values are less than a tolerance value, which can also be seen from no significant change in void configuration with iterations.

3.4 Numerical Examples

3.4 Numerical Examples

The proposed XFEM and level set based optimization algorithm is tested by several flaw detection problems. In the examples, a plate (10×10 units) made of PZT-5H with material properties shown in Table 2.1 is considered. Plane strain assumption is used. The material properties are such that the piezoelectric plate is poled in y direction as shown in figure 3.2. The elastic constants, the dielectric permittivity constants and the piezoelectric constants are of different orders, so stiffness matrix is ill-conditioned and that may lead to unstable results. Hence to overcome the matrix illness we take advantage of the dimension changing method^{72,76}.

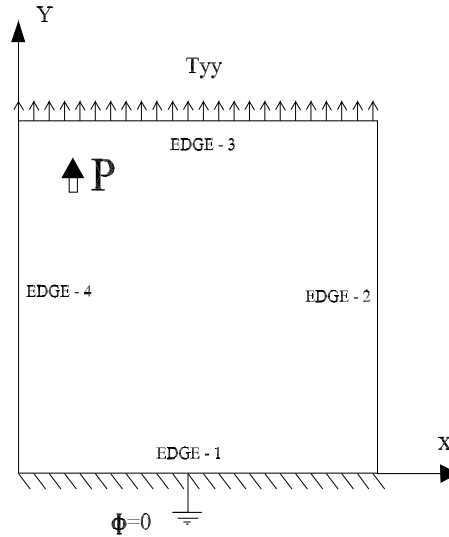


Figure 3.2: Boundary conditions and loads on the modeled Piezoelectric plate

As shown in Figure 3.2, the piezoelectric plate is subjected to a mechanical line load (T_{yy}) at edge 3 while edge 1 is fixed; the electric potential is set to zero. The horizontal displacement, u , the vertical displacement, v and the electric potential ϕ are measured along the edge 2 of the plate at 25 uniformly spaced sensor locations that are uniformly spaced. In Rus et al¹⁶, a similar setup is employed to detect voids in a piezoelectric plate and it was shown that the excitation of the piezoelectric specimen by a static mechanical traction transverse to the polarization direction provides better identifiability than applying a static electrical load. The response data from four set of experiments are utilised in each iteration. When edge 1 is fixed, T_{yy} is applied at edge 3. When edge 2 is fixed, T_{yy} is applied at edge 4 and so on. More than one setup is required to serve two purposes. First, to overcome local minima and second, when there are two voids exactly one above other, one void might hide the

3.4 Numerical Examples

other making it difficult for a single experimental setup to detect their exact locations. Inverse problems are generally ill posed. Performing several experiments constraints the search space thereby making this problem well posed.

Measurements

As there are no experimental measurements available for this study, they are simulated numerically by XFEM. Two different mesh sizes are adopted for creating the data and for solving the forward problem so as to avoid "inverse-crimes". In order to generate the target data, a finer mesh compared to the one used for solving the inverse problem is used. Besides, a random noise of about $\pm 1\%$ is added to the generated synthetic data $\chi^{EXP} = \chi^{XFEM}(1 + 0.01B)$, where B is a random number between -1 and +1.

3.4.1 Single void

In this example, the location of a single square void is detected using the proposed methodology. The initial assumption is such that the voids are uniformly distributed all over the domain. As it is evident from figure 3.3 with each iteration the trial voids which are distant from the actual void location vanish. The trial voids closer to the actual void gradually merge together and approach the square shape. This example shows the flexibility of the level set representation of voids which enables their detection of any shape. The explicit representation of void shapes may lead an increased number of parameters corresponding to the least objective function value. Evolutionary or search algorithm may require a higher number of iterations as the number of iterations depend on the number of parameters to be determined. In chapter 2, maximum of 5 parameters defining void shape have been determined with the number of iterations given by $50n^2$, n is the number of parameters, using MCS²⁵ for optimization. MCS is a zero order method which does not require gradient information. In the current proposed method, the number of iterations is considerably reduced because the gradient information is indirectly obtained from the solution of the adjoint problem. In each iteration, the governing equation is solved twice, once to determine the actual response and then to compute the adjoint variables. The Hamilton-Jacobi equation is solved explicitly, hence the time step is restricted such that it satisfies the CFL condition. Figure 3.4 shows the convergence of the algorithm with iterations.

3.4.2 Multiple voids

In this example, the location and the number of several voids present in a piezoelectric structure is detected using the proposed methodology. Similar to the previous example the initial assumption is such that the voids are uniformly distributed all over the domain. As shown in the figure 3.5, the trial voids far from the actual voids gradually reduce in size and finally vanish. The trial voids lying within or along the boundary of the actual voids merge and change shape until they match the shape of actual voids.

3.4 Numerical Examples

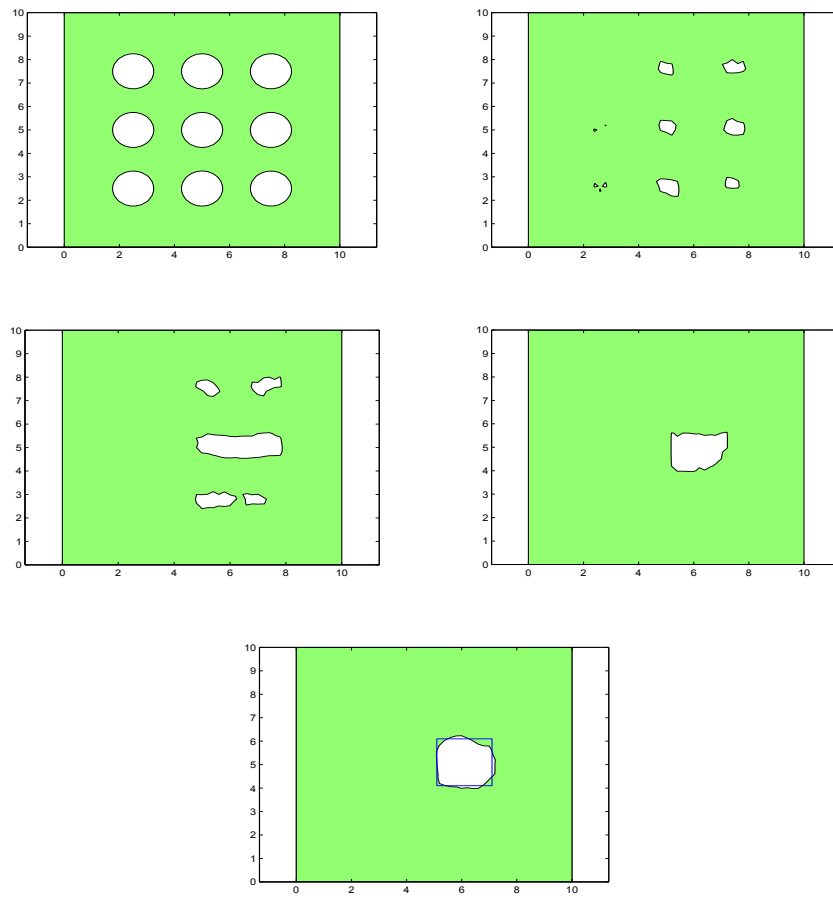


Figure 3.3: Top row : Initial void configuration, Void configuration after 20 iterations, second row : Void configuration after 40 and 80 iterations, Bottom row : Final void configuration

3.4 Numerical Examples

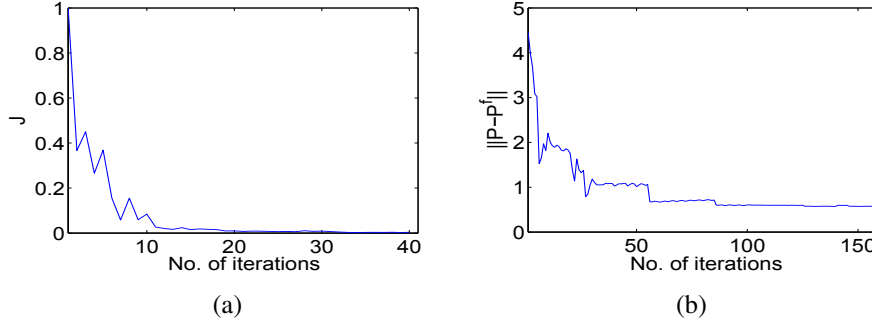


Figure 3.4: (a) Convergence of the objective function, J with iteration, (b) Convergence of L^2 norm of error in parameter space with iterations. P , approximated level set value at nodes and P^f , level set values corresponding to true void configuration

This example shows that the number of iterations is almost independent of the number of voids to be determined. The level set function is updated in each iteration by solving the HJ equation explicitly. The number of explicit time steps required to solve the HJ equation varies. For each XFEM analysis, 10 explicit time steps of the HJ transport equation is performed. Depending on the reduction in the objective function values, this number is gradually reduced such that the objective function values decreases with increasing number of iterations. Solving this inverse problem of multiple voids using search algorithm requires explicitly parametrizing the multiple void locations and their shapes. The number of parameters cannot be known a priori as the number of voids in the piezoelectric plate is unknown. This proposed method is able to determine, how many number of voids are present in the structure and where they are located. The algorithm predicts three voids in the structure and their corresponding locations. Figure 3.6 shows the convergence of the algorithm.

3.4.3 Cracks

In this example, the approximate location of cracks is detected using voids uniformly distributed over the domain as initial assumption. The algorithm is expected to locate the cracks but it cannot determine the exact profile of the crack. The algorithm can actually determine the "equivalent" void configuration. In order to analyse the cracked piezoelectric structure, the cracks are represented by two level sets, one defines the shape of the cracks, while the other defines the length of the cracks. The results obtained with increase in iteration is shown in figure 3.7. The piezoelectric domain has two cracks and location of the cracks is detected by the algorithm. The algorithm gives voids of almost elliptical shape as output in the crack locations. Figure 3.8 shows the convergence of the algorithm with iterations.

3.4 Numerical Examples

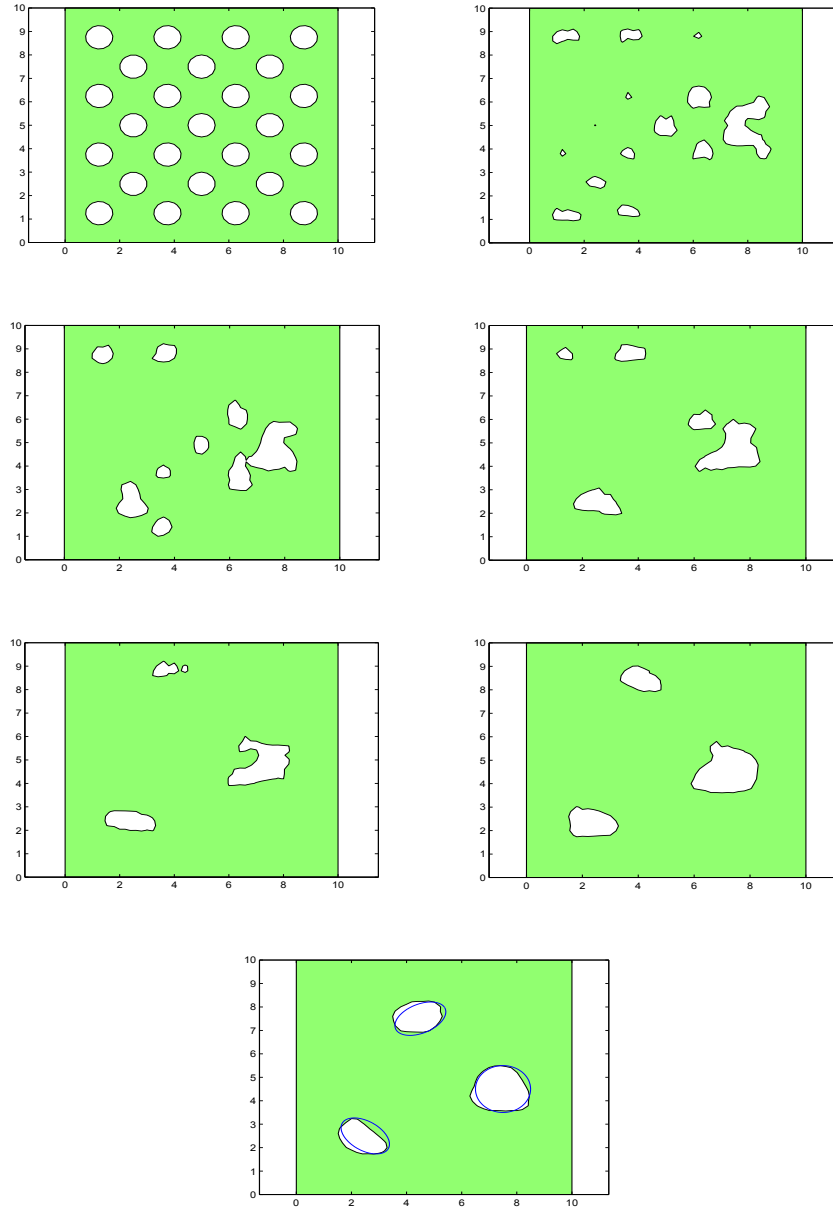


Figure 3.5: Top row : Initial void configuration, Void configuration after 20 iterations, second row : Void configuration after 30 and 50 iterations, Bottom row : Void configuration after 100 and 150 iterations, Final void configuration

3.4 Numerical Examples

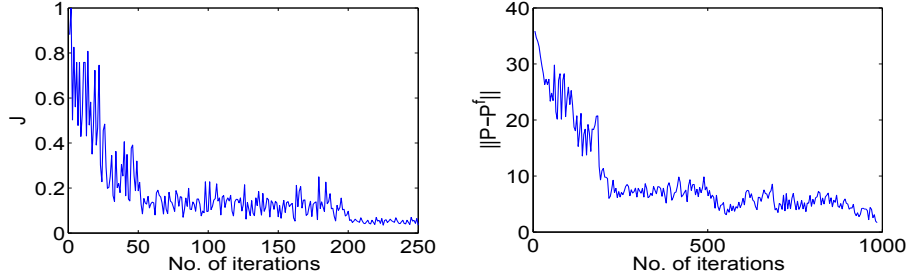


Figure 3.6: (a) Convergence of the objective function, J with iteration, (b) Convergence of L^2 norm of error in parameter space with iterations. P , approximated level set value at nodes and P^f , level set values corresponding to true void configuration

3.4.4 Voids and cracks

In this example, a more general damaged domain is studied. The structure contains both cracks and voids which is common in an actual piezoelectric domain. The algorithm should be able to locate the defects. Initially voids are assumed to be located all over the domain. As the iteration progresses, the voids that are located near a crack or void remains while other voids disappear. The remaining voids, gradually change shape into an almost elliptical void at the crack location. They also tend to the actual void profile at the void location. Figure 3.9 shows that the algorithm is able to detect the location of all three defects. Figure 3.10 shows the convergence of the algorithm with iterations.

Influence of noise and number of sensors

In the above examples the noise is restricted to ± 1 . The influence of increased proportion of noise is shown in figure 3.11. It is evident from the figure that with increase in noise there is reduction in accuracy of the algorithm. On the other hand, the accuracy of the algorithm also depends on number of sensors along the measurement boundary. In order to study the influence of number of sensors on performance of the algorithm, an example problem of detecting a circular void of radius 0.75 cm located at the center of a square piezoelectric plate (10 cm \times 10 cm) is solved several times, with different number of sensors each time. The error in parameter space with increasing number of sensors along the measurement boundary is shown in Fig. 3.12. The curve becomes almost asymptotic as the number of sensors exceeds seven. As mentioned earlier, the number of sensors used in all the numerical examples is 25 and these many sensors were sufficient to detect flaws located anywhere in the domain.

3.4 Numerical Examples

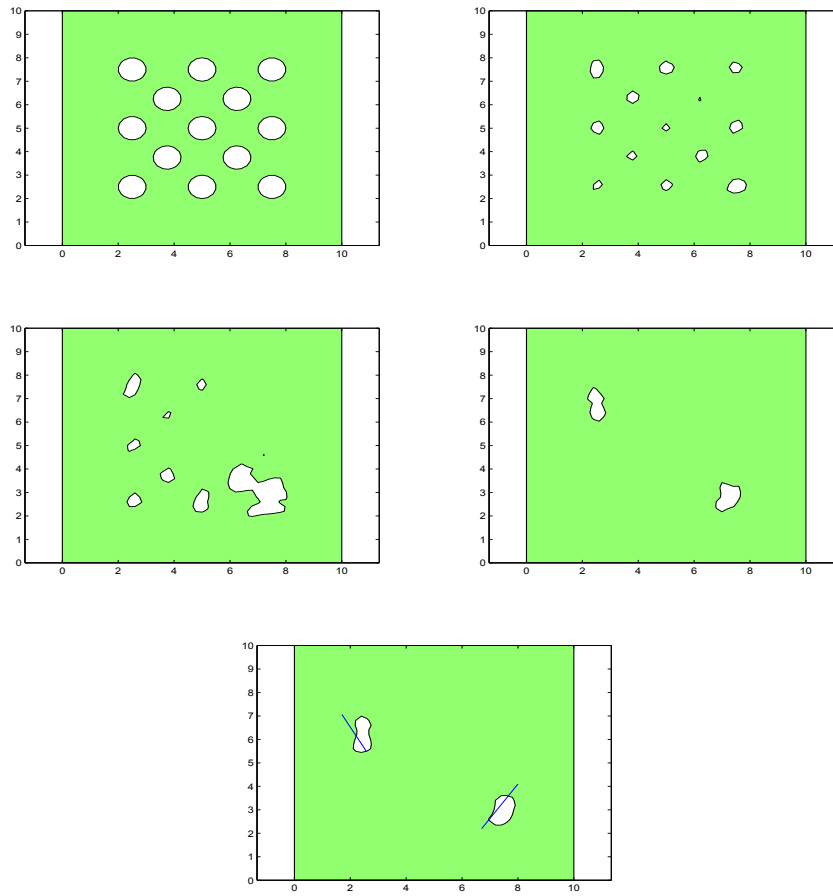


Figure 3.7: Top row : Initial void configuration, Void configuration after 20 iterations, second row : Void configuration after 50 and 100 iterations, Bottom row : Final void configuration.

3.5 Conclusion

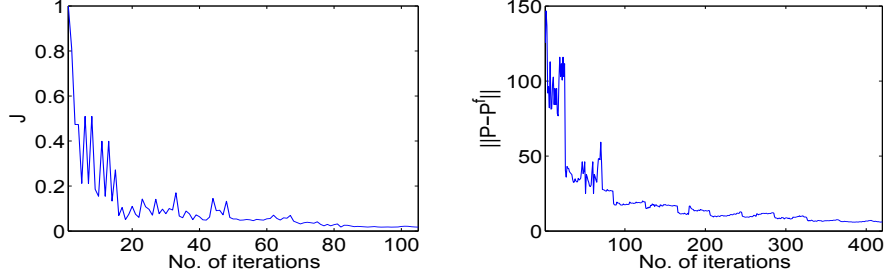


Figure 3.8: (a) Convergence of the objective function, J with iterations, (b) Convergence of L^2 norm of error in parameter space with iterations. P , approximated level set value at nodes and P^f , level set values corresponding to true void configuration

3.5 Conclusion

In this chapter a methodology to detect multiple crack and void locations in a piezo-electric specimen is proposed. In each iteration, XFEM is used to solve the direct problem. The mesh remains unchanged in all iterations thereby considerably reducing computational time. The shape derivative and level sets are used to minimize the objective function. An adjoint problem is solved in each iteration to determine the shape derivative. Multiple setups are used to overcome the problem of local optima. The void configuration does not require external parameterization as it is implicitly represented by level sets. The numerical examples demonstrate the efficiency of the method in detecting any number of cracks and voids in specimen. The method proposed is more robust compared to iterative methods previously proposed in literature in which genetic or search algorithms are used for the optimization.

3.5 Conclusion

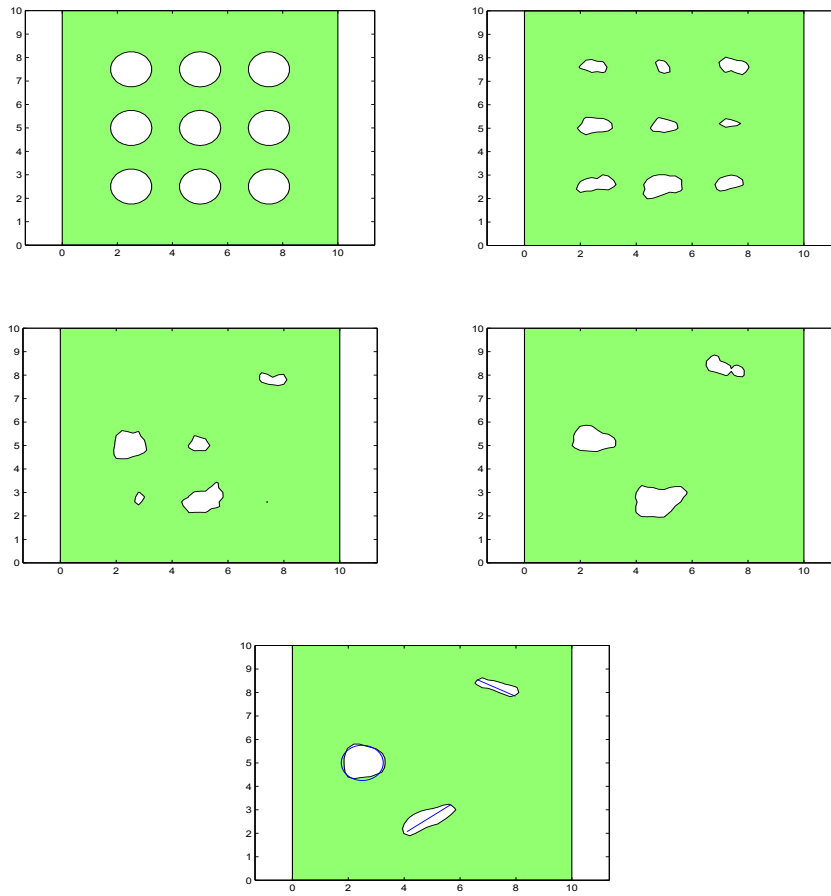


Figure 3.9: Top row : Initial void configuration, Void configuration after 20 iterations, second row : Void configuration after 50 and 100 iterations, Bottom row : Final void configuration.

3.5 Conclusion

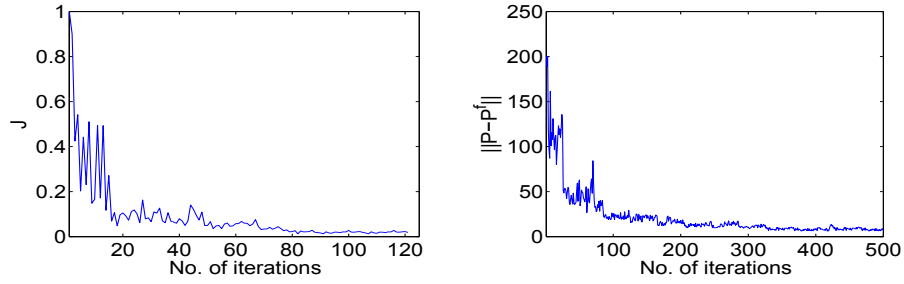


Figure 3.10: (a) Convergence of the objective function, J with iterations, (b) Convergence of L^2 norm of error in parameter space with iterations. P , approximated level set value at nodes and P^f , level set values corresponding to true void configuration

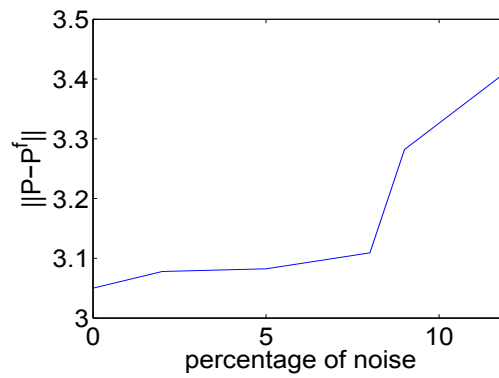


Figure 3.11: The influence of noise on accuracy of the algorithm

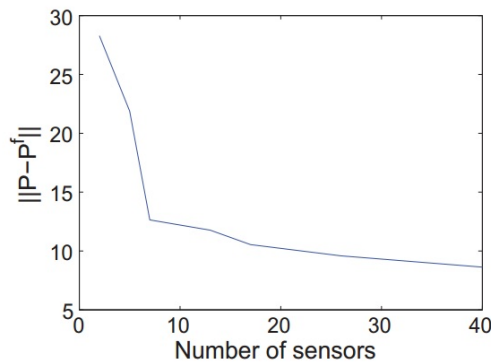


Figure 3.12: The influence of number of sensors on accuracy of the algorithm

Chapter 4

Detection of material interfaces using a regularised level set method in piezoelectric structures

4.1 Contribution of authors

The work presented in this chapter is published as, S.S.Nanthakumar, T. Lahmer, X. Zhuang, G. Zi and T. Rabczuk, (2015): Detection of material interfaces using a regularized level set method in piezoelectric structures, Inverse Problems in Science and Engineering, DOI: 10.1080/17415977.2015.1017485. The final publication is available in

<http://dx.doi.org/10.1080/17415977.2015.1017485>

The original text from this publication is used in this chapter.

- S.S.Nanthakumar
 - Literature review about multiple level sets and total variation regularization
 - Coding of the XFEM-multiple level set algorithm
 - Solving of numerical examples included
 - Preparing the manuscript
- Prof. Tom Lahmer
 - Discussions in various stages of preparing the manuscript and regarding concepts related to regularization
 - Reviewing the manuscript before submission
- Prof. Xiaoying Zhuang

4.2 Introduction

- Reviewing the manuscript before submission
- Prof. Goanseup Zi
 - Reviewing the manuscript before submission
- Prof. Timon Rabczuk
 - Discussions to improve the numerical examples
 - Reviewing the manuscript before submission

4.2 Introduction

The inverse problem of identifying material interfaces from boundary measurements arise in several fields of science and engineering. Level set method, a framework proposed initially for tracking evolving interfaces using implicit representations⁹ has received considerable attention in solving the inverse problem of interface detection. A survey on application of level set methods in inverse problems and optimal design can be found in Burger et al⁷⁷. Combination of level set method along with total variation regularization for solving inverse problems is proposed in Tai et al²⁸. Multiple level sets for determining several subdomains made of more than two different materials is presented in Nielsen et al²⁹. In this work we intend to detect the interfaces between material subdomains in a piezoelectric structure.

The aim of this work is to extend the level set algorithm utilised in chapter 3 to detect the number and location of inclusions of known material parameters in two and three dimensional piezoelectric structures. The improvements made in this work are,

- The method is extended to detection of inclusions in a three dimensional piezo-electric structure.
- The level sets are regularised by a total variation norm, so as to improve detection in the presence of noise.
- Multiple level sets are utilised in order to identify more than two material sub-domains in a piezoelectric structure.

The outline of the chapter is as follows. Sections 4.3 and 4.4 describe the level set method and the derivation of adjoint problem respectively. Numerical examples are tested in section 4.5 to prove that the algorithm can detect boundary of material sub-domains in piezoelectric structures.

4.3 Inverse problem

4.3 Inverse problem

The interface of inclusions which is represented implicitly by the level set function, Φ is to be determined using the responses measured on the boundary of the piezoelectric structure. Mechanical displacements and electric potentials are the measurements taken on the boundary. The inverse problem is solved iteratively as an optimization problem with the following objective function,

$$J = \frac{1}{2} \int_{\Gamma} |\chi_i^{EXP} - \chi_i^{NUM}(\Phi)|^2 d\Gamma + \beta R(r) \quad (4.1)$$

The level set function which minimizes the L^2 norm of the difference between numerical, χ^{NUM} and experimental responses, χ^{EXP} gives the actual inclusion interface. As defined in Tai et al²⁸, total variation norm of r , the material ratio is taken as the regularisation, $R(r) = \int_{\Omega} |\nabla r| d\Omega$. The iterative methods of solving inverse problem are expensive and time consuming as the direct problem is solved at each step. Numerical method like FEM requires remeshing in each iteration so that the element edges align with the updated inclusion interface. In contrast, the XFEM offers the advantage of maintaining a fixed mesh irrespective of the varying interface in each iteration. Therefore in XFEM only the stiffness coefficients corresponding to enriched DOFS and the DOFS of those nodes which lie within the inclusions vary in each iteration whereas the FEM portion of global stiffness matrix, which comprises the bulk of matrix, remains the same.

4.3.1 The Level set method

The interface of inclusions can be implicitly represented by using the level sets. The level set function Φ can be in turn used to construct a function, r which can represent distinct material properties in different sub-domains. If the ratio of material constants with respect to the background material is r_1 in the subdomain with negative level set values and if the ratio of material constants is r_2 in the subdomain with positive level set values, then the function r can be written as²⁹,

$$r = \frac{1}{2} [r_1(1 + \text{sign}(\Phi)) + r_2(1 - \text{sign}(\Phi))]. \quad (4.2)$$

Multiple level sets can be used to represent more than two sub-domains as shown in figure 4.1. For example, the function r for representing four regions each of different material ratios can be written as,

$$r = \frac{1}{4} [r_1(1 + S_1)(1 + S_2) + r_2(1 + S_1)(1 - S_2) + r_3(1 - S_1)(1 + S_2) + r_4(1 - S_1)(1 - S_2)] \quad (4.3)$$

S_1 and S_2 correspond to the sign of the level set functions Φ_1 and Φ_2 respectively. r_1 , r_2 , r_3 and r_4 are material ratios in the four regions. The ratios can also be replaced

4.3 Inverse problem

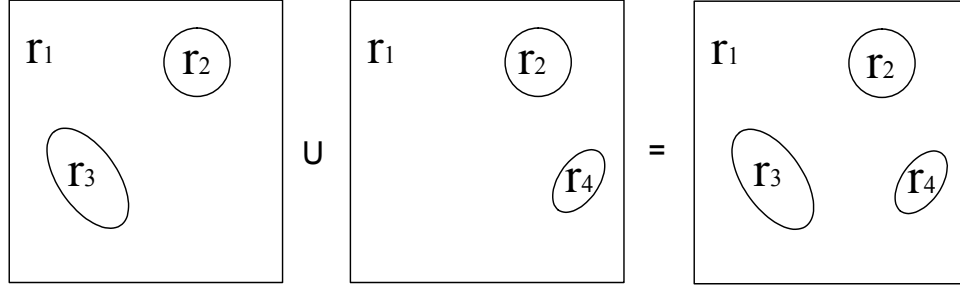


Figure 4.1: Multiple level sets representation : The union of two level set functions, ϕ_1 and ϕ_2 gives the actual domain with inclusions

directly by the material tensors of the corresponding sub regions. The evolution of level set functions and the detection of different material regions, is governed by the Hamilton-Jacobi equation⁹.

$$\frac{\partial \Phi(x, t)}{\partial t} + V |\nabla \Phi| = 0. \quad (4.4)$$

Determining Φ by solving Hamilton-Jacobi equation is equivalent to moving the level set isolines in the descent direction. The Hamilton-Jacobi equation is posed not only along the interface but on the entire domain. The velocity V is related to the sensitivity of the objective function to variation in the material properties over the domain. The change in the objective function due to perturbation of inclusion interface is given by $\frac{\partial J}{\partial r}$. In this work, the derivative $\frac{\partial J}{\partial r}$ is obtained by solving an adjoint problem.

4.3.2 Measurement techniques

The mechanical displacement in piezoelectric ceramics can be measured using fibre optics probes, laser interferometry⁷⁸ and capacitance gauge. These methods are capable of measuring displacement of less than 1 nm. In Burianova et al⁷⁸, the three dimensional deformed configuration of a bulk ceramic sample subjected an AC driving field is obtained using laser interferometry. The boundary displacements data required can be obtained by adopting these experimental methods.

Similarly there are works⁷⁹ that present ways of measuring electric potential distribution on the surface of a piezoelectric ceramic.

4.3.3 Selection of the regularisation parameter, β

In this work, the regularization parameter is determined by a variant of the L-curve criterion. Among the methods available in literature like discrepancy principle, Generalized Cross Validation (GCV), Unbiased Predictive Risk Estimator (UPRE) and so

4.4 The forward and adjoint problem

on⁸⁰, the L-curve criterion and GCV offer the advantage of not requiring prior knowledge about noise level.

An L-curve⁴ is a log-log plot of residual norm and solution norm. There are two flat regions in the curve representing under regularisation and over regularisation. The corner point which corresponds to the transition between the two regions and the associated value of β gives the optimal regularization parameter.

New variants of the L-curve criterion are proposed in literature like the residual L-curve⁸¹ and solution L-curve⁸². The residual L-curve is given by plot between regularization parameter and regularised residual norm.

4.4 The forward and adjoint problem

In literature^{28,83}, the adjoint problem for a general elliptic partial differential equation is defined, which is here extended for a piezoelectric case. Consider a problem domain Ω with boundary Γ , the piezoelectric behaviour of the domain is expressed using material constitutive equations as,

$$\sigma_{ij} = C^E_{ijkl} \epsilon_{kl} - e_{kij} E_k \quad (4.5)$$

$$D_i = e_{ikl} \epsilon_{kl} + \kappa^E_{ik} E_k, \quad (4.6)$$

where C^E_{ijkl} , e_{kij} and κ^E_{ik} are the elastic stiffness at constant electric field, the piezoelectric constant and dielectric permittivity tensor at constant strain, respectively. The Cauchy stress tensor σ_{ij} and electric displacement D_i have to satisfy the mechanical and electrostatic equilibrium equations

$$\sigma_{ij,j} + f_i = 0 \text{ in } \Omega, \quad (4.7)$$

$$D_{i,i} - q = 0 \text{ in } \Omega. \quad (4.8)$$

Based on the above equations the strong form can be written as,

$$\begin{aligned} \nabla_u \cdot (\mathbf{C} : \boldsymbol{\epsilon}(\mathbf{u}) - \mathbf{e}^T : \mathbf{E}(\boldsymbol{\phi})) &= 0 \text{ in } \Omega \\ \nabla_e (\boldsymbol{\kappa} : \mathbf{E}(\boldsymbol{\phi}) + \mathbf{e} : \boldsymbol{\epsilon}(\mathbf{u})) &= 0 \text{ in } \Omega \\ \mathbf{u} &= 0 \text{ and } \boldsymbol{\phi} = 0 \text{ on } \Gamma_D \\ \boldsymbol{\sigma}(\mathbf{u}, \boldsymbol{\phi}) \cdot \mathbf{n} &= F_i \text{ and } \mathbf{D}(\mathbf{w}, \boldsymbol{\psi}) \cdot \mathbf{n} = -Q \text{ on } \Gamma_N \end{aligned} \quad (4.9)$$

where F_i , Q and n denote the surface traction, surface charge and outward unit normal vector respectively. Γ_D and Γ_N are the displacement and force boundary respectively. ∇_u and ∇_e are defined as ,

$$\nabla_u = \begin{pmatrix} \frac{\partial}{\partial x} & 0 & 0 & 0 & \frac{\partial}{\partial z} & \frac{\partial}{\partial y} \\ 0 & \frac{\partial}{\partial y} & 0 & \frac{\partial}{\partial z} & 0 & \frac{\partial}{\partial x} \\ 0 & 0 & \frac{\partial}{\partial z} & \frac{\partial}{\partial y} & \frac{\partial}{\partial x} & 0 \end{pmatrix}^T \text{ and } \nabla_e = \begin{pmatrix} \frac{\partial}{\partial x} & \frac{\partial}{\partial y} & \frac{\partial}{\partial z} \end{pmatrix}^T.$$

4.4 The forward and adjoint problem

The weak formulation for the governing equations of piezoelectricity based on the principle of virtual work is as follows,

$$\begin{aligned} \int_{\Omega} (\boldsymbol{\varepsilon}(\mathbf{u})^T : \mathbf{C} : \boldsymbol{\varepsilon}(\mathbf{w}) - \boldsymbol{\varepsilon}(\mathbf{u})^T : \mathbf{e} : \mathbf{E}(\boldsymbol{\psi}) - \mathbf{E}(\boldsymbol{\phi})^T : \mathbf{e} : \boldsymbol{\varepsilon}(\mathbf{w}) - \mathbf{E}(\boldsymbol{\phi})^T : \boldsymbol{\kappa} : \mathbf{E}(\boldsymbol{\psi})) d\Omega \\ - \int_{\Gamma_N} \mathbf{p} \cdot \mathbf{w} d\Gamma - \int_{\Gamma_N} \mathbf{q} \cdot \boldsymbol{\psi} d\Gamma = 0 \end{aligned} \quad (4.10)$$

$\forall \mathbf{u} \in V, \forall \boldsymbol{\phi} \in V$ and $\forall \mathbf{w} \in V, \forall \boldsymbol{\psi} \in V$. V is the space containing admissible displacement and electric potential fields.

The objective function (without regularisation term) to be minimized is,

$$J(\mathbf{C}(x), \mathbf{e}(x), \boldsymbol{\kappa}(x)) = \int_{\Gamma^m} \frac{1}{2} (u - u^{meas})^2 d\Gamma + \int_{\Gamma^m} \frac{1}{2} (\phi - \phi^{meas})^2 d\Gamma \quad (4.11)$$

Let, $J_1 = \frac{1}{2} (u - u^{meas})^2$ and $J_2 = \frac{1}{2} (\phi - \phi^{meas})^2$. The material distribution in Ω is given by, $\mathbf{C}(x) = r(x)\mathbf{C}_b$, $\boldsymbol{\kappa}(x) = r(x)\boldsymbol{\kappa}_b$, $\mathbf{e}(x) = r(x)\mathbf{e}_b$. For the sake of simplicity it is assumed that the displacements and electrical potentials are measured along the same boundary, Γ^m .

The first variation of $J(\mathbf{C}(x), \mathbf{e}(x), \boldsymbol{\kappa}(x))$ is given by,

$$\delta J(\mathbf{C}(x), \mathbf{e}(x), \boldsymbol{\kappa}(x)) = \int_{\Gamma^m} \frac{\partial J_1}{\partial u} \delta u d\Gamma + \int_{\Gamma^m} \frac{\partial J_2}{\partial \phi} \delta \phi d\Gamma \quad (4.12)$$

The governing problem for the latter can be determined by differentiating the weak formulation, equation (4.10) as shown below,

$$\begin{aligned} \int_{\Omega} (\boldsymbol{\varepsilon}(\boldsymbol{\delta u})^T : \mathbf{C} : \boldsymbol{\varepsilon}(\mathbf{w}) + \boldsymbol{\varepsilon}(\mathbf{u})^T : \boldsymbol{\delta C} : \boldsymbol{\varepsilon}(\mathbf{w}) - \boldsymbol{\varepsilon}(\boldsymbol{\delta u})^T : \mathbf{e} : \mathbf{E}(\boldsymbol{\psi}) \\ - \boldsymbol{\varepsilon}(\mathbf{u})^T : \boldsymbol{\delta e} : \mathbf{E}(\boldsymbol{\psi}) - \mathbf{E}(\boldsymbol{\delta \phi})^T : \mathbf{e} : \boldsymbol{\varepsilon}(\mathbf{w}) - \mathbf{E}(\boldsymbol{\phi})^T : \boldsymbol{\delta e} : \boldsymbol{\varepsilon}(\mathbf{w}) \\ - \mathbf{E}(\boldsymbol{\delta \phi})^T : \boldsymbol{\kappa} : \mathbf{E}(\boldsymbol{\psi}) - \mathbf{E}(\boldsymbol{\phi})^T : \boldsymbol{\delta \kappa} : \mathbf{E}(\boldsymbol{\psi})) d\Omega = 0 \end{aligned} \quad (4.13)$$

Considering \mathbf{w} and $\boldsymbol{\psi}$ as the trial functions, the virtual work principle with $\boldsymbol{\delta u}$ and $\boldsymbol{\delta \phi}$ as the virtual fields yields,

$$\begin{aligned} \int_{\Omega} (\boldsymbol{\varepsilon}(\boldsymbol{\delta u})^T : \mathbf{C} : \boldsymbol{\varepsilon}(\mathbf{w}) - \boldsymbol{\varepsilon}(\boldsymbol{\delta u})^T : \mathbf{e} : \mathbf{E}(\boldsymbol{\psi}) - \mathbf{E}(\boldsymbol{\delta \phi})^T : \mathbf{e} : \boldsymbol{\varepsilon}(\mathbf{w}) - \mathbf{E}(\boldsymbol{\delta \phi})^T : \boldsymbol{\kappa} : \mathbf{E}(\boldsymbol{\psi})) d\Omega \\ - \int_{\Gamma_N} \mathbf{p} \cdot \boldsymbol{\delta u} d\Gamma - \int_{\Gamma_N} \mathbf{q} \cdot \boldsymbol{\delta \phi} d\Gamma = 0 \end{aligned} \quad (4.14)$$

4.4 The forward and adjoint problem

having set $p = \sigma(\mathbf{w}, \psi) \cdot \mathbf{n} = \frac{\partial J_1}{\partial u}$ and $q = \mathbf{D}(\mathbf{w}, \psi) \cdot \mathbf{n} = \frac{\partial J_2}{\partial \phi}$.

Comparing equations (4.13) and (4.14) we have,

$$\begin{aligned} & - \int_{\Omega} (\boldsymbol{\varepsilon}(\mathbf{u})^T : \boldsymbol{\delta} \mathbf{C} : \boldsymbol{\varepsilon}(\mathbf{w}) - \boldsymbol{\varepsilon}(\mathbf{u})^T : \boldsymbol{\delta} \mathbf{e} : \mathbf{E}(\boldsymbol{\psi}) - \mathbf{E}(\boldsymbol{\phi})^T : \boldsymbol{\delta} \mathbf{e} : \boldsymbol{\varepsilon}(\mathbf{w}) \\ & \quad - \mathbf{E}(\boldsymbol{\phi})^T : \boldsymbol{\delta} \boldsymbol{\kappa} : \mathbf{E}(\boldsymbol{\psi})) d\Omega = \int_{\Gamma_N} p \cdot \boldsymbol{\delta} \mathbf{u} d\Gamma + \int_{\Gamma_N} q \cdot \boldsymbol{\delta} \boldsymbol{\phi} d\Gamma. \end{aligned} \quad (4.15)$$

Comparing the above identity with equation 4.12, the variation of $J(\mathbf{C}(\mathbf{x}), \mathbf{e}(\mathbf{x}), \boldsymbol{\kappa}(\mathbf{x}))$ is,

$$\begin{aligned} \delta J(\mathbf{C}(\mathbf{x}), \mathbf{e}(\mathbf{x}), \boldsymbol{\kappa}(\mathbf{x})) = & \boldsymbol{\varepsilon}(\mathbf{u})^T : \boldsymbol{\delta} \mathbf{C} : \boldsymbol{\varepsilon}(\mathbf{w}) - \boldsymbol{\varepsilon}(\mathbf{u})^T : \boldsymbol{\delta} \mathbf{e} : \mathbf{E}(\boldsymbol{\psi}) - \mathbf{E}(\boldsymbol{\phi})^T : \boldsymbol{\delta} \mathbf{e} : \boldsymbol{\varepsilon}(\mathbf{w}) \\ & - \mathbf{E}(\boldsymbol{\phi})^T : \boldsymbol{\delta} \boldsymbol{\kappa} : \mathbf{E}(\boldsymbol{\psi}) \end{aligned} \quad (4.16)$$

where \mathbf{w} and $\boldsymbol{\psi}$ are solutions of the adjoint problem. The governing equations for the adjoint problem can be obtained from equation 4.14 as follows,

$$\begin{aligned} & - \int_{\Omega} \boldsymbol{\delta} \mathbf{u}^T \nabla_u \cdot (\mathbf{C} : \boldsymbol{\varepsilon}(\mathbf{w})) d\Omega + \int_{\Gamma} \boldsymbol{\delta} \mathbf{u}^T \mathbf{C} : \boldsymbol{\varepsilon}(\mathbf{w}) \mathbf{n} d\Gamma + \int_{\Omega} \boldsymbol{\delta} \mathbf{u}^T \nabla_e (\mathbf{e} : \mathbf{E}(\boldsymbol{\psi})) d\Omega \\ & \quad - \int_{\Gamma} \boldsymbol{\delta} \mathbf{u}^T \mathbf{e} : \mathbf{E}(\boldsymbol{\psi}) \mathbf{n} d\Gamma + \int_{\Omega} \boldsymbol{\delta} \boldsymbol{\phi}^T \nabla_u (\mathbf{e} : \boldsymbol{\varepsilon}(\mathbf{w})) d\Omega - \int_{\Gamma} \boldsymbol{\delta} \boldsymbol{\phi}^T \mathbf{e} : \boldsymbol{\varepsilon}(\mathbf{w}) \mathbf{n} d\Gamma \\ & \quad + \int_{\Omega} \boldsymbol{\delta} \boldsymbol{\phi}^{eT} \nabla_e (\boldsymbol{\kappa} : \mathbf{E}(\boldsymbol{\psi})) d\Omega - \int_{\Gamma} \boldsymbol{\delta} \boldsymbol{\phi}^T \boldsymbol{\kappa} : \mathbf{E}(\boldsymbol{\psi}) \mathbf{n} d\Gamma - \int_{\Gamma_N} p \cdot \boldsymbol{\delta} \mathbf{u} d\Gamma \\ & \quad - \int_{\Gamma_N} q \cdot \boldsymbol{\delta} \boldsymbol{\phi} d\Gamma = 0. \end{aligned} \quad (4.17)$$

Imposing $\int_{\Gamma_D} \boldsymbol{\delta} \mathbf{u}^T (\mathbf{C} : \boldsymbol{\varepsilon}(\mathbf{w}) - \mathbf{e} : \mathbf{E}(\boldsymbol{\psi})) \cdot \mathbf{n} d\Gamma = 0$

and $\int_{\Gamma_D} \boldsymbol{\delta} \boldsymbol{\phi}^T (\boldsymbol{\kappa} : \mathbf{E}(\boldsymbol{\psi}) + \mathbf{e} : \boldsymbol{\varepsilon}(\mathbf{w})) \cdot \mathbf{n} d\Gamma = 0$, leads to,

$$\begin{aligned} & \int_{\Omega} \boldsymbol{\delta} \mathbf{u}^T (\nabla_u (-\mathbf{C} : \boldsymbol{\varepsilon}(\mathbf{w}) + \mathbf{e}^T : \mathbf{E}(\boldsymbol{\psi}))) d\Omega + \int_{\Gamma_N} \boldsymbol{\delta} \mathbf{u}^T ((\mathbf{C} : \boldsymbol{\varepsilon}(\mathbf{w}) - \mathbf{e} : \mathbf{E}(\boldsymbol{\psi})) \cdot \mathbf{n} - p) d\Gamma + \\ & \int_{\Omega} \boldsymbol{\delta} \boldsymbol{\phi}^T (\nabla_e (\boldsymbol{\kappa} : \mathbf{E}(\boldsymbol{\psi}) + \mathbf{e} : \boldsymbol{\varepsilon}(\mathbf{w}))) d\Omega + \int_{\Gamma_N} \boldsymbol{\delta} \boldsymbol{\phi}^T ((\boldsymbol{\kappa} : \mathbf{E}(\boldsymbol{\psi}) + \mathbf{e} : \boldsymbol{\varepsilon}(\mathbf{w})) \cdot \mathbf{n} - q) d\Gamma = 0. \end{aligned} \quad (4.18)$$

4.4 The forward and adjoint problem

The strong form of the adjoint problem is,

$$\begin{aligned}
\nabla_u \cdot (\mathbf{C} : \boldsymbol{\varepsilon}(\mathbf{w}) - \mathbf{e}^T : \mathbf{E}(\boldsymbol{\psi})) &= 0 \quad \text{in } \Omega \\
\nabla_e (\boldsymbol{\kappa} : \mathbf{E}(\boldsymbol{\psi}) + \mathbf{e} : \boldsymbol{\varepsilon}(\mathbf{w})) &= 0 \quad \text{in } \Omega \\
\mathbf{w} &= 0 \quad \text{and} \quad \boldsymbol{\psi} = 0 \quad \text{on } \Gamma_D \\
\boldsymbol{\sigma}(\mathbf{w}, \boldsymbol{\psi}) \cdot \mathbf{n} &= \frac{\partial J_1}{\partial u} \quad \text{and} \quad \mathbf{D}(\mathbf{w}, \boldsymbol{\psi}) \cdot \mathbf{n} = \frac{\partial J_2}{\partial \phi} \quad \text{on } \Gamma_N
\end{aligned} \tag{4.19}$$

where, $\mathbf{C}(x) = r(x)\mathbf{C}_b$, $\boldsymbol{\kappa}(x) = r(x)\boldsymbol{\kappa}_b$, $\mathbf{e}(x) = r(x)\mathbf{e}_b$. This is the simplest case in which the ratio remains the same for \mathbf{C} , $\boldsymbol{\kappa}$ and \mathbf{e} . \mathbf{C}_b , $\boldsymbol{\kappa}_b$ and \mathbf{e}_b correspond to elastic, permittivity and piezoelectric constants of the background material (PZT-4). From equation 4.16, the derivative of objective function with respect to material ratio can be written as,

$$\begin{aligned}
\frac{\partial J}{\partial r} &= \boldsymbol{\varepsilon}(\mathbf{u}) : \frac{\partial \mathbf{C}}{\partial r} : \boldsymbol{\varepsilon}(\mathbf{w}) - \boldsymbol{\varepsilon}(\mathbf{u}) : \frac{\partial \mathbf{e}}{\partial r} : \mathbf{E}(\boldsymbol{\psi}) - \mathbf{E}(\boldsymbol{\phi}) : \frac{\partial \mathbf{e}}{\partial r} : \boldsymbol{\varepsilon}(\mathbf{w}) \\
&\quad - \mathbf{E}(\boldsymbol{\phi}) : \frac{\partial \boldsymbol{\kappa}}{\partial r} : \mathbf{E}(\boldsymbol{\psi}) \\
&= \boldsymbol{\varepsilon}(\mathbf{u}) : \mathbf{C}_b : \boldsymbol{\varepsilon}(\mathbf{w}) - \boldsymbol{\varepsilon}(\mathbf{u}) : \mathbf{e}_b : \mathbf{E}(\boldsymbol{\psi}) - \mathbf{E}(\boldsymbol{\phi}) : \mathbf{e}_b : \boldsymbol{\varepsilon}(\mathbf{w}) \\
&\quad - \mathbf{E}(\boldsymbol{\phi}) : \boldsymbol{\kappa}_b : \mathbf{E}(\boldsymbol{\psi}).
\end{aligned} \tag{4.20}$$

The extended velocity of the zero level set at node i , V_i is as shown below,

$$-V_i = \left(\frac{\partial J}{\partial \Phi} \right)_i \tag{4.21}$$

$$\frac{\partial J}{\partial \Phi} = \left(\frac{\partial J}{\partial r} + \beta \frac{\partial R}{\partial r} \right) \cdot \left(\frac{\partial r}{\partial \Phi} \right) \tag{4.22}$$

$$\frac{\partial R}{\partial r} = \nabla \cdot \left(\frac{\nabla r}{|\nabla r|} \right) \tag{4.23}$$

The Hamilton-Jacobi equations usually do not admit smooth solutions. Existence and uniqueness are achieved in the framework of viscosity solutions which help in convenient definition of generalized shape motion. The discrete solution of H-J equation is obtained by an explicit first-order upwind scheme²⁶.

The steps involved in this inclusion interface detection algorithm are as follows,

- Initialization of level set function Φ_0 . In order to avoid local optima, circular inclusions are distributed all over the domain. In the case of multiple level sets, this is the initial assumption for all the level set functions. In the case of three-dimensional structures, spherical inclusions are assumed to be distributed throughout the domain.

4.5 Numerical Examples

Table 4.1: Properties of Piezoelectric Material, PZT-4

Elastic Constants	Piezoelectric constants	Dielectric constants
$C_{11}=139 \text{ GPa}$	$e_{13}=-6.98 \text{ C/m}^2$	$\kappa_{11}=60 \text{ C/(GVm)}$
$C_{12}=77.8 \text{ GPa}$	$e_{33}=13.8 \text{ C/m}^2$	$\kappa_{33}=54.7 \text{ C/(GVm)}$
$C_{13}=74.3 \text{ GPa}$	$e_{15}=13.4 \text{ C/m}^2$	
$C_{33}=113 \text{ GPa}$		
$C_{44}=25.6 \text{ GPa}$		

- In each iteration, n the actual state u_n and adjoint state p_n are determined by performing XFEM analysis. This involves solving equations (4.9) and (4.19) for actual and adjoint states respectively. The shape derivative is obtained from equation (4.22).
- The updated inclusion interface is given by the level set function Φ_{n+1} obtained by solving the H-J equation (4.4) using upwind finite difference scheme, with time step Δt_n and velocity V_n , starting from the initial interface Φ_n .
- In case of multiple level sets, each of them is updated by solving HJ equation with its corresponding velocities. For example, in case of two level sets formulation expressed in equation (4.3), $(V_n)_1 = \frac{\partial J}{\partial r} \cdot \frac{\partial r}{\partial \Phi_1}$ and $(V_n)_2 = \frac{\partial J}{\partial r} \cdot \frac{\partial r}{\partial \Phi_2}$.
- The algorithm is regarded as converged when the gradient of the objective function is less than a fixed tolerance, which can also be seen from no significant change in the geometry of the inclusion interface between successive iterations.

4.5 Numerical Examples

Several examples are solved in this section to test the capability and correctness of the proposed method in detecting the interface of inclusions. The piezoelectric material used in the examples is PZT-4. The material properties of PZT-4 is shown in table 4.1 and the material of PZT-4 is regarded as transversely isotropic. The piezoelectric plate is subjected to a mechanical line load (T_{yy}) at edge 3 while edge 1 is fixed and the electric potential is set to zero as shown in figure 3.2. Measurements such as horizontal displacement u , vertical displacement v and electric potential ϕ are taken at 20 uniformly spaced discrete points along edges 2 and 4. The response data from four sets of experiments are utilised in each iteration. When edge 1 is fixed, T_{yy} is applied at edge 3. When edge 2 is fixed, T_{yy} is applied at edge 4 and so on.

Similarly for 3D example, a piezoelectric cube specimen is used. A strip of unit width

4.5 Numerical Examples

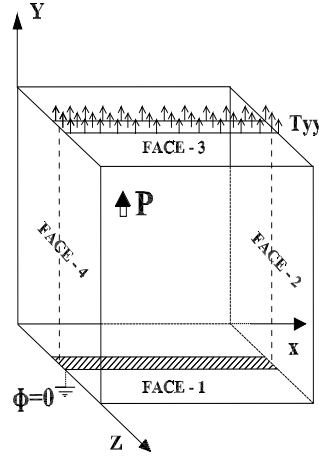


Figure 4.2: Boundary conditions and loads on the modelled Piezoelectric cube

along the face 1 is fixed; electric potential set to zero and uniform surface load is applied over the strip in face 3 as shown in figure 4.2. Three components of mechanical displacement and electric potential are measured at sensor locations along the dotted lines in faces 2 and 4. In the setup shown in figure 4.2, the centre line of load and support and the measurement line are located at the middle of the cube. The measurements are made at uniformly spaced 25 discrete points along the measurement line. Experiments are also performed with centre line of load and support and the measurement line being located at $\frac{1}{4}$ and $\frac{3}{4}$ of width of the cube (i.e.) moving along the Z-axis. Then experiments similar to these three are performed repeatedly with the support located at face 4 and load being applied along face 2, then with support at face 3 and load at face 1 and so on. Therefore the total number of experiments performed is twelve. Response data from several experiment setups are required to overcome the local minima and also when there are two inclusions exactly one above other, since one might hide the other making it difficult for a single experiment to detect inclusion locations. Inverse problems are generally ill-posed. Performing several experiments constrains the search space thereby making this problem well-posed with respect to unique identifiability. In Rus et al¹⁶, a similar setup is used to determine the location of circular voids in a piezoelectric plate and it was shown that excitation of piezoelectric specimen by static mechanical traction transverse to the polarization direction offers the highest identifiability when compared to applying a static electrical load.

Measurements

Experimental measurements are not available for this study and so they are generated

4.5 Numerical Examples

numerically using the XFEM. Different mesh sizes are used to generate the data and to solve the forward problem in order to avoid “inverse-crime”. The mesh used in target data generation is finer than the one used for solving the inverse problem. In addition, a systematic noise of about 1% is added to the generated response data.

4.5.1 Multiple inclusions

In this example, multiple inclusion interfaces in a two dimensional piezoelectric structure shown in figure 4.3 are detected. The target data is generated by XFEM analysis with a mesh size of $h = 1/75$. In inverse analysis, the mesh size used in each iteration is $h = 1/50$. The initial assumption is such that there are circular inclusions uniformly distributed all over the domain. In this example, the inclusions are made of material with $C_{11} = 13.8$ GPa; $C_{13} = 7.5$ GPa and $C_{33} = 11.5$ GPa and $C_{66} = 3.25$ GPa; $e_{13} = -6.98$ C/m², $e_{33} = 13.8$ C/m² and $e_{15} = 13.4$ C/m²; $\kappa_{11} = 15.1$ C/(GV m) and $\kappa_{33} = 13.7$ C/(GV m) ; (i.e.) stiffness ratio, $C_r \approx 0.1$ and permittivity ratio, $\kappa_r \approx 0.25$, with respect to the background material. The coupling constants are assumed to be the same throughout the domain (i.e.) the coupling ratio is one. The number of inclusions present in the domain is three. As shown in figure 4.4, the interfaces far from the actual inclusions disappear gradually with iterations while the nearer ones take the shape of true inclusions. In each iteration, the governing equation is solved twice, once to determine the actual response and then to compute the adjoint variables. The H-J equation is solved explicitly, hence the time step is restricted such that it satisfies the CFL condition. Figure 4.5 shows the convergence of the algorithm with respect to iterations. Figure 4.6 shows the final shapes of inclusions obtained with higher values of systematic noise. The regularisation parameter, β used for noise levels 2% and 5% are $0.5e-4$ and $2e-4$ respectively. Figure 4.7 shows the relationship between l^2 norm of error in parameter space with respect to varying levels of noise at appropriate values of β . The figure also shows the best values of β with increasing noise levels.

4.5.1.1 Mesh size effects and parameter uncertainty

The resolution to which a void/inclusion can be determined depends on two factors, the mesh size and spacing of sensors. For example, in a 50×50 mesh, the radius of the smallest circular inclusion that could be detected is almost equal to the width/height of a finite element. Figure 4.8 shows the detected inclusion and the actual interface, the radius of the inclusion is 0.25 units. 50 uniformly spaced pseudo sensors are assumed to be present at the measurement edges. Though a 50×50 mesh is employed in solving the inverse problem in iteration, if the pseudo sensors are restricted to 25, then this inclusion cannot be detected. This is because the inclusion might lie between two sensors and so the response measurements obtained may not be sensitive to the inclusion.

4.5 Numerical Examples

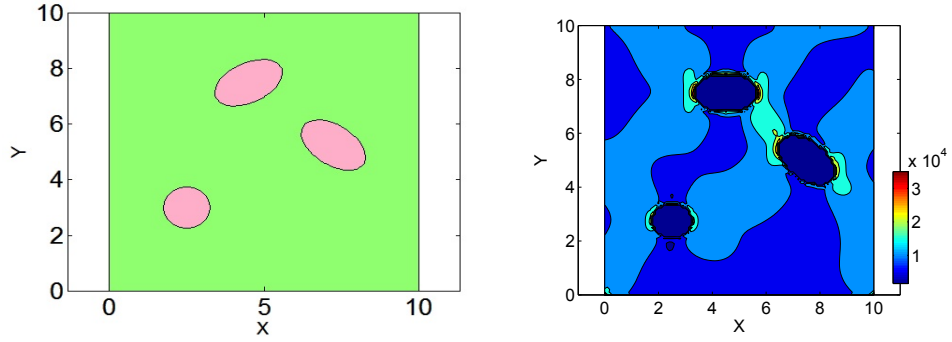


Figure 4.3: (a) Multiple inclusions in a piezoelectric specimen, (b) Energy density contour

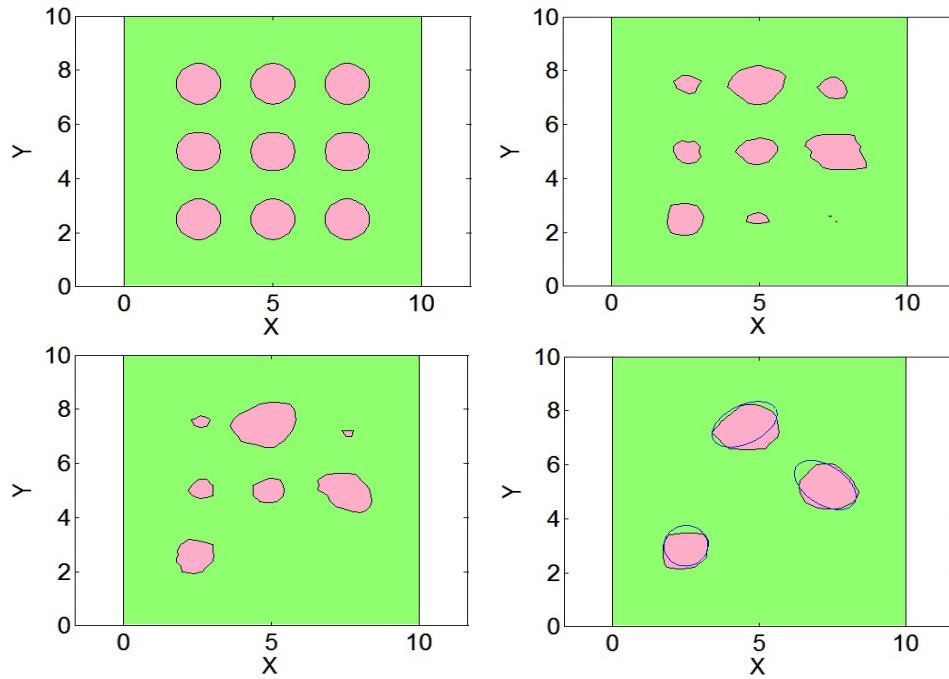


Figure 4.4: Level set function, Φ ; Top row : Initial interface configuration, Interface configuration after 50 iterations, Second row : Interface configuration after 75 iterations and final interface configuration determined by the algorithm.

4.5 Numerical Examples

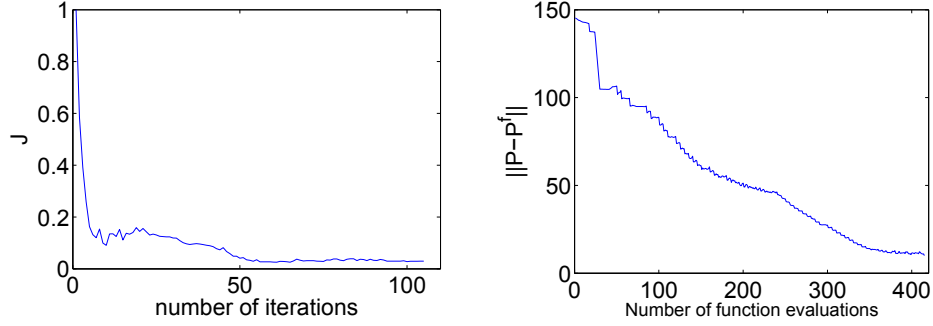


Figure 4.5: (a) Convergence of the objective function, J with iterations, (b) Convergence of l^2 norm of error in parameter space with iterations. P , approximated level set value at nodes and P^f , level set values corresponding to true interface configuration.

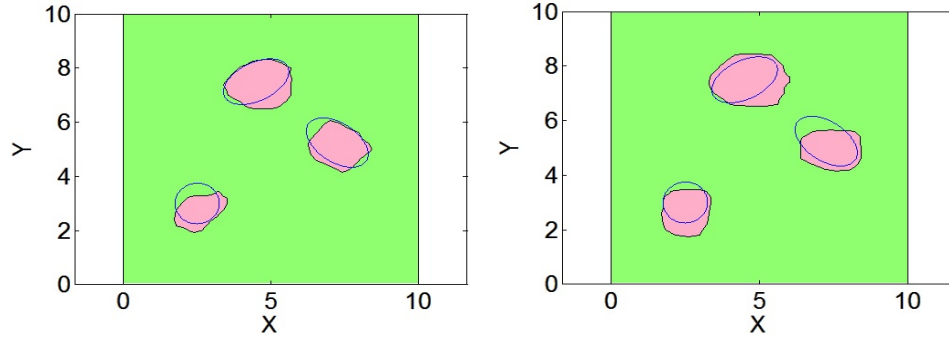


Figure 4.6: Final reconstruction: (a) with 2% noise, (b) with 5% noise

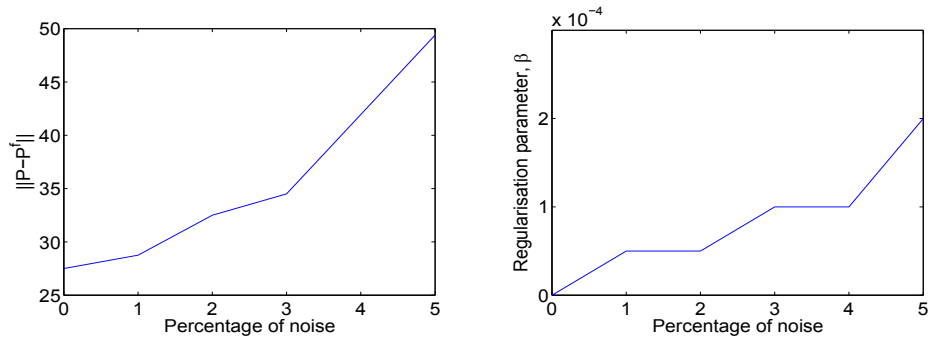


Figure 4.7: (a) Variation of l^2 norm of error in parameter space with different levels of noise, (b) Variation of regularisation parameter β with different levels of noise

4.5 Numerical Examples

The spatial resolution thereby depends on spacing between sensors and the mesh size used in each iteration of the inverse analysis.

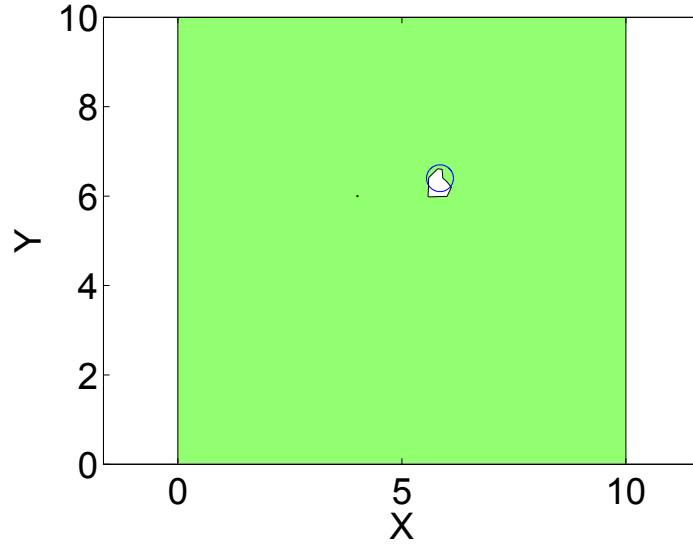


Figure 4.8: The smallest inclusion detected with a mesh of 50×50 and with 50 pseudo sensors. The radius of the actual void = 0.25 units

The uncertainty of piezoelectric strain constant obtained by dynamic resonance method⁸⁴, is evaluated as $\approx 1\%$. So there may be variations in the piezoelectric coupling constants used for the analysis. The proposed method can handle uncertainty in piezoelectric constants of upto 1%. The method becomes unstable when the uncertainty exceeds 1%. Besides there may also be uncertainty in the stiffness and permittivity ratios that define the inclusions in the specimen.

4.5.2 Multiple inclusions in a 3D piezoelectric structure

In this example, the inclusion interface in a three-dimensional piezoelectric structure shown in figure 4.9 is detected using the proposed algorithm. The target data is generated by XFEM analysis with a mesh size of $h = 1/50$. In inverse analysis, the mesh size used in each iteration is $h = 1/25$. The initial assumption is such that spherical inclusions are distributed uniformly all over the domain. The three-dimensional structure is a cube. Mechanical displacements and electric potentials are measured along the boundary of this cubic piezoelectric structure with inclusions inside the domain. In this example, the inclusion is made of a material with stiffness ratio, $C_r = 0.1$ and permittivity ratio, $\kappa_r = 0.1$, with respect to the background material (PZT-4). The number of inclusions present in the domain is two. As shown in figure 4.10, the spherical inclusions far from the true inclusions disappear after some iterations. The level set values

4.5 Numerical Examples

at nodes are updated in each iteration by solving H-J equation and the number of explicit time steps is restricted so that the objective function decreases with each iteration. The implicit representation of inclusion interface using level sets offers the flexibility of determining interface of any shape. Explicit representation is possible only when there is *a priori* information about number of inclusions in the domain, which is not required in the proposed methodology. As shown in figure 4.10, the algorithm detects the two inclusions, their corresponding locations and approximate shapes. Figure 4.11 shows the convergence of the algorithm. The noise level in the target data is increased to 2% and then to 5%. The final inclusion shapes obtained are shown in figure 4.12. The algorithm remains stable even under such higher values of noise because of total variation regularisation. The regularisation parameter, β is $1e-3$ and $2.5e-3$ for 2% and 5% of noise respectively. Figure 4.13 shows the relationship between l^2 norm of error in parameter space with respect to varying levels of noise at appropriate values of β . The residual L-curve is shown in Figure 4.14. The corner represents the optimal regularization parameter. This curve corresponds to data with noise 5%. The curve is obtained by performing inverse analysis for regularization parameters ranging from $1e0$ to $1e-3$. Figure 4.15 shows the regularised solution obtained for different values of the regularisation parameter, β .

4.5.3 Multiple defects

In this example, the algorithm proposed is employed in determining the number, approximate location and shape of defects in a damaged piezoelectric domain. The defect may be an air void, a crack or inclusion with lower stiffness or permittivity. The piezoelectric domain has two inclusions, one air void and a straight line crack as shown in figure 4.16. Among the two inclusions, one of them has stiffness ratio $C_r = 0.1$ and permittivity ratio $\kappa_r = 0.1$, while the other inclusion has stiffness ratio $C_r = 0.15$ and permittivity ratio $\kappa_r = 0.15$, with respect to the background material. The initial assumption is such that circular inclusions with stiffness ratio $C_r = 0.1$ and permittivity ratio $\kappa_r = 0.1$, are distributed throughout the domain. The initial interface configuration changes with each iteration so that the objective function decreases. As shown in figure 4.17, the interfaces far from the defects disappear and the ones nearer gradually take the shape of the defects. It is interesting to note that at the crack location a flat elliptical inclusion is formed. Though the algorithm cannot determine the crack profile it can atleast detect approximate location of crack like defects. As the inclusion material properties assumed is different from the properties of true defects in the domain, the algorithm over estimates or underestimates the size of the inclusions. The size of voids is over estimated and the size of inclusions with higher stiffness and permittivity ratios than the one assumed are underestimated. This example proves that the algorithm can determine the number of defects present in the piezoelectric structure and their corresponding approximate locations. The convergence of the algorithm is shown in

4.5 Numerical Examples

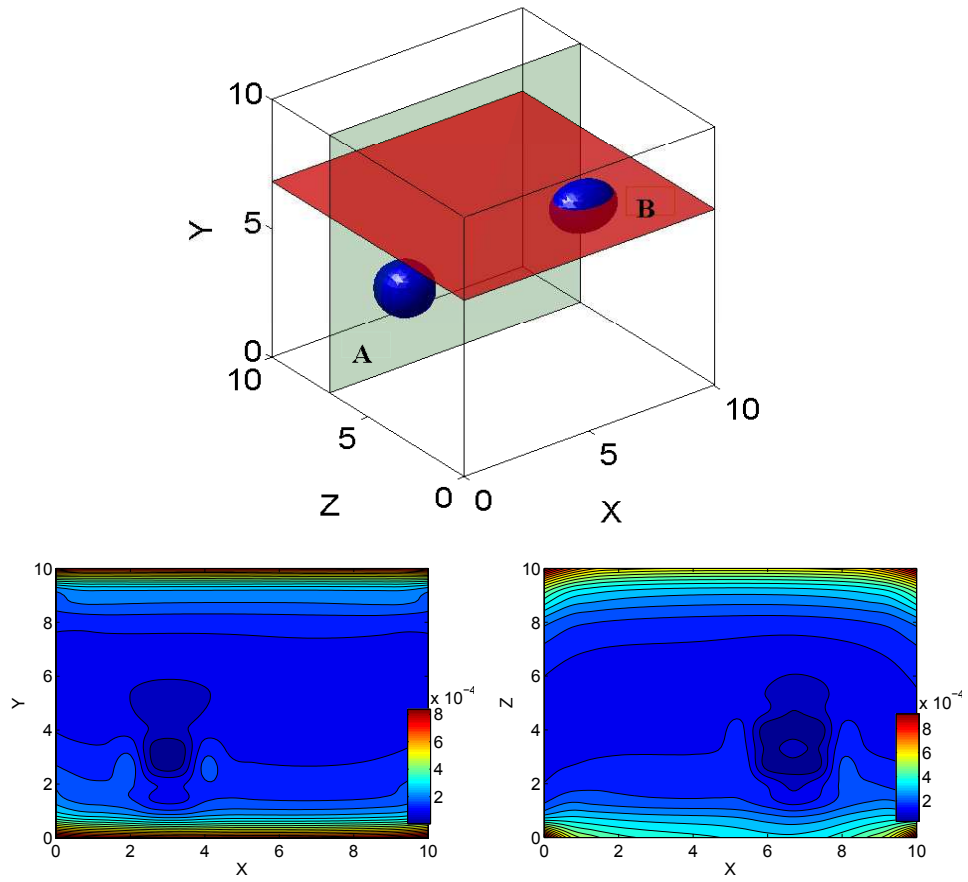


Figure 4.9: (a) Multiple inclusions in a 3D piezoelectric specimen, (b) Energy density contour across plane A, (c) Energy density contour across plane B

4.5 Numerical Examples

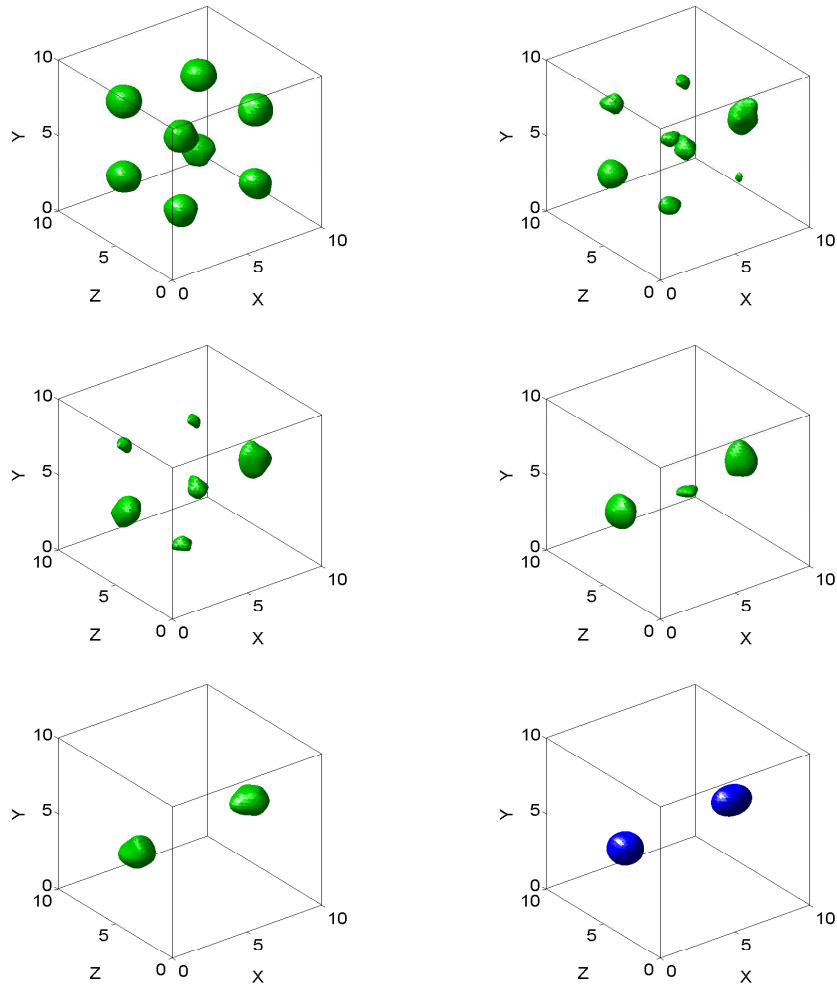


Figure 4.10: Top row : Initial interface configuration, Interface configuration after 20 iterations, second row : Void configuration after 50 and 100 iterations, Bottom row : Final void configuration and actual void configuration.

4.5 Numerical Examples

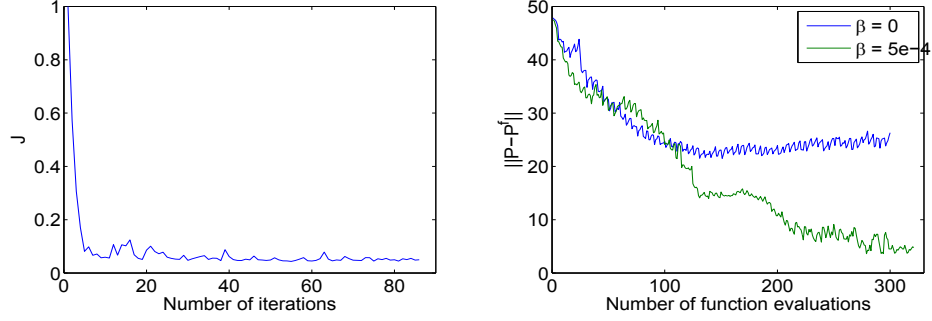


Figure 4.11: (a) Convergence of the objective function, J with iterations, (b) Convergence of l^2 norm of error in parameter space with iterations. P , approximated level set value at nodes and P^f , level set values corresponding to true interface configuration.

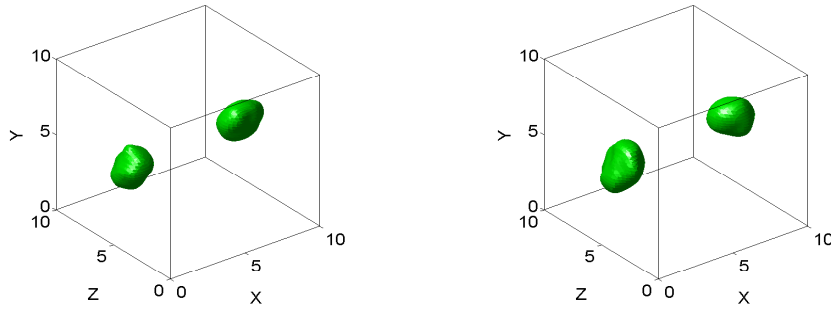


Figure 4.12: Final reconstruction: (a) with 2% noise, (b) with 5% noise

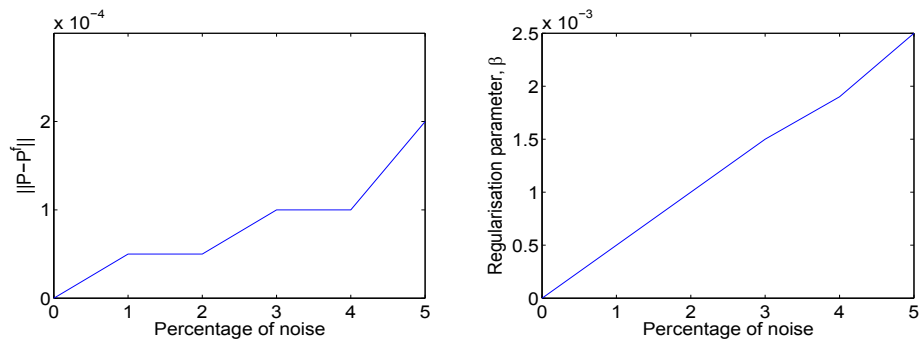


Figure 4.13: (a) Variation of l^2 norm of error in parameter space with different levels of noise, (b) Variation of regularisation parameter β with different levels of noise

4.5 Numerical Examples

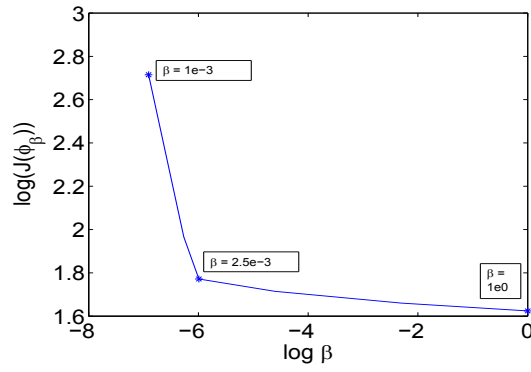


Figure 4.14: Residual L-curve - Noise level = 5%

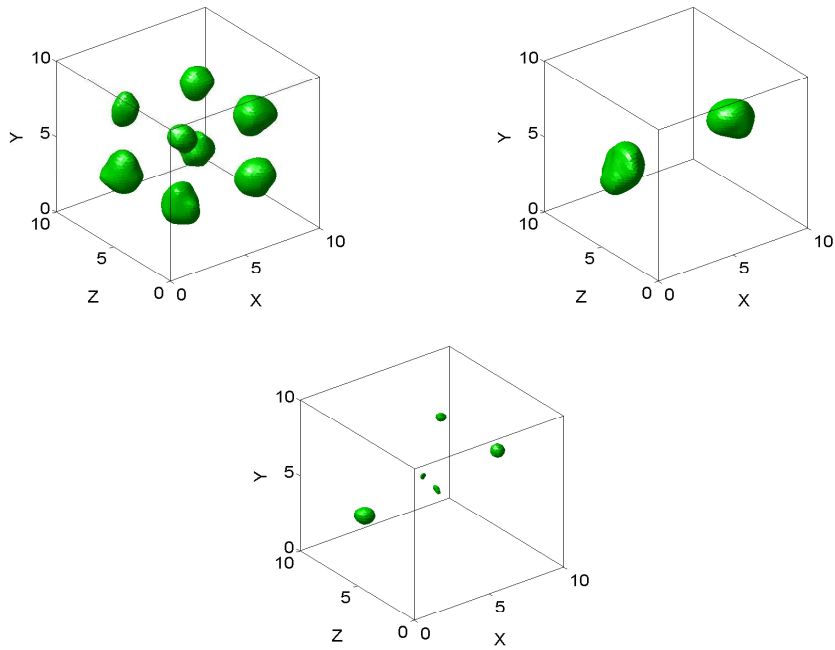


Figure 4.15: The regularised solution for (a) $\beta = 1e-3$, (b) $\beta = 2.5e-3$, (c) $\beta = 1e0$

4.5 Numerical Examples

figure 4.18. In the figure 4.18, the level set values corresponding to true interface configuration, P^f is determined assuming a flat ellipse in the crack location.

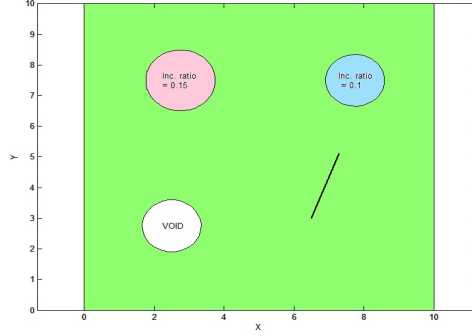


Figure 4.16: Piezoelectric domain with defects

4.5.4 Multiple level sets

In this example, multiple inclusions each made of different materials are detected by using multiple level sets. The piezoelectric domain has three inclusions, two of which has stiffness ratio, $C_r = 0.1$ and permittivity ratio, $\kappa_r = 0.25$ (Material A), while the other inclusion has stiffness ratio, $C_r = 2$ and permittivity ratio, $\kappa_r = 1.75$ (Material B). As there are two different materials, the number of level sets required to determine the interfaces is two. The first level set function, Φ_1 corresponds to interface between material A and the actual piezoelectric domain. The second level set function, Φ_2 corresponds to interface between material B and the actual piezoelectric domain. Two level sets can represent up to four regions but in this example we need to find interfaces between only three regions. As shown in figure 4.19, the initial assumption is such that inclusions made of material A and B are distributed all over the domain for level set function, Φ_1 and Φ_2 respectively. The level set functions Φ_1 and Φ_2 are updated by solving H-J equation in each iteration. As shown in figure 4.19, Φ_1 determines the interface of two inclusions made of material A and Φ_2 determines the interface of the inclusion made of material B. The actual piezoelectric domain is represented by the union of Φ_1 and Φ_2 . The convergence of the algorithm is shown in figure 4.20.

4.5 Numerical Examples

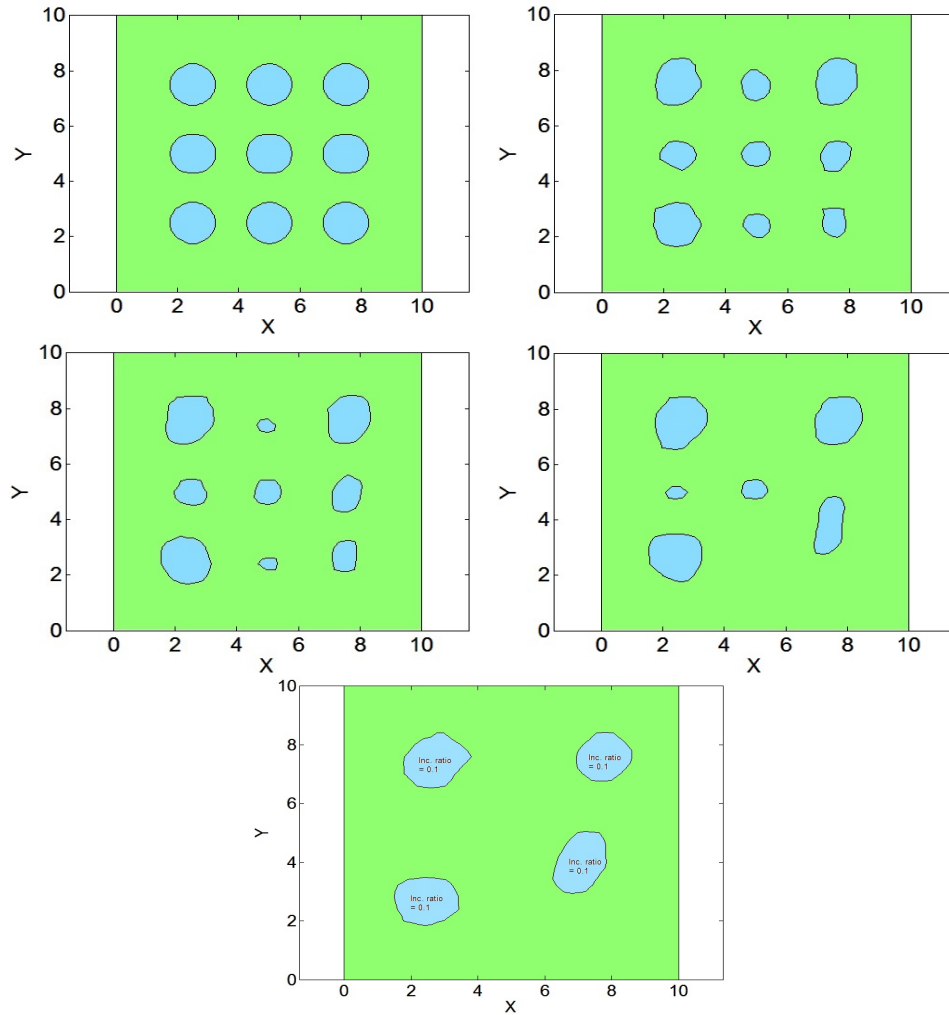


Figure 4.17: Top row : Initial assumption and interface after 50 iterations, second row : Interface after 100 and 300 iterations, bottom row : Inclusion locations detected by the proposed algorithm (stiffness and permittivity ratio = 0.1).

4.6 Conclusion

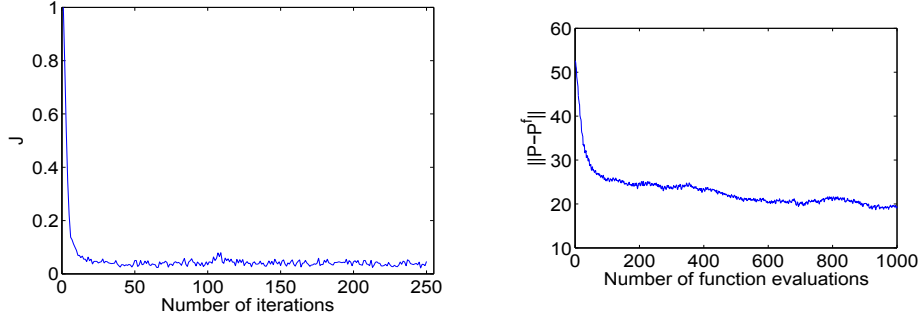


Figure 4.18: (a) Convergence of the objective function, J with iterations, (b) Convergence of l^2 norm of error in parameter space with iterations. P , approximated level set value at nodes and P^f , level set values corresponding to true interface configuration.

4.6 Conclusion

In this work, a methodology to identify the interface of inclusions in piezoelectric structures is proposed. The inclusion materials may either be with lesser or higher stiffness and permittivity compared to the background material. The XFEM is used in determining the responses for varying inclusion interfaces in each iteration as it offers the advantage of mesh independence. If the interface has to be parameterized explicitly, prior information about the number of material subdomains may be required, while the proposed algorithm detects multiple inclusion interface inspite of no prior information. The approximate location of defects like voids, cracks and impurities with low stiffness and permittivity than the actual piezoelectric material can be identified using the proposed methodology. The method is then extended to show that the detection of inclusions made of two different materials is also possible by using multiple level sets. The method requires several experiment setups so as to overcome local optima and to ensure uniqueness. The influence of total variation regularisation in enabling detection in the presence higher noise levels is studied.

4.6 Conclusion

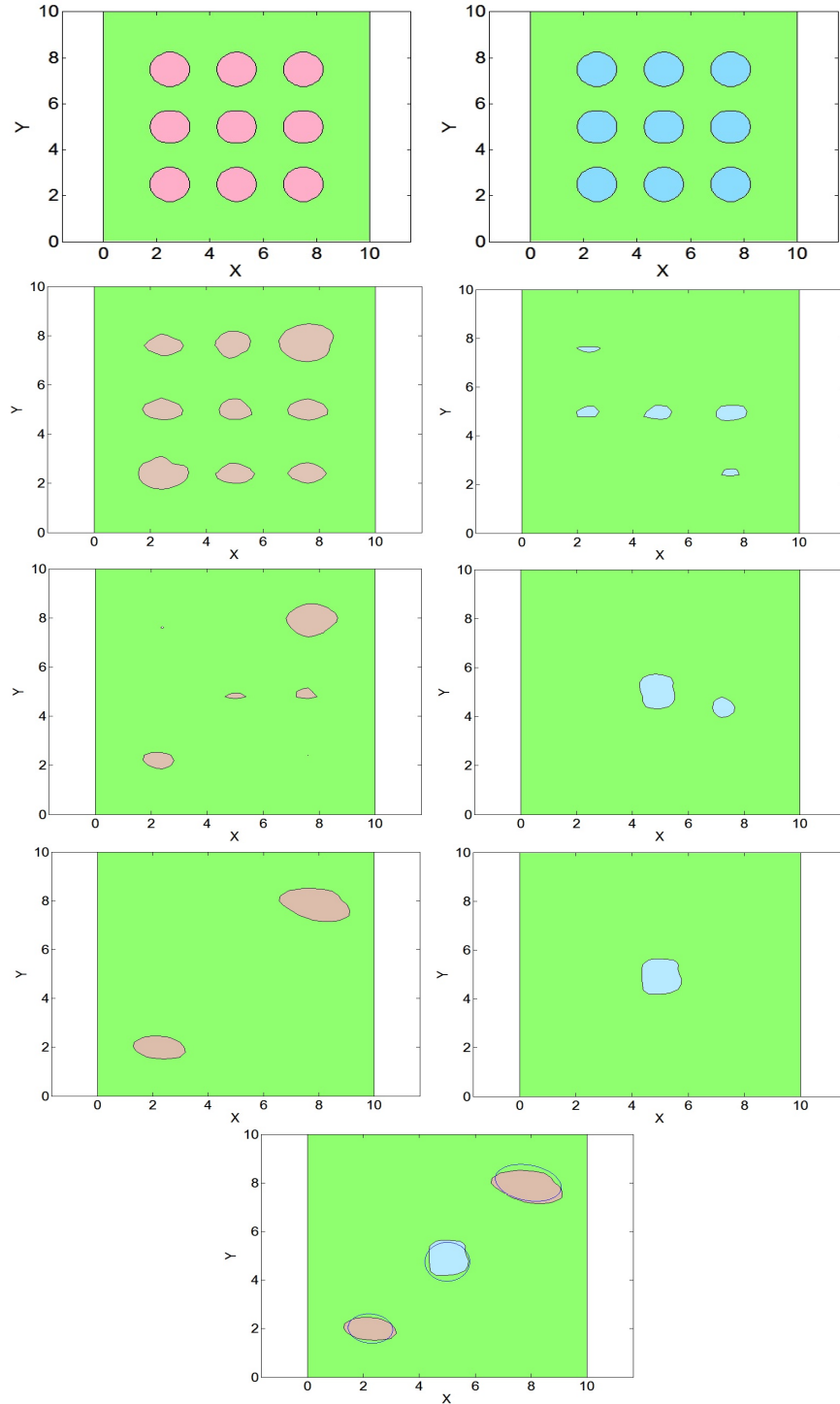


Figure 4.19: Evolution of level set functions, ϕ_1 and ϕ_2 ; Top row : Initial interface configuration, Second row : Interface configuration after 100 iterations, Third row : Interface configuration after 250 iterations, Fourth row : Final configuration of ϕ_1 and ϕ_2 , Bottom row : Union of ϕ_1 and ϕ_2 and true interface configuration.

4.6 Conclusion

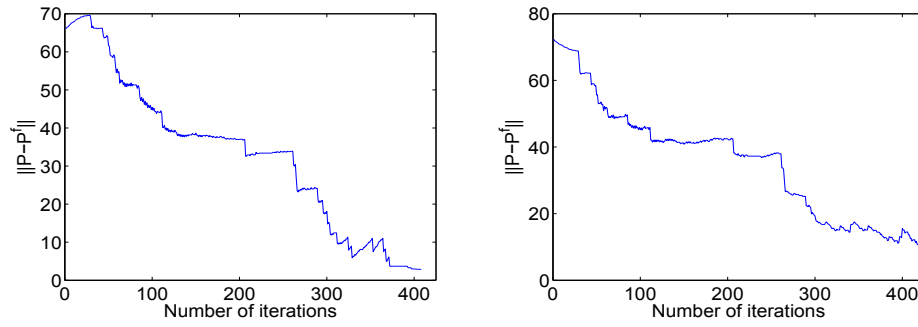


Figure 4.20: (a) Convergence of l^2 norm of error in parameter space with iterations. P , approximated level set value at nodes and P^f , level set values corresponding to true level set function ϕ_1 , (b) Convergence of l^2 norm of error in parameter space with iterations. P , approximated level set value at nodes and P^f , level set values corresponding to true level set function ϕ_2 .

Chapter 5

Topology optimization of nano elastic beams

5.1 Contribution of authors

The work presented in this chapter is published as, S.S.Nanthakumar, N. Valizadeh, H.S. Park and T. Rabczuk, Surface effects on shape and topology optimization of nanostructures, Computational Mechanics (2014). The final publication is available in

<http://dx.doi.org/10.1007/s00466-015-1159-9>.

The original text from this publication is used in this chapter.

- S.S.Nanthakumar
 - Literature review about nano elasticity
 - Coding of the XFEM-level set algorithm for optimizing nano structures
 - Solving of numerical examples
 - Preparing the manuscript
- Navid Valizadeh
 - Assistance in preparing the manuscript except numerical examples section
 - Discussions to better understand nano elasticity
- Prof. Harold S Park
 - Discussions in various stages of preparing the manuscript and concepts related to surface effects in nano elasticity.

5.2 Introduction

- Reviewing the manuscript and making several improvements before submission
- Prof. Timon Rabczuk
 - Discussions to improve the numerical examples
 - Reviewing the manuscript before submission

5.2 Introduction

Due to their unique physical properties, nanostructures^{85,86} have recently attracted significant attention from the scientific community. In addition to their electronic, thermal and optical properties, nanostructures can exhibit mechanical behavior and properties that are superior to those of the corresponding bulk material. The underlying physical mechanism for the changes in the mechanical and other physical properties with decreasing structure size, is the increasing significance of surface effects, which is due to increasing surface area to volume ratio⁸⁷.

The physical origin of the surface effects is that atoms at the surfaces of a material have fewer bonding neighbors than atoms that lie within the material bulk¹⁰. This so-called undercoordination of the surface atoms causes them to exhibit different elastic properties than atoms in the bulk, which can lead to either stiffening or softening of the nanostructure, as described by Zhou and Huang³⁰ and recently reviewed by Park et al¹¹. Surface effects also have a first order effect on the deformation mechanisms and plasticity in nanostructures, as illustrated in various works^{88,89,90} and recently summarized by Weinberger and Cai⁹¹. Therefore, it is critical to consider surface effects when discussing the mechanical behavior and properties of nanomaterials, particularly when any characteristic dimension of the nanostructure is smaller than about 100 nm¹¹.

These unique mechanical properties have motivated researchers to develop computational approaches that capture these surface effects based on either linear or nonlinear continuum theories. For example, many computational approaches^{31,92,93,94} are based on the well-known Gurtin-Murdoch linear surface elasticity theory¹², which considers the surface to be an entity of zero thickness that has its own elastic properties that are distinct from the bulk. Other approaches have considered a bulk plus surface ansatz of various forms incorporating finite deformation kinematics. The approaches not bound on the Gurtin-Murdoch framework include the work by Steinmann and co-workers^{95,96}, and the surface Cauchy-Born approach of Park and co-workers^{97,98,99}. The interested reader is also referred to the recent review of Javili et al¹⁰⁰.

However, most theoretical and computational studies have focused on determining how surface effects impact specific mechanical properties, i.e. the Young's modulus¹¹, plastic deformation mechanisms^{91,88}, resonant frequencies^{101,102}, bending response^{103,104}, and more generally the mechanical response of nanostructures such as

5.3 Continuum model

nanowires or nanobeams. What has not been done to-date is to investigate how surface effects impact the topology of nanostructures within the concept of optimally performing structures. This topic has a significant history and literature for bulk materials^{105,26,106}, but has not been studied for surface-dominated nanostructures.

The objective of this work is therefore to present a numerical method that can be used to study the optimization of nanostructures, while accounting for the critical physics of interest, that of nanoscale surface effects. The formulation is general, and can be applied to different materials such as FCC metals or silicon so long as the relevant surface elastic constants are known. This is done through a coupling of the extended finite element method (XFEM)⁶⁴ and the level set method²⁶. By using XFEM to solve the nanomechanical boundary value problem including surface effects based on Gurtin-Murdoch surface elasticity theory^{12,94,31}, we are able to maintain a fixed background FE mesh while only the structural topology varies. The level set method in which the front velocity is derived from a shape sensitivity analysis by solving an adjoint problem is based on the ideas proposed by Allaire et al.²⁶.

The outline of this chapter is as follows. In Sect. 5.3, based on Gurtin-Murdoch surface elasticity theory¹², the continuum model for an elastic solid considering surface effects is presented. Sect. 5.4 illustrates the level set method for structural optimization. In Sect. 5.5, the objective functions and the material derivative for shape sensitivity analysis are presented. A brief overview on the XFEM formulation is given in Sect. 5.6 followed by numerical examples in Sect. 5.7, and finally concluding remarks.

5.3 Continuum model

We consider an elastic solid Ω with a material surface $\partial\Omega$. According to continuum theory of elastic material surfaces¹², the equilibrium equations for a nanostructure can be written as:

$$\nabla \cdot \boldsymbol{\sigma} + \mathbf{b} = 0 \quad \text{in } \Omega \quad (5.1)$$

$$\nabla_s \cdot \boldsymbol{\sigma}_s + [\boldsymbol{\sigma} \cdot \mathbf{n}] = 0 \quad \text{on } \Gamma \quad (5.2)$$

where the first equation refers to bulk equilibrium and the second equation refers to the generalized Young-Laplace equation¹² resulting from mechanical equilibrium on the surface. In the above equations, $\boldsymbol{\sigma}$ represents bulk Cauchy stress tensor, \mathbf{b} represents the body force vector, $\boldsymbol{\sigma}_s$ denotes the surface stress tensor, \mathbf{n} is the outward unit normal vector to Γ , and $\nabla_s \cdot \boldsymbol{\sigma}_s = \nabla \boldsymbol{\sigma}_s : \mathbf{P}$. Here \mathbf{P} is the tangential projection tensor to Γ at $\mathbf{x} \in \Gamma$ which is defined as $\mathbf{P}(\mathbf{x}) = \mathbf{I} - \mathbf{n}(\mathbf{x}) \otimes \mathbf{n}(\mathbf{x})$, \mathbf{I} is the second order unit tensor. Γ is the boundary of the domain Ω . Furthermore, the boundary conditions are given by

$$\begin{aligned} \boldsymbol{\sigma} \cdot \mathbf{n} &= \bar{\mathbf{t}} & \text{on } \Gamma_N \\ \mathbf{u} &= \bar{\mathbf{u}} & \text{on } \Gamma_D \end{aligned} \quad (5.3)$$

5.3 Continuum model

where $\bar{\mathbf{t}}$ and $\bar{\mathbf{u}}$ are the prescribed traction and displacement, respectively, and Γ_N and Γ_D are the Neumann and Dirichlet boundaries. The bulk strain tensor $\boldsymbol{\varepsilon}$ and surface strain tensor $\boldsymbol{\varepsilon}_s$ are written as

$$\boldsymbol{\varepsilon} = \frac{1}{2}(\nabla \mathbf{u} + (\nabla \mathbf{u})^T) \quad (5.4)$$

$$\boldsymbol{\varepsilon}_s = \mathbf{P} \cdot \boldsymbol{\varepsilon} \cdot \mathbf{P} \quad (5.5)$$

where \mathbf{u} is the displacement vector. Assuming a linear elastic bulk material and an isotropic linear elastic surface, the constitutive equations for the bulk and surface can be written as

$$\boldsymbol{\sigma} = \mathbb{C}^{bulk} : \boldsymbol{\varepsilon} \quad (5.6)$$

$$\boldsymbol{\sigma}_s = \frac{\partial \gamma}{\partial \boldsymbol{\varepsilon}_s} \quad (5.7)$$

where γ is the surface energy density given by

$$\gamma = \gamma_0 + \boldsymbol{\tau}_s : \boldsymbol{\varepsilon}_s + \frac{1}{2} \boldsymbol{\varepsilon}_s : \mathbb{C}^s : \boldsymbol{\varepsilon}_s \quad (5.8)$$

where γ_0 is the surface free energy density that exists even when $\boldsymbol{\varepsilon}_s = 0$, and $\boldsymbol{\tau}_s = \boldsymbol{\tau}_s \mathbf{P}$ is the surface residual stress tensor. By substituting 5.8 into 5.7, $\boldsymbol{\sigma}_s$ can be obtained by

$$\boldsymbol{\sigma}_s = \boldsymbol{\tau}_s + \mathbb{C}^s : \boldsymbol{\varepsilon}_s \quad (5.9)$$

In the above equations, \mathbb{C}^{bulk} and \mathbb{C}^s are the fourth-order elastic stiffness tensors associated with the bulk and surface, respectively, and are defined as

$$\mathbb{C}_{ijkl}^{bulk} = \lambda \delta_{ij} \delta_{kl} + \mu (\delta_{ik} \delta_{jl} + \delta_{il} \delta_{jk}) \quad (5.10)$$

$$\mathbb{C}_{ijkl}^s = \lambda_s P_{ij} P_{kl} + \mu_s (P_{ik} P_{jl} + P_{il} P_{jk}) \quad (5.11)$$

where λ and μ , and λ_s and μ_s are the Lamé constants of the bulk and surface, respectively.

It should be noted that the surface is considered as a special case of a coherent imperfect interface between two materials when one of them exists in a vacuum phase⁹². It is assumed that the surface adheres to the bulk and therefore we have:

$$\mathbf{u} = 0 \quad (i.e.) \quad (\mathbf{u})^+ - (\mathbf{u})^- = 0 \quad \text{on } \Gamma \quad (5.12)$$

Having defined the constitutive and field equations, we derive the weak form of the boundary value problem based on the principle of stationary potential energy. The total potential energy Π of the system is given by

$$\Pi = \Pi_{bulk} + \Pi_s - \Pi_{ext} \quad (5.13)$$

5.4 Level set method

where Π_{bulk} , Π_s , and Π_{ext} represent the bulk elastic strain energy, surface elastic energy and the work of external forces, respectively, which are given by

$$\Pi_{bulk} = \frac{1}{2} \int_{\Omega} \boldsymbol{\varepsilon} : \mathbb{C}^{bulk} : \boldsymbol{\varepsilon} d\Omega \quad (5.14)$$

$$\Pi_s = \int_{\Gamma} \gamma d\Gamma \quad (5.15)$$

$$\Pi_{ext} = \int_{\Gamma_N} \mathbf{u} \cdot \bar{\mathbf{t}} d\Gamma + \int_{\Omega} \mathbf{u} \cdot \mathbf{b} d\Omega \quad (5.16)$$

The stationary condition of 6.10 is given by

$$D_{\delta \mathbf{u}} \Pi = 0 \quad (5.17)$$

where $D_{\mathbf{m}} \Upsilon$ is the directional derivative (or Gâteaux derivative) of the functional Υ in the direction \mathbf{m} . Applying the stationary condition, the weak form of the equilibrium equations can be obtained by finding $\mathbf{u} \in \{\mathbf{u} = \bar{\mathbf{u}} \text{ on } \Gamma_D, \mathbf{u} \in H^1(\Omega)\}$ such that

$$\begin{aligned} & \int_{\Omega} \boldsymbol{\varepsilon}(\mathbf{u}) : \mathbb{C}^{bulk} : \boldsymbol{\varepsilon}(\delta \mathbf{u}) d\Omega + \int_{\Gamma} \boldsymbol{\varepsilon}_s(\mathbf{u}) : \mathbb{C}^s : \boldsymbol{\varepsilon}_s(\delta \mathbf{u}) d\Gamma \\ &= - \int_{\Gamma} \boldsymbol{\tau}_s : \boldsymbol{\varepsilon}_s(\delta \mathbf{u}) d\Gamma + \int_{\Gamma_N} \delta \mathbf{u} \cdot \bar{\mathbf{t}} d\Gamma + \int_{\Omega} \delta \mathbf{u} \cdot \mathbf{b} d\Omega \end{aligned} \quad (5.18)$$

for all $\delta \mathbf{u} \in \{\delta \mathbf{u} = 0 \text{ on } \Gamma_D, \delta \mathbf{u} \in H^1(\Omega)\}$. This weak form can be written in a simplified form as

$$a(\mathbf{u}, \delta \mathbf{u}) + a_s(\mathbf{u}, \delta \mathbf{u}) = -l_s(\delta \mathbf{u}) + l(\delta \mathbf{u}) \quad (5.19)$$

where the bilinear functionals $a(\mathbf{u}, \delta \mathbf{u})$ and $a_s(\mathbf{u}, \delta \mathbf{u})$, and linear functionals $l(\delta \mathbf{u})$ and $l_s(\delta \mathbf{u})$ are defined as

$$\begin{aligned} a(\mathbf{u}, \delta \mathbf{u}) &= \int_{\Omega} c(\mathbf{u}, \delta \mathbf{u}) d\Omega = \int_{\Omega} \boldsymbol{\varepsilon}(\mathbf{u}) : \mathbb{C}^{bulk} : \boldsymbol{\varepsilon}(\delta \mathbf{u}) d\Omega \\ a_s(\mathbf{u}, \delta \mathbf{u}) &= \int_{\partial\Omega} c_s(\mathbf{u}, \delta \mathbf{u}) d\Gamma = \int_{\partial\Omega} \boldsymbol{\varepsilon}_s(\mathbf{u}) : \mathbb{C}^s : \boldsymbol{\varepsilon}_s(\delta \mathbf{u}) d\Gamma \\ l(\delta \mathbf{u}) &= \int_{\partial\Omega_N} \delta \mathbf{u} \cdot \bar{\mathbf{t}} d\Gamma + \int_{\Omega} \delta \mathbf{u} \cdot \mathbf{b} d\Omega \\ l_s(\delta \mathbf{u}) &= \int_{\partial\Omega} \boldsymbol{\tau}_s : \boldsymbol{\varepsilon}_s(\delta \mathbf{u}) d\Gamma \end{aligned} \quad (5.20)$$

5.4 Level set method

The level set method (LSM), which was first introduced by Osher and Sethian¹⁰⁷ for tracking moving interfaces, has been extensively applied to many different research

5.4 Level set method

fields such as image processing, computer graphics, fluid mechanics, and crack propagation over the past three decades. The first research work on incorporating the level set method¹⁰⁷ in structural shape and topology optimization was performed by Sethian and Wiegmann¹⁰⁸. They used the level set method to represent the design structure and to alter the design shape based on a Von Mises equivalent stress criterion. Later, Osher and Santosa¹⁰⁹, Allaire et al.²⁶, and Wang et al.¹¹⁰ independently proposed a new class of structural optimization method based on a combination of the level set method with the shape sensitivity analysis framework. The main idea of this method is to model the process of structural optimization via a scalar level set function which dynamically changes in time. Therefore, the evolution of the design shape is governed by the Hamilton-Jacobi (H-J) partial differential equation (PDE) in which the front speed (or velocity vector) links the H-J equation with the shape sensitivity analysis. This method is usually called conventional level set method and is widely used in structural optimization^{110,111}.

We assume $\mathbf{D} \subset \mathbb{R}^d$ ($d=2$ or 3) as the whole structural shape and topology design domain including all admissible shapes Ω , i.e. $\Omega \subset \mathbf{D}$. A level set function $\Phi(\mathbf{x})$ which partitions the design domain \mathbf{D} into three parts, i.e. the solid, void and the boundary which are defined as

$$\begin{aligned} \text{Solid} : \quad & \Phi(\mathbf{x}) < 0 \quad \forall \mathbf{x} \in \Omega \setminus \partial\Omega \\ \text{Boundary} : \quad & \Phi(\mathbf{x}) = 0 \quad \forall \mathbf{x} \in \partial\Omega \cap \mathbf{D} \\ \text{Void} : \quad & \Phi(\mathbf{x}) > 0 \quad \forall \mathbf{x} \in \mathbf{D} \setminus \Omega \end{aligned} \tag{5.21}$$

The basic idea of the level set method for structural optimization is to describe the structural design boundary, $\Gamma(\mathbf{x})$ implicitly by the zero level set of a higher dimensional level set function (see 5.1):

$$\Gamma(\mathbf{x}) = \{\mathbf{x} \in \mathbb{R}^d \mid \Phi(\mathbf{x}) = 0\} \tag{5.22}$$

To allow the design boundary for a dynamic evolution in the optimization process, we introduce t as a fictitious time. Thus the dynamic design boundary is defined as

$$\Gamma(t) = \{\mathbf{x}(t) \in \mathbb{R}^d \mid \Phi(\mathbf{x}(t), t) = 0\} \tag{5.23}$$

By differentiating $\{\Phi(\mathbf{x}(t), t) = 0\}$ with respect to time¹, we obtain the well-known Hamilton-Jacobi partial differential equation

$$\frac{\partial \Phi(\mathbf{x}(t), t)}{\partial t} + \nabla \Phi(\mathbf{x}(t), t) \cdot \mathbf{V} = 0 \tag{5.24}$$

¹This is the same as taking the material derivative of $\{\Phi(\mathbf{x}(t), t) = 0\}$.

5.4 Level set method

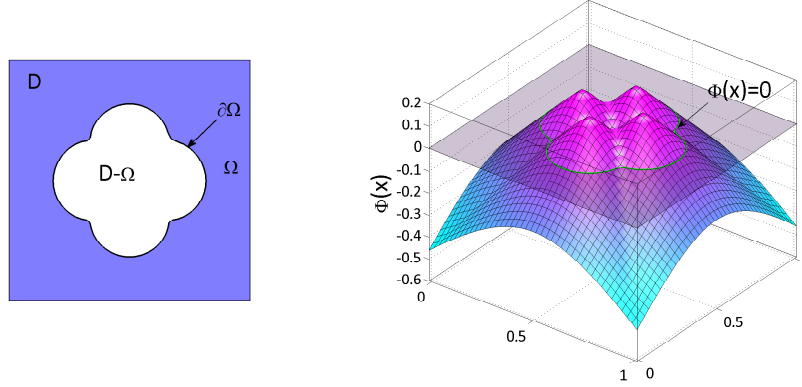


Figure 5.1: Level set description of a plate with a hole. (left) Design domain (right) level set function.

where $\mathbf{V} = \frac{d\mathbf{x}}{dt}$ denotes the velocity vector of the design boundary. This equation can be further written considering the unit outward normal $\mathbf{n} = \frac{\nabla\Phi}{|\nabla\Phi|}$ to the boundary and normal component of velocity vector $V_n = \mathbf{V} \cdot \mathbf{n}$,

$$\frac{\partial\Phi}{\partial t} + V_n |\nabla\Phi| = 0 \quad (5.25)$$

By solving this Hamilton-Jacobi equation, the level set function and consequently the structural design boundary is updated during the optimization process. It should be noted that here V_n is a quantity that links the level set method to the shape design sensitivity analysis¹¹⁰.

The Hamilton-Jacobi equations usually do not admit smooth solutions. Existence and uniqueness are achieved in the framework of viscosity solutions which provide a convenient definition of the generalized shape motion. The discrete solution of the H-J equation is obtained by an explicit first-order upwind scheme²⁶. The level set function is regularized periodically by solving

$$\frac{\partial\Phi}{\partial t} + \text{sign}(\Phi_0) (|\nabla\Phi| - 1) = 0. \quad (5.26)$$

Solving this equation gives a signed distance function with respect to an initial isoline, Φ_0 . This ensures smoother interfaces and also that the signed distance from the interface can be used as enrichment values for the nodes whose support is cut by the zero level sets, for the XFEM analysis performed in each iteration.

5.5 Material derivative approach and sensitivity analysis

In this work, we consider two objective functions. The first considers the total potential energy of the nanostructure under equilibrium and volume constraints. For this case, the topology optimization problem can be defined as

$$\text{Minimize } J_1(\mathbf{\Omega}) = \int_{\Omega} \mathbf{u} \cdot \mathbf{b} d\Omega + \int_{\Gamma_N} \mathbf{u} \cdot \mathbf{t} d\Gamma \quad (5.27)$$

$$\text{Subject to } \int_{\Omega} d\Omega - \bar{V} = 0 \quad (5.28)$$

$$a(\mathbf{u}, \mathbf{v}, \mathbf{\Omega}) + a_s(\mathbf{u}, \mathbf{v}, \mathbf{\Omega}) = -l_s(\mathbf{v}, \mathbf{\Omega}) + l(\mathbf{v}, \mathbf{\Omega}) \quad (5.29)$$

The second is a least square error objective function compared to a target displacement, which can be written as

$$\text{Minimize } J_2(\mathbf{\Omega}) = \left(\int_{\Gamma} |\mathbf{u} - \mathbf{u}_0|^2 d\Gamma \right)^{\frac{1}{2}} \quad (5.30)$$

$$\text{Subject to} \quad (5.31)$$

$$a(\mathbf{u}, \mathbf{v}, \mathbf{\Omega}) + a_s(\mathbf{u}, \mathbf{v}, \mathbf{\Omega}) = -l_s(\mathbf{v}, \mathbf{\Omega}) + l(\mathbf{v}, \mathbf{\Omega}) \quad (5.32)$$

Here we assume $\mathbf{v} = \delta \mathbf{u}$ and $\gamma_0 = 0$. To perform shape optimization, it is essential to find the relationship between a variation in design variables and the resulting variations in cost functional¹¹² using a sensitivity analysis method. For this purpose, we use the material derivative concept from continuum mechanics.

5.5.1 Material derivative

Consider an initial structural domain $\mathbf{\Omega}$ which is transformed into a deformed (or perturbed) structural domain $\mathbf{\Omega}_\tau$ in a fictitious time τ . This transformation can be viewed as a mapping $\mathbf{T} : x \rightarrow x_\tau(x), x \in \mathbf{\Omega}$ such that

$$\begin{aligned} x_\tau &\equiv \mathbf{T}(x, \tau) \\ \mathbf{\Omega}_\tau &\equiv \mathbf{T}(\mathbf{\Omega}, \tau) \end{aligned} \quad (5.33)$$

A design velocity field can be defined as

$$\mathbf{V}(x_\tau, \tau) \equiv \frac{dx_\tau}{d\tau} = \frac{d\mathbf{T}(x, \tau)}{d\tau} = \frac{\partial \mathbf{T}(x, \tau)}{\partial \tau} \quad (5.34)$$

5.5 Material derivative approach and sensitivity analysis

Based on the linear Taylor's series expansion of $\mathbf{T}(x, \tau)$ around $\tau = 0$, any material point in the initial domain $x \in \Omega$ can be mapped onto a new material point in the perturbed domain $x_\tau \in \Omega_\tau$ as

$$x_\tau(x) = \mathbf{T}(x, \tau) = x + \tau \mathbf{V}(x) \quad (5.35)$$

The material derivative of quantity z is defined as

$$\dot{z}(x) = \left. \frac{d}{d\tau} z_\tau(x + \tau \mathbf{V}(x)) \right|_{\tau=0} = z'(x) + \nabla z(x) \cdot \mathbf{V}(x) \quad (5.36)$$

where the over dot represents the material derivative and the prime denotes a local derivative.

Lemma 1 Let Ψ_1 be a domain functional defined as

$$\Psi_1 = \int_{\Omega_\tau} f_\tau(x_\tau) d\Omega_\tau$$

with f_τ being a regular function defined in Ω_τ , then the material derivative of Ψ_1 is given by

$$\begin{aligned} \dot{\Psi}_1 &= \int_{\Omega} [\dot{f}(x) + f(x)(\nabla \cdot \mathbf{V}(x))] d\Omega \\ &= \int_{\Omega} [f'(x) + \nabla \cdot (f(x) \mathbf{V}(x))] d\Omega \\ &= \int_{\Omega} f'(x) d\Omega + \int_{\Gamma} f(x)(\mathbf{V}(x) \cdot \mathbf{n}) d\Gamma \end{aligned}$$

Lemma 2 Let Ψ_2 be a boundary functional defined as

$$\Psi_2 = \int_{\Gamma_\tau} g_\tau(x_\tau) d\Gamma_\tau$$

with g_τ being a regular function defined on Γ_τ , then the material derivative of Ψ_2 is given by

$$\begin{aligned} \dot{\Psi}_2 &= \int_{\Gamma} [\dot{g}(x) + \kappa g(x)(\mathbf{V}(x) \cdot \mathbf{n})] d\Gamma \\ &= \int_{\Gamma} [g'(x) + (\nabla g(x) \cdot \mathbf{n} + \kappa g(x))(\mathbf{V}(x) \cdot \mathbf{n})] d\Gamma \end{aligned}$$

5.5 Material derivative approach and sensitivity analysis

where $\kappa = \text{div} \mathbf{n} = \nabla \cdot \mathbf{n}$ is the curvature of Γ in \mathbb{R}^2 and twice the mean curvature of Γ in \mathbb{R}^3 .

With these Lemmas¹¹² at hand, the material derivative of the objective functionals can be obtained as (see appendix A.1 for details),

$$J_1 = \int_{\Omega} u' \cdot b \, d\Omega + \int_{\Gamma} u \cdot b \, V_n \, d\Gamma + \int_{\Gamma_N} (\nabla u \cdot t \cdot n + \kappa u \cdot t) \, V_n \, d\Gamma \quad (5.37)$$

$$J_2 = c_0 \cdot \left(\int_{\Gamma} 2|u - u_0| u' \, d\Gamma + \int_{\Gamma} (\nabla(|u - u_0|^2)) \cdot n + \kappa |u - u_0|^2 \right) V_n \, d\Gamma \quad (5.38)$$

$$c_0 = \frac{1}{2} \left(\int_{\Gamma} |u - u_0|^2 \, d\Gamma \right)^{-\frac{1}{2}} \quad (5.39)$$

5.5.2 Sensitivity analysis

In order to convert the constrained optimization problem to an unconstrained problem, an augmented objective functional L is constructed as

$$L = J(\mathbf{u}, \mathbf{\Omega}) + \chi(\mathbf{\Omega}) \quad (5.40)$$

$$\chi(\mathbf{\Omega}) = \lambda \left(\int_{\Omega} d\Omega - \bar{V} \right) + \frac{1}{2\Lambda} \left(\int_{\Omega} d\Omega - \bar{V} \right)^2$$

in which λ is the Lagrange multiplier and Λ is a penalization parameter. These parameters are updated at each iteration k of the optimization process by the following rule

$$\lambda^{k+1} = \lambda^k + \frac{1}{\Lambda^k} \left(\int_{\Omega} d\Omega - \bar{V} \right) \quad (5.41)$$

$$\Lambda^{k+1} = \zeta \Lambda^k$$

where $\zeta \in (0, 1)$ is a constant parameter.

The shape derivative of augmented Lagrangian L is defined as

$$L' = J'(\mathbf{u}, \mathbf{\Omega}) + \chi'(\mathbf{\Omega}) \quad (5.42)$$

$$J' = \int_{\Gamma} G \cdot V_n \, d\Gamma \quad (5.43)$$

5.6 Extended finite element method

$$\begin{aligned}
G = & - \int_{\Gamma} \boldsymbol{\varepsilon}(\mathbf{u}) : \mathbb{C}^{bulk} : \boldsymbol{\varepsilon}(\mathbf{w}) d\Gamma \\
& - \int_{\Gamma} \kappa(\mathbf{P}\boldsymbol{\varepsilon}(\mathbf{w})\mathbf{P} : \boldsymbol{\tau}_s) d\Gamma \\
& - \int_{\Gamma} \kappa(\mathbf{P}\boldsymbol{\varepsilon}(\mathbf{u})\mathbf{P} : \mathbb{C}^s : \mathbf{P}\boldsymbol{\varepsilon}(\mathbf{w})\mathbf{P}) d\Gamma
\end{aligned} \tag{5.44}$$

$$\chi'(\boldsymbol{\Omega}) = \int_{\partial\Omega} \max\{0, \lambda + \frac{1}{\Lambda}(\int_{\Omega} d\Omega - \bar{V})\} V_n d\Gamma \tag{5.45}$$

Based on the steepest descent direction,

$$\begin{aligned}
V_n = & - \int_{\Gamma} \boldsymbol{\varepsilon}(\mathbf{u}) : \mathbb{C}^{bulk} : \boldsymbol{\varepsilon}(\mathbf{w}) d\Gamma \\
& - \int_{\Gamma} \kappa(\mathbf{P}\boldsymbol{\varepsilon}(\mathbf{w})\mathbf{P} : \boldsymbol{\tau}_s) d\Gamma \\
& - \int_{\Gamma} \kappa(\mathbf{P}\boldsymbol{\varepsilon}(\mathbf{u})\mathbf{P} : \mathbb{C}^s : \mathbf{P}\boldsymbol{\varepsilon}(\mathbf{w})\mathbf{P}) d\Gamma
\end{aligned} \tag{5.46}$$

$$J' = - \int_{\Gamma} V_n^2 d\Gamma \leq 0 \tag{5.47}$$

Velocity extension The normal velocity of the front V_n is to be extended from the front to the whole design domain in order to solve the HJ equation 5.25. Different techniques for velocity extension have been proposed in the literature e.g. the normal, natural, Hilbertian and Helmholtz velocity extension methods (see¹¹³ for a review on different velocity extension strategies). It is obvious from 5.46 that the velocity comprises two parts, the bulk, V_b and surface terms, V_s . The bulk part of velocity, V_b can be obtained at each node whereas the surface part, V_s can be determined only along the surface. In order to solve HJ equation 5.25 that is posed throughout the domain, the surface part of velocity V_s is extended by extrapolation to the nodes that belong to the cut elements. The value of the speed function at the closest point on the surface is assigned as the extension velocity to the nodal point¹¹⁴, such that the condition $V_{ext} = V_n$ at $\Phi = 0$ is satisfied.

5.6 Extended finite element method

XFEM is a robust numerical approach that enables modelling the evolution of discontinuities such as cracks without remeshing. It is used to analyze the nanobeams

5.6 Extended finite element method

in each step of the iterative optimization process, where the XFEM formulation for solving nanomechanical boundary value problems including surface effects is based on the work of Farsad et al.⁹⁴. In XFEM, the cracks, voids and material interfaces are implicitly represented by using level set functions^{65,21}. In XFEM, the approximation of the displacement field in a material with several material subdomains is given by

$$\mathbf{u}^h(\mathbf{X}) = \sum_{i \in I} N_i(\mathbf{X}) \mathbf{u}_i + \mathbf{u}^{enr} \quad (5.48)$$

$$\mathbf{u}^{enr} = \sum_{N=1}^{n_c} \sum_{j \in J} N_j(\mathbf{X}) \mathbf{a}_j^{(N)} F(\mathbf{X}) \quad (5.49)$$

where \mathbf{a}_j is the additional degrees of freedom (DOF) that accounts for the jump in the strain field, n_c denotes the number of material interfaces, and J is the set of all nodes whose support is cut by the material interface. In this work, the absolute enrichment function $F(\mathbf{X})$ ³

$$F(\mathbf{X}) = \sum_I N_i(\mathbf{X}) |\phi_i(\mathbf{X})| - |N_i(\mathbf{X}) \phi_i(\mathbf{X})| \quad (5.50)$$

is used in order to account for the discontinuous strain field along Γ . The voids are assumed to be filled with a material that is 1000 times softer than the stiffness of the nanostructure. The usage of a softer material enables the traction and displacement boundary to intersect with the void boundary. The stiffness coefficients are determined by numerical integration performed over sub triangles on either side of the inclusion interface. Substituting the displacement field in equation 5.48 to the weak formulation 5.18, the algebraic finite element equations can be obtained. The expressions for $a(\mathbf{u}, \delta \mathbf{u})$, $a_s(\mathbf{u}, \delta \mathbf{u})$, $l_s(\delta \mathbf{u})$ and $l(\delta \mathbf{u})$ for an element can be rewritten using the FE approximation as,

$$a^e(\mathbf{u}, \delta \mathbf{u}) = \delta \mathbf{u}^e T \left(\int_{\Omega^e} \mathbf{B}^T \{\mathbb{C}^{bulk}\} \mathbf{B} d\Omega^e \right) \mathbf{u}^e \quad (5.51)$$

$$\begin{aligned} a_s^e(\mathbf{u}, \delta \mathbf{u}) + l_s^e(\delta \mathbf{u}) &= \int_{\Gamma^e} (\mathbf{P} \boldsymbol{\varepsilon}(\mathbf{u}) \mathbf{P}) \{\mathbb{C}^s\} (\mathbf{P} \boldsymbol{\varepsilon}(\delta \mathbf{u}) \mathbf{P}) d\Gamma^e \\ &\quad + \int_{\Gamma^e} \boldsymbol{\tau}_s (\mathbf{P} \boldsymbol{\varepsilon}(\mathbf{u}) \mathbf{P}) d\Gamma^e \\ &= \delta \mathbf{u}^e T \left(\int_{\Gamma^e} \mathbf{B}^T \mathbf{M}_p^T \{\mathbb{C}^s\} \mathbf{M}_p \mathbf{B} d\Gamma^e \right) \mathbf{u}^e \\ &\quad + \delta \mathbf{u}^e T \int_{\Gamma^e} \mathbf{B}^T \mathbf{M}_p^T \boldsymbol{\tau}_s d\Gamma^e \end{aligned} \quad (5.52)$$

5.7 Numerical examples

$$l^e(\delta \mathbf{u}) = \delta \mathbf{u}^e T \left(\int_{\Gamma_N^e} \mathbf{N}^T \bar{\mathbf{t}} d\Gamma^e + \int_{\Omega^e} \mathbf{N}^T \mathbf{b} d\Omega^e \right) \quad (5.53)$$

where $\mathbf{u} \in H^1(\Omega)$ and $\delta \mathbf{u} \in H^1(\Omega)$.

The final system of discrete algebraic XFEM equations is,

$$(\mathbf{K}_b + \mathbf{K}_s) \mathbf{u} = -\mathbf{f}_s + \mathbf{f}_{ext} \quad (5.54)$$

$$\begin{aligned} \mathbf{K}_b &= \int_{\Omega} \mathbf{B}^T \{\mathbb{C}^{bulk}\} \mathbf{B} d\Omega \\ \mathbf{K}_s &= \int_{\Gamma} \mathbf{B}^T \mathbf{M}_p^T \cdot \{\mathbb{C}^s\} \cdot \mathbf{M}_p \mathbf{B} d\Gamma \\ \mathbf{f}_s &= \int_{\Gamma} \mathbf{B}^T \cdot \mathbf{M}_p^T \boldsymbol{\tau}_s d\Gamma \\ \mathbf{f}_{ext} &= \int_{\Gamma_N} \mathbf{N}^T \bar{\mathbf{t}} d\Gamma + \int_{\Omega} \mathbf{N}^T \mathbf{b} d\Omega \end{aligned} \quad (5.55)$$

where \mathbf{K}_s is the surface stiffness matrix, while \mathbf{f}_s is the surface residual. \mathbf{M}_p and \mathbb{C}^s are defined as in Farsad et al.⁹⁴,

$$\mathbf{M}_p = \begin{pmatrix} P_{11}^2 & P_{12}^2 & P_{11}P_{12} \\ P_{12}^2 & P_{22}^2 & P_{12}P_{22} \\ 2P_{11}P_{12} & 2P_{12}P_{22} & P_{12}^2 + P_{11}P_{22} \end{pmatrix} \quad (5.56)$$

$$\mathbf{C}^s = \mathbf{M}_p^T \mathbf{S}^s \mathbf{M}_p \quad (5.57)$$

$$\mathbf{S}^s = \begin{pmatrix} S_{1111} & S_{1122} & 0 \\ S_{1122} & S_{2222} & 0 \\ 0 & 0 & S_{1212} \end{pmatrix} \quad (5.58)$$

The steps involved in the process of optimizing nano structures using XFEM and level set coupled methodology is shown as a flowchart in figure 5.2.

5.7 Numerical examples

In this section, several examples are solved to determine the influence of surface effects on the optimum topology of nanostructures specifically, nanobeams. Our choice of nanobeams is driven by multiple reasons. First, nanobeams are the basic functional element in most nanoelectromechanical systems (NEMS)^{115,116,117}. Second, the topology optimization of beams has been widely studied in the literature, and as a result,

5.7 Numerical examples

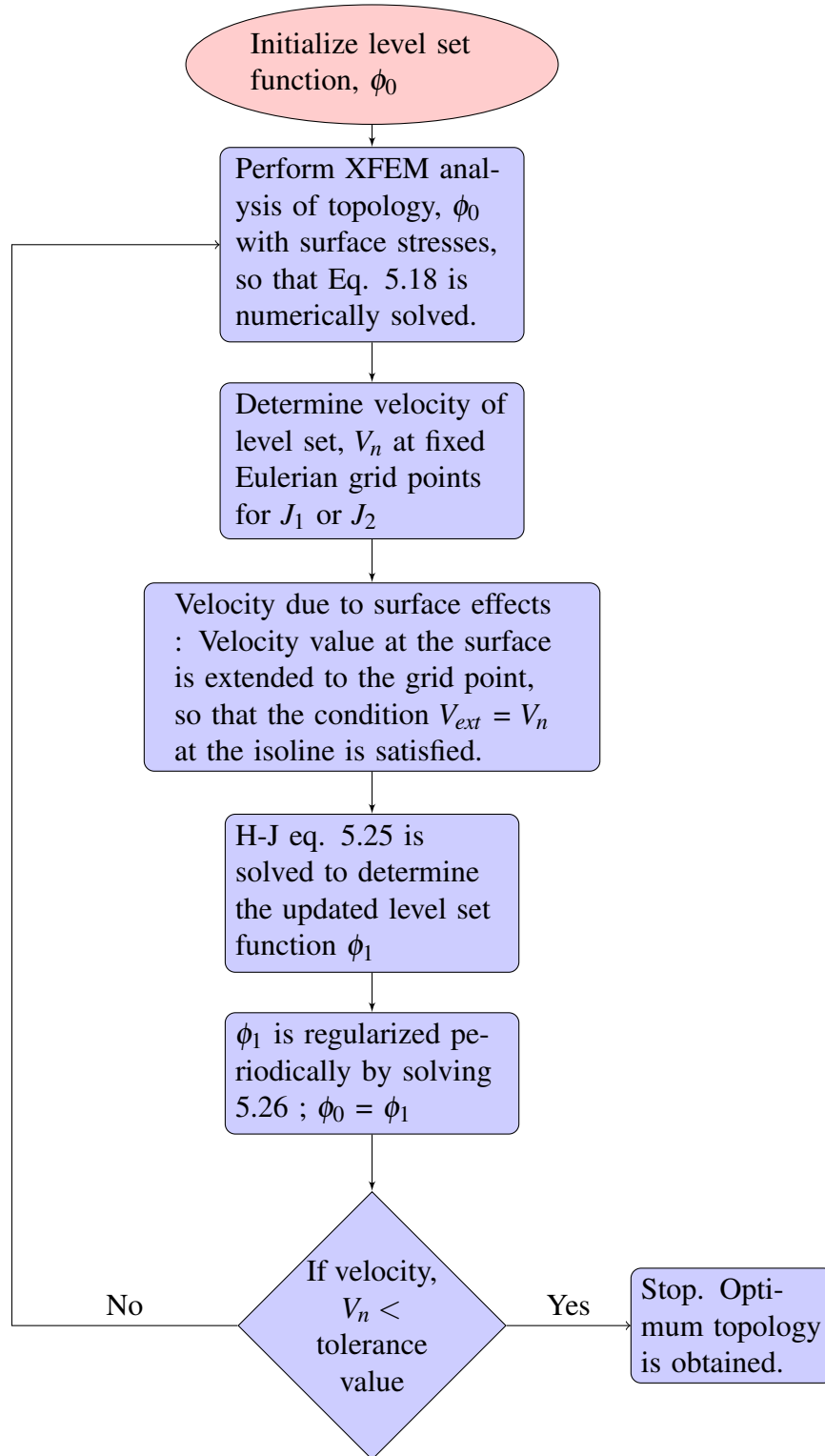


Figure 5.2: Flowchart showing steps involved in the process of optimizing nano structures with surface effects

5.7 Numerical examples

Table 5.1: E (bulk Youngs modulus), ν (Poisson ratio) and S_{ijkl} (surface stiffness) for Gold (Au) from atomistic calculations.⁶

$E(GPa)$	ν	$S_{1111}=S_{2222} (J/m^2)$		
36	0.44	5.26		

$S_{1122}=S_{2211} (J/m^2)$	$S_{1212} (J/m^2)$	$\tau^0 (J/m^2)$
2.53	3.95	1.57

it would be interesting to examine how surface effects alter the optimal topologies of nanobeams when surface effects are accounted for. Manufacturability of the optimal topologies may be an issue with regards to the smallest nanobeams we have optimized in this work.

The topology optimization is performed for two different beams, i.e. cantilever and fixed beam. The objective functions discussed in Section 5.5 are employed, i.e. minimum total potential energy and minimum least square error compared to a target displacement. The nanobeam is assumed to be made of gold, where the bulk and surface properties are given in Table 5.1. For the XFEM analysis, the domain is discretized by using bilinear quadrilateral (Q4) elements.

In the following numerical examples, the velocity of the level set function, V_n is evaluated at all node points, so as to solve the HJ equation throughout the domain. From equation 5.46, it can be seen that it also includes surface terms which are available only along the interface. The surface terms are extrapolated to nodes of those elements which are cut by the interface, while these terms are neglected at all other nodal locations.

A short cantilever beam of size 32×20 units subjected to a point load at the free end is optimized using the level set method. The optimum topology for a volume ratio of 0.4 is shown in figure 5.3 (b). The optimum topology is similar to the one shown in Sigmund et al.⁵, obtained by SIMP.

In order to obtain best results using conventional level set method, the optimization process is initialized with sufficiently large number of voids that are uniformly distributed all over the domain²⁶ as shown in figure 5.3 (a).

5.7.1 Cantilever beam

5.7.1.1 Objective function J_1

In this section, optimization of nanobeams subject to cantilever boundary conditions is performed such that total potential energy is minimized. The first geometry is an

5.7 Numerical examples

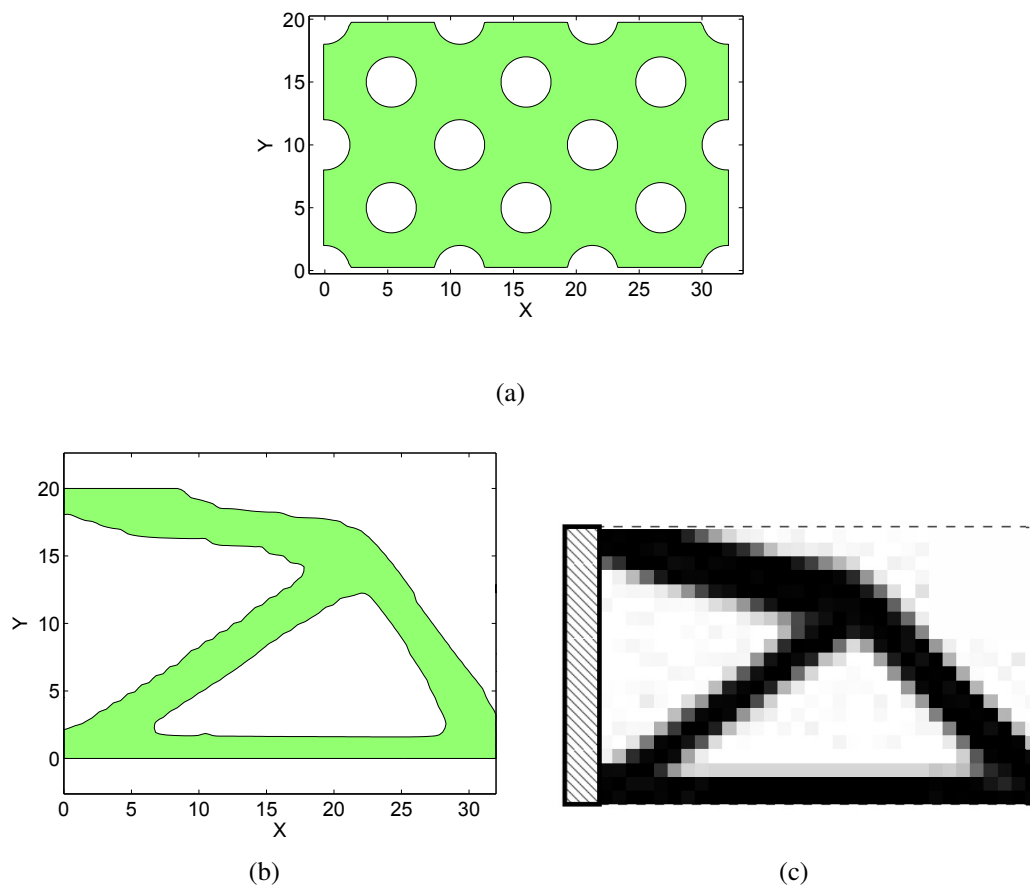


Figure 5.3: (a) Initialization (b) Optimum topology for a short cantilever beam subjected to a point load at free end by Level set method (c) by SIMP⁵.

5.7 Numerical examples

80×20 nm beam that is optimized for minimum total potential energy. The load applied at the free end is a point load of magnitude 3.6 nN, while the volume ratio, which is defined as the ratio of volume of the optimized beam to the initial volume, is restricted to 70%. The optimum topology with a mesh of 120×30 bilinear quadrilateral elements is shown in Figure 5.4(a). The optimization process is then repeated by neglecting surface effects, i.e. taking $\mathbb{C}_s = 0$ and $\tau_s = 0$, with the result seen in Figure 5.4(b).

It is evident from the optimum topologies shown in Figure 5.4 that surface effects do not influence the optimum topology for the minimum energy objective function. This occurs though the stiffness ratio, which is defined as the ratio between the difference in vertical displacement at the load location with and without surface effects, and the vertical displacement at the load location with surface effects, is about 4.25%.

Besides the thickness, the aspect ratio is known to have an important effect on the mechanical properties of nano beams^{88,118}, and thus we consider a nanobeam with dimensions of 200×20 nm, for an aspect ratio of 10. The stiffness ratio of this beam is found to be 4.35%, while the volume ratio is again constrained to 70%. Again, no noticeable differences for the J_1 objective function was observed even when surface effects are accounted for.

The main reason why little difference is observed between the optimal topologies with and without surface effects in Figures 5.4 and 5.5 is due to the fact that the volume constraint is the same for both problems. As will be shown in the subsequent examples with the J_2 objective function, for that objective function the volume fraction is allowed to vary. This will prove to be key in allowing surface effects to change the optimal design as less material is needed due to the stiffening that is induced by surface effects^{30,94}.

5.7.1.2 Objective function J_2

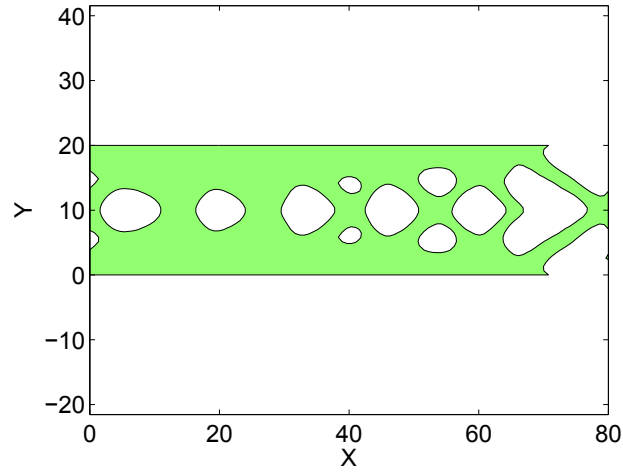
We now consider a different objective function, i.e. the minimization of the least square error objective function, for the cantilever nanobeam.

A cantilever nanobeam of size 40×10 nm is subjected to a point load of 3.6 nN at the free (40,0) nm end. The target displacement at the load location is 16 nm. The optimum topology obtained is shown in Figure 5.6, where the volume ratio of the optimum topology is 0.59 and the stiffness ratio of the 40×10 nm beam is 8.6%.

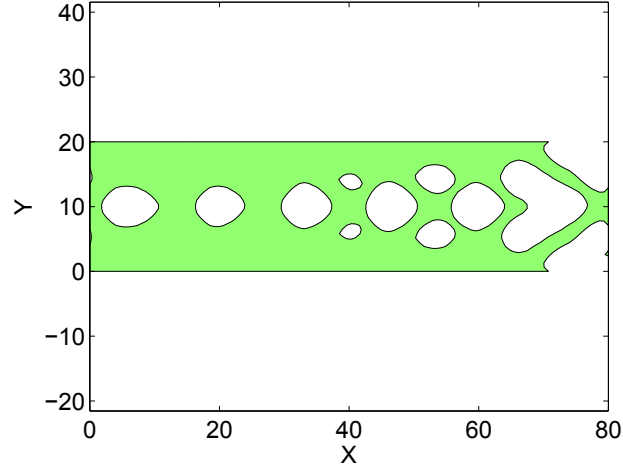
Now the aspect ratio is maintained as 4 and the thickness of the beam is increased. Thus, Figure 5.6 shows the optimum shape obtained for beam of size 320×80 nm, which have stiffness ratios of 1.05% and volume ratio of 0.71.

The optimum topology obtained for the 320×80 nm beam with and without surface effects appear similar, which suggests that for this particular aspect ratio and objective function, surface effects lose their effect once the nanobeam thickness is larger than about 80 nm. However, the 10 nm thick nanobeam have different optimal designs,

5.7 Numerical examples



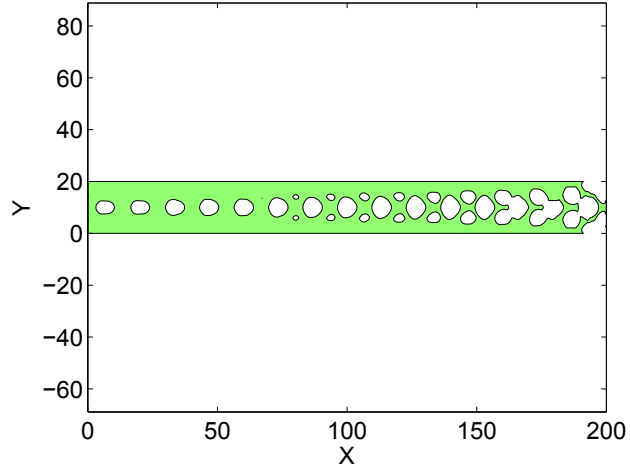
(a)



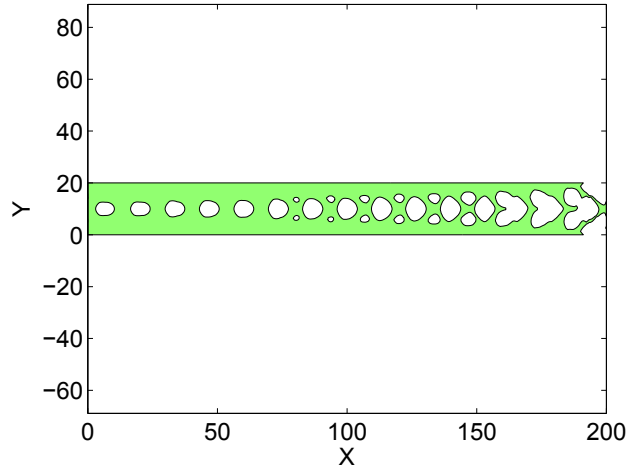
(b)

Figure 5.4: Optimal topology for 80×20 nm cantilever nano beam for objective function J_1 (a) with surface effects , (b) without surface effects, i.e. taking \mathbb{C}_s and τ_s to be zero.

5.7 Numerical examples



(a)



(b)

Figure 5.5: Optimal topology for 200×20 nm cantilever nano beam for objective function J_1 (a) with surface effects, (b) without surface effects, i.e. taking \mathbb{C}_s and τ_s to be zero.

5.7 Numerical examples

which is driven by the fact that the smaller nanostructures are stiffer¹¹ as demonstrated by the stiffness ratios, and thus require less material to conform to the maximum displacement constraint.

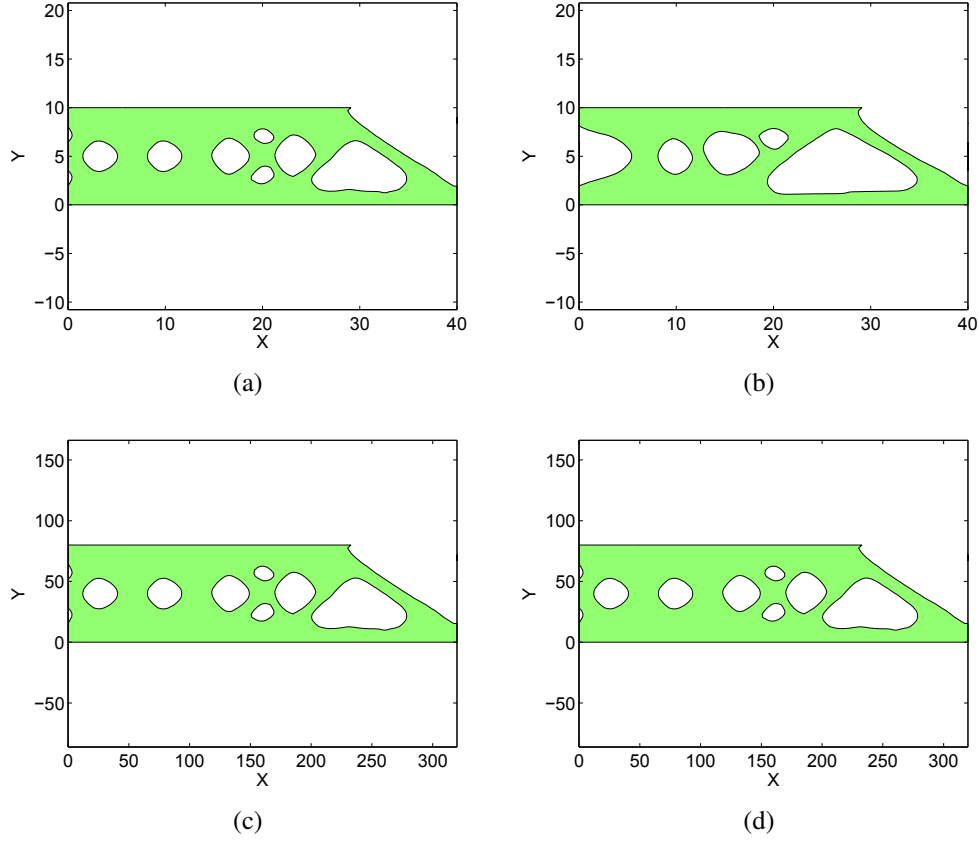


Figure 5.6: The optimal topology obtained for J_2 objective function for 40×10 nm and 320×80 nm cantilever beams without surface effects (a),(c) and with surface effects (b),(d).

The intermediate topologies obtained at various iteration steps are shown in figure 5.7, for the optimization of the 40×10 cantilever nano beam with surface effects. The convergence of the optimization process with decrease in mesh size is shown in figure 5.8. It is evident from the figure that volume ratio of the optimum topology converges for a mesh size smaller than 120×30 (i.e.) $h = \frac{1}{3}$ for the problem solved in this example. The optimum topology obtained for three different mesh sizes 120×30 , 160×40 and 180×45 are shown in the figure 5.9.

5.7 Numerical examples

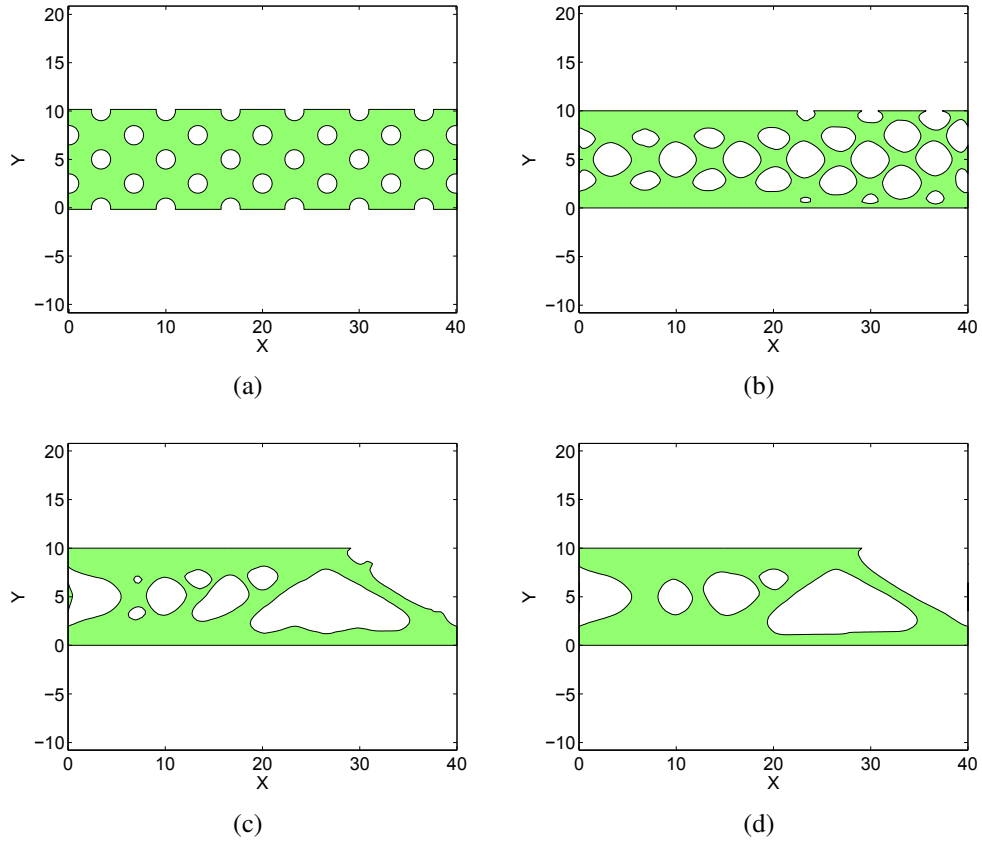


Figure 5.7: Intermediate topologies for optimization of objective function J_2 for 40×10 nm cantilever nanobeam with surface effects at iteration (a)1, (b)15, (c)35, (d)75, (e)200.

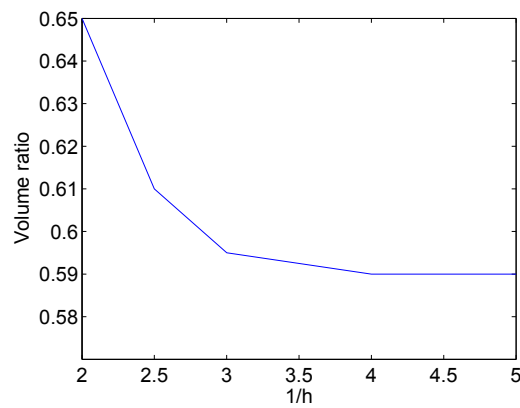


Figure 5.8: Convergence of Volume ratio, for objective function J_2 with iterations

5.7 Numerical examples

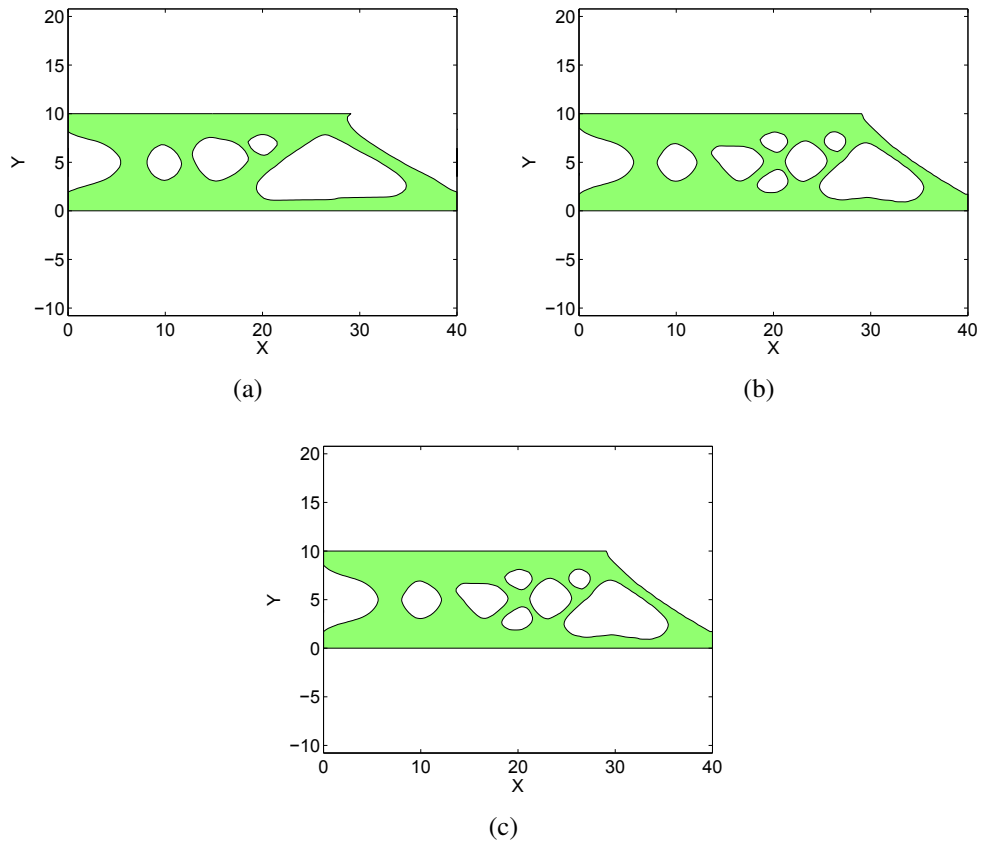


Figure 5.9: Optimal topology for objective function J_2 for 40×10 nm cantilever nanobeam with surface effects for mesh sizes (a) 120×30 (b) 160×40 and (c) 180×45 .

5.7 Numerical examples

5.7.2 Fixed beam

5.7.2.1 Objective function J_1

We now consider a nanobeam with fixed boundary conditions subject to both objective functions. For the minimum potential energy (J_1) constraint, we first consider a fixed nanobeam of dimensions 80×10 nm. A load of 3.6 nN is applied at the midpoint and the volume ratio is constrained to 70%. We exploit the symmetry boundary conditions and thus model only half of the nanobeam. The stiffness ratio of the 80×10 nm nanobeam is found to be 6.9%, and the optimum topology both with and without surface effects is shown in figure 5.10, where again only slight differences are observed for the structure including surface effects.

We also consider larger aspect ratio nanobeam of dimensions 200×10 nm, which leads to a stiffness ratio of 8.4%, while the volume ratio was constrained to be 70%. The topologies obtained do not change for the J_1 objective function with inclusion of surface effects even for an increased nanobeam aspect ratio.

5.7.2.2 Objective function J_2

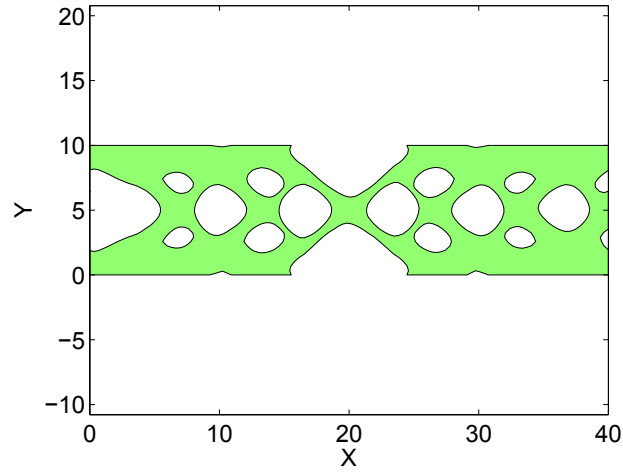
We next consider the optimal design of a fixed nanobeam subjected to the J_2 objective function. The 80×10 nm fixed nanobeam is subjected, as for the J_1 case above, to a point load of 3.6 nN at the midspan where the displacement at the load location is restricted to 4.7 nm, and where again exploiting symmetry only half of the beam is modeled.

The optimum topology obtained is shown in Figure 5.11(a), where the volume ratio of the optimum topology is 0.65. The optimization process is again repeated by increasing the dimension to 160×20 nm in figure 5.11(b), which thus keeps the aspect ratio constant at 8. The volume ratio of 0.71 for the larger nanobeam is higher than that of the 80×10 beam due to reduced stiffness that occurs for larger nanobeam sizes^{101,94}, which enables the nanobeam in figure 5.11(a) to have more voids while still allowing only the maximal displacement at the load location.

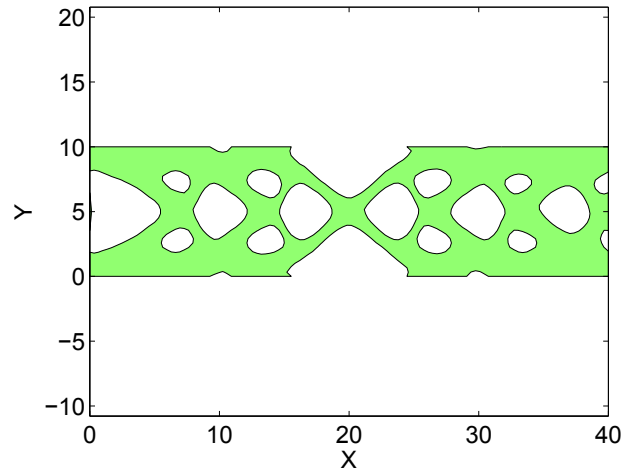
While figure 5.11 shows the optimal design for an aspect ratio of 8, figure 5.12 shows the optimal design when the aspect ratio is increased to 12, for nanobeam thicknesses of 10 and 20 nm, and when the displacement at the load location is restricted to 12 nm. The volume ratio of the optimum topology is 0.65 for the 10 nm thick nanobeam, and 0.7 for the 20 nm thick nanobeam. It is evident from figure 5.12 that increasing the aspect ratio causes the surface effects to play a strong role in influencing the optimal design of the fixed nanobeams.

The stiffness ratios for 80×10 nm and 120×10 nm are 6.9% and 7.9% respectively. The stiffness ratios increase with increase in length of the fixed beam until the beam length reaches 320 nm (at a constant depth of 10 nm) after which they gradually start decreasing. A stiffness ratio of around 8% or more leads to significant difference

5.7 Numerical examples



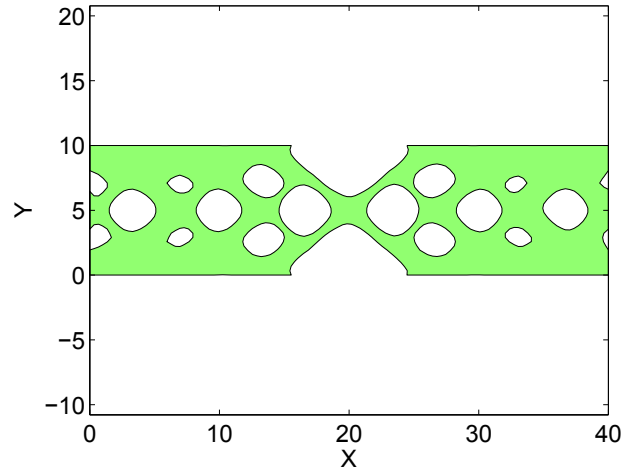
(a)



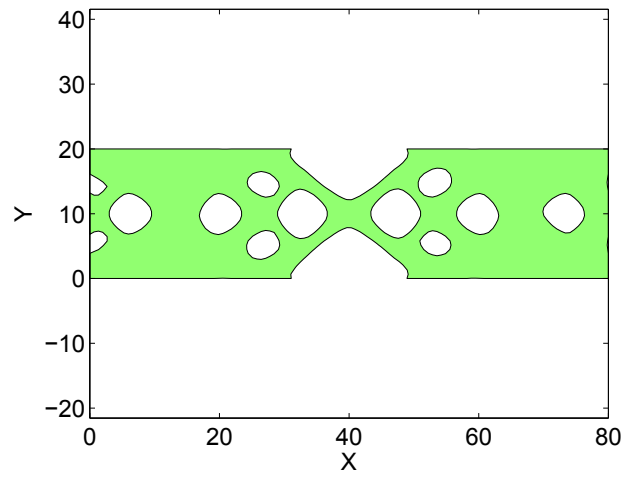
(b)

Figure 5.10: Optimal topology for objective function J_1 for 80×10 nm fixed nanobeam (a) with surface effects, (b) without surface effects, i.e. taking \mathbb{C}_s and τ_s to be zero.

5.7 Numerical examples



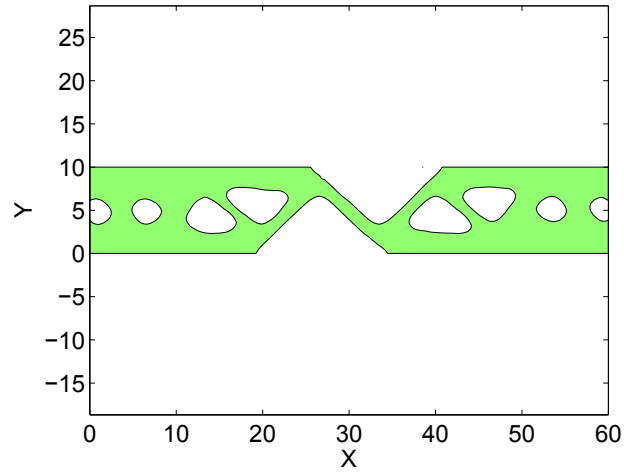
(a)



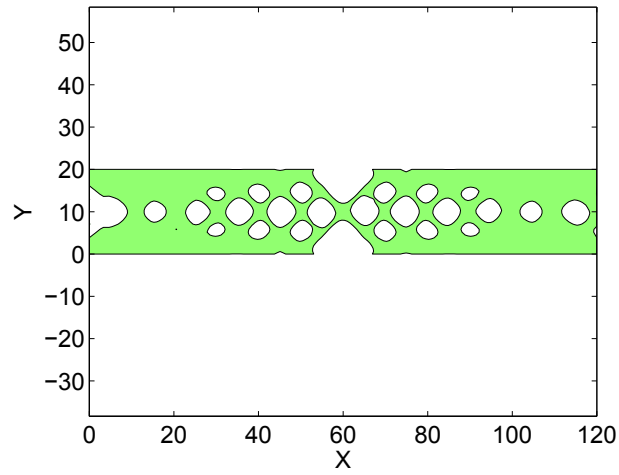
(b)

Figure 5.11: Optimal topology for objective function J_2 for (a) 80×10 nm and (b) 160×20 nm fixed nanobeam.

5.7 Numerical examples



(a)



(b)

Figure 5.12: Optimal topology for objective function J_2 for (a) 120×10 nm and (b) 240×20 nm fixed nanobeam.

5.8 Conclusion

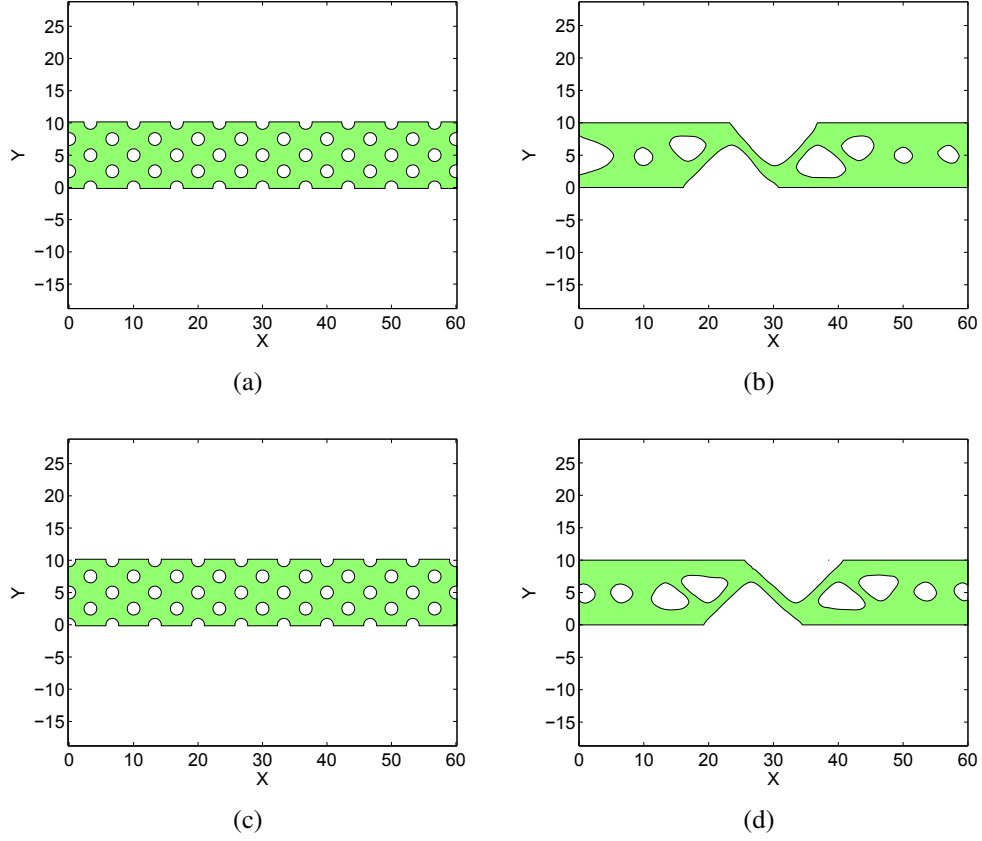


Figure 5.13: Initialization (a),(c) and their corresponding Optimal topologies (b),(d) for objective function J_2 for 120×10 nm

in optimum topology in a fixed nano beam compared to a micro/macro fixed beam subjected to point load at mid span for objective function J_2 .

Different initializations are tried and the optimum topology shown in figure 5.12(a), is the one with least volume ratios among the optimum topologies obtained. The initializations and the corresponding optimum topologies are shown in figure 5.13.

5.8 Conclusion

We have presented a coupled XFEM/level set methodology to perform shape and topology optimization of nanostructures while accounting for nanoscale surface effects. The new formulation was used in conjunction with two objective functions, those of minimum potential energy and least square error to the targeted displacement. While surface effects did not impact the optimized structure for the minimum potential energy

5.8 Conclusion

objective function, substantial size and aspect ratio effects were observed for the least square displacement error objective function. These arise due to the change in volume and stiffness ratios. Thus optimum topologies are influenced by the size-dependent stiffening of nanostructures that occurs with decreasing size as a result of the surface effects. Overall, the methodology presented here should enable new insights and approaches to designing and engineering the behavior and performance of nanoscale structural elements.

Chapter 6

Topology optimization of nano piezoelectric structures

6.1 Contribution of authors

The work presented in this chapter is yet to be submitted to a journal.

- S.S.Nanthakumar
 - Literature review about nano piezoelectricity and energy harvesting
 - Coding of the XFEM-level set algorithm for optimizing nano piezoelectric structures
 - Solving of numerical examples
 - Preparing the manuscript
- Tom Lahmer
 - Improvements in derivation of adjoint problem
- Prof. Harold S Park
 - Discussions in various stages of preparing the manuscript and concepts related to surface effects in nano piezoelectricity.
 - Reviewing the manuscript and making several improvements
- Prof. Timon Rabczuk
 - Discussions to improve the numerical examples

6.2 Introduction

Piezoelectric energy harvesters have garnered significant attention because of their ability to convert ambient mechanical energy into electrical energy^{119,120}. These energy harvesters have been utilized in a wide range of applications, where a review of vibration based energy harvesters is presented in Sodano et al¹²¹.

Because of their wide usage, approaches to design piezoelectric energy harvesters with higher energy conversion efficiency have also been developed. One such approach is using computational topology optimization, where the geometry of the energy harvesters can be tuned to maximize the energy conversion efficiency. Examples of using topology optimization to design superior piezoelectric energy harvesters abound, including maximizing electromechanical conversion for a certain vibration mode¹²², designing a layout comprising the energy harvester as well as the electrical circuit¹²³, maximizing the energy conversion factor in cantilever plate energy harvesters subject to static loads³⁴, performing topology optimization of energy harvesters using as the design variables the densities that define the presence of piezoelectric material in each finite element¹²⁴, topology optimization of cantilevered energy harvesters with the design variable as the geometry of elastic substructure¹²⁵, and designing the optimal configuration of a cantilever and a cylindrical piezoelectric energy harvesters with single and multiple materials³⁵.

However, most piezoelectric energy harvesters have been used in bulk material systems. The exciting possibility of using nanoscale piezoelectric energy harvesters emerged in 2006 with the discovery of piezoelectricity from ZnO nanowires by Wang et al¹⁴. Many researchers have since extended the original seminal work, including the development of self-powered nano generators that can provide gate voltage to effectively control charge transport¹⁴, lateral and vertical integration of ZnO nanowires into arrays that are capable of producing sufficient power to operate real devices¹⁵, and the experimental determination that the piezoelectric coefficient d_{33} of ZnO nanobelt is much larger compared to bulk ZnO through measurements made using piezoresponse force microscope¹²⁶. A recent review on the electromechanical properties and performance of ZnO, and other piezoelectric nanostructures was performed by Espinosa et al¹²⁷.

Along with experimental work, there have been some recent theoretical studies into the surface piezoelectric properties of nanostructures and nanowires. Dai et al.³⁹ highlighted the concept of surface piezoelectricity using combination of theory and atomistic calculations, and then analyzed the (0001) surfaces of ZnO. Other works have also found that ZnO nanostructures exhibit different piezoelectric properties as compared to bulk ZnO^{128,129}, while surface effects the piezoelectricity of ZnO nanowires was studied by Dai et al⁴⁰. Other researchers have developed analytic surface piezoelectric studies, including an explicit formula for the electromechanical coupling coefficient considering surface effects⁴¹ for piezoelectric nanowires, an Euler-Bernoulli

6.3 Governing equations of surface piezoelectricity

beam theory for the vibrational and buckling behavior of piezoelectric nanobeams¹³⁰, and the electroelastic response of thin piezoelectric plates considering surface effects using Kirchhoff plate theory⁴².

The objective of this work is to develop and apply topology optimization techniques to study how surface electromechanical effects impact the energy conversion efficiency of piezoelectric nanostructures. We accomplish this by discretizing the equations of surface piezoelectricity using the extended finite element method (XFEM), and using this numerical formulation to study energy harvesting from piezoelectric nanowires, nanoplates, and piezoelectric layers in energy harvesters accounting for both surface elastic and surface piezoelectric effects.

6.3 Governing equations of surface piezoelectricity

We consider a piezoelectric domain Ω with a material surface Γ . Based on the continuum theory of surface piezoelectricity³⁹, the equilibrium equations are

$$\nabla \cdot \boldsymbol{\sigma} + \mathbf{b} = 0 \quad \text{in } \Omega \quad (6.1)$$

$$\nabla \cdot \mathbf{D} - \mathbf{q} = 0 \quad \text{in } \Omega \quad (6.2)$$

$$\nabla_s \cdot \boldsymbol{\sigma}_s = 0 \quad \text{on } \Gamma \quad (6.3)$$

$$\nabla_s \cdot \mathbf{D}_s = 0 \quad \text{on } \Gamma \quad (6.4)$$

where $\boldsymbol{\sigma}$ and \mathbf{D} are mechanical stress and electric displacement, respectively, while $\boldsymbol{\sigma}_s$ and \mathbf{D}_s are the surface stress and the surface electric displacement, respectively. In the above equation, $\nabla_s \boldsymbol{\sigma}_s = \nabla \boldsymbol{\sigma} : \mathbf{P}$, where \cdot is the double tensor contraction.

The linear piezoelectric constitutive relations for the bulk and surface are,

$$\boldsymbol{\sigma} = \mathbb{C} : \boldsymbol{\varepsilon} - \mathbf{e}^T : \mathbf{E} \quad (6.5)$$

$$\mathbf{D} = \mathbf{e} : \boldsymbol{\varepsilon} + \boldsymbol{\kappa} : \mathbf{E} \quad (6.6)$$

$$\boldsymbol{\sigma}_s = \boldsymbol{\tau}_s + \mathbb{C}^s : \boldsymbol{\varepsilon}_s - \mathbf{e}_s : \mathbf{E}_s \quad (6.7)$$

$$\mathbf{D}_s = \boldsymbol{\omega}_s + \mathbf{e}_s^T : \boldsymbol{\varepsilon}_s + \boldsymbol{\kappa}_s : \mathbf{E}_s \quad (6.8)$$

where \mathbb{C} and \mathbb{C}^s are the fourth-order elastic stiffness tensors associated with the bulk and surface, respectively, while \mathbf{e} and \mathbf{e}_s correspond to the bulk and surface piezoelectric third order tensors, respectively. $\boldsymbol{\tau}_s$ and $\boldsymbol{\omega}_s$ give the residual surface stress and residual surface electric displacement respectively. $\boldsymbol{\varepsilon}$ and \mathbf{E} are the bulk strain tensor and bulk electric field vector while $\boldsymbol{\varepsilon}_s$ and \mathbf{E}_s are their corresponding surface counterparts.

The surface energy density γ is given as,

$$\gamma = \gamma_0 + \boldsymbol{\tau}_s : \boldsymbol{\varepsilon}_s + \boldsymbol{\omega}_s : \mathbf{E}_s + \frac{1}{2} \boldsymbol{\varepsilon}_s : \mathbb{C}^s : \boldsymbol{\varepsilon}_s + \frac{1}{2} \mathbf{E}_s : \boldsymbol{\kappa}_s : \mathbf{E}_s + \mathbf{E}_s : \mathbf{e}_s : \boldsymbol{\varepsilon}_s \quad (6.9)$$

6.3 Governing equations of surface piezoelectricity

Having defined the constitutive and field equations, we derive the weak form of the boundary value problem based on the principle of stationary potential energy. The total potential energy Π of the system is given by

$$\Pi = \Pi_{bulk} + \Pi_s - \Pi_{ext} \quad (6.10)$$

where Π_{bulk} , Π_s and Π_{ext} represent the bulk internal energy, surface internal energy and the work of external forces, respectively. The stationary condition of 6.10 is given by

$$D_{\delta \mathbf{u}} \Pi = 0 \quad (6.11)$$

where $D_{\delta \mathbf{u}} \Pi$ is the directional derivative (or Gâteaux derivative) of the functional Π in the direction $\delta \mathbf{u}$. Applying the stationary condition, the weak formulation of the governing equations is as follows,

$$\begin{aligned} & \int_{\Omega} \boldsymbol{\varepsilon}(\mathbf{u})^T : \mathbb{C} : \boldsymbol{\varepsilon}(\delta \mathbf{u}) d\Omega - \int_{\Omega} \boldsymbol{\varepsilon}(\mathbf{u})^T : \mathbf{e}^T : \mathbf{E}(\delta \boldsymbol{\phi}) d\Omega \\ & - \int_{\Omega} \mathbf{E}(\boldsymbol{\phi})^T : \mathbf{e} : \boldsymbol{\varepsilon}(\delta \mathbf{u}) d\Omega - \int_{\Omega} \mathbf{E}(\boldsymbol{\phi})^T : \boldsymbol{\kappa} : \mathbf{E}(\delta \boldsymbol{\phi}) d\Omega \\ & + \int_{\Gamma} \boldsymbol{\varepsilon}_s(\mathbf{u})^T : \mathbb{C}_s : \boldsymbol{\varepsilon}_s(\delta \mathbf{u}) d\Gamma - \int_{\Gamma} \boldsymbol{\varepsilon}_s(\mathbf{u})^T : \mathbf{e}_s^T : \mathbf{E}_s(\delta \boldsymbol{\phi}) d\Gamma \\ & - \int_{\Gamma} \mathbf{E}_s(\boldsymbol{\phi})^T : \mathbf{e}_s : \boldsymbol{\varepsilon}_s(\delta \mathbf{u}) d\Gamma - \int_{\Gamma} \mathbf{E}_s(\boldsymbol{\phi})^T : \boldsymbol{\kappa}_s : \mathbf{E}_s(\delta \boldsymbol{\phi}) d\Gamma \\ & = - \int_{\Gamma} \boldsymbol{\tau}_s : \boldsymbol{\varepsilon}_s(\delta \mathbf{u}) d\Gamma - \int_{\Gamma} \boldsymbol{\omega}_s : \mathbf{E}_s(\delta \boldsymbol{\phi}) d\Gamma + \int_{\Gamma_N} \delta \mathbf{u} \cdot \bar{\mathbf{t}} d\Gamma \\ & + \int_{\Omega} \delta \mathbf{u} \cdot \mathbf{b} d\Omega - \int_{\Omega} \delta \boldsymbol{\phi} \cdot \mathbf{q} d\Omega \end{aligned} \quad (6.12)$$

This weak formulation can be written in simplified form as,

$$a(\mathbf{u}, \boldsymbol{\phi}, \delta \mathbf{u}, \delta \boldsymbol{\phi}) + a_s(\mathbf{u}, \boldsymbol{\phi}, \delta \mathbf{u}, \delta \boldsymbol{\phi}) = -l_s(\delta \mathbf{u}, \delta \boldsymbol{\phi}) + l(\delta \mathbf{u}, \delta \boldsymbol{\phi}) \quad (6.13)$$

The expressions for an element using the finite element (FE) approximation can be written as follows,

$$\begin{aligned} & d^e(\mathbf{u}, \boldsymbol{\phi}, \delta \mathbf{u}, \delta \boldsymbol{\phi}) \\ & = \delta \mathbf{u}^{eT} \left(\int_{\Omega^e} \mathbf{B}_u^T \{ \mathbb{C} \} \mathbf{B}_u d\Omega \right) \mathbf{u}^e + \mathbf{u}^{eT} \left(\int_{\Omega^e} \mathbf{B}_u^T \{ \mathbf{e} \}^T \mathbf{B}_{\phi} d\Omega \right) \delta \boldsymbol{\phi}^e \\ & + \boldsymbol{\phi}^{eT} \left(\int_{\Omega^e} \mathbf{B}_{\phi}^T \{ \mathbf{e} \} \mathbf{B}_u d\Omega \right) \delta \mathbf{u}^e - \boldsymbol{\phi}^{eT} \left(\int_{\Omega^e} \mathbf{B}_{\phi}^T \{ \boldsymbol{\kappa} \} \mathbf{B}_{\phi} d\Omega \right) \delta \boldsymbol{\phi}^e \end{aligned} \quad (6.14)$$

6.4 XFEM formulation for nano-piezoelectricity

$$\begin{aligned}
& a_s^e(\mathbf{u}, \boldsymbol{\phi}, \delta \mathbf{u}, \delta \boldsymbol{\phi}) \\
&= \int_{\Gamma} (\mathbf{P}\boldsymbol{\varepsilon}(\mathbf{u})\mathbf{P}) : \{\mathbb{C}_s\} : (\mathbf{P}\boldsymbol{\varepsilon}(\delta \mathbf{u})\mathbf{P}) d\Gamma + \int_{\Gamma} (\mathbf{P}\boldsymbol{\varepsilon}(\mathbf{u})\mathbf{P}) : \{\mathbf{e}_s\} : (\mathbf{P}_\phi \mathbf{E}(\delta \boldsymbol{\phi})) d\Gamma \\
&+ \int_{\Gamma} (\mathbf{P}_\phi \mathbf{E}(\boldsymbol{\phi})) : \{\mathbf{e}_s\} : (\mathbf{P}\boldsymbol{\varepsilon}(\delta \mathbf{u})\mathbf{P}) d\Gamma - \int_{\Gamma} (\mathbf{P}_\phi \mathbf{E}(\boldsymbol{\phi})) : \{\boldsymbol{\kappa}_s\} : (\mathbf{P}_\phi \mathbf{E}(\delta \boldsymbol{\phi})) d\Gamma \\
&= \mathbf{u}^{eT} \left(\int_{\Gamma} \mathbf{B}_u^T \mathbf{M}_p^T \{\mathbb{C}_s\} \mathbf{M}_p \mathbf{B}_u d\Gamma \right) \delta \mathbf{u}^e - \mathbf{u}^{eT} \left(\int_{\Gamma} \mathbf{B}_u^T \mathbf{M}_p^T \{\mathbf{e}_s\}^T \mathbf{P}_\phi \mathbf{B}_\phi d\Gamma \right) \delta \boldsymbol{\phi}^e \\
&- \boldsymbol{\phi}^{eT} \left(\int_{\Gamma} \mathbf{B}_\phi^T \mathbf{P}_\phi^T \{\mathbf{e}_s\} \mathbf{M}_p \mathbf{B}_u d\Gamma \right) \delta \mathbf{u}^e - \boldsymbol{\phi}^{eT} \left(\int_{\Gamma} \mathbf{B}_\phi^T \mathbf{P}_\phi^T \{\boldsymbol{\kappa}_s\} \mathbf{P}_\phi \mathbf{B}_\phi d\Gamma \right) \delta \boldsymbol{\phi}^e
\end{aligned} \tag{6.15}$$

$$\begin{aligned}
l_s^e(\delta \mathbf{u}, \delta \boldsymbol{\phi}) &= \int_{\Gamma} \boldsymbol{\tau}_s : (\mathbf{P}\boldsymbol{\varepsilon}(\delta \mathbf{u})\mathbf{P}) d\Gamma + \int_{\Gamma} \boldsymbol{\omega}_s : (\mathbf{P}_\phi \mathbf{E}(\delta \boldsymbol{\phi})) d\Gamma \\
&= \delta \mathbf{u}^{eT} \int_{\Gamma} \mathbf{B}_u^T \mathbf{M}_p^T \boldsymbol{\tau}_s d\Gamma + \delta \boldsymbol{\phi}^{eT} \int_{\Gamma} \mathbf{B}_\phi^T \mathbf{P}_\phi^T \boldsymbol{\omega}_s d\Gamma
\end{aligned} \tag{6.16}$$

$$l^e(\delta \mathbf{u}, \delta \boldsymbol{\phi}) = \delta \mathbf{u}^{eT} \left(\int_{\Gamma_N} \mathbf{N}^T \bar{\mathbf{t}} d\Gamma + \int_{\Omega} \mathbf{N}^T \mathbf{b} d\Omega \right) - \delta \boldsymbol{\phi}^{eT} \int_{\Omega} \mathbf{N}^T \mathbf{q} d\Omega \tag{6.17}$$

where \mathbf{B}_u and \mathbf{B}_ϕ are strain-displacement and electric field-potential matrix respectively. The projection tensor \mathbf{P} and transformation matrix \mathbf{M}_p are as defined in literature^{131,94}.

6.4 XFEM formulation for nano-piezoelectricity

In this work, we utilized the extended finite element method (XFEM), to discretize the finite element equations given previously in Eqs. (6.14),(6.15),(6.16),(6.17) and the weak form (6.12). We utilize XFEM, rather than the standard FEM in the present work due to its ability to represent evolving interfaces and discontinuities, which is essential in the topology optimization process.

The displacement field, u^h and electric potential field, ϕ^h for a piezoelectric material in the XFEM formulation are expressed as:

$$u^h(\mathbf{X}) = \sum_{i \in I} N_i(\mathbf{X}) \mathbf{u}_i + \sum_{N=1}^{n_c} \sum_{l \in L} N_l(\mathbf{X}) \boldsymbol{\alpha}_l^{(N)} F_l^{(N)} \tag{6.18}$$

$$\phi^h(\mathbf{X}) = \sum_{i \in I} N_i(\mathbf{X}) \phi_i + \sum_{N=1}^{n_c} \sum_{l \in L} N_l(\mathbf{X}) \alpha_l^{(N)} F_l^{(N)} \tag{6.19}$$

6.5 Topology optimization of piezoelectric nano energy harvesters

where \mathbf{a}_I and $\boldsymbol{\alpha}_I$ are the additional degrees of freedom that account for the jump in displacement and electric potential field, respectively, n_c denotes the number of inclusion interfaces, J is the set of all nodes whose support is cut by the material interface. $F^{(N)}$ in equations (6.18) and (6.19) is absolute signed distance function values from the interfaces. Substituting the test and trial functions (6.18) and (6.19), into the weak form (6.13) yields the final discrete system of equations:

$$(\mathbf{K}_{uu}^b + \mathbf{K}_{uu}^s)\mathbf{u}^e + (\mathbf{K}_{\phi u}^b + \mathbf{K}_{\phi u}^s)\boldsymbol{\phi}^e = -(\mathbf{f}_u^s + \mathbf{f}_u^{ext}) \quad (6.20)$$

$$(\mathbf{K}_{u\phi}^b + \mathbf{K}_{u\phi}^s)\mathbf{u}^e + (\mathbf{K}_{\phi\phi}^b + \mathbf{K}_{\phi\phi}^s)\boldsymbol{\phi}^e = -(\mathbf{g}_u^s + \mathbf{g}_u^{ext}) \quad (6.21)$$

where the specific form of the bulk and surface stiffness matrices can be found in appendix B.2. The piezoelectric energy harvesters we consider are thin flexible structures, and so a Kirchoff plate theory adopted in Erturk et al.³³ is employed in this work. Details are given in the appendix B.3.

6.5 Topology optimization of piezoelectric nano energy harvesters

6.5.1 Objective function

A common objective function in topology optimization of piezoelectric energy harvesters is the maximization of energy conversion. The electromechanical coupling coefficient (EMCC), k is defined as¹³²,

$$k^2 = \frac{\Pi_m^2}{\Pi_e \Pi_d} \quad (6.22)$$

where Π_m is elasto-dielectric energy, Π_e and Π_d are the stored elastic and dielectric energy respectively.

$$\Pi_m = \int_{\Omega} \boldsymbol{\varepsilon}(u)^T \mathbf{e}^T \mathbf{E}(\phi) d\Omega \quad (6.23)$$

$$\Pi_e = \int_{\Omega} \boldsymbol{\varepsilon}(u)^T \mathbb{C} \boldsymbol{\varepsilon}(u) d\Omega \quad (6.24)$$

$$\Pi_d = \int_{\Omega} \mathbf{E}(\phi)^T \boldsymbol{\kappa} \mathbf{E}(\phi) d\Omega \quad (6.25)$$

The energy harvesting device is assumed to be subjected only to mechanical static load and so the EMCC may be rewritten as³⁵,

$$k^2 = \frac{\Pi_d}{\Pi_e} \quad (6.26)$$

6.5 Topology optimization of piezoelectric nano energy harvesters

The higher the coupling coefficient higher the energy conversion and thereby better the performance of the energy harvesting device. The shape and topology of the piezoelectric layer is modified such as maximum energy conversion is obtained. The geometry of the piezoelectric layer is defined by the level set function. So the design variable in this optimization problem is the level set function, Φ . The objective function is ,

$$\text{Minimize } J(\Phi) = \frac{1}{k^2} = \frac{\Pi_e}{\Pi_d} \quad (6.27)$$

$$\text{Subject to } \int_{\Omega} d\Omega - \bar{V} = 0 \quad (6.28)$$

$$a(\mathbf{u}, \phi, \delta\mathbf{u}, \delta\phi) + a_s(\mathbf{u}, \phi, \delta\mathbf{u}, \delta\phi) = -l_s(\delta\mathbf{u}, \delta\phi) + l(\delta\mathbf{u}, \delta\phi) \quad (6.29)$$

The optimum configuration is obtained by using the level set based topology optimization method described in the following section.

6.5.2 Level set method and sensitivity analysis

In Osher et al.¹⁰⁷ the level set method (LSM) is proposed, which is a numerical technique to track moving interfaces and shapes. The LSM has been used in structural sensitivity, analysis, i.e. by Allaire et al²⁶ and Wang et al.¹³³. In topology optimization, the LSM is valuable as it enables several initial defined voids to merge, move and change shapes leading to a modified topology of the structure that minimizes the objective function. In LSM, optimal structures obtained are free from grayscale, since the structural boundaries are represented as the iso-surface of level set function. Level set function is dynamically updated at each time step by solving Hamilton-Jacobi partial differential equation to minimize the objective function.

$$\frac{\partial \Phi}{\partial t} + V_n |\nabla \Phi| = 0 \quad (6.30)$$

The above H-J equation is solved to obtain the updated level set function and thereby the updated topology of the design structure. More details on level set based TO for nano structures may be found in Nanthakumar et al¹³¹. The velocity to update level set function, V_n is obtained by performing sensitivity analysis as discussed subsequently. The material derivative approach and the related lemmas presented in Choi et al.¹¹² are adopted to determine the material time derivative of the objective function (see B.1 for details).

$$j = \frac{\dot{\Pi}_e(u, u)}{\Pi_d(\phi, \phi)} - \frac{\Pi_e(u, u) \dot{\Pi}_d(\phi, \phi)}{\Pi_d(\phi, \phi)^2} \quad (6.31)$$

$$= C_1 \dot{\Pi}_e(u, u) + C_2 \dot{\Pi}_d(\phi, \phi) \quad (6.32)$$

6.5 Topology optimization of piezoelectric nano energy harvesters

where,

$$\begin{aligned}\dot{\Pi}_e(u, u) &= \int_{\Omega} 2 \boldsymbol{\varepsilon}(u')^T : \mathbb{C}^{bulk} : \boldsymbol{\varepsilon}(u) d\Omega + \int_{\Gamma} \boldsymbol{\varepsilon}(u)^T : \mathbb{C}^{bulk} : \boldsymbol{\varepsilon}(u) V_n d\Gamma \\ &\quad + \int_{\Gamma} 2 \boldsymbol{\varepsilon}_s(u')^T : \mathbb{C}^s : \boldsymbol{\varepsilon}_s(u) d\Gamma \\ &\quad + \int_{\Gamma} [\nabla(\boldsymbol{\varepsilon}_s(u)^T : \mathbb{C}^s : \boldsymbol{\varepsilon}_s(u)) \cdot \mathbf{n} + (\boldsymbol{\varepsilon}_s(u)^T : \mathbb{C}^s : \boldsymbol{\varepsilon}_s(u)) \eta] V_n d\Gamma\end{aligned}\quad (6.33)$$

$$\begin{aligned}\dot{\Pi}_d(\phi, \phi) &= \int_{\Omega} 2 \mathbf{E}(\phi')^T : \boldsymbol{\kappa}^{bulk} : \mathbf{E}(\phi) d\Omega + \int_{\Gamma} \mathbf{E}(\phi)^T : \boldsymbol{\kappa}^{bulk} : \mathbf{E}(\phi) V_n d\Gamma \\ &\quad + \int_{\Gamma} 2 \mathbf{E}_s(\phi')^T : \boldsymbol{\kappa}^s : \mathbf{E}_s(\phi) d\Gamma \\ &\quad + \int_{\Gamma} [\nabla(\mathbf{E}(\phi)^T : \boldsymbol{\kappa}^s : \mathbf{E}_s(\phi)) \cdot \mathbf{n} + (\mathbf{E}_s(\phi)^T : \boldsymbol{\kappa}^s : \mathbf{E}_s(\phi)) \eta] V_n d\Gamma\end{aligned}\quad (6.34)$$

$$C_1 = \frac{1}{\Pi_d(\phi, \phi)} \quad (6.35)$$

$$C_2 = -\frac{\Pi_e(u, u)}{\Pi_d(\phi, \phi)^2} \quad (6.36)$$

The augmented Lagrangian, L defining the unconstrained optimization problem is

$$L = J(u, \phi, \Omega) + \chi(\Omega) \quad (6.37)$$

The shape derivative of augmented Lagrangian L is defined as

$$L' = J'(u, \phi, \Omega) + \chi'(\Omega) \quad (6.38)$$

$$J' = \int_{\Gamma} G \cdot V_n d\Gamma \quad (6.39)$$

$$\begin{aligned}G &= \int_{\Omega} C_1 \boldsymbol{\varepsilon}(u')^T : \mathbb{C}^{bulk} : \boldsymbol{\varepsilon}(u) d\Omega + \int_{\Gamma} C_1 \boldsymbol{\varepsilon}_s(u)^T : \mathbb{C}^s : \boldsymbol{\varepsilon}_s(u) d\Gamma \\ &\quad + \int_{\Omega} C_2 \mathbf{E}(\phi')^T : \boldsymbol{\kappa}^{bulk} : \mathbf{E}(\phi) d\Omega + \int_{\Gamma} C_2 \mathbf{E}_s(\phi)^T : \boldsymbol{\kappa}^s : \mathbf{E}_s(\phi) d\Gamma \\ &\quad - \int_{\Gamma} \boldsymbol{\varepsilon}_s(w) \boldsymbol{\tau}_s \cdot \boldsymbol{\eta} d\Gamma - \int_{\Gamma} \boldsymbol{\varepsilon}_s(u)^T : \mathbb{C}^s : \boldsymbol{\varepsilon}_s(w) \cdot \boldsymbol{\eta} d\Gamma \\ &\quad + \int_{\Gamma} \boldsymbol{\varepsilon}_s(u)^T : \mathbf{e}^{sT} : \mathbf{E}_s(\boldsymbol{\psi}) \cdot \boldsymbol{\eta} d\Gamma + \int_{\Gamma} \mathbf{E}_s(\phi)^T : \mathbf{e}^s : \boldsymbol{\varepsilon}_s(w) \boldsymbol{\eta} d\Gamma \\ &\quad + \int_{\Gamma} \mathbf{E}_s(\phi)^T : \boldsymbol{\kappa}^s : \mathbf{E}_s(\boldsymbol{\psi}) \boldsymbol{\eta} d\Gamma - \int_{\Omega} \boldsymbol{\varepsilon}(u)^T : \mathbb{C}^{bulk} : \boldsymbol{\varepsilon}(w) d\Omega \\ &\quad + \int_{\Omega} \boldsymbol{\varepsilon}(u)^T : \mathbf{e}^{bulkT} : \mathbf{E}(\boldsymbol{\psi}) d\Gamma + \int_{\Omega} \mathbf{E}(\phi)^T : \mathbf{e}^{bulk} : \boldsymbol{\varepsilon}(w) d\Gamma \\ &\quad + \int_{\Omega} \mathbf{E}(\phi)^T : \boldsymbol{\kappa}^{bulk} : \mathbf{E}(\boldsymbol{\psi}) d\Omega\end{aligned}\quad (6.40)$$

6.6 Numerical Examples

Table 6.1: Electromechanical properties of bulk ZnO
Elastic Constants Piezoelectric constants Dielectric constants

$C_{11}=206 \text{ GPa}$	$e_{31}=-0.58 \text{ C/m}^2$	$\kappa_{11}=8.11 \text{ C/(GVm)}$
$C_{12}=117 \text{ GPa}$	$e_{33}=1.55 \text{ C/m}^2$	$\kappa_{33}=11.2 \text{ C/(GVm)}$
$C_{13}=118 \text{ GPa}$	$e_{15}=0.48 \text{ C/m}^2$	
$C_{33}=211 \text{ GPa}$		
$C_{44}=44.3 \text{ GPa}$		

Table 6.2: Electromechanical properties of surface ZnO
Elastic Constants Piezoelectric constants

$C_{11}^s=44.2 \text{ N/m}$	$e_{31}^s=0.216 \text{ C/m}$
$C_{12}^s=14.2 \text{ N/m}$	$e_{33}^s=0.451 \text{ C/m}$
$C_{13}^s=14.2 \text{ N/m}$	$e_{15}^s=0.253 \text{ C/m}$
$C_{33}^s=35 \text{ N/m}$	
$C_{44}^s=11.7 \text{ N/m}$	

Based on steepest descent direction

$$G = -V_n$$

$$J' = - \int_{\Gamma} V_n^2 d\Gamma \leq 0 \quad (6.41)$$

In equation A.9, u and ϕ are the actual variables while w and ψ are the adjoint variables.

6.6 Numerical Examples

In this section we study the energy harvesting capability of a piezoelectric nanobeam, nanoplate and a cantilever energy harvester with nanoscale piezoelectric layers. We also perform topology optimization of these piezoelectric structures. We consider examples both with and without surface piezoelectricity to examine the effects that surface effects have on the energy harvesting ability. In all examples, ZnO is the piezoelectric material of choice, where the surface elastic and piezoelectric properties of ZnO are shown in tables 6.1 and 6.2³⁷.

6.6 Numerical Examples

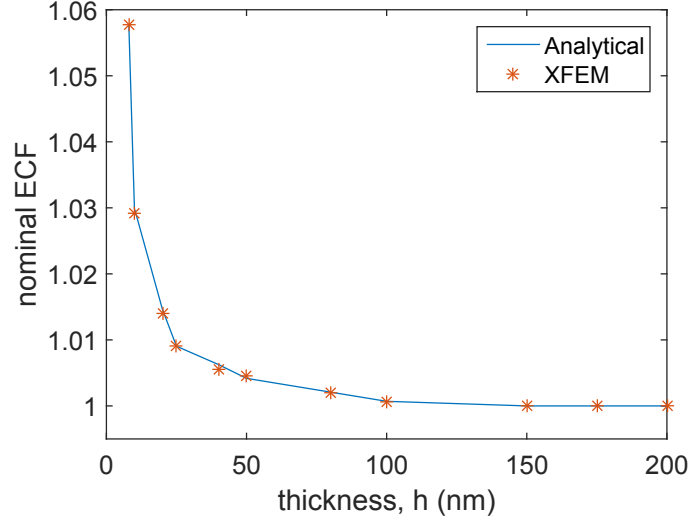


Figure 6.1: Variation of nominal energy conversion factor with nanobeam depth, with the beam aspect ratio constant at 20.

6.6.1 Piezoelectric nano beam

6.6.1.1 Finite Element Model Validation

In our first example, we consider a two-dimensional cantilever beam of dimension 200×10 nm subject to a constant mechanical load at the free end. The beam is meshed with 200×10 , 4-node bilinear quadrilateral finite elements, and the poling direction is vertically upwards along the thickness direction. The bulk energy conversion factor (ECF_b) for this case can be analytically obtained by the following expression⁴¹,

$$ECF_b = \frac{e_{31}^2}{(C_{11}\kappa_{33} + e_{31}^2)} \quad (6.42)$$

The expression including surface effects can be obtained based on the derivation given in Jiang et al.⁴¹ for this example problem as,

$$ECF_s = \frac{h e_{31}^2 + 2 e_{31} e_{31}^s}{h(C_{11}\kappa_{33} + e_{31}^2) + 2(C_{11}^s\kappa_{33} + e_{31} e_{31}^s)} \quad (6.43)$$

Figure 6.1 shows the variation of ECF with increasing nanobeam depth for a constant aspect ratio of 20, where the y-axis of the figure plots the nominal ECF (i.e.) the value ECF_s/ECF_b . This aspect ratio is chosen as it is clear in plane strain conditions from Eq. 6.43 that the ECF is dependent only on the nanobeam thickness. As expected the surface elastic and piezoelectric effects lose their significance as the depth increases. The plot shows good agreement between XFEM and the analytical results.

6.6 Numerical Examples

size	nominal EMCC ($C^s, e^s \neq 0$)	nominal EMCC ($e^s \neq 0$)
40×10	1.16	
80×20	1.034	
160×40	0.98	1.05

Table 6.3: Nominal EMCC of optimized piezoelectric nano beam under open circuit condition

size	nominal EMCC ($C^s, e^s \neq 0$)
40×10	2.4
80×20	2.2
160×40	2.1

Table 6.4: Nominal EMCC of optimized piezoelectric nano beam under closed circuit condition

6.6.1.2 Optimization of Piezoelectric Nanobeam

We now perform topology optimization of the two-dimensional nanobeams under both open and closed circuit boundary conditions to examine not only the enhancements in ECF that are possible, but also to delineate the relative effects of surface piezoelectricity and elasticity on the ECF. To do so, we again subject the cantilever nanobeam to a mechanical point load acting vertically downwards at its free end, while the nanobeam is poled along the thickness direction. The nanobeam is placed over a substrate made of material with a Young's modulus of $E=150$ GPa, where the substrate dimensions are the same as the nanobeam, though surface effects on the substrate are neglected. Electrodes are placed above and below the nanobeam; open circuit conditions are achieved by grounding the bottom electrode while the top electrode is free, while in closed circuit both the top and bottom electrodes are grounded.

Tables 6.3 and 6.4 show the various sizes considered for both open and closed circuit electrical boundary conditions. Different thicknesses were chosen to illustrate the size-dependent nature of the surface effects. There are several noticeable and interesting trends, which we now discuss.

The first effect is that, for both open and closed circuit, the nominal EMCC decreases with increasing nanobeam thickness. In fact, for some cases the optimized EMCC is actually less than one, which means that the optimized topology results in a smaller increase in energy conversion than would be obtained by just keeping the pre-optimized, solid beam.

When voids are created in the material through the topology optimization process, both surface piezoelectric and surface elastic effects compete to drive the trend in energy conversion, as illustrated in Table 6.3 for the open circuit boundary condition. To delineate these effects, we considered two separate cases, first including both sur-

6.6 Numerical Examples

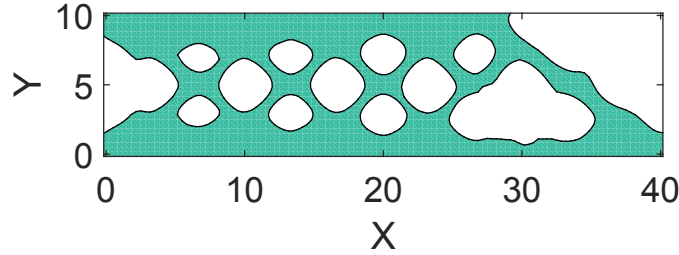


Figure 6.2: Optimal topology for maximizing ECF of a piezoelectric nano cantilever beam, 40×10 nm.

face piezoelectric and elastic effects (C^s , $e^s \neq 0$), and then considering only surface piezoelectric effects ($e^s \neq 0$). As shown in Table 6.3, when surface elastic constants are ignored, the nominal EMCC increases. This demonstrates that the surface elastic effects in ZnO act to reduce the energy conversion ability of the nanobeams.

The second effect is that the energy conversion is substantially higher for the closed circuit boundary condition, which corresponds to the flow of current across the nanobeam cross section, as compared to the open circuit boundary condition, which corresponds to a build up of voltage across the nanobeam cross section.

A cantilever nano beam (40×10 nm) made of Zinc Oxide is optimized to maximise energy conversion. The beam is meshed with 120×30 Q4 elements. The nominal EMCC (ratio of EMCC with and without including surface effects) of the cantilever nano beam before optimization is 1.05 for open circuit and 1.16 for closed circuit.

The optimised topology of 40×10 nm beam with surface effects is shown in figure 6.2. Under open circuit condition, the nominal EMCC of the optimised topology of the cantilever nano beam 40×10 nm (aspect ratio = 4) is 1.16. The size of the nano piezoelectric beam is increased to 80×20 nm, 160×40 nm with the same aspect ratio of 4. The nominal EMCC obtained for 80×20 nm and 160×40 nm are 1.04 and 0.98 respectively. The nominal EMCC of 160×40 nm, when surface elasticity is excluded and only when surface piezoelectricity is included, is 1.05.

Under closed circuit condition, the nominal EMCC of the optimised topology of the cantilever nano beam 40×10 nm (aspect ratio = 4) is 2.4. The size of the nano

6.6 Numerical Examples

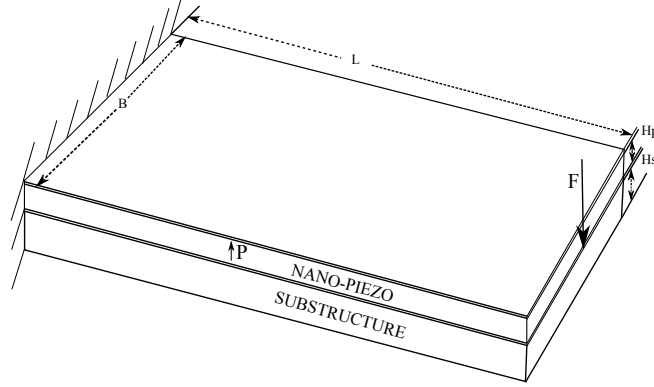


Figure 6.3: A cantilever energy harvester with piezoelectric nano layer subjected to point load, F at free end.

piezoelectric beam is increased to 80×20 nm, 160×40 nm with the same aspect ratio of 4. The nominal EMCC obtained for 80×20 nm and 160×40 nm are 2.2 and 2.1 respectively.

6.6.2 Three-Dimensional Piezoelectric Nanoplate

In this section, we examine the piezoelectric behavior of a three-dimensional nanoplate on substrate, as illustrated in Figure 6.3. We refer to this system as an energy harvesting device (EHD) in the following discussion. This particular geometry was chosen because while the two-dimensional nanobeam geometry studied previously is simple, manufacturing the complex shapes that emerge from the topology optimization may pose significant challenges, particularly with a beam thickness of around 10 nm. In this example, the in-plane dimensions of the nano plate are kept fixed with dimensions in the hundreds of nanometers. Thus, the holes that are formed through the thickness, which have feature sizes larger than tens of nanometers, could likely be lithographically manufactured using technology that is available today.

The EHD is comprised of a substrate and a piezoelectric layer. The substrate is assumed to be made of aluminum, and the thickness of the substrate, H_s and the piezoelectric layer, H_p are taken to be 125 nm and 100 nm respectively. The length and width of this EHD is assumed to be 4×2 μm . Two electrical boundary conditions are considered, with electrodes on the top of the nanoplate and underneath the substrate. In boundary condition A, both the top and bottom electrodes are grounded. In boundary condition B, only the bottom electrode is grounded. The nominal EMCC under boundary condition A and B is 1.03 and 1.01 respectively. The nominal EMCC is close to one because the thickness of the piezo layer large enough such that the surface effects

6.6 Numerical Examples

have a minimal effect on the EMCC.

We then optimize the geometry of the piezoelectric nanoplate to maximize the EMCC of the EHD, while the geometry and shape of the substrate remains unchanged. The optimized topology of the 100 nm thick piezoelectric nanoplate is shown in figure 6.4(a). The nominal EMCC of this optimized EHD is 1.32 and 1.3 under boundary conditions A and B respectively.

To examine size effects on the EMCC and optimized topology, we then studied the effect of replacing the 100 nm nanoplate with a 10 nm thick nanoplate, with the optimized topology for the 10 nm nanoplate shown in Figure 6.4(b). The nominal EMCC of the optimized EHD for 10 nm thick piezoelectric layer is 1.7 and 1.44 under boundary conditions A and B respectively.

Topology optimization and surface effects improve the efficiency of the EHDs if the thickness of the attached piezoelectric layer is reduced below about 100 nm. Manufacturing such optimum topologies is practically possible as the nano thick cross section remains uniform throughout. The optimized topology for EHD with 10 nm nano plate has more material removal compared to EHD with 100 nm nano plate and the EHD with 10 nm nano plate exhibits increased energy conversion efficiency comparatively. Figure 6.5 shows the variation of nominal EMCC with thickness of piezo layer under open and closed circuit conditions.

6.6.3 Piezoelectric nano bimorph

Our final example considers a nanoscale bimorph, which as shown in Figure 6.6 is comprised of two cantilever piezoelectric nanoplates each of dimension $600 \times 300 \times 10$ nm placed one over another subjected to point load at the free end. Surface elasticity and surface piezoelectricity are accounted for at the top and bottom surfaces of the bimorph, while interface effects between the two nanoplates are neglected. Three electrodes in total, which are placed at the top, middle and bottom of the bimorph, are present. Under open circuit conditions, the electrode at the middle of the bimorph is grounded, while under closed circuit conditions, all the electrodes are grounded.

An analytic expression for the deflection of a piezoelectric nanoplate including surface piezoelectric and elastic effects based on Kirchhoff plate theory was recently given by Jiang et al.⁴² as

$$w(x, y) = \sum_{m=1}^{\infty} \sum_{n=1}^{\infty} A_{mn} \sin\left(\frac{m\pi x}{a}\right) \sin\left(\frac{n\pi y}{b}\right) \quad (6.44)$$

where

$$A_{mn} = \frac{16q}{mn\pi^2 Y} \quad (6.45)$$

6.6 Numerical Examples

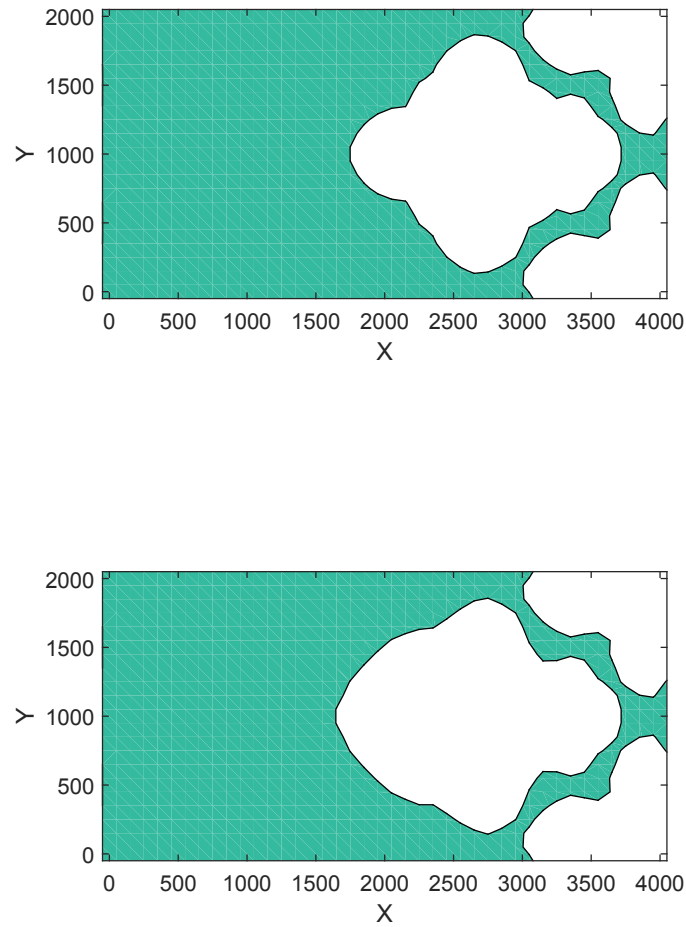


Figure 6.4: Optimized topology (top view) of the piezoelectric layer of an EHD subjected to point load at free end. (a) 100 nm thick nanoplate; (b) 10 nm thick nanoplate.

6.6 Numerical Examples

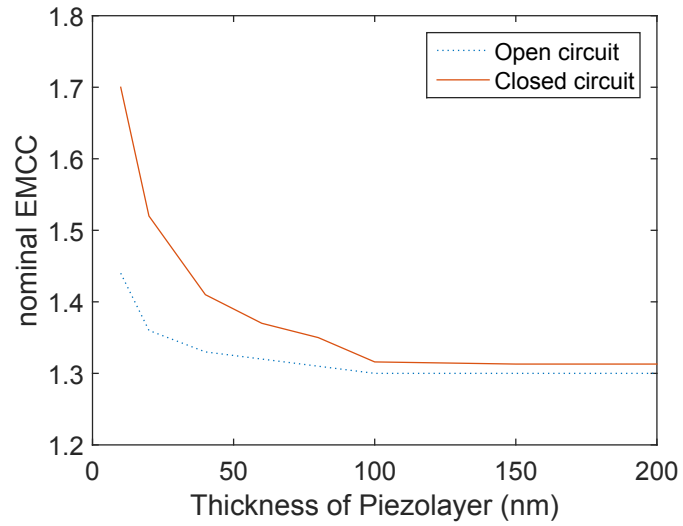


Figure 6.5: The variation of nominal EMCC with varying thickness of piezo layer in EHD under open and closed circuit conditions.

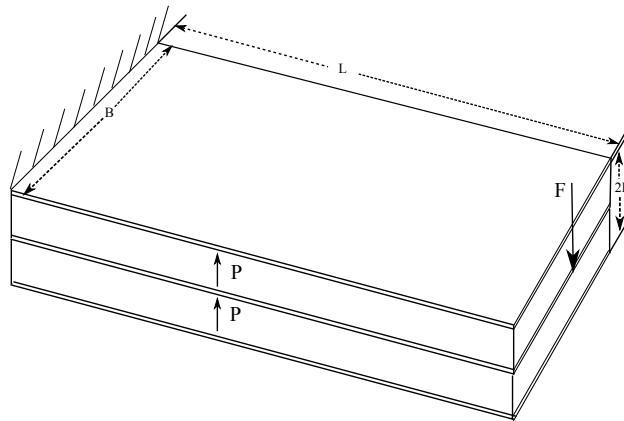


Figure 6.6: A piezoelectric nano cantilever plate subjected to point load, F at free end.

6.6 Numerical Examples

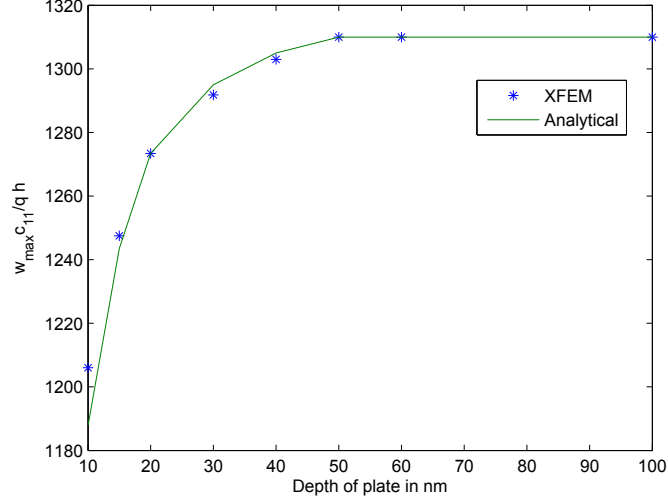


Figure 6.7: Variation of dimensionless maximum deflection with depth of plate.

$$Y = \left[\left(\tilde{c}_{11} + \frac{\tilde{e}_{31}^2}{\tilde{\kappa}_{33}} \right) \frac{h^3}{12} + \left(c_{11}^s + \frac{e_{31}^s \tilde{e}_{31}}{\tilde{\kappa}_{33}} \right) \frac{h^2}{2} \right] X \left[\left(\frac{m\pi}{a} \right)^4 + \left(\frac{n\pi}{b} \right)^4 \right] + \left[\left(\tilde{c}_{12} + \frac{\tilde{e}_{31}^2}{\tilde{\kappa}_{33}} \right) \frac{h^3}{6} + \left(2c_{66}^s + c_{12}^s + \frac{e_{31}^s \tilde{e}_{31}}{\tilde{\kappa}_{33}} \right) h^2 \right] X \left(\frac{m^2 n^2 \pi^4}{a^2 b^2} \right) \quad (6.46)$$

q refers to uniformly distributed load over the plate; $\tilde{c}_{11} = c_{11} - \frac{c_{13}^2}{c_{33}}$, $\tilde{c}_{12} = c_{12} - \frac{c_{13}^2}{c_{33}}$, $\tilde{e}_{31} = e_{31} - \frac{c_{13}e_{33}}{c_{33}}$, $\tilde{\kappa}_{33} = \kappa_{33} - \frac{e_{33}^2}{c_{33}}$ and $m, n = 1, 3, 5 \dots$

The FE model of the piezoelectric nano plate is performed by an equivalent 2D model.

The approximation of the electric potential field is made by discretizing the plate into several sublayers with linear variation of electric potential within each sublayer⁴³. The number of sublayers for electric potential discretization is taken to be ten. The piezoelectric plate considered in this example is poled vertically upwards along the thickness direction as shown in Fig. 6.6. Figure 6.7 shows good agreement between the analytic and FE solutions, where the dimensions of the nano plate were 200×50 nm for the length and width, while the depth was varied from 10 to 100 nm.

Before performing topology optimization, it was determined that the nominal EMCC of the piezoelectric bimorph, where each plate had dimension $600 \times 300 \times 10$ nm, is 1.25 and 1.07 under closed and open circuit conditions respectively.

We then perform topology optimization of the piezoelectric bimorph to maximize energy conversion. Level set optimization method is adopted and the velocity of level sets is determined by solving an adjoint problem. The volume fraction of the optimized topology is 0.69. The optimized topology of the cantilever piezoelectric nano bimorph

6.7 Conclusion

is shown in figure 6.8. The optimized topology has more material concentrated close to the fixed end because of higher strain in this region. The ratio of EMCC of the optimized nano cantilever plate with surface effects to a solid nano bimorph plate without surface effects is 1.6 and 1.32 under closed and open circuit conditions respectively.

Maintaining the ratio between dimensions, the depth of each bimorph plate is increased to 20 nm. The ratio of EMCC of the optimized nano cantilever bimorph to a solid nano bimorph without surface effects is 1.45 and 1.27 under closed and open circuit conditions respectively. The optimized topology of the cantilever piezoelectric nano bimorph is shown in figure 6.8. It is clear from the results that as we approach nano scale the inclusion of surface effects leads to increase in efficiency of a nano plate.

The optimized topology without including surface effects for a bimorph made of plates of size $600 \times 300 \times 10$ nm is shown in figure 6.9. When the ratio between the dimensions of the plate is maintained, the optimal topology remains unchanged provided the surface effects are not included.

The inclusion of surface effects has led to removal of more material close to the fixed end. In figure 6.8(a), material is removed upto 150 nm from the clamped end. In figure 6.8(b), material is removed upto around $(2 \times) 225$ nm from the clamped end, while for a cantilever plate without including surface effects material is removed only upto 250 nm from the clamped end as shown in figure 6.9. In figure 6.9, it can be seen that more material is removed far from the clamped end. When the surface piezoelectric effects are included increase in energy conversion occurs inspite of more material removal compared to a nano piezoelectric plate without surface effects.

6.7 Conclusion

In this work piezoelectric nano structures are used as components of energy harvesting devices. The size dependent behaviour of ZnO has led to increased energy conversion as we approach nano scale. Finite element formulation for analysis of such piezoelectric nano beams and piezoelectric nano plates is presented. The numerical examples exhibit the ability of nano sized piezoelectric structures in increasing the efficiency of EHDs. It is shown that the energy conversion can further be improved by performing optimization of the geometry of the piezoelectric layers. As an initial study the topology optimization is performed for static loads imposed at free end of cantilever energy harvesters. The future work may deal with the behaviour of piezoelectric nano based energy harvesters to vibration in the vicinity of resonant modes.

6.7 Conclusion

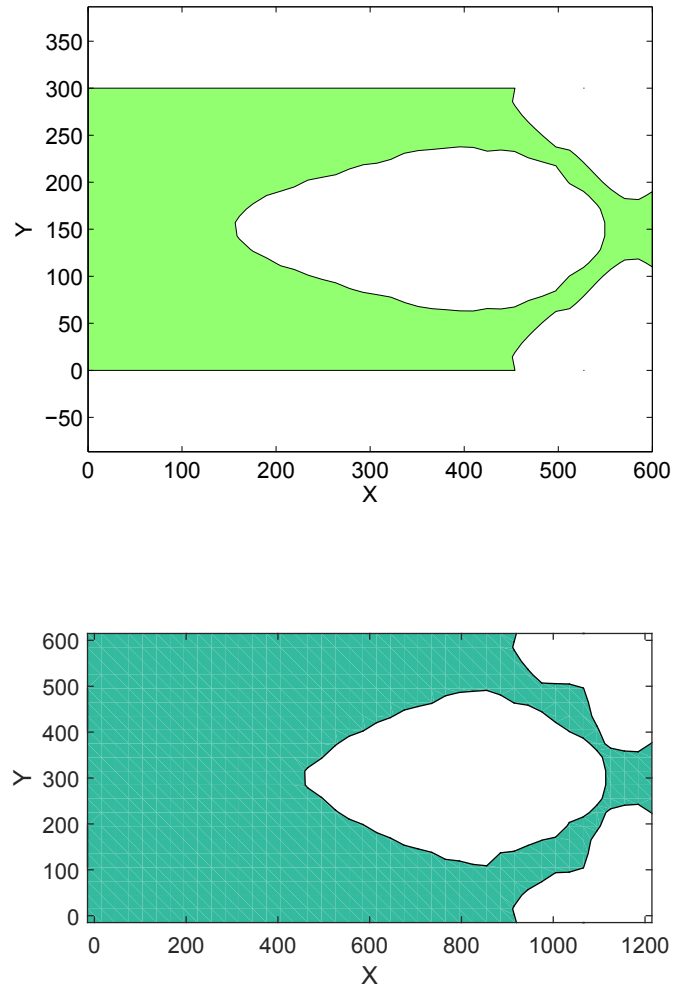


Figure 6.8: (a) Optimized topology (top view) of a $600 \times 300 \times 10$ nm cantilever piezoelectric nano bimorph plate subjected to point load at free end including surface effects; (b) Optimized topology (top view) of a $600 \times 300 \times 10$ nm cantilever piezoelectric nano bimorph plate subjected to point load at free end including surface effects.

6.7 Conclusion

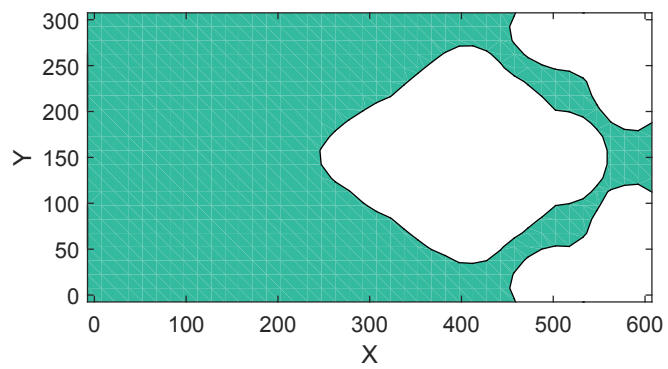


Figure 6.9: Optimized topology (top view) of same geometry but without surface effects.

Chapter 7

Conclusions

7.1 Summary of findings

This dissertation is devoted to develop an algorithm to solve inverse and optimization problems in piezoelectricity. Piezoelectric materials are widely used as sensors, actuators and components in energy harvesters. If there are inherent flaws in these brittle ceramics, they may lead to premature failure during service. The main work in this thesis is the coupled extended finite element method and level set algorithm for solving the inverse problem of detecting flaws in the piezoelectric domain using displacement and electric potential measurements made along the external boundary.

Energy harvesting in nano scale involves converting external kinetic energy into electrical energy based on energy conversion by nano structured piezoelectric materials. Surface elasticity and surface piezoelectricity lead to different behaviour in nano piezoelectric materials compared to their bulk counterparts. The influence of these surface effects on the energy conversion of nano piezoelectric structures is studied. An attempt to increase energy conversion by performing topology optimization of these nano components is made. From the work that has been done, the findings are summarized as follows:

- Inverse problems
 - XFEM-MCS methodology : The coupled XFEM and MCS methodology is adopted to detect the location of an edge crack. The number of parameters to define an edge crack in a two dimensional structure is two. The method is extended to determine an interior crack. In this case the number of parameters to be determined is four. An elliptical void which requires four parameters and an irregular void requiring five parameters are successfully detected by using this methodology. In case of irregular void, an equivalent elliptical void is determined. The number of iterations depend

7.1 Summary of findings

on number of parameters. The method performs with a parametric error of less than 5% for a noise value of upto 4%. In the MCS method, the maximum number of function evaluations suggested is $50 * N^2 + 10$, where N is the number of parameters to be determined.

- XFEM - level set methodology for detecting voids : The XFEM and level set coupled method adopted in shape optimization is extended to detect flaws in two dimensional piezoelectric plate. The domain is initialized with circular voids uniformly distributed all over the domain. The initial level set function gradually changes with iteration to define the shape of the target void. A square void in a domain is detected and then multiple voids are detected. The method does not require initial information about number of voids. The method can detect the number of voids in the domain , their location and approximate shape. The method is also adopted to find location of cracks in which the cracks are approximated as flat elliptical voids. In the examples shown in this work , the method is able to detect (a) a square void, (b) three voids with different shapes, (c) locations of two cracks, (d) location of two cracks and a void in a piezoelectric domain.
- XFEM - level set methodology for detecting inclusions : The XFEM and level set method is extended to determine the location of inclusions in two and three dimensional structures. The domain is initialized with circular inclusions in two dimension and spherical inclusions in three dimension structures. Multiple inclusions are detected in a piezoelectric plate and in a piezoelectric cube. Multiple level sets are adopted to detect inclusions made of more than one material. The multiple level set is adopted to detect the location and approximate shape of two inclusions each made of different material compared to the domain. In case of two and three dimensional inclusion detection problems the method remains stable upto a noise of 5% because of Total Variation regularization.
- Optimization problems
 - Nano elastic structures : The surface effects do not have significant influence on the optimized topology for the minimum compliance objective function. While the optimized topology obtained for the minimum least square error objective function is different before and after including the surface effects. A nano cantilever beam and a nano fixed beam are optimized. When the depth of beams approach 10 nm, stiffness ratio is more than 8% which in turn leads to significant difference in optimum topology with and without surface effects.
 - Nano piezoelectric structures : The surface piezoelectricity plays a significant role in increasing the energy conversion of piezoelectric nano beams

7.2 Scope for future work

and nano plates. The comparison between different electrical boundary conditions show that under closed circuit condition the nominal electromechanical coupling coefficient is better than the one under open circuit condition. A nominal energy conversion of upto 2.3 is obtained when topology optimization of nano piezoelectric beam of depth 10 nm, is optimized under closed circuit condition. The optimization of piezoelectric nano plate layer in an energy harvesting device leads to a nominal electromechanical coupling coefficient of upto 1.7 for a thickness of 10 nm.

7.2 Scope for future work

In the presented work inverse problem of void, crack and inclusion detection in piezoelectric structures is solved. In addition optimization of topology of nano piezoelectric layers in an energy harvesting device is performed to enhance energy conversion. A few possible extensions to the current work can be as follows:

- The inverse problem relies mainly on the static response of the piezoelectric domain. The dynamic response of piezoelectric structure such as resonant frequency or electrical impedance may also be utilised to determine the defects in the domain. Measuring such parameters are quite easier practically compared to measuring displacements and potentials at certain discrete points.
- The XFEM - level set methodology developed for detecting defects is not restricted to electromechanical problems. The method may be extended to other coupled fields like hydromechanical problems.
- In practical applications the external kinetic energy is converted into cyclic oscillations in case of nano energy harvesters. As an initial study the topology optimization of nano piezoelectric plates is performed for static loads imposed at free end of cantilever energy harvesters. The future work may deal with the behaviour of piezoelectric nano based energy harvesters to vibration in the vicinity of resonant modes.
- The XFEM - level set methodology adopted relies on initialization. Several level set methods are proposed to overcome this problem of optimal topology depending on initial topology. So the proposed algorithm for optimization and inverse problems may be further improved to negate initialization step.

Appendix A

A.1 Derivation of shape derivative

Firstly, the total potential energy objective function is considered. The objective function and its constraints are as follows,

$$\text{Minimize } J(\Omega) = \int_{\Omega} \mathbf{u} \cdot \mathbf{b} d\Omega + \int_{\Gamma_N} \mathbf{u} \cdot \mathbf{t} d\Gamma$$

subject to :

$$a(\mathbf{u}, \delta \mathbf{u}, \Omega) + a_s(\mathbf{u}, \delta \mathbf{u}, \Omega) = -l_s(\mathbf{u}, \Omega) + l(\mathbf{u}, \Omega)$$

(i.e.)

$$\begin{aligned} & \int_{\Omega} \boldsymbol{\varepsilon}(\delta \mathbf{u}) : \mathbb{C}^{bulk} : \boldsymbol{\varepsilon}(\mathbf{u}) d\Omega + \int_{\Gamma} (\mathbf{P} \boldsymbol{\varepsilon}(\delta \mathbf{u}) \mathbf{P}) : \boldsymbol{\tau}_s d\Gamma + \\ & \int_{\Gamma} (\mathbf{P} \boldsymbol{\varepsilon}(\delta \mathbf{u}) \mathbf{P}) : \mathbb{C}^s : (\mathbf{P} \boldsymbol{\varepsilon}(\mathbf{u}) \mathbf{P}) d\Gamma = \int_{\Omega} \mathbf{u} \cdot \mathbf{b} d\Omega + \int_{\Gamma_N} \mathbf{u} \cdot \mathbf{t} d\Gamma. \end{aligned}$$

A.1 Derivation of shape derivative

$$\begin{aligned}
& \dot{a}(\mathbf{u}, \mathbf{w}, \Omega) + \dot{a}_s(\mathbf{u}, \mathbf{w}, \Omega) + \dot{l}_s(\mathbf{w}, \Omega) \\
&= \int_{\Omega} \boldsymbol{\varepsilon}(\mathbf{u}') : \mathbb{C}^{bulk} : \boldsymbol{\varepsilon}(\mathbf{w}) d\Omega + \int_{\Omega} \boldsymbol{\varepsilon}(\mathbf{u}) : \mathbb{C}^{bulk} : \boldsymbol{\varepsilon}(\mathbf{w}') d\Omega + \\
& \int_{\Gamma} \boldsymbol{\varepsilon}(\mathbf{u}) : \mathbb{C}^{bulk} : \boldsymbol{\varepsilon}(\mathbf{w}) V_n d\Gamma + \int_{\Gamma} \mathbf{P} \boldsymbol{\varepsilon}(\mathbf{w}') \mathbf{P} : \boldsymbol{\tau}_s d\Gamma + \\
& \int_{\Gamma} (\nabla_s(\mathbf{P} \boldsymbol{\varepsilon}(\mathbf{w}) \mathbf{P} : \boldsymbol{\tau}_s) \cdot \mathbf{n} + \kappa(\mathbf{P} \boldsymbol{\varepsilon}(\mathbf{w}) \mathbf{P} : \boldsymbol{\tau}_s)) V_n d\Gamma + \\
& \int_{\Gamma} (\mathbf{P} \boldsymbol{\varepsilon}(\mathbf{u}') \mathbf{P}) : \mathbb{C}^s : (\mathbf{P} \boldsymbol{\varepsilon}(\mathbf{w}) \mathbf{P}) d\Gamma + \int_{\Gamma} (\mathbf{P} \boldsymbol{\varepsilon}(\mathbf{u}) \mathbf{P}) : \mathbb{C}^s : (\mathbf{P} \boldsymbol{\varepsilon}(\mathbf{w}') \mathbf{P}) d\Gamma + \quad (A.1) \\
& \int_{\Gamma} (\nabla_s(\mathbf{P} \boldsymbol{\varepsilon}(\mathbf{u}) \mathbf{P}) : \mathbb{C}^s : \mathbf{P} \boldsymbol{\varepsilon}(\mathbf{w}) \mathbf{P}) \cdot \mathbf{n} V_n d\Gamma + \\
& \int_{\Gamma} (\mathbf{P} \boldsymbol{\varepsilon}(\mathbf{u}) \mathbf{P}) : \mathbb{C}^s : \nabla_s(\mathbf{P} \boldsymbol{\varepsilon}(\mathbf{w}) \mathbf{P}) \cdot \mathbf{n} V_n d\Gamma + \\
& \int_{\Gamma} \kappa(\mathbf{P} \boldsymbol{\varepsilon}(\mathbf{u}) \mathbf{P} : \mathbb{C}^s : \mathbf{P} \boldsymbol{\varepsilon}(\mathbf{w}) \mathbf{P}) V_n d\Gamma.
\end{aligned}$$

$$\begin{aligned}
\dot{l}(\mathbf{w}, \Omega) &= \int_{\Omega} \mathbf{w}' \cdot \mathbf{b} d\Omega + \int_{\Gamma} \mathbf{w} \cdot \mathbf{b} V_n d\Gamma + \int_{\Gamma_N} \mathbf{w}' \cdot \mathbf{t} d\Gamma \\
&+ \int_{\Gamma_N} (\nabla(\mathbf{w} \cdot \mathbf{t}) \cdot \mathbf{n} + \kappa \mathbf{w} \cdot \mathbf{t}) V_n d\Gamma \quad (A.2)
\end{aligned}$$

$$J = \int_{\Omega} \mathbf{u}' \cdot \mathbf{b} d\Omega + \int_{\Gamma} \mathbf{u} \cdot \mathbf{b} V_n d\Gamma + \int_{\Gamma_N} (\nabla(\mathbf{u} \cdot \mathbf{t}) \cdot \mathbf{n} + \kappa \mathbf{u} \cdot \mathbf{t}) V_n d\Gamma. \quad (A.3)$$

The Lagrangian of the objective functional is,

$$L = J + l(\mathbf{w}, \Omega) - a(\mathbf{u}, \mathbf{w}, \Omega) - a_s(\mathbf{u}, \mathbf{w}, \Omega) - l_s(\mathbf{w}, \Omega). \quad (A.4)$$

The material derivative of the Lagrangian is defined as ,

$$\dot{L} = \dot{J} + \dot{l}(\mathbf{w}, \Omega) - \dot{a}(\mathbf{u}, \mathbf{w}, \Omega) - \dot{a}_s(\mathbf{u}, \mathbf{w}, \Omega) - \dot{l}_s(\mathbf{w}, \Omega). \quad (A.5)$$

A.1 Derivation of shape derivative

All the terms that contain \mathbf{w}' in the material derivative of Lagrangian are collected and the sum of these terms is set to zero, to get the weak form of the state equation,

$$\begin{aligned} \int_{\Omega} \mathbf{w}' \cdot \mathbf{b} \, d\Gamma + \int_{\Gamma_N} \mathbf{w}' \cdot \mathbf{t} \, d\Gamma &= \int_{\Omega} \boldsymbol{\varepsilon}(\mathbf{u}) : \mathbb{C}^{bulk} : \boldsymbol{\varepsilon}(\mathbf{w}') \, d\Omega \\ &+ \int_{\Gamma} \mathbf{P}\boldsymbol{\varepsilon}(\mathbf{w}')\mathbf{P} : \boldsymbol{\tau}_s \, d\Gamma \\ &+ \int_{\Gamma} (\mathbf{P}\boldsymbol{\varepsilon}(\mathbf{u})\mathbf{P} : \mathbb{C}^s : \mathbf{P}\boldsymbol{\varepsilon}(\mathbf{w}')\mathbf{P}) \, d\Gamma. \end{aligned} \quad (\text{A.6})$$

All the terms that contain \mathbf{u}' in the material derivative of Lagrangian are collected and the sum of these terms is set to zero, to get the weak form of the adjoint equation,

$$\begin{aligned} \int_{\Omega} \mathbf{u}' \cdot \mathbf{b} \, d\Gamma + \int_{\Gamma_N} \mathbf{u}' \cdot \mathbf{t} \, d\Gamma &= \int_{\Omega} \boldsymbol{\varepsilon}(\mathbf{u}') : \mathbb{C}^{bulk} : \boldsymbol{\varepsilon}(\mathbf{w}) \, d\Omega + \\ &\int_{\Gamma} (\mathbf{P}\boldsymbol{\varepsilon}(\mathbf{u}')\mathbf{P} : \mathbb{C}^s : \mathbf{P}\boldsymbol{\varepsilon}(\mathbf{w})\mathbf{P}) \, d\Gamma. \end{aligned} \quad (\text{A.7})$$

Considering that Γ_N and Γ_D are not modified in the optimization process and assuming that the body forces are zero, the shape derivative of the objective functional can be obtained from equation B.9,

$$J' = \int_{\Gamma_H} G \cdot V_n \, d\Gamma \quad (\text{A.8})$$

where,

$$\begin{aligned} G &= - \int_{\Gamma} \boldsymbol{\varepsilon}(\mathbf{u}) : \mathbb{C}^{bulk} : \boldsymbol{\varepsilon}(\mathbf{w}) \, d\Gamma - \int_{\Omega} \kappa(\mathbf{P}\boldsymbol{\varepsilon}(\mathbf{w})\mathbf{P} : \boldsymbol{\tau}_s) \, d\Gamma \\ &- \int_{\Gamma} \kappa(\mathbf{P}\boldsymbol{\varepsilon}(\mathbf{u})\mathbf{P} : \mathbb{C}^s : \mathbf{P}\boldsymbol{\varepsilon}(\mathbf{w})\mathbf{P}) \, d\Gamma \end{aligned} \quad (\text{A.9})$$

The G obtained can be considered as the negative of velocity, V_n required in order to optimize the level set function. Therefore,

$$J' = - \int_{\Gamma_H} G^2 \, d\Gamma. \quad (\text{A.10})$$

From the above equation it is evident that the derivative is negative (i.e.) it ensures decrease in the objective function with iterations.

A.1 Derivation of shape derivative

If the objective function is a least square error compared to target displacement as shown below,

$$J(\Omega) = \left(\int_{\Gamma_N} |\mathbf{u} - \mathbf{u}_0|^2 d\Gamma \right)^{\frac{1}{2}} \quad (\text{A.11})$$

$$\begin{aligned} \dot{J} = c_0 \cdot \left(\int_{\Gamma_N} 2|\mathbf{u} - \mathbf{u}_0| \mathbf{u}' d\Gamma + \int_{\Gamma_N} (\nabla(|\mathbf{u} - \mathbf{u}_0|^2) \cdot \mathbf{n} \right. \\ \left. + \kappa |\mathbf{u} - \mathbf{u}_0|^2) V_n d\Gamma \right). \end{aligned} \quad (\text{A.12})$$

Substituting in equation B.9 and collecting terms with \mathbf{u}' , the weak form of the adjoint can be obtained as,

$$\begin{aligned} c_0 \int_{\Gamma_N} 2|\mathbf{u} - \mathbf{u}_0| \mathbf{u}' d\Gamma = \int_{\Omega} \boldsymbol{\varepsilon}(\mathbf{u}') \mathbb{C}^{bulk} \boldsymbol{\varepsilon}(\mathbf{w}) d\Omega \\ + \int_{\Gamma} (\mathbf{P} \boldsymbol{\varepsilon}(\mathbf{u}') \mathbf{P} : \mathbb{C}^s : \mathbf{P} \boldsymbol{\varepsilon}(\mathbf{w}) \mathbf{P}) d\Gamma \end{aligned} \quad (\text{A.13})$$

where,

$$c_0 = \frac{1}{2} \left(\int_{\Gamma_N} |\mathbf{u} - \mathbf{u}_0|^2 d\Gamma \right)^{-\frac{1}{2}} \quad (\text{A.14})$$

Appendix B

B.1 Derivation of adjoint problem

The objective function and its constraints are as follows,

$$\text{Minimize } J(\Phi) = \frac{1}{k^2} = \frac{\Pi_e}{\Pi_d} \quad (\text{B.1})$$

$$\text{Subject to } \int_{\Omega} d\Omega - \bar{V} = 0 \quad (\text{B.2})$$

$$a(\mathbf{u}, \boldsymbol{\phi}, \delta \mathbf{u}, \boldsymbol{\delta \phi}) + a_s(\mathbf{u}, \boldsymbol{\phi}, \delta \mathbf{u}, \boldsymbol{\delta \phi}) = -l_s(\delta \mathbf{u}, \boldsymbol{\delta \phi}) + l(\delta \mathbf{u}, \boldsymbol{\delta \phi}) \quad (\text{B.3})$$

$$\begin{aligned} \dot{a}(\mathbf{u}, \boldsymbol{\phi}, \mathbf{w}, \boldsymbol{\psi}) = & \int_{\Omega} \boldsymbol{\varepsilon}^T(\mathbf{u}') : \mathbb{C}^{bulk} : \boldsymbol{\varepsilon}(\mathbf{w}) d\Omega + \int_{\Omega} \boldsymbol{\varepsilon}^T(\mathbf{u}) : \mathbb{C}^{bulk} : \boldsymbol{\varepsilon}(\mathbf{w}') d\Omega + \\ & - \int_{\Omega} \boldsymbol{\varepsilon}(\mathbf{u}')^T : \mathbf{e}^T : \mathbf{E}(\boldsymbol{\psi}) d\Omega - \int_{\Omega} \boldsymbol{\varepsilon}(\mathbf{u})^T : \mathbf{e}^T : \mathbf{E}(\boldsymbol{\psi}') d\Omega - \int_{\Gamma} \boldsymbol{\varepsilon}(\mathbf{u})^T : \mathbf{e}^T : \mathbf{E}(\boldsymbol{\psi}) \cdot \mathbf{V}_n d\Gamma \\ & \int_{\Gamma} \boldsymbol{\varepsilon}^T(\mathbf{u}) : \mathbb{C}^{bulk} : \boldsymbol{\varepsilon}(\mathbf{w}) \cdot \mathbf{V}_n d\Gamma - \int_{\Omega} \mathbf{E}(\boldsymbol{\phi}')^T : \mathbf{e}^{bulk} : \boldsymbol{\varepsilon}(\mathbf{w}) d\Omega - \\ & \int_{\Omega} \mathbf{E}(\boldsymbol{\phi})^T : \mathbf{e}^{bulk} : \boldsymbol{\varepsilon}(\mathbf{w}') d\Omega - \int_{\Gamma} \mathbf{E}(\boldsymbol{\phi})^T : \mathbf{e}^{bulk} : \boldsymbol{\varepsilon}(\mathbf{w}) \cdot \mathbf{V}_n d\Gamma - \int_{\Omega} \mathbf{E}(\boldsymbol{\phi}')^T : \boldsymbol{\kappa} : \mathbf{E}(\boldsymbol{\psi}) d\Omega - \\ & \int_{\Omega} \mathbf{E}(\boldsymbol{\phi})^T : \boldsymbol{\kappa} : \mathbf{E}(\boldsymbol{\psi}') d\Omega - \int_{\Gamma} \mathbf{E}(\boldsymbol{\phi})^T : \boldsymbol{\kappa} : \mathbf{E}(\boldsymbol{\psi}) \cdot \mathbf{V}_n d\Gamma \end{aligned} \quad (\text{B.4})$$

B.1 Derivation of adjoint problem

$$\begin{aligned}
\dot{a}_s(\mathbf{u}, \boldsymbol{\phi}, \mathbf{w}, \boldsymbol{\psi}) = & \int_{\Gamma} \boldsymbol{\varepsilon}_s(\mathbf{u}')^T : \mathbf{C}_s : \boldsymbol{\varepsilon}_s(\mathbf{w}) d\Gamma + \int_{\Gamma} \boldsymbol{\varepsilon}_s(\mathbf{u})^T : \mathbf{C}_s : \boldsymbol{\varepsilon}_s(\mathbf{w}') d\Gamma + \\
& \int_{\Gamma} [\nabla(\boldsymbol{\varepsilon}_s(\mathbf{u}) : \mathbf{C}_s : \boldsymbol{\varepsilon}_s(\mathbf{w})) \cdot \mathbf{n} + (\boldsymbol{\varepsilon}_s(\mathbf{u}) : \mathbf{C}_s : \boldsymbol{\varepsilon}_s(\mathbf{w})) \cdot \boldsymbol{\eta}] \cdot V_n d\Gamma \\
& - \int_{\Gamma} \boldsymbol{\varepsilon}_s(\mathbf{u}')^T : \mathbf{e}_s^T : \mathbf{E}_s(\boldsymbol{\psi}) d\Gamma - \int_{\Gamma} \boldsymbol{\varepsilon}_s(\mathbf{u})^T : \mathbf{e}_s^T : \mathbf{E}_s(\boldsymbol{\psi}') d\Gamma \\
& \int_{\Gamma} [\nabla(\boldsymbol{\varepsilon}_s(\mathbf{u})^T : \mathbf{e}_s^T : \mathbf{E}_s(\boldsymbol{\psi})) \cdot \mathbf{n} + (\boldsymbol{\varepsilon}_s(\mathbf{u})^T : \mathbf{e}_s^T : \mathbf{E}_s(\boldsymbol{\psi})) \boldsymbol{\eta}] \cdot V_n d\Gamma \\
& - \int_{\Gamma} \mathbf{E}_s(\boldsymbol{\phi}')^T : \mathbf{e}_s : \boldsymbol{\varepsilon}_s(\mathbf{w}) d\Gamma - \int_{\Gamma} \mathbf{E}_s(\boldsymbol{\phi})^T : \mathbf{e}_s : \boldsymbol{\varepsilon}_s(\mathbf{w}') d\Gamma \\
& - \int_{\Gamma} [\nabla(\mathbf{E}_s(\boldsymbol{\phi})^T : \mathbf{e}_s : \boldsymbol{\varepsilon}_s(\mathbf{w})) \cdot \mathbf{n} + (\mathbf{E}_s(\boldsymbol{\phi})^T : \mathbf{e}_s : \boldsymbol{\varepsilon}_s(\mathbf{w})) \boldsymbol{\eta}] \cdot V_n d\Gamma \\
& - \int_{\Gamma} \mathbf{E}_s(\boldsymbol{\phi}')^T : \boldsymbol{\kappa}_s : \mathbf{E}_s \boldsymbol{\psi} d\Gamma - \int_{\Gamma} \mathbf{E}_s(\boldsymbol{\phi})^T : \boldsymbol{\kappa}_s : \mathbf{E}_s(\boldsymbol{\psi}') d\Gamma \\
& - \int_{\Gamma} [\nabla(\mathbf{E}_s(\boldsymbol{\phi})^T : \boldsymbol{\kappa}_s : \mathbf{E}_s(\boldsymbol{\psi})) \cdot \mathbf{n} + (\mathbf{E}_s(\boldsymbol{\phi})^T : \boldsymbol{\kappa}_s : \mathbf{E}_s(\boldsymbol{\psi})) \boldsymbol{\eta}] \cdot V_n d\Gamma
\end{aligned} \tag{B.5}$$

$$\begin{aligned}
l_s(\mathbf{w}) = & \int_{\Gamma} \boldsymbol{\varepsilon}_s(\mathbf{w}') \mathbf{P} : \boldsymbol{\tau}_s d\Gamma + \int_{\Gamma} (\nabla_s(\boldsymbol{\varepsilon}_s(\mathbf{w}) : \boldsymbol{\tau}_s) \cdot \mathbf{n} \\
& + \boldsymbol{\eta}(\boldsymbol{\varepsilon}_s(\mathbf{w}) : \boldsymbol{\tau}_s)) V_n d\Gamma
\end{aligned} \tag{B.6}$$

$$\begin{aligned}
l(\mathbf{w}) = & \int_{\Omega} \mathbf{w}' \cdot \mathbf{b} d\Omega + \int_{\Gamma} \mathbf{w} \cdot \mathbf{b} V_n d\Gamma + \int_{\Gamma_N} \mathbf{w}' \cdot \mathbf{t} d\Gamma \\
& + \int_{\Gamma_N} (\nabla(\mathbf{w} \cdot \mathbf{t}) \cdot \mathbf{n} + \boldsymbol{\eta} \mathbf{w} \cdot \mathbf{t}) V_n d\Gamma
\end{aligned} \tag{B.7}$$

The Lagrangian of the objective functional is,

$$L = J + l(\mathbf{w}) - a(\mathbf{u}, \boldsymbol{\phi}, \mathbf{w}, \boldsymbol{\psi}) - a_s(\mathbf{u}, \boldsymbol{\phi}, \mathbf{w}, \boldsymbol{\psi}) - l_s(\mathbf{w}). \tag{B.8}$$

The material derivative of the Lagrangian is defined as ,

$$\dot{L} = \dot{J} + \dot{l}(\mathbf{w}) - \dot{a}(\mathbf{u}, \boldsymbol{\phi}, \mathbf{w}, \boldsymbol{\psi}) - \dot{a}_s(\mathbf{u}, \boldsymbol{\phi}, \mathbf{w}, \boldsymbol{\psi}) - \dot{l}_s(\mathbf{w}). \tag{B.9}$$

All the terms that contain \mathbf{u}' and $\boldsymbol{\phi}'$ in the material derivative of Lagrangian are collected and the sum of these terms is set to zero, to get the weak form of the adjoint

B.2 Bulk and Surface Stiffness Matrices

equation,

$$\begin{aligned}
& \int_{\Omega} \boldsymbol{\varepsilon}^T(\mathbf{u}') : \mathbb{C}^{bulk} : \boldsymbol{\varepsilon}(\mathbf{w}) d\Omega - \int_{\Omega} \boldsymbol{\varepsilon}(\mathbf{u}')^T : \mathbf{e}^T : \mathbf{E}(\boldsymbol{\psi}) d\Omega - \\
& \int_{\Gamma} \boldsymbol{\varepsilon}_s(\mathbf{u}')^T : \mathbf{C}_s : \boldsymbol{\varepsilon}_s(\mathbf{w}) d\Gamma - \int_{\Gamma} \boldsymbol{\varepsilon}_s(\mathbf{u}')^T : \mathbf{e}_s^T : \mathbf{E}_s(\boldsymbol{\psi}) d\Gamma \\
& = \int_{\Omega} 2C_1 \boldsymbol{\varepsilon}(\mathbf{u}')^T : \mathbb{C}^{bulk} : \boldsymbol{\varepsilon}(\mathbf{u}) d\Omega
\end{aligned} \tag{B.10}$$

$$\begin{aligned}
& \int_{\Omega} \mathbf{E}(\boldsymbol{\phi}')^T : \mathbf{e}^{bulk} : \boldsymbol{\varepsilon}(\mathbf{w}) d\Omega - \int_{\Omega} \mathbf{E}(\boldsymbol{\phi}')^T : \boldsymbol{\kappa} : \mathbf{E}(\boldsymbol{\psi}) d\Omega - \\
& \int_{\Gamma} \mathbf{E}_s(\boldsymbol{\phi}')^T : \mathbf{e}_s : \boldsymbol{\varepsilon}_s(\mathbf{w}) d\Gamma - \int_{\Gamma} \mathbf{E}_s(\boldsymbol{\phi}')^T : \boldsymbol{\kappa}_s : \mathbf{E}_s \boldsymbol{\psi} d\Gamma \\
& = \int_{\Omega} 2C_2 \mathbf{E}(\boldsymbol{\phi}')^T : \boldsymbol{\kappa} : \mathbf{E}(\boldsymbol{\phi}) d\Omega
\end{aligned} \tag{B.11}$$

B.2 Bulk and Surface Stiffness Matrices

The bulk and surface stiffness matrices are defined as follows,

$$\begin{aligned}
\mathbf{K}_{uu}^b &= \int_{\Omega} \mathbf{B}_u^T \{\mathbb{C}\} \mathbf{B}_u d\Omega \\
\mathbf{K}_{uu}^s &= \int_{\Gamma} \mathbf{B}_u^T \mathbf{M}_p^T \{\mathbb{C}^s\} \mathbf{M}_p \mathbf{B}_u d\Gamma
\end{aligned} \tag{B.12}$$

$$\begin{aligned}
\mathbf{K}_{\phi u}^b &= \int_{\Omega} \mathbf{B}_{\phi}^T \{\mathbf{e}\} \mathbf{B}_u d\Omega \\
\mathbf{K}_{\phi u}^s &= \int_{\Gamma} \mathbf{B}_{\phi}^T \mathbf{P}_{\phi}^T \{\mathbf{e}_s\} \mathbf{M}_p \mathbf{B}_u d\Gamma
\end{aligned} \tag{B.13}$$

$$\begin{aligned}
\mathbf{K}_{u\phi}^b &= \int_{\Omega} \mathbf{B}_u^T \{\mathbf{e}\}^T \mathbf{B}_{\phi} d\Omega \\
\mathbf{K}_{u\phi}^s &= \int_{\Gamma} \mathbf{B}_u^T \mathbf{M}_p^T \{\mathbf{e}_s\}^T \mathbf{P}_{\phi} \mathbf{B}_{\phi} d\Gamma
\end{aligned} \tag{B.14}$$

B.3 Finite element modelling of piezoelectric nano energy harvester plate

$$\begin{aligned} K_{\phi\phi}^b &= - \int_{\Omega} \mathbf{B}_{\phi}^T \{\boldsymbol{\kappa}\} \mathbf{B}_{\phi} d\Omega \\ K_{\phi\phi}^s &= - \int_{\Gamma} \mathbf{B}_{\phi}^T P^T \{\boldsymbol{\kappa}_s\} P \mathbf{B}_{\phi} d\Gamma \end{aligned} \quad (\text{B.15})$$

$$\begin{aligned} f_u^s &= \int_{\Gamma} \mathbf{B}_u^T M_p^T \boldsymbol{\tau}_s d\Gamma \\ f_u^{ext} &= \int_{\Gamma_N} \mathbf{N}^T \bar{\mathbf{t}} d\Gamma + \int_{\Omega} \mathbf{N}^T \mathbf{b} d\Omega \end{aligned} \quad (\text{B.16})$$

$$\begin{aligned} g_u^s &= \int_{\Gamma} \mathbf{B}_{\phi}^T P^T \boldsymbol{\omega}_s d\Gamma \\ g_u^{ext} &= - \int_{\Omega} \mathbf{N}^T \mathbf{q} d\Omega \end{aligned}$$

$$\begin{aligned} \mathbf{B}_u &= \begin{pmatrix} N_x & 0 \\ 0 & N_y \\ N_y & N_x \end{pmatrix} \\ \mathbf{B}_{\phi} &= \begin{pmatrix} N_x \\ N_y \end{pmatrix} \end{aligned} \quad (\text{B.17})$$

B.3 Finite element modelling of piezoelectric nano energy harvester plate

Piezoelectric energy harvesters are usually thin flexible structures and so Kirchhoff plate theory adopted in Erturk et al.³³ is employed in this work. A rectangular finite element with three mechanical degrees of freedom (u,v and w in x,y and z directions) is adopted to model displacements in substructure and nano-piezo layer. The transverse displacement is assumed to vary in polynomial form in an element,

$$w = \mathbf{T} \mathbf{a} \quad (\text{B.18})$$

where the polynomial terms,

$$\mathbf{T} = [1 \ x \ y \ x^2 \ xy \ y^2 \ x^3 \ x^2y \ xy^2 \ y^3 \ x^3y \ xy^3] \quad (\text{B.19})$$

\mathbf{a} is a vector of generalized coordinates. w_i in terms of nodal displacements can written as

$$w = \mathbf{N} \mathbf{W} \quad (\text{B.20})$$

B.3 Finite element modelling of piezoelectric nano energy harvester plate

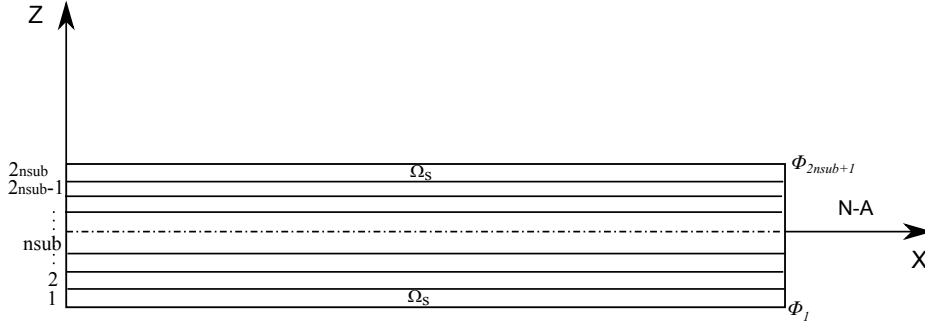


Figure B.1: Discretization for electric potential field with top and bottom layers having surface material properties

where $\mathbf{N} = \mathbf{T}\mathbf{A}^{-1}$, \mathbf{A} is a 12X12 transformation matrix comprising nodal values of \mathbf{T} and its derivatives while \mathbf{W} is a vector of nodal variables. The vector of transverse displacement and rotations and vector of curvatures are as follows,

$$\left[\frac{\partial w}{\partial x} \quad \frac{\partial w}{\partial y} \quad w \right]^T = \mathbf{B}_m \mathbf{W} \quad (\text{B.21})$$

$$\left[\frac{\partial^2 w}{\partial^2 x} \quad \frac{\partial^2 w}{\partial^2 y} \quad 2 \frac{\partial^2 w}{\partial x \partial y} \right]^T = \mathbf{B}_u \mathbf{W} \quad (\text{B.22})$$

Approximation of electric potential field can be obtained by discretizing the nano-piezoelectric plate into sublayers as shown in figure B.1 with linear potential distribution across the thickness for each sublayer as presented in Wang et al⁴³.

The electric potential field across the thickness can be defined as,

$$\phi^k(z) = \mathbf{N}_\phi^k \bar{\phi}^k \quad (\text{B.23})$$

where \mathbf{N}_ϕ^k is the shape function of the electric potential function and ϕ^k denotes electric potential at top and bottom surfaces of the sublayer.

$$\mathbf{N}_\phi^k = \frac{1}{t_i} [z - z_i \quad z_{i+1} - z] \quad (\text{B.24})$$

where t_i is the thickness of the sublayer. The electric field for each sublayer element is

$$\mathbf{E}^k = \mathbf{B}_\phi^k \bar{\phi}^k \quad (\text{B.25})$$

where $\mathbf{B}_\phi^k = \frac{1}{t_i} [1 \quad -1]$ and $\bar{\phi}^k = [\phi^k \quad \phi^{k+1}]^T$.

The element mass and stiffness matrices as given in Erturk et al³³ are,

$$\mathbf{M} = \int_{\Omega} \mathbf{B}_m \mathbf{Z}^t \rho \mathbf{Z} \mathbf{B}_m d\Omega \quad (\text{B.26})$$

B.3 Finite element modelling of piezoelectric nano energy harvester plate

$$K = \begin{pmatrix} \int_{\Omega} z^2 \mathbf{B}_u^T \bar{\mathbf{C}} \mathbf{B}_u d\Omega & \int_{\Omega} z \mathbf{B}_u^T \bar{\mathbf{e}}^T \mathbf{B}_{\phi} d\Omega \\ \int_{\Omega} z \mathbf{B}_{\phi}^T \bar{\mathbf{e}} \mathbf{B}_u d\Omega & \int_{\Omega} \mathbf{B}_{\phi}^T \bar{\mathbf{k}} \mathbf{B}_{\phi} d\Omega \end{pmatrix} \quad (\text{B.27})$$

$\bar{\mathbf{C}}$, $\bar{\mathbf{e}}$ and $\bar{\mathbf{k}}$ are the plane stress (2D) constants in terms of 3D material constants³³. The piezoelectric nano plate (PNP) exhibit different surface elastic and surface piezoelectric behaviour compared to the bulk. The PNP may be assumed to be a bulk plate with surface elastic constants and surface piezoelectric constants at the top and bottom sublayers of the discretization for electric potential field.

The surface stiffness matrix may be defined as,

$$K_s = \begin{pmatrix} \int_{\Omega_s} z^2 \mathbf{B}_u^T \bar{\mathbf{C}} + \bar{\mathbf{C}}_s \mathbf{B}_u d\Omega_s & \int_{\Omega_s} z \mathbf{B}_u^T \bar{\mathbf{e}} + \bar{\mathbf{e}}_s^T \mathbf{B}_p d\Omega_s \\ \int_{\Omega_s} z \mathbf{B}_{\phi}^T \bar{\mathbf{e}} + \bar{\mathbf{e}}_s \mathbf{B}_u d\Omega_s & \int_{\Omega_s} \mathbf{B}_{\phi}^T \bar{\mathbf{k}} + \bar{\mathbf{k}}_s \mathbf{B}_{\phi} d\Omega_s \end{pmatrix} \quad (\text{B.28})$$

where Ω_s corresponds to the top and bottom sublayers, z is the distance of the mid-surface of the top/bottom sublayers from the neutral surface. $\bar{\mathbf{C}}_s$, $\bar{\mathbf{e}}_s$ and $\bar{\mathbf{k}}_s$ are the surface elastic, piezoelectric and dielectric constants.

Bibliography

- [1] A Safari and E K Akdogan. *Piezoelectric and Acoustic Materials for Transducer Applications*. Springer, 2007.
- [2] R Calio, U B Rongala, D Camboni, M Milazzo, C Stefanini, G Petris, and C M Oddo. Piezoelectric energy harvesting solutions. *Sensors*, 14:4755–4790, 2014.
- [3] N Moes, M Cloirec, P Cartraud, and J F Remacle. A computational approach to handle complex microstructure geometries. *Computer Methods in Applied Mechanics and Engineering*, 192:3163–3177, 2003.
- [4] P C Hansen and D P OLeary. The use of the L-curve in the regularization of discrete ill-posed problems. *SIAM J. Sci. Comput*, 14:1487–1503, 1993.
- [5] O Sigmund. A 99 line topology optimization code written in matlab. *Structural and Multidisciplinary Optimization*, 21:120–127, 2001.
- [6] C Mi, S Jun, D A Kouris, and S Y Kim. Atomistic calculations of interface elastic properties in noncoherent metallic bilayers. *Physical Review B*, 77:075425, 2008.
- [7] T Belytschko and T Black. Elastic crack growth in finite elements with minimal remeshing. *International journal for numerical methods in engineering*, 45:60–620, 1999.
- [8] J Baumeister and A Leita. Topics in inverse problems. *Lecture Notes: 25th CBM, IMPA*, July 2005.
- [9] S Osher and J A Sethian. Front propagating with curvature dependent speed: algorithms based on hamilton-jacobi formulations. *Journal of Computational Physics*, 78:12–49, 1988.
- [10] R C Cammarata. Surface and interface stress effects in thin films. *Progress in Surface Science*, 46(1):1–38, 1994.

BIBLIOGRAPHY

- [11] H S Park, W Cai, H D Espinosa, and H Huang. Mechanics of crystalline nanowires. *MRS Bulletin*, 34(3):178–183, 2009.
- [12] M E Gurtin and A Murdoch. A continuum theory of elastic material surfaces. *Archives of Rational Mechanics and Analysis*, 57:291–323, 1975.
- [13] A Marin, S Bressers, and S Priya. Multiple cell configuration electromagnetic vibration energy harvester. *Journal of Physics D: Applied Physics*, 44:295501, 2011.
- [14] Z L Wang and J Song. Piezoelectric nanogenerators based on zinc oxide nanowire arrays. *Science*, 312:242–246, 2006.
- [15] S Xu, Y Qin, C Xu, Y Wei, and R Yang and Z L Wang. Self-powered nanowire devices. *Nature Nanotechnology*, 5:366–373, 2010.
- [16] G Rus, R Palma, and J L Prez-Aparicio. Optimal measurement setup for damage detection in piezoelectric plates. *International Journal of Engineering Science*, 47:554–572, 2009.
- [17] D Rabinovich, D Givoli, and S Vigdergauz. Xfem-based crack detection scheme using a genetic algorithm. *Computers & Fluids*, 71:1051–1080, 2007.
- [18] H Waisman, E Chatzi, and A W Smyth. Detection and quantification of flaws in structures by the extended finite element method and genetic algorithms. *International Journal for Numerical Methods in Engineering*, 82:303–328, 2010.
- [19] H Waisman E N Chatzi, B Hiriyyur and A W Smyth. Experimental application and enhancement of the xfemga algorithm for the detection of flaws in structures. *Computers and Structures*, 89:556–570, 2011.
- [20] N Moes, J Dolbow, and T Belytschko. A finite element method for crack growth without remeshing. *International Journal for Numerical Methods in Engineering*, 46(1):133–150, 1999.
- [21] N Sukumar, D L Chopp, N Moes, and T Belytschko. Modeling holes and inclusions by level sets in the extended finite-element method. *Computer methods in Applied Mechanics and Engineering*, 190:6183–6200, 2001.
- [22] Elie Chahine, Patrick Laborde, Julien Pommier, Yves Renard, and Michel Salan. *Study of Some Optimal XFEM Type Methods*, volume 5. 2007.
- [23] E Bechet, M Scherzer, and M Kuna. Application of the XFEM to the fracture of piezoelectric materials. *International Journal for Numerical Methods in Engineering*, 77:1535–1565, 2009.

BIBLIOGRAPHY

- [24] H Nguyen Vinh, I Bakar, M A Msekh, J H Song, J Muthu, G Zi, P Le, S Bordas, R Simpson, S Natararajan, T Lahmer, and T Rabczuk. Extended finite element method for dynamic fracture of piezo-electric materials. *Engineering Fracture Mechanics*, 92:19–31, 2012.
- [25] W Huyer and A Neumaier. Global optimization by multilevel coordinate search. *Journal of Global Optimization*, 14:331–355, 1999.
- [26] G. Allaire, F. Jouve, and A. M. Toader. Structural optimization using sensitivity analysis and a level-set method. *Journal of Computational Physics*, 194:363–393, 2004.
- [27] M Y Wang L Li and P Wei. XFEM schemes for level set based structural optimization. *Frontiers of Mechanical Engineering*, 7:335–356, 2012.
- [28] E T Chung, T F Chan, and X C Tai. Electrical impedance tomography using level set representation and total variational regularization. *Journal of Computational Physics*, 205:357–372, 2005.
- [29] L K Nielsen, X C Tai, S I Aanonsen, and M Espedal. A binary level set model for elliptic inverse problems with discontinuous coefficients. *International Journal Of Numerical Analysis And Modeling*, 4(1):74–99, 2007.
- [30] L G Zhou and H Huang. Are surfaces elastically softer or stiffer? *Applied Physics Letters*, 84(11):1940–1942, 2004.
- [31] J Yvonnet, H Le Quang, and Q-C He. An XFEM/level set approach to modelling surface/interface effects and to computing the size-dependent effective properties of nanocomposites. *Computational Mechanics*, 42:119–131, 2008.
- [32] M Farsad, F.J. Vernerey, and H.S.Park. An extended finite element/level set method to study surface effects on the mechanical behavior and properties of nanomaterials. *International Journal for Numerical Methods in Engineering*, 84:1466–1489, 2010.
- [33] C D M Junior, A Erturk, and D J Inman. An electromechanical finite element model for piezoelectric energy harvester plates. *Journal of Sound and Vibration*, 327:9–25, 2009.
- [34] B. Zheng, C.J. Chang, and H.C. Gea. Topology optimization of energy harvesting devices using piezoelectric materials. *Structural and Multidisciplinary Optimization*, 38(1):17–23, 2009.

BIBLIOGRAPHY

- [35] S Chen, S Gonella, W Chen, and W K Liu. A level set approach for optimal design of smart energy harvesters. *Computer Methods in Applied Mechanics and Engineering*, 199:2532–2543, 2010.
- [36] J Y Noh and G H Yoon. Topology optimization of piezoelectric energy harvesting devices considering static and harmonic dynamic loads. *Advances in Engineering Software*, 53:45–60, 2012.
- [37] M T Hoang, J Yvonnet, A Mitrushchenkov, and G Chambaud. First-principles based multiscale model of piezoelectric nanowires with surface effects. *Journal of Applied Physics*, 113(1), 2013.
- [38] Z L Wang and J Song. Piezoelectric nanogenerators based on Zinc Oxide nanowire arrays. *Science*, 312:242–246, 2006.
- [39] S Dai, M Gharbi, P Sharma, and H S Park. Surface piezoelectricity: Size-effects in nanostructures and the emergence of piezoelectricity in non-piezoelectric materials. *Journal of Applied Physics*, 110:104305, 2011.
- [40] S Dai and H S Park. Surface effects on the piezoelectricity of zno nanowires. *Journal of the Physics and Mechanics of Solids*, 61:385–397, 2013.
- [41] Z Yan and L Jiang. Surface effects on the electromechanical coupling and bending behaviours of piezoelectric nanowires. *J. Phys. D: Appl. Phys.*, 44:075404, 2011.
- [42] S Y Wang. Surface effects on the electroelastic responses of a thin piezoelectric plate with nanoscale thickness. *J. Phys. D: Appl. Phys.*, 45:255401, 2012.
- [43] S Y Wang. A finite element model for the static and dynamic analysis of a piezoelectric bimorph. *International Journal of Solids and Structures*, 41:4075–4096, 2004.
- [44] M Li, J Xian Yuan, D Guan, and W Chen. Application of piezoelectric fiber composite actuator to aircraft wing for aerodynamic performance improvement. *Science China technological sciences*, 54:394–408, 2011.
- [45] S W Park, J W Kim, and C S Lee. Effect of injector type on fuel-air mixture formulation of high-speed diesel sprays. *Proceedings of the Institution of Mechanical Engineers, Part D: Journal of Automobile Engineering*, 220:647, 2006.
- [46] Y E Pak. Linear electro-elastic fracture mechanics of piezoelectric materials. *International Journal of Fracture*, 54:79–100, 1992.

BIBLIOGRAPHY

- [47] Q H Qin. *Fracture Mechanics of Piezoelectric materials*. WIT Press, Southampton, Boston, 2001.
- [48] Z Suo, C M Kuo, D M Barnett, and J R Willis. Fracture mechanics for piezoelectric ceramics. *Journal of the mechanics and physics of solids*, 40(4):739–765, 1992.
- [49] H Sosa. Plane problems in piezoelectric media with defects. *International Journal of Solids and Structures*, 28(4):491–505, 1991.
- [50] X L Xu and R K N D Rajapakse. Analytical solution for an arbitrarily oriented void/crack and fracture of piezoceramics. *Acta Materialia*, 47(6):1735–1747, 1999.
- [51] M Kuna. Fracture mechanics of piezoelectric materials ? where are we right now? *Engineering Fracture Mechanics*, 77:3635–3647, 2010.
- [52] Marco Enderlein, A Ricoeur, and M Kuna. Finite element techniques for dynamic crack analysis in piezoelectrics. *International Journal of Fracture*, 134:191–208, 2005.
- [53] M Kaltenbacher. *Numerical Simulation of Mechatronic Sensors and Actuators*. Springer, 2007.
- [54] M Kuna. Finite element analyses of cracks in piezoelectric structures - a survey. *Computer Aided Design*, 76:725–745, 2006.
- [55] T Rabczuk and T Belytschko. Cracking particles: a simplified meshfree method for arbitrary evolving cracks. *International Journal for Numerical Methods in Engineering*, 61(13):2316–2343, 2004.
- [56] T Rabczuk and T Belytschko. A three dimensional large deformation meshfree method for arbitrary evolving cracks. *Computer Methods in Applied Mechanics and Engineering*, 196(29-30):2777–2799, 2007.
- [57] X Zhuang, C Augarde, and K Mathisen. Fracture modelling using meshless methods and level sets in 3d: framework and modelling. *International Journal for Numerical Methods in Engineering*, 92:969–998, 2012.
- [58] T Rabczuk, R Gracie, J H Song, and T Belytschko. Immersed particle method for fluid-structure interaction. *International Journal for Numerical Methods in Engineering*, 81(1):48–71, 2010.
- [59] T Belytschko, Y Y Lu, and L Gu. Element-free galerkin method. *International Journal for Numerical Methods in Engineering*, 37:229–256, 1994.

BIBLIOGRAPHY

- [60] T Rabczuk, S Bordas, and G Zi. On three-dimensional modelling of crack growth using partition of unity methods. *Computers Structures*, 88(23-24):1391–1411, 2010.
- [61] X Zhuang, C Heaney, and C Augarde. On error control in the element-free galerkin method. *Engineering Analysis with Boundary Elements*, 36:351–360, 2012.
- [62] X Zhuang and C Augarde. Aspects of the use of orthogonal basis functions in the element free galerkin method. *International Journal for Numerical Methods in Engineering*, 81:366–380, 2010.
- [63] X Liu, Y Deng, Z Zeng, L Udpa, and S S Udpa. Model-based inversion technique using element-free galerkin method and state space search. *Magnetics, IEEE Transactions*, 45(3):1486–1489, 2009.
- [64] J M Melenk and I Babuska. The partition of unity finite element method: basic theory and applications. *Computer methods in Applied Mechanics and Engineering*, 139(1-4):289–314, 1996.
- [65] M Stolarska, D L Chopp, N Moes, and T Belytschko. Modeling crack growth by level sets in the extended finite element method. *International Journal for Numerical Methods in Engineering*, 51:943–960, 2001.
- [66] L Chen, T Rabczuk, S Bordas, G R Liu, K Y Zeng, and P Kerfriden. Extended finite element method with edge-based strain smoothing (esm-xfem) for linear elastic crack growth. *Computer Methods in Applied Mechanics and Engineering*, 209-212(4):250–265, 2012.
- [67] T Lahmer, B Kaltenbacher, and V Schulz. Optimal measurement selection for piezoelectric material tensor identification. *Inverse Problems in Science and Engineering*, 16:369–387, 2010.
- [68] D R Jones, C D Perttunen, and B E Stuckman. Lipschitzian optimization without the lipschitz constant. *Journal of Optimization Theory and Application*, 79(1):157–181, 1993.
- [69] E Bechet, H Minnebol, N Moes, and B Burgardt. Improved implementation and robustness study of the x-fem for stress analysis around cracks. *International journal for numerical methods in engineering*, 64:1033–1056, 2005.
- [70] V Piefort and A Pneumont. Finite element modeling of piezoelectric structures. *Active Structures Laboratory. ULBCP*, 165/42:1959–1977, 2001.

BIBLIOGRAPHY

- [71] C T Kelley. *Iterative Methods of Optimization*. Society for Industrial and Applied Mathematics, Philadelphia, 1999.
- [72] H Qi, D Fang, and Z Yao. Fem analysis of electro-mechanical coupling effect of piezoelectric materials. *Computational Materials Science*, 8:283–290, 1997.
- [73] T Lahmer, M Kaltenbacher, B Kaltenbacher, B Leder, and R Lerch. Fem based determination of real and complex elastic, dielectric and piezoelectric moduli in piezoceramic materials. *IEEE Transactions on Ultrasonics, Ferroelectrics, and Frequency Control*, 55(2):465–475, 2008.
- [74] P Wei and M Y Wang. Structural optimization using sensitivity analysis and a level-set method. *Proceedings of the TMCE 2008*, 2008.
- [75] X. Zhuang, C. Augarde, and K. Mathisen. Fracture modelling using meshless methods and level sets in 3d: framework and modelling. *International Journal for Numerical Methods in Engineering*, 92:969–998, 2012.
- [76] B Kaltenbacher, T Lahmer, M Mohr, and M Kaltenbacher. Pde based determination of piezoelectric material tensors. *European Journal of Applied Mathematics*, 17:383–416, 2006.
- [77] M Burger and S J Osher. A survey on level set methods for inverse problems and optimal design. *European Journal of Applied Mathematics*, null:263–301, 2005.
- [78] L. Burianova, C R Bowen, M Prokopova, and M Sulc. Laser interferometric displacement measurements of multi-layer actuators and pzt ceramics. *Ferroelectrics*, 320:161–169, 2005.
- [79] T. Martin, F. Pigache, and S. Martin. Measurement of the electric potential distribution on piezoelectric ceramic surface. *IEEE 11th International Workshop of Electronics, Control, Measurement, Signals and their application to Mechatronics (ECMSM)*, pages 1–5, June 2013.
- [80] C. Vogel. *Computational Methods for Inverse Problems*. Society for Industrial and Applied Mathematics, 2002.
- [81] L Reichela and H Sadok. A new L-curve for ill-posed problems. *Journal of Computational and Applied Mathematics*, 219:493–508, 2008.
- [82] M. Rezghi and S. Mohammad Hosseini. A new variant of L-curve for Tikhonov regularization. *Journal of Computational and Applied Mathematics*, 231:914–924, 2009.

BIBLIOGRAPHY

- [83] D. Àlvarez, O. Dorn, N. Irishina, and M. Moscoso. Crack reconstruction using a level-set strategy. *Journal of Computational Physics*, 228(16):5710–5721, 2009.
- [84] R. W. Zhang, L. B. He, H. J. Zhu, and P. Yang. Uncertainty evaluation of piezo-electric constant measurement based on dynamic resonance method. *Symposium on Piezoelectricity, Acoustic Waves and Device Applications (SPAWDA)*, 2013, pages 1–5, Oct 2013.
- [85] Y Xia, P Yang, Y Sun, Y Wu, B Mayers, B Gates, Y Yin, F Kim, and H Yan. One-dimensional nanostructures: synthesis, characterization, and applications. *Advanced Materials*, 15(5):353–389, 2003.
- [86] C M Lieber and Z L Wang. Functional nanowires. *MRS Bulletin*, 32:99–108, 2007.
- [87] W Haiss. Surface stress of clean and adsorbate-covered solids. *Reports on Progress in Physics*, 64:591–648, 2001.
- [88] H S Park, K Gall, and J A Zimmerman. Deformation of FCC nanowires by twinning and slip. *Journal of the Mechanics and Physics of Solids*, 54(9):1862–1881, 2006.
- [89] H S Park, K Gall, and J A Zimmerman. Shape memory and pseudoelasticity in metal nanowires. *Physical Review Letters*, 95:255504, 2005.
- [90] W Liang, M Zhou, and F Ke. Shape memory effect in Cu nanowires. *Nano Letters*, 5(10):2039–2043, 2005.
- [91] C R Weinberger and W Cai. Plasticity of metal nano wires. *Journal of Materials Chemistry*, 22(8):3277–3292, 2012.
- [92] J Yvonnet, A Mitrushchenkov, G Chambaud, and Q-C He. Finite element model of ionic nanowires with size-dependent mechanical properties determined by *ab initio* calculations. *Computer Methods in Applied Mechanics and Engineering*, 200:614–625, 2011.
- [93] W Gao, SW Yu, and GY Huang. Finite element characterization of the size-dependent mechanical behaviour in nanosystems. *Nanotechnology*, 17(4):1118–1122, 2006.
- [94] M Farsad, F J Vernerey, and H S Park. An extended finite element/level set method to study surface effects on the mechanical behavior and properties of nanomaterials. *International Journal for Numerical Methods in Engineering*, 84:1466–1489, 2010.

BIBLIOGRAPHY

- [95] A Javili and P Steinmann. A finite element framework for continua with boundary energies. part I: the two-dimensional case. *Computer Methods in Applied Mechanics and Engineering*, 198:2198–2208, 2009.
- [96] A Javili and P Steinmann. A finite element framework for continua with boundary energies. part II: the three-dimensional case. *Computer Methods in Applied Mechanics and Engineering*, 199:755–765, 2010.
- [97] H S Park, P A Klein, and G J Wagner. A surface cauchy-born model for nanoscale materials. *International Journal for Numerical Methods in Engineering*, 68:1072–1095, 2006.
- [98] H S Park and P A Klein. Surface cauchy-born analysis of surface stress effects on metallic nanowires. *Physical Review B*, 75:085408, 2007.
- [99] H S Park and P A Klein. A surface cauchy-born model for silicon nanostructures. *Computer Methods in Applied Mechanics and Engineering*, 197:3249–3260, 2008.
- [100] A Javili, A McBride, and P Steinmann. Thermomechanics of solids with lower-dimensional energetics: on the importance of surface, interface, and curve structures at the nanoscale. a unifying review. *Applied Mechanics Reviews*, 65:010802, 2012.
- [101] H S Park and P A Klein. Surface stress effects on the resonant properties of metal nanowires: The importance of finite deformation kinematics and the impact of the residual surface stress. *Journal of the Mechanics and Physics of Solids*, 56:3144–3166, 2008.
- [102] S Natarajan, S Chakraborty, M Thangavel, S Bordas, and T Rabczuk. Size-dependent free flexural vibration behavior of functionally graded nanoplates. *Computational Materials Science*, 65:74–80, 2012.
- [103] G Yun and H S Park. Surface stress effects on the bending properties of fcc metal nanowires. *Physical Review B*, 79:195421, 2009.
- [104] J He and C M Lilley. Surface effect on the elastic behavior of static bending nanowires. *Nanoletters*, 8(7):1798–1802, 2008.
- [105] M P Bendsoe and N Kikuchi. Generating optimal topologies in structural design using a homogenization method. *Computer Methods in Applied Mechanics and Engineering*, 71:197–224, 1988.

BIBLIOGRAPHY

- [106] Z Luo, M Y Wang, S Wang, and P Wei. A level set-based parameterization method for structural shape and topology optimization. *International Journal for Numerical Methods in Engineering*, 76(1):1–26, October 2008.
- [107] S J Osher and J A Sethian. Fronts propagating with curvature dependent speed: algorithms based on the Hamilton-Jacobi formulation. *Journal of Computational Physics*, 79:12–49, 1988.
- [108] J A Sethian and A Wiegmann. Structural boundary design via level set and immersed interface methods. *Journal of Computational Physics*, 163:489–528, 2000.
- [109] S Osher and F Santosa. Level-set methods for optimization problem involving geometry and constraints: I. frequencies of a two-density inhomogeneous drum. *Journal of Computational Physics*, 171:272–288, 2001.
- [110] M Y Wang, X M Wang, and D M Guo. A level set method for structural topology optimization. *Computer Methods in Applied Mechanics and Engineering*, 192:217–224, 2003.
- [111] S S Nanthakumar, Tom Lahmer, and Timon Rabczuk. Detection of multiple flaws in piezoelectric structures using XFEM and level sets. *Computer Methods in Applied Mechanics and Engineering*, 275:98–112, 2014.
- [112] K K Choi and N H Kim. *Structural sensitivity analysis and optimization*. Springer, New York, 2005.
- [113] N P van Dijk, K Maute, M Langelaar, and F van Keulen. Level-set methods for structural topology optimization: a review. *Struct Multidisc Optim*, 48:437–472, 2013.
- [114] R Malladi, J A Sethian, and B C Vemuri. Shape modeling with front propagation: A level set approach. *IEEE Transactions on Pattern Analysis and Machine Intelligence*, 17:158–175, 1995.
- [115] H G Craighead. Nanoelectromechanical systems. *Science*, 290:1532–1535, 2000.
- [116] K L Ekinici and M L Roukes. Nanoelectromechanical systems. *Review of Scientific Instruments*, 76:061101, 2005.
- [117] X M H Huang, C A Zorman, M Mehregany, and M L Roukes. Nanodevice motion at microwave frequencies. *Nature*, 42:496, 2003.

BIBLIOGRAPHY

- [118] C Ji and H S Park. Geometric effects on the inelastic deformation of metal nanowires. *Applied Physics Letters*, 89:181916, 2006.
- [119] D J Inman S Priya. *Energy Harvesting Technologies*. Springer, 2009.
- [120] S.Priya. Advances in energy harvesting using low profile piezoelectric transducers. *Journal of Electroceramics*, 19:167–184, 2007.
- [121] H A Sodano, D J Inman, and G Park. A review of power harvesting from vibration using piezoelectric materials. *Shock Vibr Dig*, 36:197–205, 2004.
- [122] E C N Silva and N Kikuchi. Design of piezoelectric transducers using topology optimization. *Journal of Electroceramics*, 19:167–184, 2007.
- [123] C J Rupp, A Evgrafov, k MAute, and M L Dunn. Design of piezoelectric energy harvesting systems: A topology optimization approach based on multi-layer plates and shells. *Journal of Intelligent Material Systems and Structures*, 16:1923–1939, 2009.
- [124] P H Nakasone and E C N Silva. Design of piezoelectric energy harvesting devices and laminate structures by applying topology optimization, modeling, signal processing, and control for smart structures. *Proc. of SPIE*, pages 728601–728611, 2009.
- [125] F Wein, M Kaltenbacher, and M Stingl. Topology optimization of a cantilevered piezoelectric energy harvester using stress norm constraints. *Structural and Multidisciplinary Optimization*, 48:173–185, 2013.
- [126] M H Zhao, Z L Wang, and S X Mao. Piezoelectric characterization of individual Zinc oxide nnnobelt probed by piezoresponse force microscope. *Nanoletters*, 4(4):587–590, 2004.
- [127] H D Espinosa, R A Bernal, and M Minary-Jolandan. A review of mechanical and electromechanical properties of piezoelectric nanowires. *Advanced Materials*, 24:4656–4675, 2012.
- [128] A Mitrushchenkov, R Linguerri, and G Chambaud. Piezoelectric properties of AlN, ZnO, and $\text{Hg}_x\text{Zn}_{1-x}\text{O}$ nanowires by first-principles calculations. *Journal of Physical Chemistry C*, 113:6883–6886, 2009.
- [129] K Momeni, G M Odegard, and R S Yassar. Finite size effect on the piezoelectric properties of zno nanobelts: a molecular dynamics approach. *Acta Materialia*, 60:5117–5124, 2012.

BIBLIOGRAPHY

- [130] Z Yan and L Y Jiang. The vibrational and buckling behaviors of piezoelectric nanobeams with surface effects. *Nanotechnology*, 22:245703, 2011.
- [131] S S Nanthakumar, N Valizadeh, H S Park, and T Rabczuk. Surface effects on shape and topology optimization of nanostructures. *Computational Mechanics*, 2015.
- [132] M A Trindade and A Benjeddou. Effective electromechanical coupling coefficients of piezoelectric adaptive structures: Critical evaluation and optimization. *Mechanics Of Advanced Materials And Structures*, 16(3):210–223, 2009.
- [133] S Y Wang, K M Lim, B C Khoo, and M Y Wang. An extended level set method for shape and topology optimization. *Journal of Computational Physics*, 221:395–421, 2007.

Curriculum Vitae

Srivilliputtur Subbiah Nanthakumar

Institute of Structural Mechanics

Bauhaus-University Weimar

Marienstrasse 15, 99423 Weimar, Germany

Email: nanthakumar.srivilliputtur.subbiah@uni-weimar.de

Date of Birth: May 5th, 1985

Nationality : Indien

Education and work

- | | |
|----------------|---|
| 2012 - present | PhD, Institut für Struktur Mechanik, Bauhaus Universität Weimar, Germany. |
| 2010 - 2012 | Lecturer, Thiagarajar College of Engineering, Madurai, India. |
| 2008 - 2010 | Engineer (design), TATA Consulting Engineers, Chennai, India. |
| 2006 - 2008 | M.Tech in structural engineering, National Institute of Technology Karnataka, Surathkal, India. |
| 2002 - 2006 | B.E in civil engineering, Mepco Schlenk engineering college, Anna university, Tamilnadu, India. |

Publications

1. S S Nanthakumar, Tom Lahmer, and Timon Rabczuk. Detection of flaws in piezoelectric structures using extended FEM. International Journal for Numerical Methods in Engineering, 96:373389, 2013.
2. S S Nanthakumar, Tom Lahmer, and Timon Rabczuk. Detection of multiple flaws in piezoelectric structures using XFEM and level sets. Computer Methods in Applied Mechanics and Engineering, 275:98112, 2014.
3. S S Nanthakumar, T Lahmer, X Zhuang, G Zi and T Rabczuk. Detection of material interfaces using a regularized level set method in piezoelectric structures, Inverse Problems in Science and Engineering, 2015.
4. S S Nanthakumar, N Valizadeh, H S Park, and T Rabczuk. Surface effects on shape and topology optimization of nanostructures. Computational Mechanics, 2015.